

International Ultraviolet Explorer  
New Spectral Image Processing System  
Information Manual  
Version 2.0

Prepared By

M.P. Garhart, M.A. Smith, B.E. Turnrose,  
K.L. Levay, and R.W. Thompson

*Computer Sciences Corporation*

## Abstract

This document is intended for use by researchers who wish to analyze data acquired by the *International Ultraviolet Explorer (IUE)* and processed for the *IUE* Final Archive with the New Spectral Image Processing System (NEWSIPS) at either Goddard Space Flight Center (GSFC) or the European Space Agency (ESA) Villafranca del Castillo *IUE* Observatory (VILSPA). The information contained in this document explains the instrument characteristics and the processing methodology and calibration techniques used in the NEWSIPS system to produce the output products available to researchers. This second version of the *IUE* NEWSIPS Information Manual has been updated to include the processing techniques for LWR low-dispersion and LWP, LWR, and SWP high-dispersion data.

# Acknowledgments

The authors wish to acknowledge the efforts of Howard A. Bushouse, Michele De La Peña, and Richard A. Shaw, currently at the Space Telescope Science Institute, and Joy S. Nichols, currently at the California Institute of Technology, who contributed to this document and the Final Archive effort while employed by Computer Sciences Corporation. Credit is also due to C. L. Imhoff and T. Meylan for their thoughtful input and proofreading, and to J. Caplinger for assistance in the preparation of several of the figures. In addition, much support was provided by our European colleagues working at the *IUE* Observatory at VILSPA, as they developed several of the files and algorithms used in the final calibration. We wish to thank the members and participants of the Final Archive Definition Committee, the Development Coordination Group of the *IUE* Three Agencies, and the *IUE* Users' Committee, who provided much useful input towards the Final Archive effort. The basis of the text for Chapter 12 was taken from a document written by the Development Coordination Group. Some of the text, tables, and diagrams for Chapters 2 and 4 were taken directly from the *International Ultraviolet Explorer Image Processing Information Manual, Version 2.0* which was prepared by B. E. Turnrose and R. W. Thompson. The bulk of this manual was taken from the *IUE NEWSIPS Information Manual: Low-Dispersion Data, Version 1.0* written by J. S. Nichols, M. P. Garhart, M. D. De La Peña, and K. L. Levay.

# Table of Contents

<b>1</b>	<b>Introduction</b>	<b>1</b>
1.1	Purpose of Document . . . . .	1
1.2	Philosophy of the IUE Final Archive Image Processing . . . . .	1
1.2.1	Uniform Archive . . . . .	2
1.2.2	New Processing Algorithms and Calibrations . . . . .	3
1.2.3	Core Data Item Verifications . . . . .	4
1.2.4	Community Involvement . . . . .	5
<b>2</b>	<b>Description of IUE Data</b>	<b>6</b>
2.1	Raw Image Data and Label Parameters . . . . .	6
2.2	Spectrograph Geometry . . . . .	7
2.3	Instrumental Resolution . . . . .	27
2.3.1	Low-Dispersion Mode . . . . .	27
2.3.2	High-Dispersion Mode . . . . .	29
<b>3</b>	<b>Data Quality Flag Description</b>	<b>57</b>
<b>4</b>	<b>Raw Image Screening (<i>RAW_SCREEN</i>)</b>	<b>61</b>
4.1	Bright-Spot Detection . . . . .	61
4.2	Microphonic Noise Detection . . . . .	62
4.3	Partial-Read Image Preprocessing . . . . .	66
4.4	Missing Minor Frame Detection . . . . .	66
4.5	DMU Corrupted Pixel Detection . . . . .	67
4.6	Source-Type Determination . . . . .	67
4.7	Serendipitous Spectrum Recognition . . . . .	68
4.8	Background and Continuum Intensity Estimation . . . . .	69
4.9	High-Dispersion Order Registration ( <i>ORDERG</i> ) . . . . .	70
4.9.1	Order Registration Process . . . . .	71
4.9.2	Potential Problem Areas . . . . .	72
4.10	<i>RAW_SCREEN</i> Output . . . . .	73

<b>5</b>	<b>Raw Image Registration (<i>CROSS-CORR</i>)</b>	<b>74</b>
5.1	Registration Fiducial . . . . .	74
5.2	General Method . . . . .	74
5.3	Pattern Matching Algorithm – Step by Step . . . . .	75
5.3.1	Intermediate <i>CROSS-CORR</i> Output . . . . .	77
5.4	Evaluation of the Raw Correlations . . . . .	78
5.5	<i>CROSS-CORR</i> Output . . . . .	81
<b>6</b>	<b>Photometric Correction (<i>PHOTOM</i>)</b>	<b>82</b>
6.1	Construction of the ITFs . . . . .	82
6.1.1	LWP ITF . . . . .	83
6.1.2	LWR ITF . . . . .	84
6.1.3	SWP ITF . . . . .	84
6.1.4	Periodic Noise . . . . .	84
6.2	Determination of the Effective Exposure Times . . . . .	85
6.3	Description of the Photometric Correction . . . . .	86
6.3.1	Determination of the ITF Pixels . . . . .	86
6.3.2	Determination of the Flux Values . . . . .	86
6.4	Associated $\nu$ Flags and Reference Images . . . . .	88
6.4.1	Non-photometrically Corrected Image Regions . . . . .	88
6.4.2	Warning Track . . . . .	88
6.4.3	ITF Artifacts . . . . .	88
6.5	<i>PHOTOM</i> Output . . . . .	89
<b>7</b>	<b>Image Resampling (<i>GEOM</i>)</b>	<b>92</b>
7.1	Corrections Common to Both Dispersions . . . . .	93
7.1.1	Measurement of Distortions . . . . .	93
7.1.2	Image Rotation . . . . .	94
7.1.3	Wavelength Linearization . . . . .	94
7.2	Additional Corrections for Low Dispersion . . . . .	98
7.2.1	Aperture Alignment . . . . .	98
7.2.2	Wiggle Corrections . . . . .	98
7.2.3	Large-Aperture Tilt Correction . . . . .	100
7.2.4	Wavelength and Spatial Normalization . . . . .	106
7.3	Additional Corrections for High Dispersion . . . . .	107
7.3.1	Order De-displaying . . . . .	107
7.3.2	Wavelength and Spatial Normalization . . . . .	107
7.3.3	Wiggle Corrections . . . . .	108
7.4	Flux Resampling Algorithm . . . . .	108
7.5	Data Quality ( $\nu$ ) Flag Resampling . . . . .	108
7.6	High-Dispersion Cosmic Ray Detection Algorithm ( <i>COSMIC_RAY</i> ) . . . . .	109
7.7	<i>GEOM</i> Output . . . . .	110

7.7.1	Low-Dispersion . . . . .	110
7.7.2	High-Dispersion . . . . .	110
7.8	<i>COSMIC_RAY</i> Output . . . . .	111
<b>8</b>	<b>Wavelength Calibration (<i>TTDC</i>)</b>	<b>112</b>
8.1	Image Field-Distortions . . . . .	112
8.2	Low-Dispersion Wavelength Calibration . . . . .	114
8.2.1	Parameterization of the Dispersion Relations . . . . .	114
8.2.2	Application of the Dispersion Relations . . . . .	114
8.2.3	1995 Wavelength Calibration Updates . . . . .	117
8.3	High-Dispersion Wavelength Calibration . . . . .	124
8.3.1	Parameterization of Dispersion Relations . . . . .	124
8.3.2	Calculation of the Dispersion Coefficients . . . . .	125
8.3.3	Time and THDA Dependence of the Wavelength Zeropoint . . . . .	126
8.3.4	Checks Against Other Calibrations . . . . .	126
8.3.5	Pertinent Spectrograph Parameters . . . . .	126
8.4	<i>TTDC</i> Output . . . . .	130
8.4.1	Low-Dispersion . . . . .	130
8.4.2	High-Dispersion . . . . .	130
<b>9</b>	<b>Low-Dispersion Flux Extraction (<i>SWET</i>)</b>	<b>131</b>
9.1	Noise Models . . . . .	132
9.2	Background Flux Extraction . . . . .	132
9.3	Spectrum Location and Signal Level . . . . .	133
9.4	Profile Fitting . . . . .	135
9.5	Extraction of Flux and Cosmic Ray Removal . . . . .	136
9.6	One-Dimensional $\nu$ Flag Spectrum . . . . .	137
9.7	<i>SWET</i> Output . . . . .	138
<b>10</b>	<b>High-Dispersion Flux Extraction</b>	<b>140</b>
10.1	Background Flux Determination ( <i>BCKGRD</i> ) . . . . .	140
10.1.1	Pass 1: Cross-Dispersion Swaths . . . . .	140
10.1.2	Pass 2: Dispersion Direction Swaths . . . . .	144
10.1.3	Non-continuum images . . . . .	144
10.1.4	Data Pathology Assessments . . . . .	144
10.1.5	Failure Modes . . . . .	146
10.1.6	Caveat . . . . .	146
10.1.7	<i>BCKGRD</i> Output . . . . .	147
10.2	Spectral Flux Extraction ( <i>EXTRACT</i> ) . . . . .	147
10.2.1	Determination of Echelle-Order Locations . . . . .	148
10.2.2	Description of Spectral Flux Extraction Process . . . . .	148
10.2.3	Noise Models . . . . .	152
10.2.4	One-Dimensional $\nu$ Flag Spectrum . . . . .	153

10.2.5	<i>EXTRACT</i> Output . . . . .	153
<b>11</b>	<b>Calibration of the Net Flux</b>	<b>155</b>
11.1	Low-Dispersion Absolute Flux Calibration . . . . .	155
11.1.1	1985-EPOCH Point Source Calibrations . . . . .	155
11.1.2	Aperture Response Corrections . . . . .	156
11.1.3	Gain Factors . . . . .	157
11.1.4	Time-Dependent Degradation Correction . . . . .	166
11.1.5	Temperature-Dependent Degradation Correction . . . . .	169
11.1.6	Application of Calibrations and Corrections . . . . .	169
11.2	High-Dispersion Absolute Flux Calibration . . . . .	170
11.2.1	Ripple Correction . . . . .	170
11.2.2	Absolute Flux Calibration Function . . . . .	170
11.2.3	Application of Calibrations and Corrections . . . . .	171
<b>12</b>	<b>Final Archive Data Products</b>	<b>173</b>
12.1	FITS File Formats . . . . .	173
12.2	FITS Header Format . . . . .	174
12.2.1	Basic FITS keywords . . . . .	176
12.2.2	Core Data Items . . . . .	177
12.2.3	Original IUE VICAR Label . . . . .	177
12.2.4	NEWSIPS Image Processing History . . . . .	178
12.3	Raw Image FITS File (RILO/RIHI) . . . . .	190
12.4	Linearized Image FITS File (LILO/LIHI) . . . . .	192
12.5	Vector Displacement FITS File (VDLO/VDHI) . . . . .	194
12.6	Low-Dispersion Resampled Image FITS File (SILO) . . . . .	196
12.7	High-Dispersion Resampled Image FITS File (SIHI) . . . . .	198
12.8	Low-Dispersion Merged Extracted Image FITS File (MXLO) . . . . .	202
12.9	High-Dispersion Merged Extracted Image FITS File (MXHI) . . . . .	204
<b>13</b>	<b>Assessing NEWSIPS Data Quality</b>	<b>208</b>
<b>14</b>	<b>Core Data Items</b>	<b>215</b>
14.1	The Sources for Core Data Items . . . . .	215
14.2	The Core Data Items . . . . .	215
<b>A</b>	<b>High-Dispersion Background Determination Algorithm (BCKGRD)</b>	<b>246</b>
A.1	Overview . . . . .	246
A.2	Background Determination: Step-by-Step . . . . .	247
A.2.1	Data Screening . . . . .	247
A.2.2	Pass 1: Cross-Dispersion Swath Grid . . . . .	249
A.2.3	Pass 2: Dispersion Direction Swaths . . . . .	253
A.2.4	Non-continuum images . . . . .	253

A.2.5 Data Pathology Assessments . . . . .	253
A.3 Failure Modes . . . . .	257
A.4 Problem Areas . . . . .	257
<b>B Glossary</b>	<b>260</b>
<b>C References</b>	<b>265</b>



# List of Tables

2.1	Officially Adopted Dimensions for the Apertures in Each Spectrograph, Measured on LWP, LWR, and SWP Images . . . . .	7
2.2	Standard Offsets from the Small to the Large Spectrograph Aperture as used by low-dispersion NEWSIPS (in pixels) . . . . .	23
2.3	Approximate Spectral Scales in Each Dispersion Mode . . . . .	23
3.1	$\nu$ Flag Values . . . . .	58
4.1	Hot Pixels in the LWR Camera . . . . .	63
4.2	Hot Pixels in the SWP Camera . . . . .	63
4.3	Permanent Blemishes in the LWP and LWR Cameras . . . . .	64
4.4	Low-Dispersion Camera Artifacts ( $\text{\AA}$ ) . . . . .	64
4.5	High-Dispersion Camera Artifacts . . . . .	65
4.6	Source Type Determination Values (number of pixels) . . . . .	67
4.7	FES Coordinates of the Apertures . . . . .	69
4.8	Low-Dispersion Wavelength Regions for DN Measurements ( $\text{\AA}$ ) . . . . .	70
5.1	Number of Fiducial Locations . . . . .	77
6.1	ITF Effective Exposure Times (seconds) . . . . .	85
7.1	LWP True Reseau Positions in X Direction . . . . .	95
7.2	LWP True Reseau Positions in Y Direction . . . . .	95
7.3	LWR True Reseau Positions in X Direction . . . . .	96
7.4	LWR True Reseau Positions in Y Direction . . . . .	96
7.5	SWP True Reseau Positions in X Direction . . . . .	97
7.6	SWP True Reseau Positions in Y Direction . . . . .	97
8.1	Low-Dispersion Pt-Ne Line Libraries . . . . .	116
8.2	LWP and SWP Low-Dispersion Time and THDA Coefficients (pre-1990) . .	118
8.3	LWR Low-Dispersion Time and THDA Coefficients . . . . .	118
8.4	LWP and SWP Low-Dispersion Time and THDA Coefficients (post-1990) . .	119
8.5	IRAF Solutions Used for the Wavelength Linearization Step . . . . .	125
8.6	IRAF Solutions Used for Time and Temperature Correlation Step . . . . .	126
8.7	IUE Spectrograph Parameters . . . . .	127

8.8	Approximate Wavelength Ranges for the Echelle Orders - continued on next page . . . . .	128
10.1	Fiducial Line Positions for the Echelle Orders . . . . .	149
10.2	Extraction Slit Lengths for the Echelle Orders - continued on next page . . .	150
11.1	LWP Absolute Calibration . . . . .	158
11.2	LWR ITFA Absolute Calibration . . . . .	159
11.3	LWR ITFB Absolute Calibration . . . . .	160
11.4	SWP Absolute Calibration . . . . .	161
11.5	LWP S/L and T/L Relative Sensitivities* . . . . .	162
11.6	LWR ITFA S/L and T/L Relative Sensitivities* . . . . .	163
11.7	LWR ITFB S/L and T/L Relative Sensitivities* . . . . .	164
11.8	SWP S/L and T/L Relative Sensitivities* . . . . .	165
11.9	Temperature Coefficients and Reference THDAs . . . . .	169
11.10	High-Dispersion Ripple Coefficients . . . . .	171
11.11	High-Dispersion Calibration Function Coefficients . . . . .	171
12.1	Low-Dispersion File Formats . . . . .	175
12.2	High-Dispersion File Formats . . . . .	175
12.3	Summary of the IUE Raw Image VICAR Header . . . . .	178
12.4	RILO/RIHI - Basic FITS Keywords . . . . .	190
12.5	RILO Partial Read - Basic FITS Keywords . . . . .	191
12.6	LILO/LIHI - Basic FITS Keywords . . . . .	193
12.7	VDLO/VDHI - Basic FITS Keywords . . . . .	195
12.8	SILO - Basic FITS Keywords . . . . .	197
12.9	SIHI - Basic FITS Keywords (continued on next page) . . . . .	200
12.10	MXLO - Basic FITS Keywords . . . . .	203
12.11	MXHI - Basic FITS Keywords (continued on next page) . . . . .	206
13.1	Mean ITF THDAs . . . . .	211
A.1	Recourses to Various Pathological Trial Solutions . . . . .	258

# List of Figures

2.1	LWP small-aperture high-dispersion (even orders) format. . . . .	8
2.2	LWP small-aperture high-dispersion (odd orders) format. . . . .	9
2.3	LWP large-aperture high-dispersion (even orders) format. . . . .	10
2.4	LWP large-aperture high-dispersion (odd orders) format. . . . .	11
2.5	LWP large- and small-aperture low-dispersion format. . . . .	12
2.6	LWR small-aperture high-dispersion (even orders) format. . . . .	13
2.7	LWR small-aperture high-dispersion (odd orders) format. . . . .	14
2.8	LWR large-aperture high-dispersion (even orders) format. . . . .	15
2.9	LWR large-aperture high-dispersion (odd orders) format. . . . .	16
2.10	LWR large- and small-aperture low-dispersion format. . . . .	17
2.11	SWP small-aperture high-dispersion (even orders) format. . . . .	18
2.12	SWP small-aperture high-dispersion (odd orders) format. . . . .	19
2.13	SWP large-aperture high-dispersion (even orders) format. . . . .	20
2.14	SWP large-aperture high-dispersion (odd orders) format. . . . .	21
2.15	SWP large- and small-aperture low-dispersion format. . . . .	22
2.16	LWP Geometry . . . . .	24
2.17	LWR Geometry . . . . .	25
2.18	SWP Geometry . . . . .	26
2.19	Low-dispersion spectral resolution. . . . .	28
2.20	Low-dispersion spatial resolution. . . . .	30
2.21	LWP high-dispersion spectral resolution from WAVECAL analysis. . . . .	33
2.22	LWR high-dispersion spectral resolution from WAVECAL analysis. . . . .	34
2.23	SWP high-dispersion spectral resolution from WAVECAL analysis. . . . .	35
2.24	LWP high-dispersion spectral resolution from analysis of large-aperture Zeta Oph data. . . . .	36
2.25	SWP high-dispersion spectral resolution from analysis of large- and small-aperture Zeta Oph data. Small-aperture data is horizontally offset to the left of the large-aperture data by half an order. . . . .	37
2.26	SWP high-dispersion spectral resolution from large-aperture stellar source analysis. Absorption line data is horizontally offset to the left of the emission line data by half an order. . . . .	38

2.27	SWP high-dispersion spectral resolution from small-aperture stellar source analysis. Absorption line data is horizontally offset to the left of the emission line data by half an order. . . . .	39
2.28	LWP high-dispersion spatial resolution for sample position 134. Small-aperture data is horizontally offset to the left of the large-aperture data by half an order. . . . .	42
2.29	LWP high-dispersion spatial resolution for sample position 258. Small-aperture data is horizontally offset to the left of the large-aperture data by half an order. . . . .	43
2.30	LWP high-dispersion spatial resolution for sample position 384. Small-aperture data is horizontally offset to the left of the large-aperture data by half an order. . . . .	44
2.31	LWP high-dispersion spatial resolution for sample position 507. Small-aperture data is horizontally offset to the left of the large-aperture data by half an order. . . . .	45
2.32	LWP high-dispersion spatial resolution for sample position 615. Small-aperture data is horizontally offset to the left of the large-aperture data by half an order. . . . .	46
2.33	LWR high-dispersion spatial resolution for sample position 134. Small-aperture data is horizontally offset to the left of the large-aperture data by half an order. . . . .	47
2.34	LWR high-dispersion spatial resolution for sample position 258. Small-aperture data is horizontally offset to the left of the large-aperture data by half an order. . . . .	48
2.35	LWR high-dispersion spatial resolution for sample position 384. Small-aperture data is horizontally offset to the left of the large-aperture data by half an order. . . . .	49
2.36	LWR high-dispersion spatial resolution for sample position 507. Small-aperture data is horizontally offset to the left of the large-aperture data by half an order. . . . .	50
2.37	LWR high-dispersion spatial resolution for sample position 615. Small-aperture data is horizontally offset to the left of the large-aperture data by half an order. . . . .	51
2.38	SWP high-dispersion spatial resolution for sample position 134. Small-aperture data is horizontally offset to the left of the large-aperture data by half an order. . . . .	52
2.39	SWP high-dispersion spatial resolution for sample position 258. Small-aperture data is horizontally offset to the left of the large-aperture data by half an order. . . . .	53
2.40	SWP high-dispersion spatial resolution for sample position 384. Small-aperture data is horizontally offset to the left of the large-aperture data by half an order. . . . .	54
2.41	SWP high-dispersion spatial resolution for sample position 507. Small-aperture data is horizontally offset to the left of the large-aperture data by half an order. . . . .	55
2.42	SWP high-dispersion spatial resolution for sample position 615. Small-aperture data is horizontally offset to the left of the large-aperture data by half an order. . . . .	56
5.1	(a) Displacements computed between an SWP low-dispersion image and the SWP ITF. (b) Magnitude of the correlation coefficients corresponding to the results shown in Panel <i>a</i> . . . . .	79
5.2	(a) Displacements computed between an SWP high-dispersion image and the SWP ITF. (b) Magnitude of the correlation coefficients corresponding to the results shown in Panel <i>a</i> . . . . .	80
6.1	White Dwarf SWP spectra showing the 1515Å artifact. . . . .	90

7.1	Low-dispersion wavelength linearization correction vectors. . . . .	99
7.2	Spectrum centroid location in LWP low-dispersion SI data. . . . .	101
7.3	Spectrum centroid location in LWR low-dispersion SI data. . . . .	102
7.4	Spectrum centroid location in “dewiggled” LWP low-dispersion SI data. . . .	103
7.5	Spectrum centroid location in “dewiggled” LWR low-dispersion SI data. . . .	104
7.6	Geometry of the spectrograph apertures as they appear in the low-dispersion SI. . . . .	105
8.1	Short and long wavelength low-dispersion WAVECAL spectra. Pt-Ne features included in the low-dispersion line libraries are marked. . . . .	115
8.2	Low-dispersion time and temperature correlations with wavelength and spatial zeropoints for the LWP camera. . . . .	120
8.3	Low-dispersion time and temperature correlations with wavelength and spatial zeropoints for the LWR camera (ITF A). . . . .	121
8.4	Low-dispersion time and temperature correlations with wavelength and spatial zeropoints for the LWR camera (ITF B). . . . .	122
8.5	Low-dispersion time and temperature correlations with wavelength and spatial zeropoints for the SWP camera. . . . .	123
9.1	Locations of the extraction and background fitting regions within the low- dispersion SI. . . . .	134
10.1	Layout of the background extraction swaths on a sample SWP high-dispersion image. Lines running in the vertical (spatial) direction are the Pass 1 extrac- tions. The reconstructed background solutions created in Pass 2 are placed in the positions of the echelle orders (horizontal lines). . . . .	141
10.2	Crosscut of background fluxes from a central “Pass 1” swath through an SWP image. Stellar fluxes are off-scale in this diagram. The triangular area describes the local raw background fluxes in the Interorder-Overlap Region where order crowding is severe; the halation region is shown to the right. Small crosses denote the raw fluxes corrected for overlap by the PSF model. The solid line is the Pass 1 solution, a Chebyshev, degree-7 polynomial. . . .	143
10.3	Final background solution for SWP20931, Order 95 (smooth solid line). The comb structure connected to the solution reflects the solutions for the various Pass 1 swaths sampled at the line position of this order. . . . .	145
A.1	Layout of the background extraction swaths on a sample SWP high-dispersion image. Lines running in vertical (spatial) direction are the Pass 1 extractions. Raw fluxes are sampled along these lines that are within the target ring and outside or between the echelle orders. The reconstructed background solutions created in Pass 2 are placed in the positions of the echelle orders (horizontal lines). . . . .	248

A.2	Crosscut of background fluxes from a central “Pass 1” swath through an SWP image. Stellar fluxes are off-scale in this diagram. The triangular area describes the local raw background fluxes in the Interorder-Overlap Region where order crowding is severe; the halation region is shown to the right. Small crosses denote the raw fluxes corrected for overlap by the PSF model. The solid line is the Pass 1 solution, a Chebyshev, degree-7 polynomial. . . .	251
A.3	A depiction of the influence of interorder overlap in progressively raising the intensity of (unit height) orders towards shorter wavelengths (left). The dashed lines represent intensities the orders would have if there were no overlap. . .	254
A.4	Final background solution for SWP20931, order 95 (smooth solid line). The comb structure connected to the solution reflects the solutions for the various Pass 1 swaths sampled at the line position of this order. . . . .	255

# Chapter 1

## Introduction

### 1.1 Purpose of Document

This document provides the researcher who plans to analyze images acquired with the *International Ultraviolet Explorer* (IUE) with the information necessary to understand the raw data characteristics and image processing operations, and to interpret the processed output products for data processed with the New Spectral Image Processing System (NEWSIPS). The document also provides detailed descriptions of each procedure and algorithm in the image processing system, the techniques used to calibrate the data in wavelength and absolute flux, and a complete specification of output file formats.

Data acquired with the IUE satellite were originally processed with the IUE Spectral Image Processing System (IUESIPS) from the time of satellite launch. Over the years, IUESIPS underwent a number of enhancements and modifications, which were documented in the IUE Image Processing Information Manual Versions 1.0 (Turnrose and Harvel 1980), 1.1 (Turnrose et al. 1981), and 2.0 (Turnrose and Thompson 1984). These manuals are still the standard reference to be used with Guest Observer (GO) format data processed with IUESIPS. The NEWSIPS system described in this document is fundamentally different in algorithm and technique from the previous IUESIPS. For FITS format data processed with NEWSIPS, this document supersedes and replaces all previous versions of the IUE Image Processing Information Manual, as well as the IUE NEWSIPS Manual Version 1.0 (Nichols et al. 1993).

### 1.2 Philosophy of the IUE Final Archive Image Processing

The philosophy that governed the development of the NEWSIPS system was intended to address four fundamental requirements:

1. *Create a uniformly processed and calibrated archive as the final product of the IUE mission*

IUE data have been processed using the IUESIPS system since launch in 1978. However, the IUESIPS system has undergone a number of modifications and enhancements since that time, rendering the IUESIPS archived data inhomogeneous and not fully intercomparable. The original IUESIPS system was documented in the IUE Image Processing Information Manual Versions 1.0 and 1.1. A major change to the IUESIPS system occurred in 1981 and this newer version of the software is documented in the IUE Image Processing Information Manual Version 2.0. A modification to the resampling algorithm used to create the spatially resolved (ELBL) file for low dispersion was implemented in 1985. A new photometric calibration was implemented for the LWP camera data in 1988. Later changes have customarily been documented in IUE Newsletters.

2. *Exploit new image processing techniques to improve the photometric accuracy and signal-to-noise ratio of the data*

A number of new image processing techniques had been identified since the design of IUESIPS that were demonstrated to produce a more accurate photometric correction and increased signal-to-noise ratio of the extracted IUE data. Implementation of these techniques significantly improves the quality of the Final Archive.

3. *Verify and correct fundamental information for each image*

In addition to providing a uniformly processed archive with improved photometric and signal-to-noise properties, the IUE Project has expended considerable effort in verifying the information available for each image.

4. *Base the contents of the Final Archive on requirements from the research community*

In defining the specifications for the IUE Final Archive, and in developing the new processing algorithms and calibrations, the IUE Project was guided by the recommendations of the Final Archive Definition Committee, chaired by Dr. Jeffrey Linsky. This very active committee represented a unique grassroots effort by the astronomical community to assist in defining the scientific content of a NASA space mission, optimizing its utility for future researchers.

*It is important to note that the data processed with NEWSIPS differ in fundamental ways from the data processed with IUESIPS. Images processed with these two systems are not directly intercomparable.*

### 1.2.1 Uniform Archive

One of the primary assets of the IUE archive is the long timeline of observations taken with a remarkably stable photometric instrument. To exploit this asset, observations must be fully intercomparable over the entire lifetime of IUE. In order to satisfy the first requirement, that of uniformity, it was essential to develop a fully automated system that allowed no human intervention and was sufficiently robust to process all images acquired by IUE. Thus the



algorithms developed were designed to yield the best overall result for all types of images. These algorithms may not yield the best result for a particular image or particular class of images because of this design requirement. This represents a change in philosophy from IUESIPS. For example, the data were processed with IUESIPS according to Guest Observer (GO) specifications concerning the width of the extraction slit and the registration of the spectrum with respect to the pseudo extraction slit. In the NEWSIPS low-dispersion system, the width of the extraction slit is automatically determined and registration is always automatic. The NEWSIPS high-dispersion system uses a boxcar extraction where the width of the extraction slit is set according to an automated source type determination (i.e., point or extended). As is the case in low-dispersion, the high-dispersion registration is also always automatic.

### 1.2.2 New Processing Algorithms and Calibrations

The new processing algorithms that have been developed by the NASA IUE Project allow several significant improvements in the processed data. The new approach exploits the presence of fixed pattern noise (pixel-to-pixel sensitivity variations in the cameras) as a reliable fiducial to register the raw science image with the raw Intensity Transfer Function (ITF) image. Proper registration of IUE images is crucial to accurate photometric correction because the variability of the geometrical distortions introduced by the SEC-Vidicon cameras ensures that raw science images are never perfectly aligned with the ITF. While reseau marks etched on the faceplates of the cameras were intended to be used to rectify geometrically the science images, they cannot be detected at the low exposure levels usually found in the background of IUE images. Therefore, the IUESIPS method of processing IUE images uses predicted reseau positions to align the science images with the ITF images. Unfortunately, these mean positions are poorly known and the application of a mis-registered ITF (by more than about 0.2 pixel) manifests itself as systematic noise in the photometrically corrected image, and ultimately in the spectrum.

To achieve proper alignment of the ITF images with each science image for the Final Archive reprocessing, the fixed pattern inherent in IUE images is used as a fiducial. Small patches of the science image are cross-correlated against corresponding areas on the appropriate ITF image to determine the spatial displacement between these two images. The displacement of each pixel in the science image from its corresponding pixel in the ITF can thus be determined to sub-pixel accuracy. Such an approach has several advantages: (1) a large number of fiducials can be found anywhere on the image, (2) fixed pattern can be detected even at the lowest exposure levels, and (3) fiducials are available near the edge of the image, where distortion is greatest. In the IUESIPS processing of IUE data, the ITF images have been resampled to geometrically correct space, significantly smoothing these calibration data. In the new processing system, the ITF images are retained in raw space, increasing the accuracy of the pixel-to-pixel photometric correction.

Only one resampling of the data is performed in the new processing system, minimizing the smoothing inherent in such an operation. The linearized pixel values are resampled into

a geometrically rectified and rotated image, such that the spectral orders are horizontal in the image and the dispersion function of the spectral data within an order is linearized. The resampling algorithm used is a modified Shepard method which preserves not only the flux to 1–3 in the image, but also the spectral line shapes.

The low-dispersion spectral data are extracted by a weighted slit extraction method developed by Kinney et al. (1991). The advantages of this method over the IUESIPS boxcar extraction are: (1) the signal-to-noise ratio (S/N) of the spectrum is usually improved while flux is conserved, (2) most of the cosmic rays are automatically removed, and (3) the output includes an error estimate for each point in the flux spectrum. The high-dispersion spectral data are extracted using an IUESIPS style boxcar extraction method. As a result the S/N improvements may not be as good as those seen in low-dispersion data.

An entirely new data product for the IUE Final Archive is a geometrically rectified and rotated high-dispersion image, with horizontal spectral orders. This new data product will allow future investigators to perform customized extractions and background determinations on the high-dispersion data. One of the most significant problems with the analysis of high-dispersion IUE data has been the proper determination of the background in the region where the echelle orders are most closely spaced and begin to overlap. The new processing system includes a background removal algorithm that determines the background level of each high-dispersion image by fitting, in succession, one-dimensional Chebyshev polynomials, first in the spatial and then the wavelength direction. The extracted high-dispersion spectral data are available order-by-order with wavelengths uniformly sampled within an order.

In addition to the new algorithms for processing the IUE data for the Final Archive, all absolute flux calibrations have been rederived. The new calibrations use white dwarf models to determine the relative shapes of the instrumental sensitivity functions, while previous UV satellite and rocket observations of  $\eta$  UMa and other standard stars are used to set the overall flux scale. The IUE Final Archive extracted spectral data are also corrected for sensitivity degradation of the detectors over time and temperature, a calibration not previously available with IUESIPS processing.

These new processing algorithms for the creation of the Final Archive allow a significant improvement in the signal-to-noise ratio of the processed data, resulting largely from a more accurate photometric correction of the fluxes and weighted slit extraction, and greater spectral resolution due to a more accurate resampling of the data. Improvement in the signal-to-noise ratio of the extracted low-dispersion spectral data has been shown to range from 10–50% for most images, with factors of 2–4 improvement in cases of high-background and underexposed data (Nichols-Bohlin 1990).

### 1.2.3 Core Data Item Verifications

A set of “core” data items (CDIs) has been identified, which were verified from observatory records available at each station. These core items are generally the information necessary to process correctly the image and/or are crucial for scientific analysis. While many of the verification procedures are automated, it is necessary in some cases to consult the hand-

written scripts or logs to obtain the correct information. The verification of the CDIs is performed before each image is reprocessed for the Final Archive.

### 1.2.4 Community Involvement

The IUE Final Archive Definition Committee (FADC), chaired by Jeffrey Linsky, was formed in November 1987 to provide recommendations and advice to the NASA IUE Project on the content of the Final Archive and on the algorithms and methods used to process the data for the Archive. The FADC also provided estimates of resources needed to accomplish the recommended goals. The committee was composed of 24 people, selected for having demonstrated interest in improving the S/N of IUE data for their own research. The committee met every 3–6 months for 5 years, producing at each meeting a written report of recommendations and near-term goals. These reports are published in the IUE Newsletters Nos. 34, 36, 38, and 48. The FADC provided user representation by the astronomical community to define the content of the IUE Final Archive, optimizing its utility for future investigators.

# Chapter 2

## Description of IUE Data

### 2.1 Raw Image Data and Label Parameters

Each raw IUE image consists of a  $768 \times 768$  array of 8-bit picture elements or “pixels”. Partial-read images, which are not full  $768 \times 768$  images, are discussed in Chapter 4.3. Each vidicon scan line consists of 768 pixels or “samples” obtained in minor frame units of 96 pixels; 768 such scan lines compose the entire image. Line 1, sample 1 is at the upper left corner of the image; line 768, sample 768 is at the lower right corner of the image. Each raw pixel value lies in the range 0 to 255 (integers only). The units of raw pixel values are data numbers (DN), which are proportional (up to the telemetry system limit of 255) to the integrated charge read out from the SEC Vidicon target in the camera scanning process. Since the telemetry system saturates at 255, the DN/charge proportionality breaks down at that level.

Associated with each raw image is a set of 20 header, or label, records. Each record is 360 8-bit bytes long and is a concatenation of five 72-byte logical records. This set of 20 label records was generated by the IUE Operations Control Center (IUEOCC) software during image acquisition and contains various identifying parameters and scientific/engineering data pertinent to the image.

Raw IUE images must be corrected for the instrumental effects of the SEC Vidicon camera system before quantitatively meaningful data can be extracted from them. The correction for radiometric (photometric) non-linearities and non-uniformities is discussed in Chapter 6. The removal of geometric distortions introduced by the vidicon system are described in Chapter 7. The layout of the spectral format in either dispersion mode is mathematically set forth by the methods related in Chapter 8. Figures 2.1 through 2.15 illustrate schematically the spectral formats in both dispersion modes, for both apertures, for all three operational cameras and refer to raw image space. The square border defines the  $768 \times 768$  array comprising the whole image, whereas the inscribed arcs roughly define the target ring, which is the area within which the photometric correction is applied (Chapter 6) and from which spectral information is extracted. For high dispersion, the extracted odd and even echelle orders are shown in separate figures. Numbers and tick marks mark the

wavelengths in Ångstroms.

## 2.2 Spectrograph Geometry

Both the long- and short-wavelength IUE spectrographs have two entrance apertures: a small aperture (nominal 3 arcsec diameter circle) and a large aperture (nominal 10 arcsec by 20 arcsec slot). Although the various methods available for determining the fundamental dimensions do not always yield results which agree to within the limits set by the internal consistency of each (see Panek 1982), the IUE Three Agency Committee adopted recommended values for certain dimensions, which are presented in Table 2.1. These values do not reflect the true physical dimensions of the apertures but rather the size as projected on the camera faceplate. As a result, each spectrograph has its own distinct measurement of aperture sizes. Accurate measurements of the trail lengths are necessary, as such information

Table 2.1: Officially Adopted Dimensions for the Apertures in Each Spectrograph, Measured on LWP, LWR, and SWP Images

Dimension	LWP	SWP	LWR
Major Axis Trail Length ( <i>arcsec</i> )	21.84±0.39	21.48±0.39	22.55±0.62
Large-Aperture Length ( <i>arcsec</i> )	22.51±0.40	21.65±0.39	23.24±0.64
Minor Axis Trail Length ( <i>arcsec</i> )	10.21±0.18	9.24±0.11	9.88±0.42
Large-Aperture Width ( <i>arcsec</i> )	9.91±0.17	9.07±0.11	9.59±0.41
Large-Aperture Area ( <i>arcsec</i> <sup>2</sup> )	218.17±10.12	215.33±6.55	209.29±9.25
Small-Aperture Area ( <i>arcsec</i> <sup>2</sup> )	6.78±0.97	6.72±0.96	6.31±0.75

is used to calculate exposure times for trailed images. In addition, knowledge of the effective aperture area is needed to calibrate properly spectra of extended objects.

The camera plate scales have been redetermined (Garhart 1996; LWP 1.5644, LWR 1.5526, and SWP 1.5300 arcseconds per pixel) using the most recent measurements for the small-to-large aperture offsets in pixels (Table 2.2) and FES aperture center locations in arcseconds (Pitts 1988). These latest incarnations replace the oft-quoted plate scale figure of 1.525 arcseconds per pixel (Bohlin et al. 1980), a value that had been used for all three cameras. The aperture separations in the directions along and perpendicular to the dispersion are given in Table 2.2 for low dispersion. The corresponding values for the high-dispersion offsets are obtained by transposing the entries for the low-dispersion offsets along and perpendicular to the dispersion in Table 2.2. Refer to Figures 2.16 through 2.18 to determine the correct sign for the high-dispersion offsets. These values are defined in a geometrically corrected frame of reference. The total offset is defined as the square root of the sum of the squares of the individual terms. In low dispersion, the offsets along the dispersion

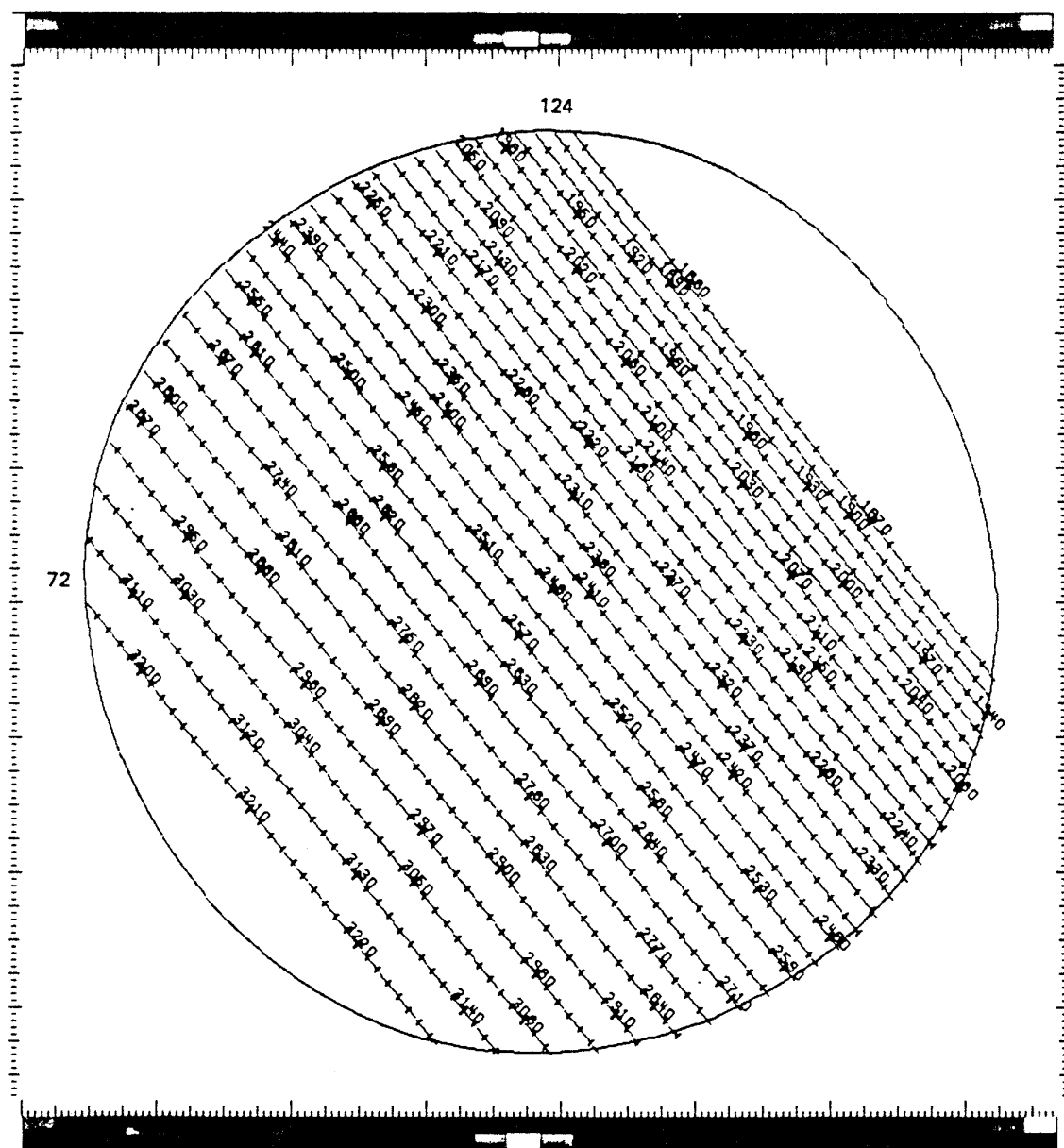


Figure 2.1: LWP small-aperture high-dispersion (even orders) format.

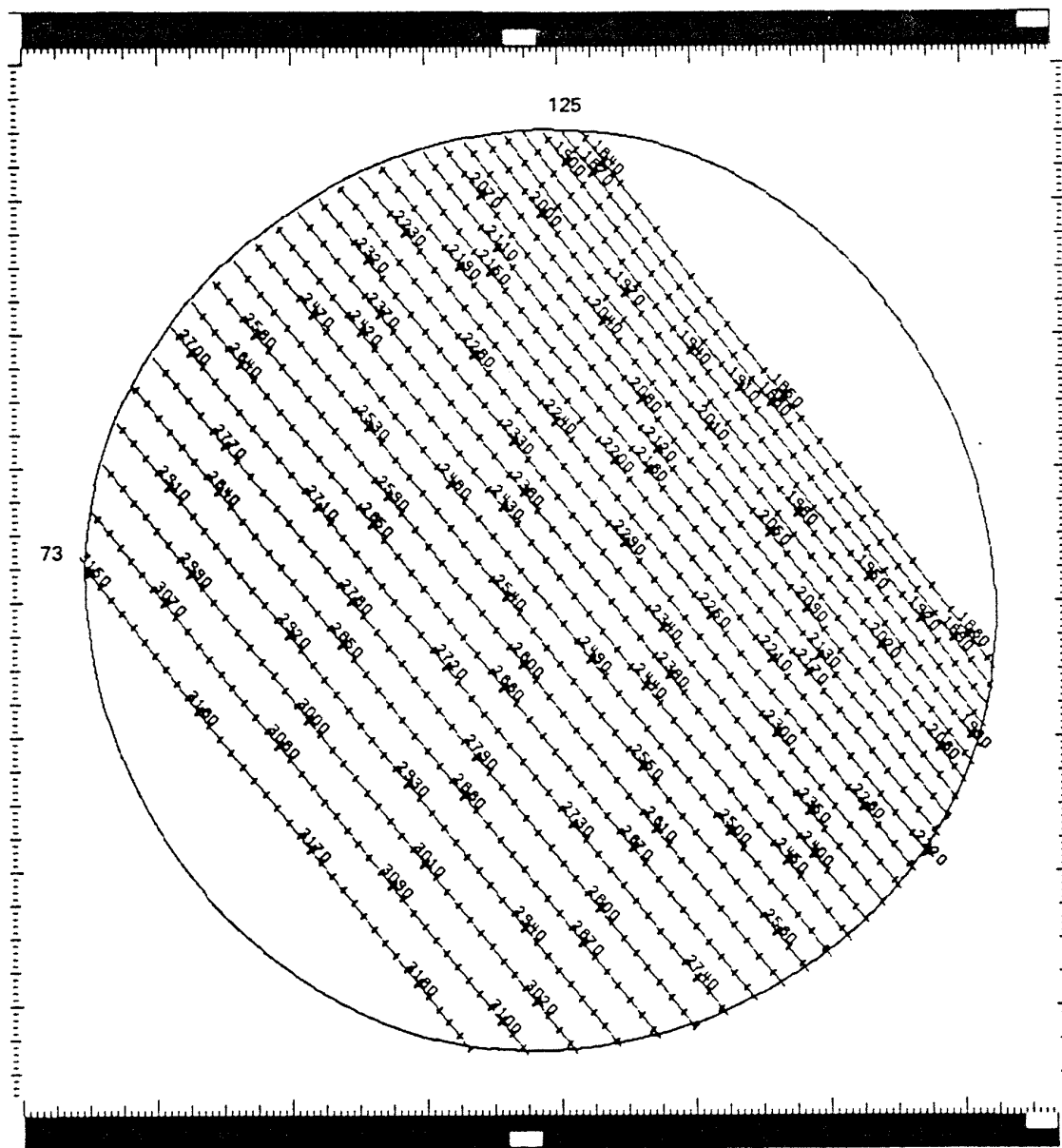


Figure 2.2: LWP small-aperture high-dispersion (odd orders) format.

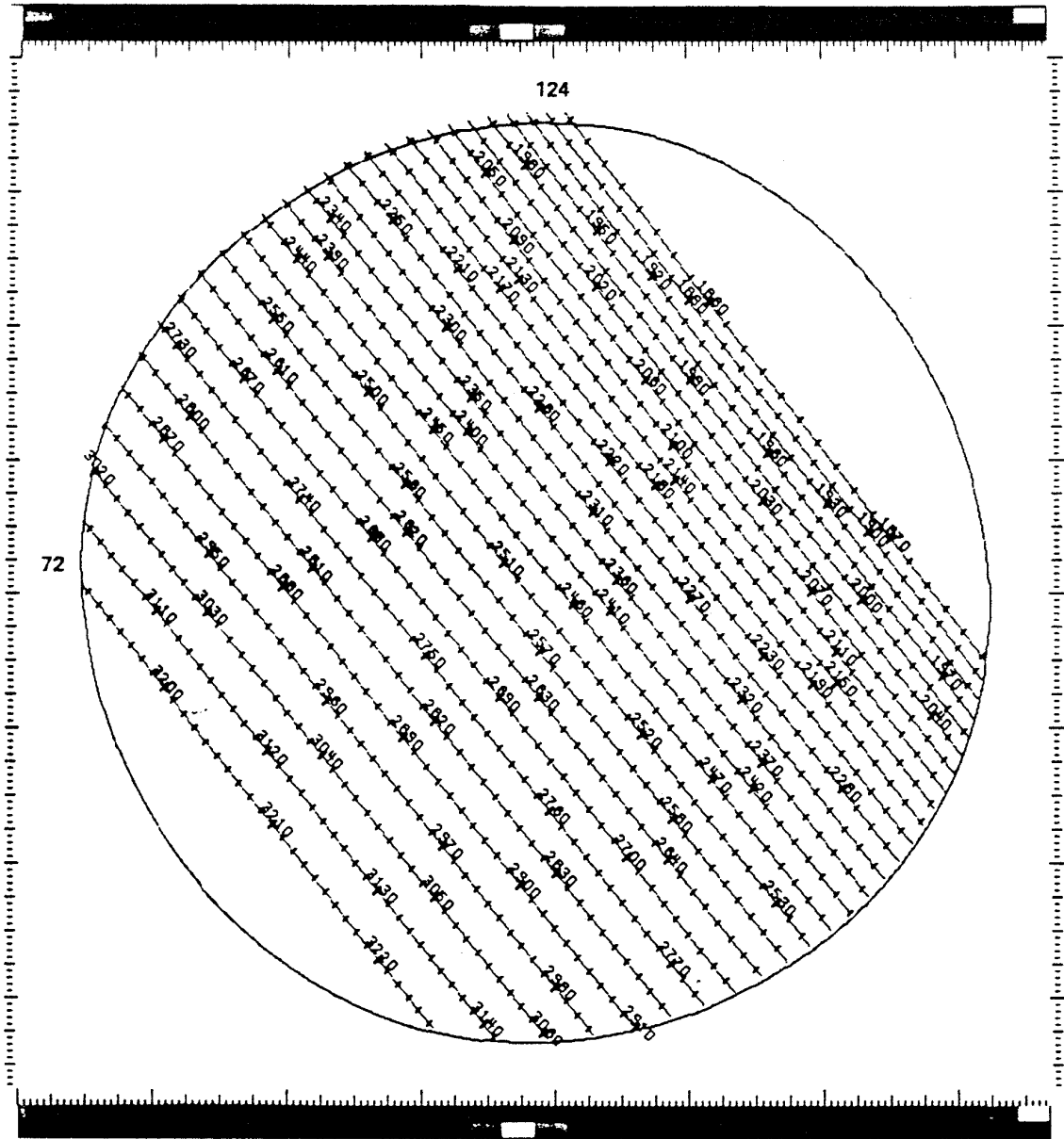


Figure 2.3: LWP large-aperture high-dispersion (even orders) format.



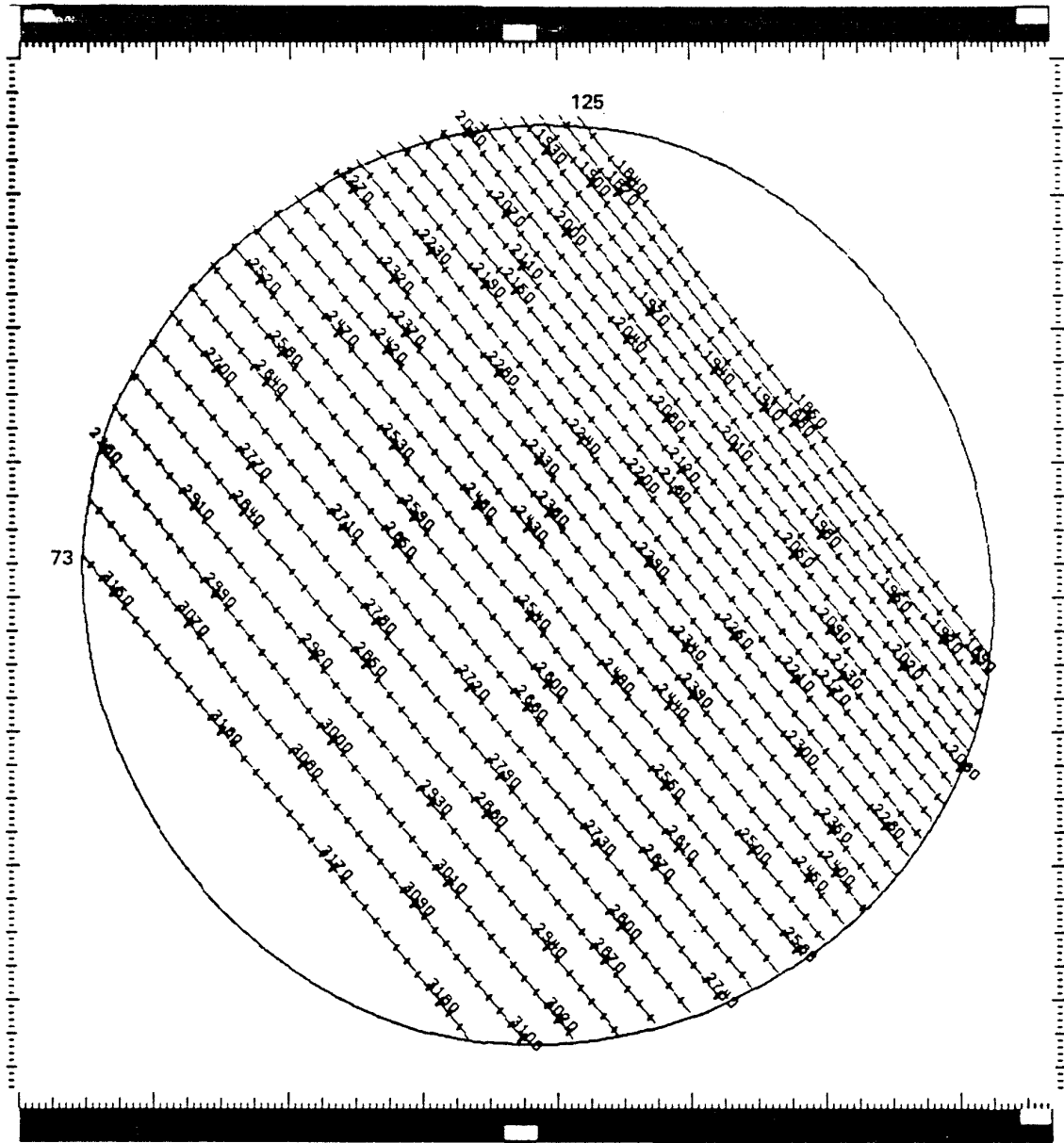


Figure 2.4: LWP large-aperture high-dispersion (odd orders) format.

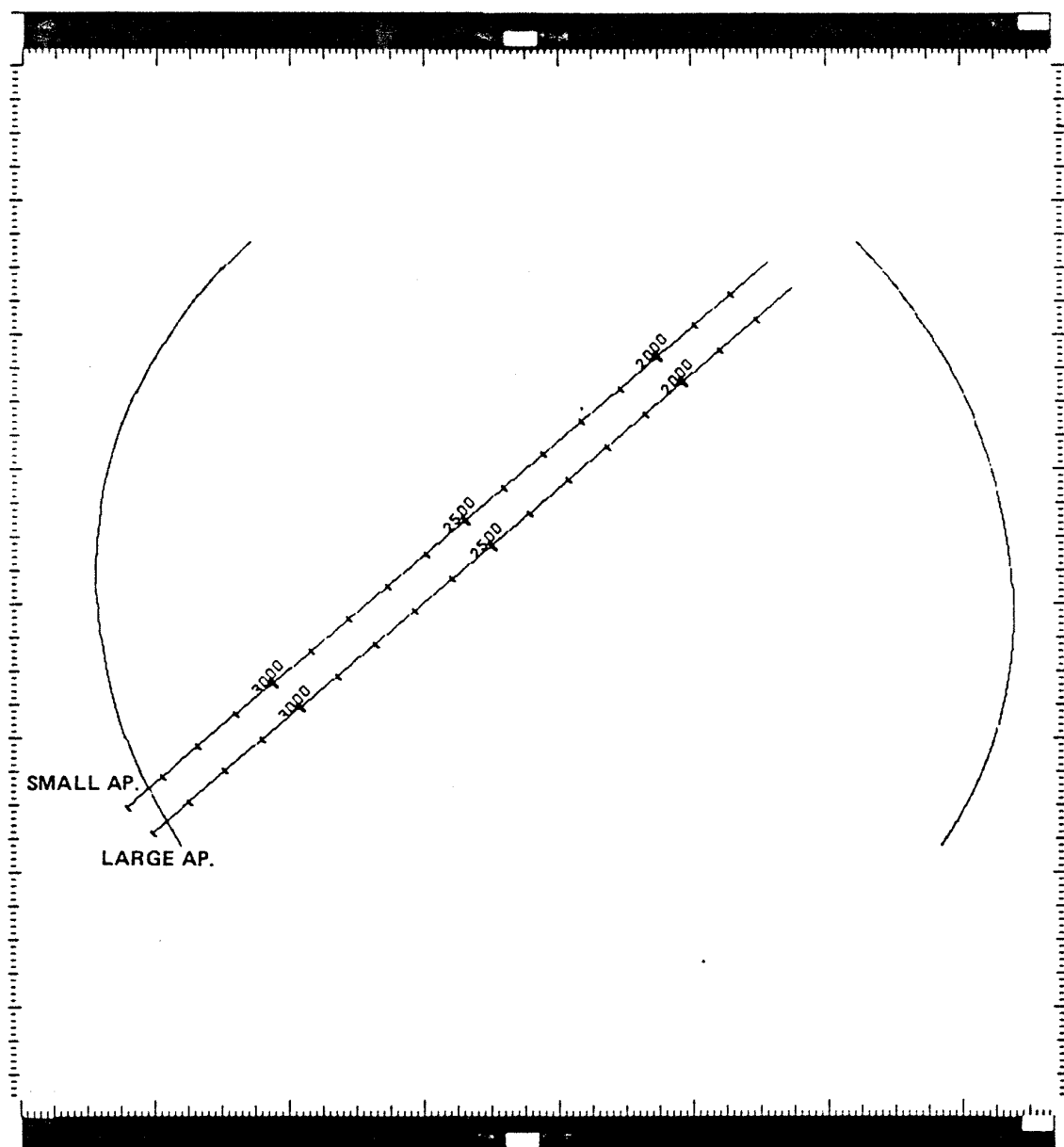


Figure 2.5: LWP large- and small-aperture low-dispersion format.

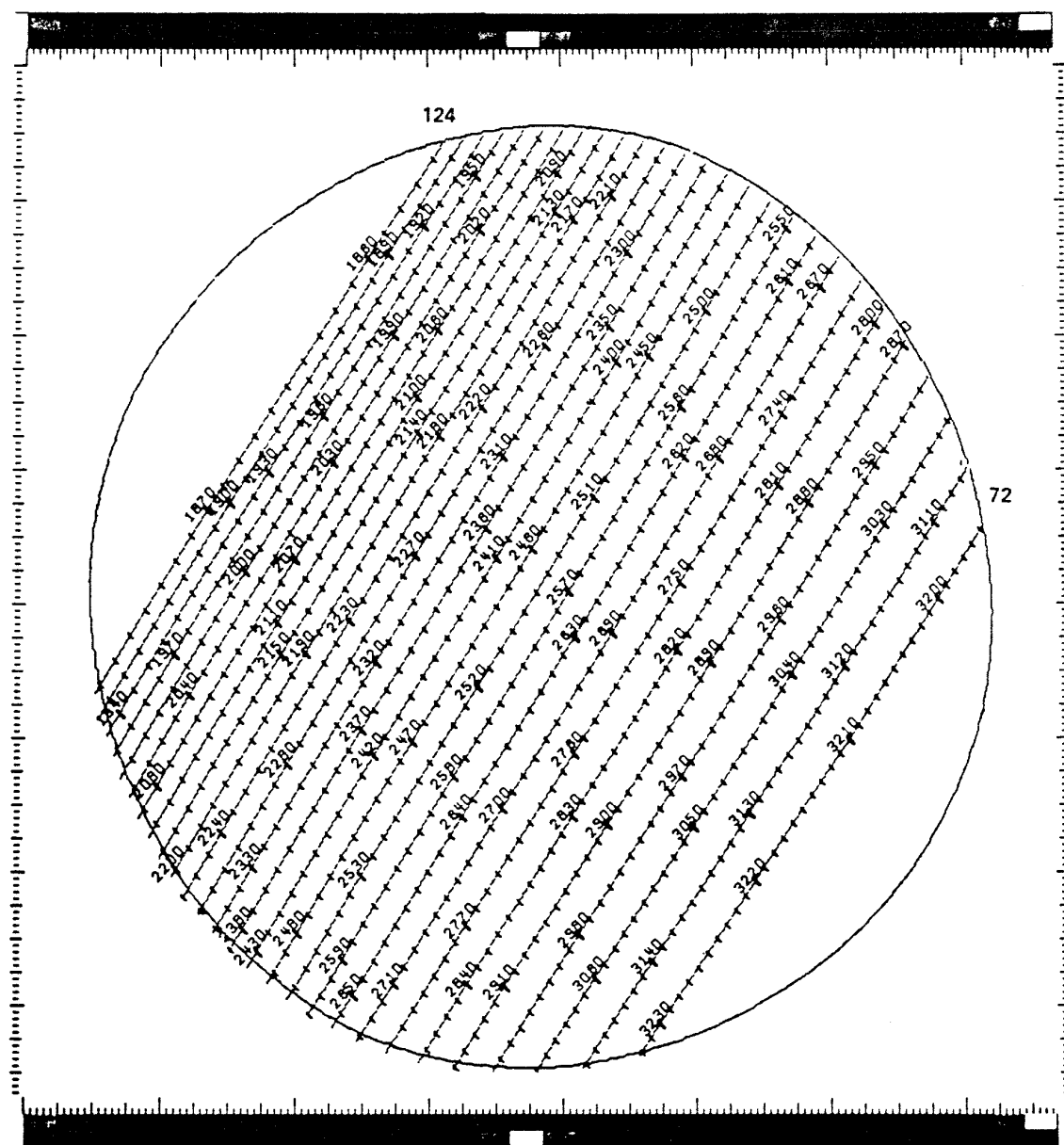


Figure 2.6: LWR small-aperture high-dispersion (even orders) format.

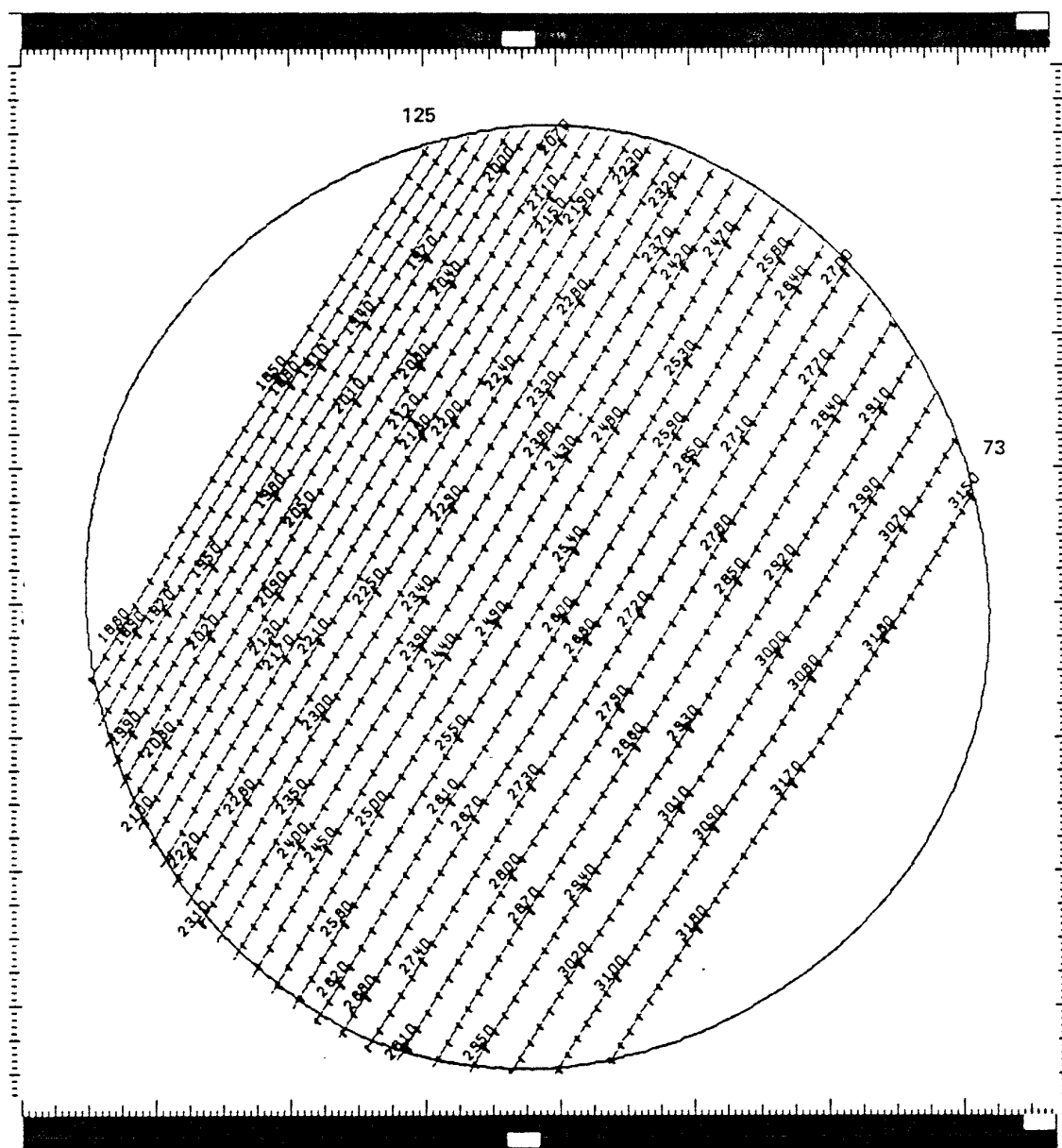


Figure 2.7: LWR small-aperture high-dispersion (odd orders) format.

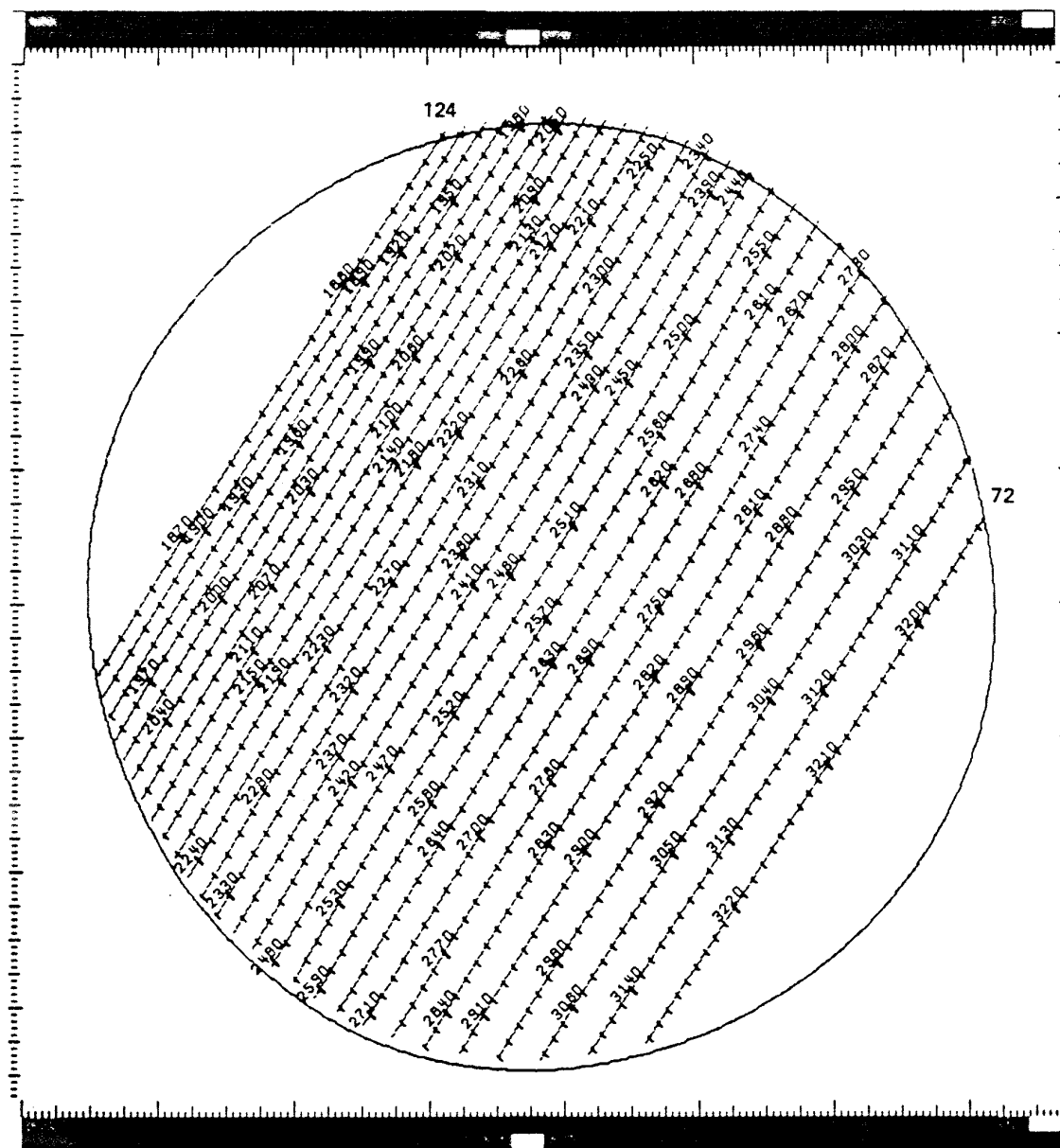


Figure 2.8: LWR large-aperture high-dispersion (even orders) format.

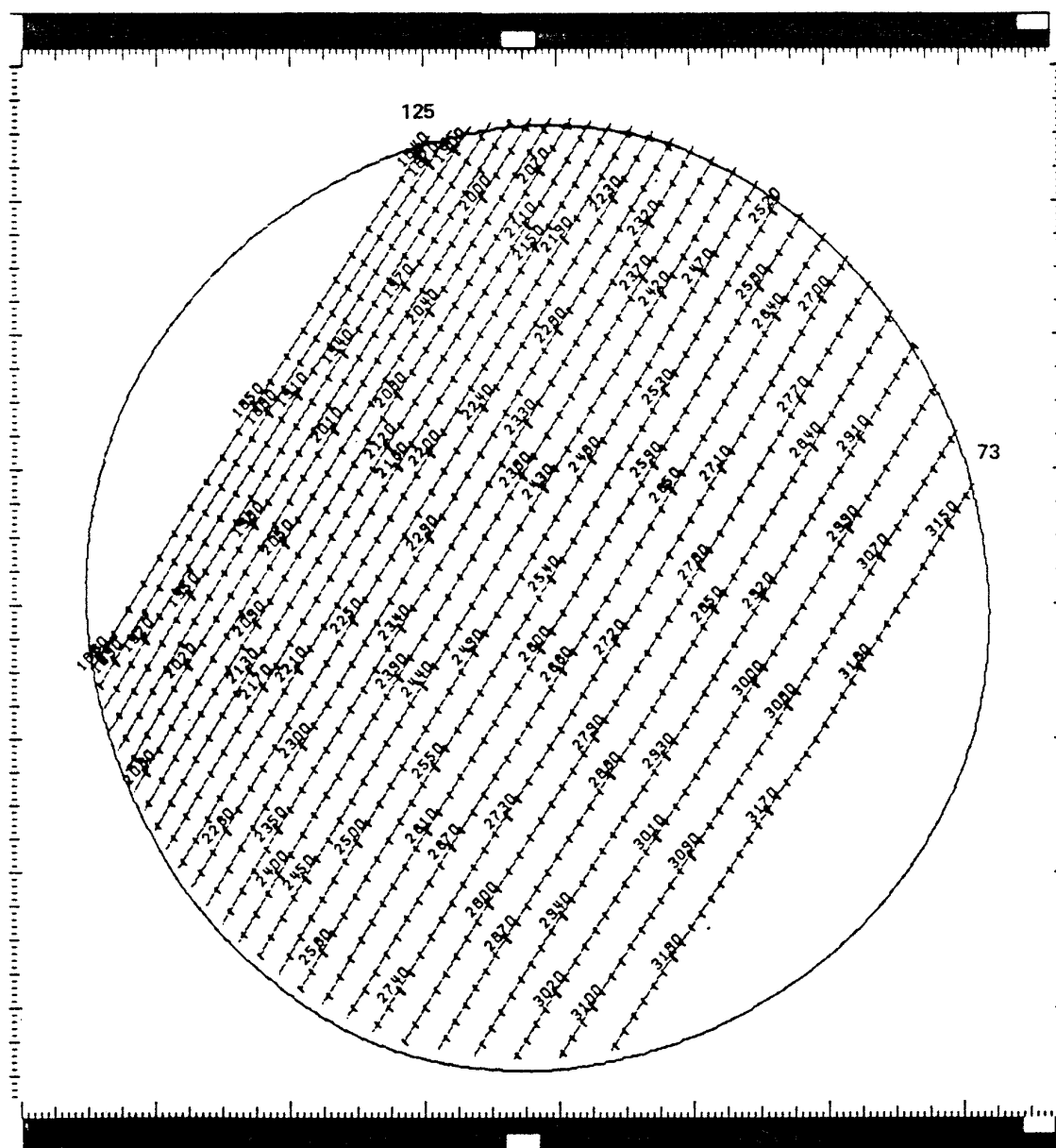


Figure 2.9: LWR large-aperture high-dispersion (odd orders) format.

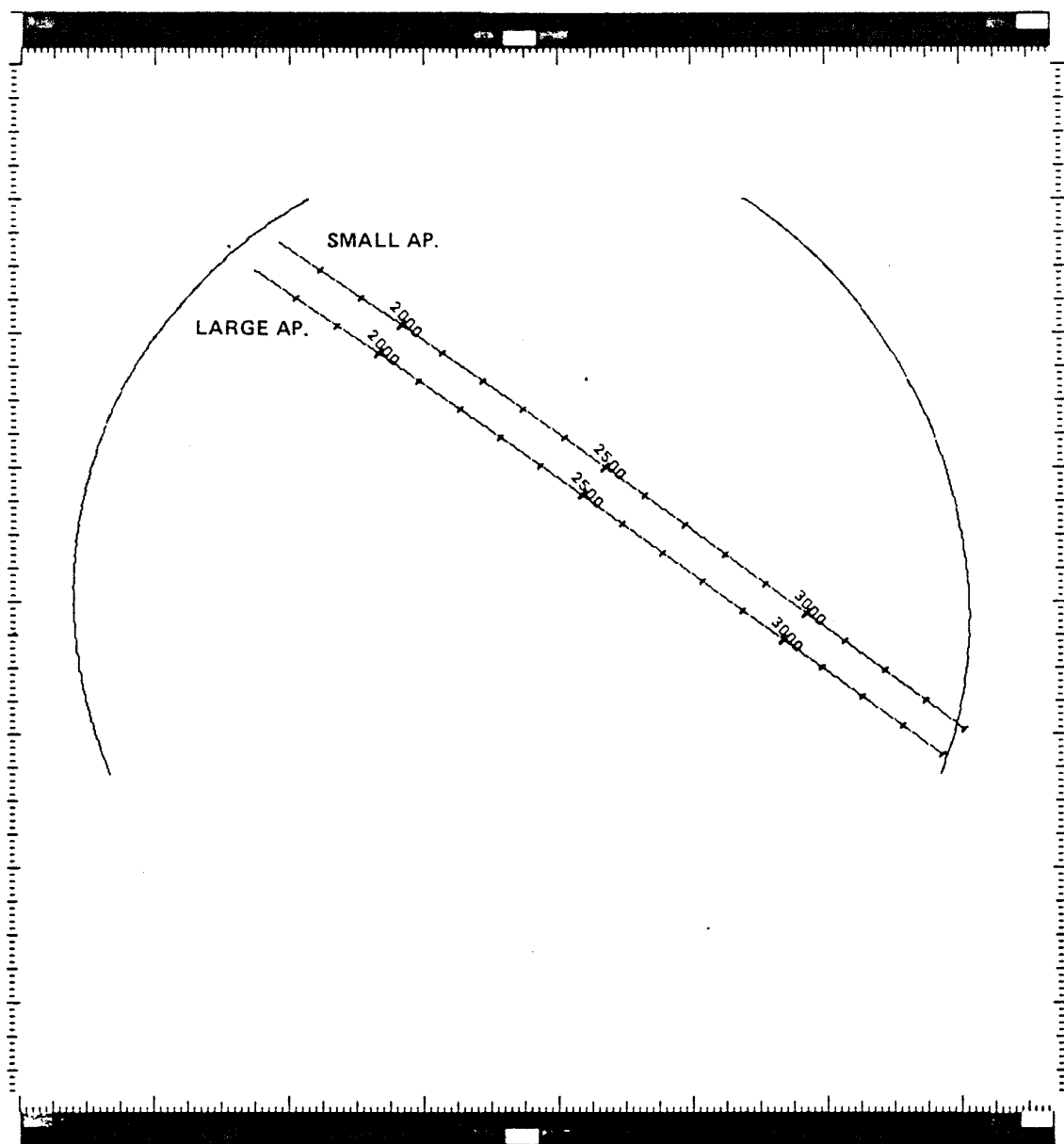


Figure 2.10: LWR large- and small-aperture low-dispersion format.

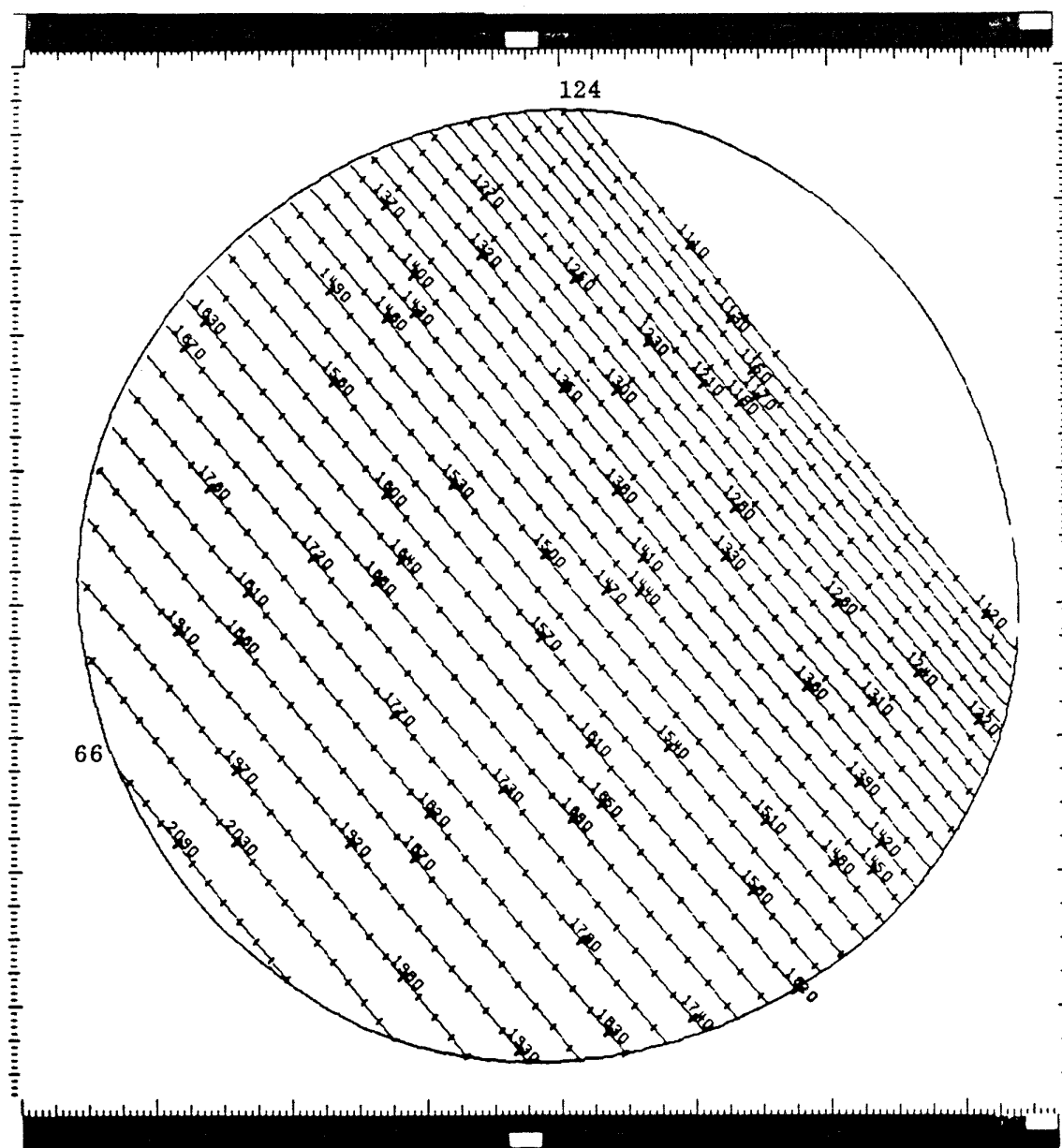


Figure 2.11: SWP small-aperture high-dispersion (even orders) format.



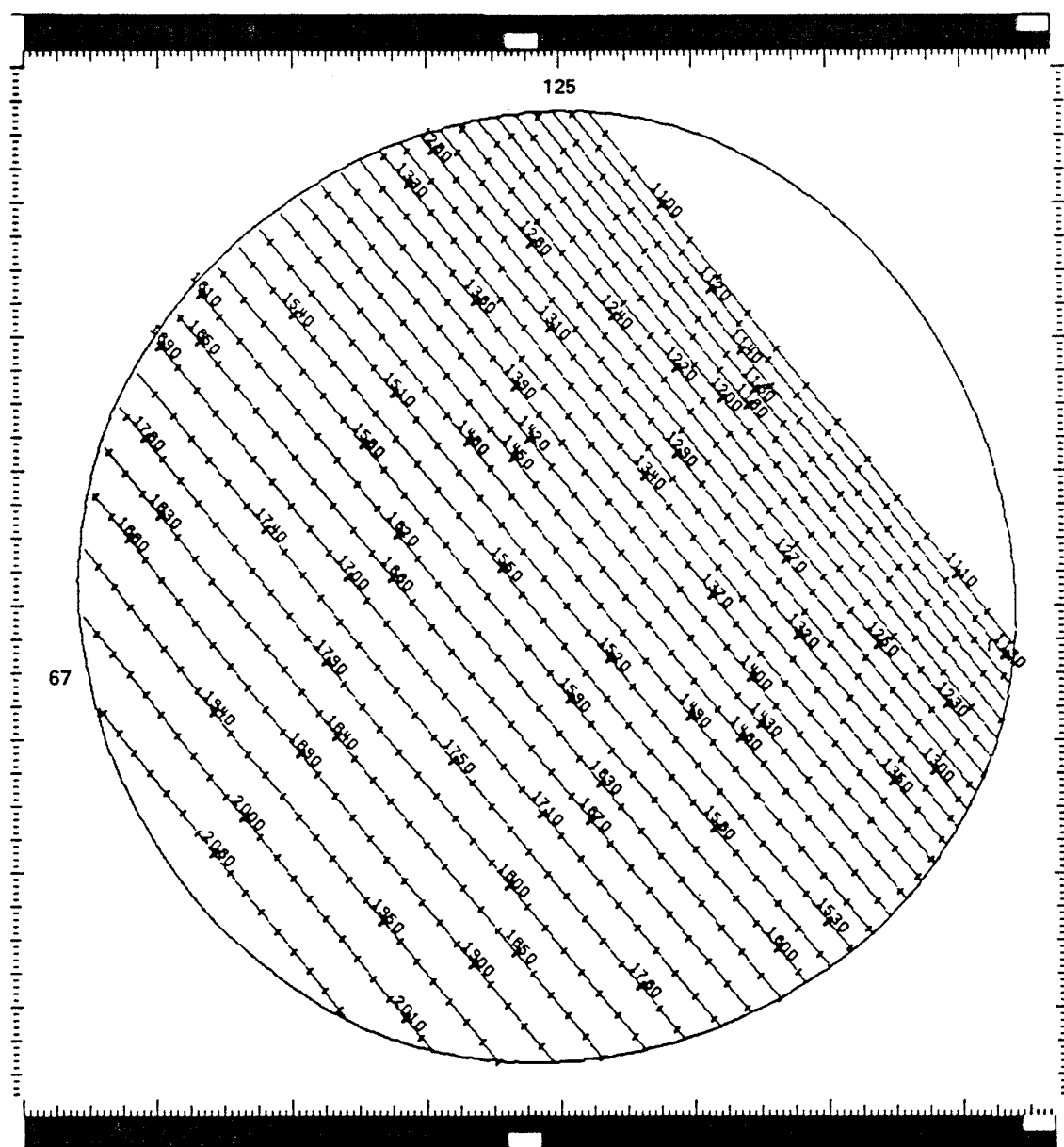


Figure 2.12: SWP small-aperture high-dispersion (odd orders) format.

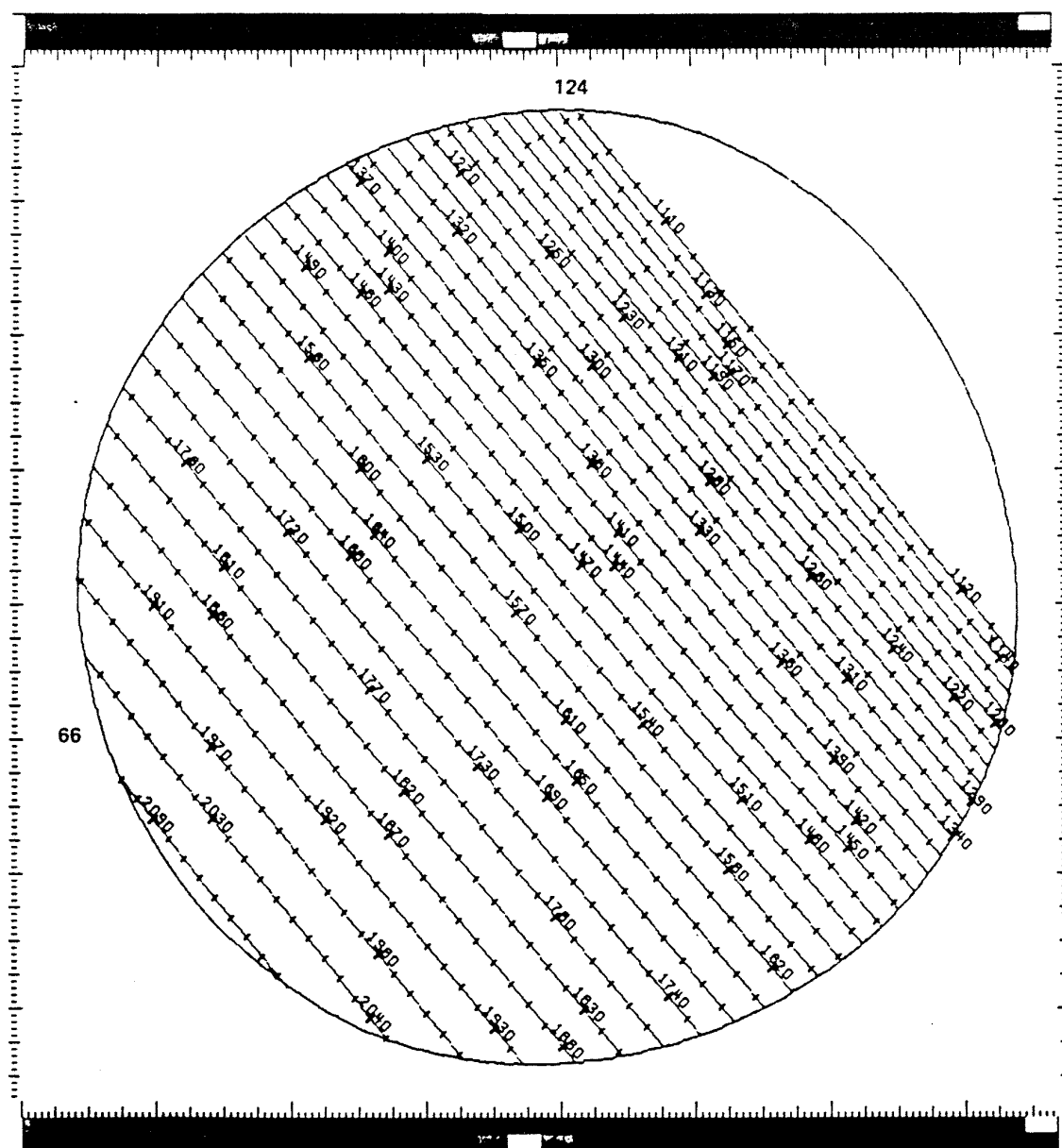


Figure 2.13: SWP large-aperture high-dispersion (even orders) format.

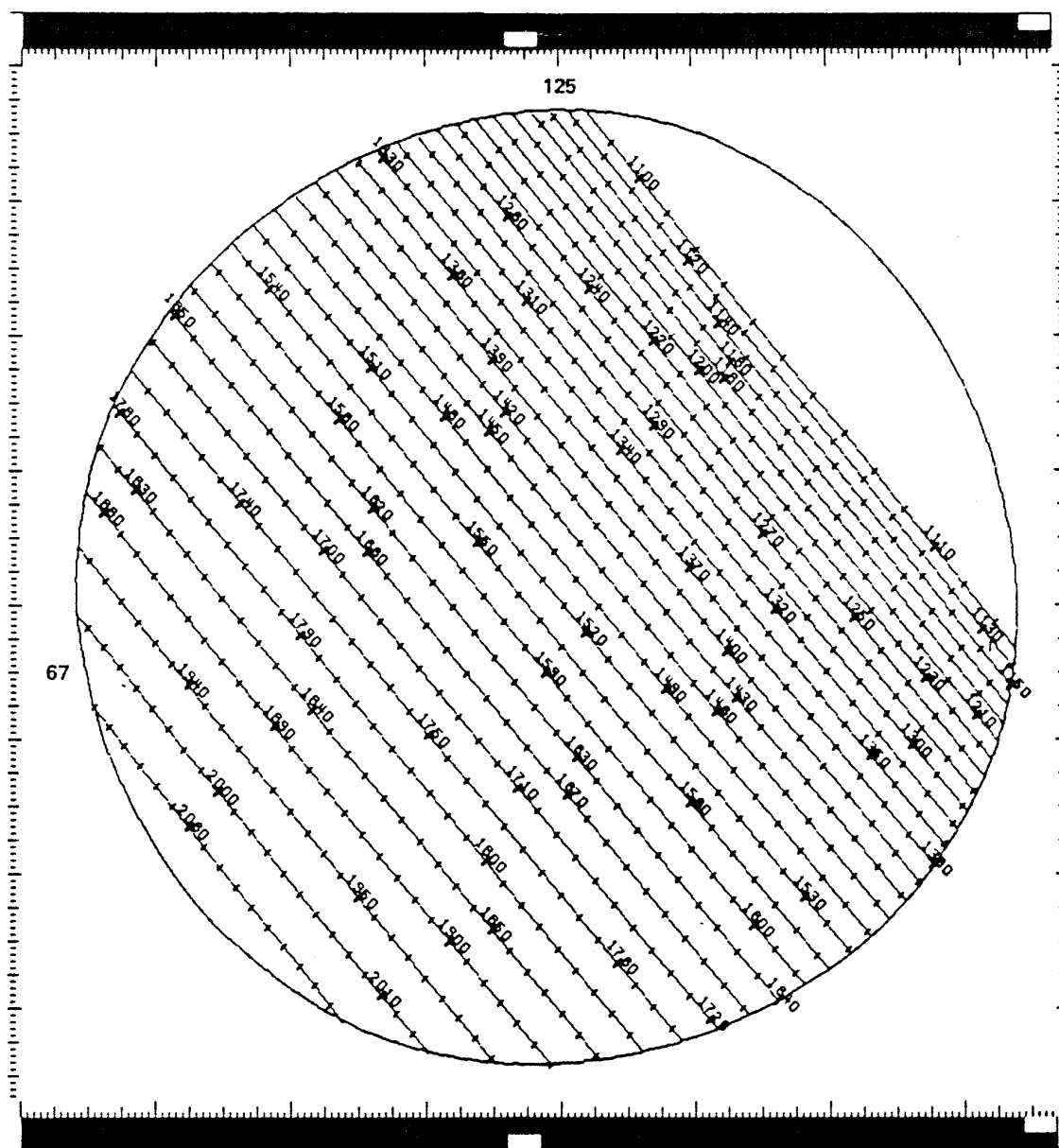


Figure 2.14: SWP large-aperture high-dispersion (odd orders) format.

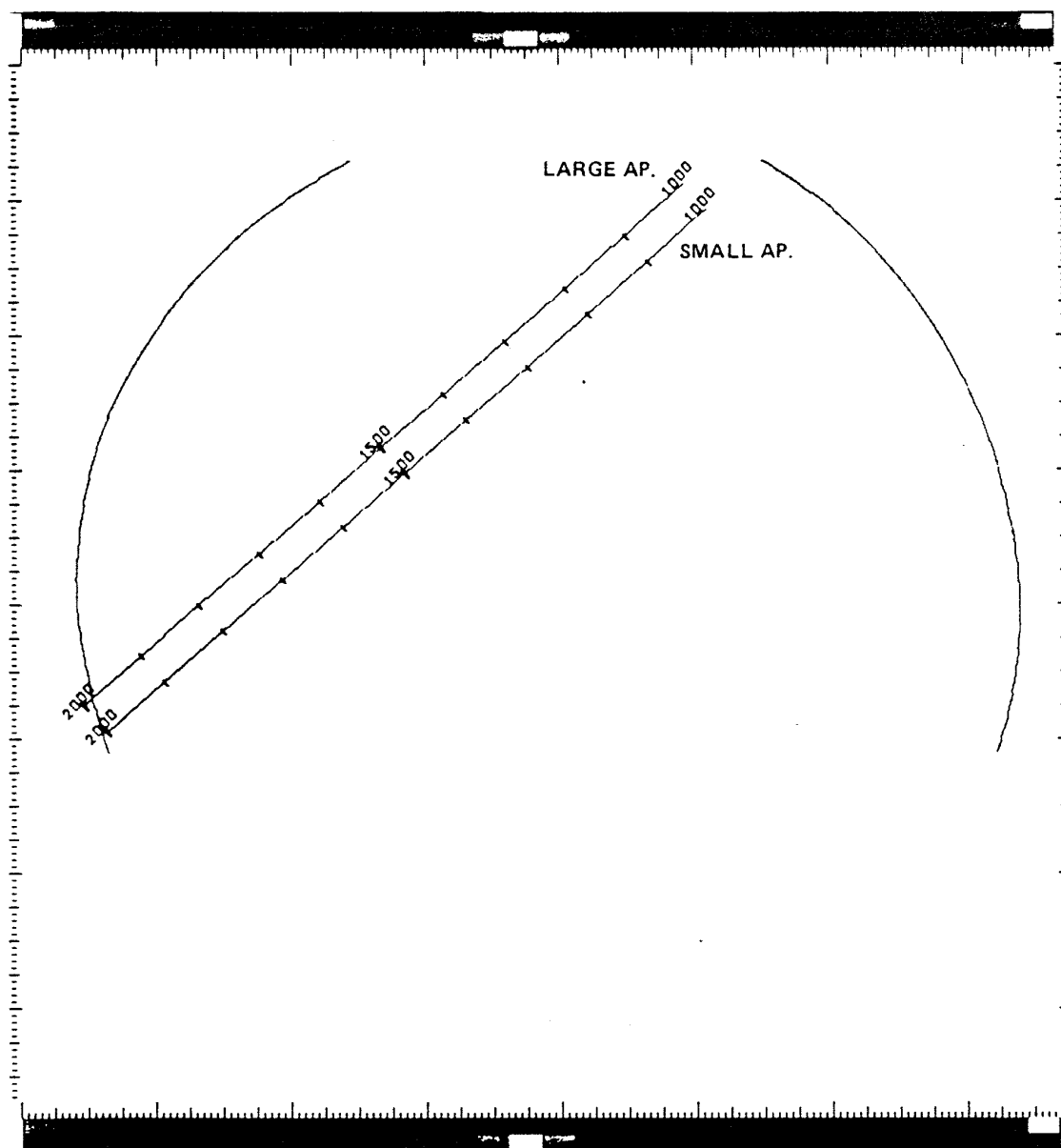


Figure 2.15: SWP large- and small-aperture low-dispersion format.

Table 2.2: Standard Offsets from the Small to the Large Spectrograph Aperture as used by low-dispersion NEWSIPS (in pixels)

Camera	Along Dispersion	$\perp$ to Dispersion	Total Offset
LWP	-2.3	26.2	26.3
LWR	-2.3	26.4	26.5
SWP	0.8	26.1	26.1

have been incorporated into the geometric correction step such that the wavelength scales for the small and large apertures are aligned.

The geometry of the two entrance apertures in relation to the image scan lines and the high and low resolution dispersion directions are shown in Figures 2.16 through 2.18 for the LWP, LWR, and SWP cameras. Note particularly the fact that the displacement between the short-wavelength large aperture (SWLA) and the short-wavelength small aperture (SWSA) is very nearly along the echelle dispersion direction. Therefore, short-wavelength high-dispersion images in which both apertures are exposed will result in nearly complete superposition of the large- and small-aperture spectra (with a wavelength offset). The displacement of the long-wavelength large aperture (LWLA) and the long-wavelength small aperture (LWSA) is less coincident with the echelle dispersion direction in this spectrograph, so that superposition of large- and small-aperture high-dispersion spectra is not as serious in the long-wavelength spectrograph.

For the purposes of judging the extent and separation of the apertures in the spectral domain, the scales given in Table 2.3 may be used in conjunction with the quantities in Tables 2.1 and 2.2. Note that in high dispersion a given shift along the dispersion corresponds closely to a constant Doppler velocity shift, whereas in low dispersion a given shift corresponds to a constant wavelength shift.

Table 2.3: Approximate Spectral Scales in Each Dispersion Mode

Camera	Low ( $\text{\AA}/\text{px}$ )	High ( $\text{km/s/px}$ )
LWP	2.66	7.21
LWR	2.66	7.27
SWP	1.68	7.72

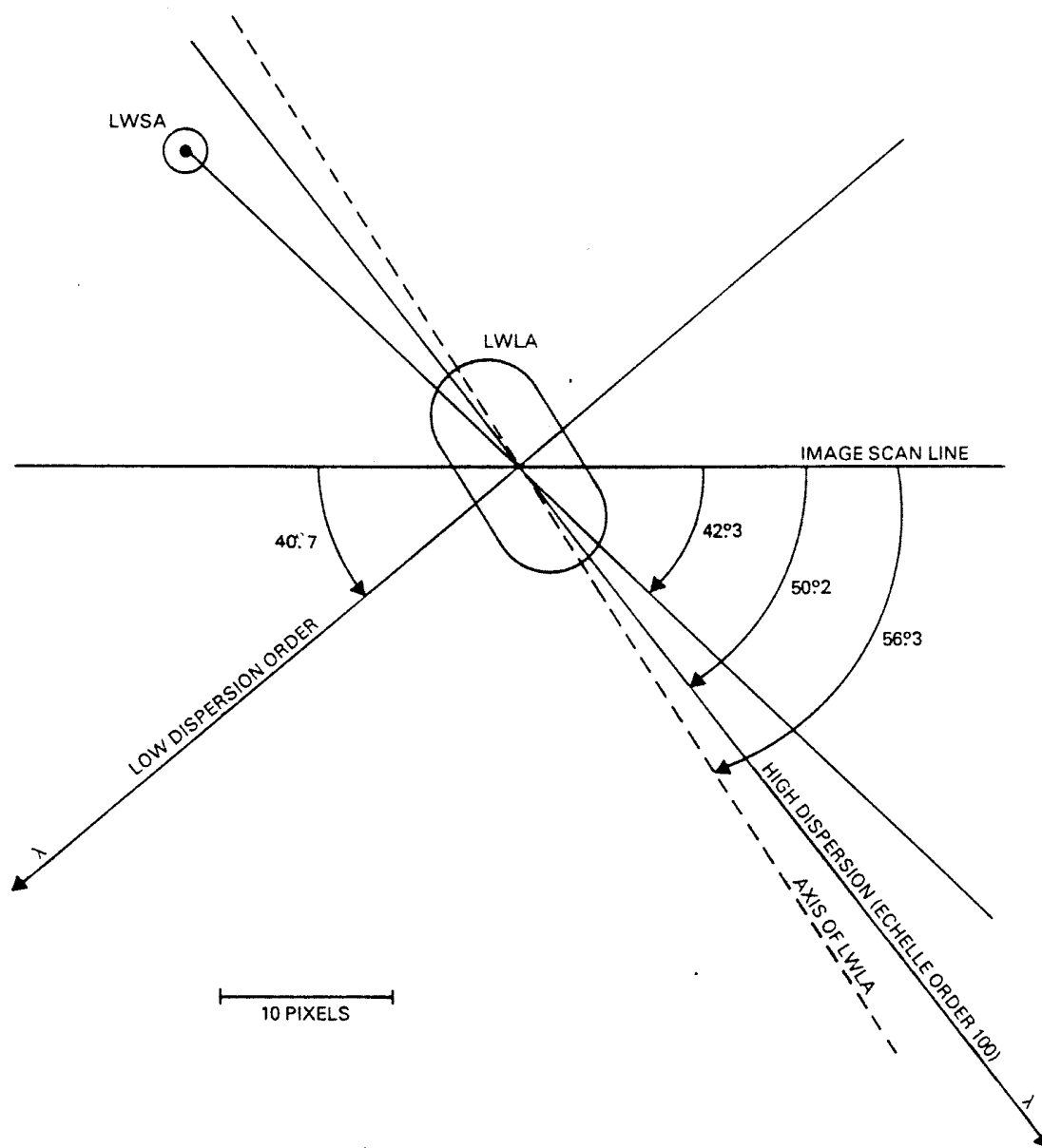


Figure 2.16: LWP Geometry

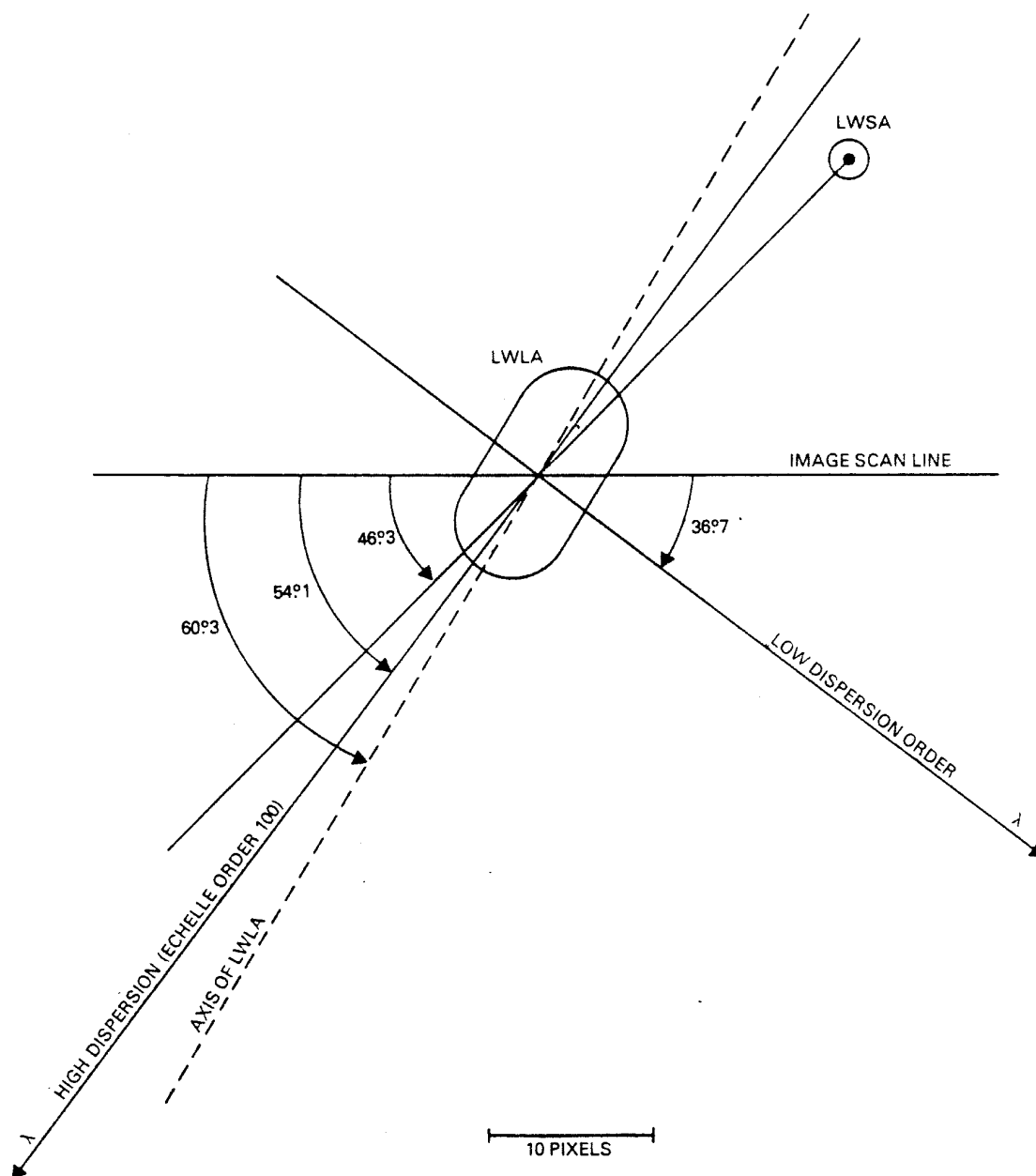


Figure 2.17: LWR Geometry

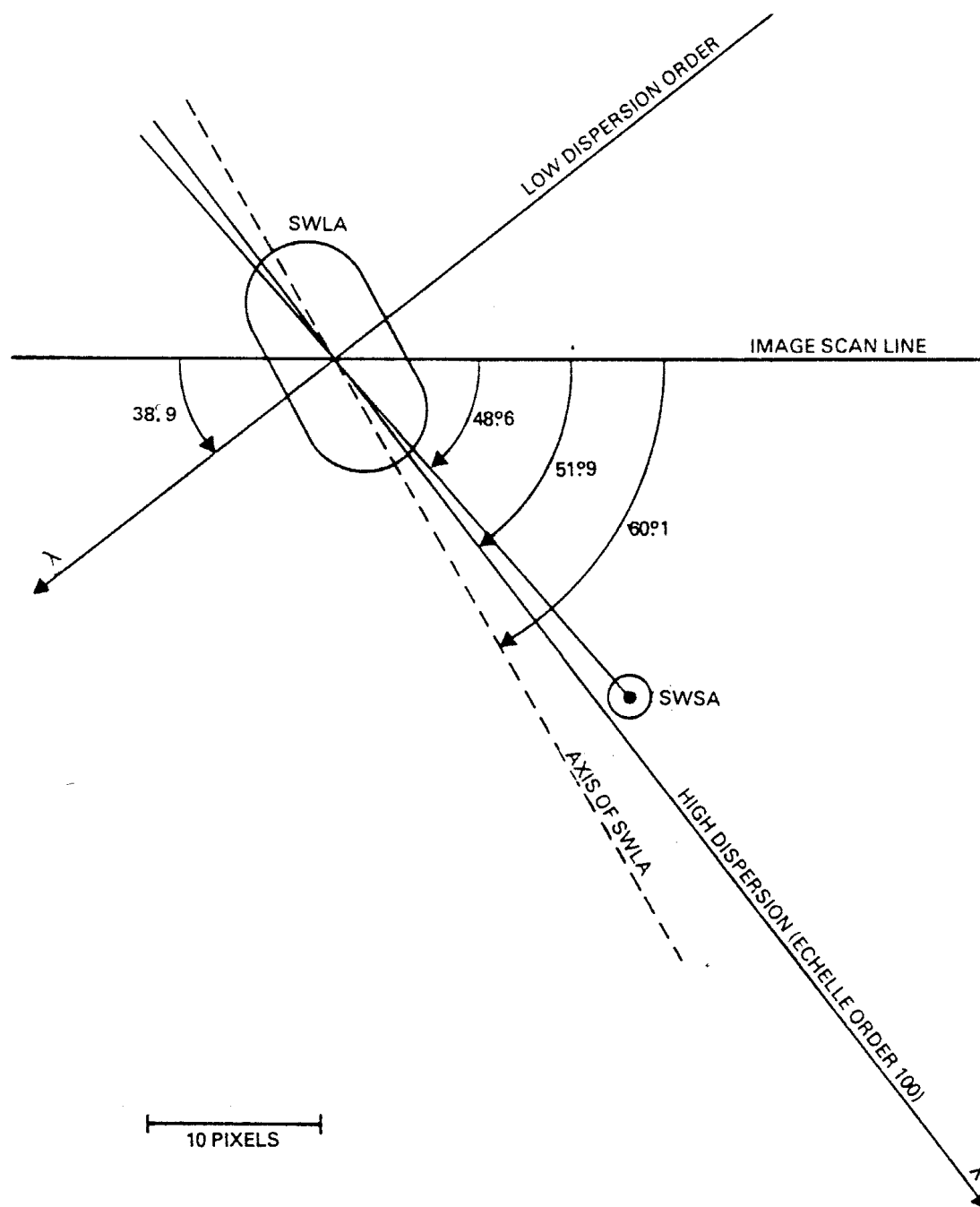


Figure 2.18: SWP Geometry



## 2.3 Instrumental Resolution

The instrumental resolution (both spectral and spatial) is a convolution of the camera resolution, dispersion mode, spectrograph entrance aperture, telescope focus, and spacecraft pointing stability. While the dominant effect is due to the camera, telescope focus and spacecraft pointing stability also play a major role in defining the resolution. In addition, it is well known that the camera resolution is highly wavelength dependent. According to the IUE Camera Users Guide (Coleman et al. 1977), the camera point spread function (PSF) consists of a narrow gaussian-like core having a full width at half maximum (FWHM) of 2 to 5 pixels and a weak long-range tail. The actual resolution in either the spatial or spectral direction can be defined as a function of the FWHM. The Rayleigh criterion of instrumental resolution specifies that two spectra (spatial direction) or two spectral features (spectral direction) can be resolved provided their separation is as follows (Weinstein and Pérez 1992):

$$d \geq 0.849 \times FWHM$$

where  $d$  is the distance separating the two features (or spectra). The gaussian fitting routine used in this analysis was GAUSSFITS, taken from the IUE Data Analysis Center software library. This procedure outputs the one-sigma width of the fitted gaussian profile which was then converted to FWHM using the statistical equality (Bevington 1969):

$$FWHM = 2.3548 \times \sigma$$

### 2.3.1 Low-Dispersion Mode

#### 2.3.1.1 Resolution Along the Dispersion

A study of the NEWSIPS spectral resolution was performed by measuring the FWHM of several features for the emission line sources V1016 Cyg, RR Tel, AG Dra, CI Cyg, and Z And. The analysis indicates a slight improvement in the NEWSIPS resolution (approximately 10% for the SWP and 7% for the LWR) over the IUESIPS results reported by Cassatella, Barbero, and Benvenuti (1985). Plots of the spectral resolution data are shown in Figure 2.19. The small-aperture data are slightly offset in wavelength from the large-aperture data for clarity.

**LWP** – Large-aperture spectral resolution is best between 2700 and 2900Å with an average FWHM of 5.2Å and decreases to approximately 8.0Å on either side of this range. Small-aperture resolution is optimal between 2400 and 3000Å with an average FWHM of 5.5Å and decreases to 8.1Å at the extreme wavelengths.

**LWR** – Maximum resolution in the large aperture occurs longward of 2300Å, with an average FWHM of 5.3Å, while shortward of this point the FWHM decreases to 7.7Å. Small-aperture resolution is best from 2700–3200Å, with an average FWHM of 5.4Å, and decreases to 7.7Å at 3350Å and 7.5Å shortward of 2400Å.

**SWP** – The best resolution occurs around 1200Å, with a FWHM of 4.6Å in the large aperture and 3.0Å in the small aperture, and gradually worsens towards longer wavelengths: 6.7Å at 1900Å in the large aperture and 6.3Å in the small. On average, the small-aperture resolution is approximately 10% better than the large-aperture resolution.

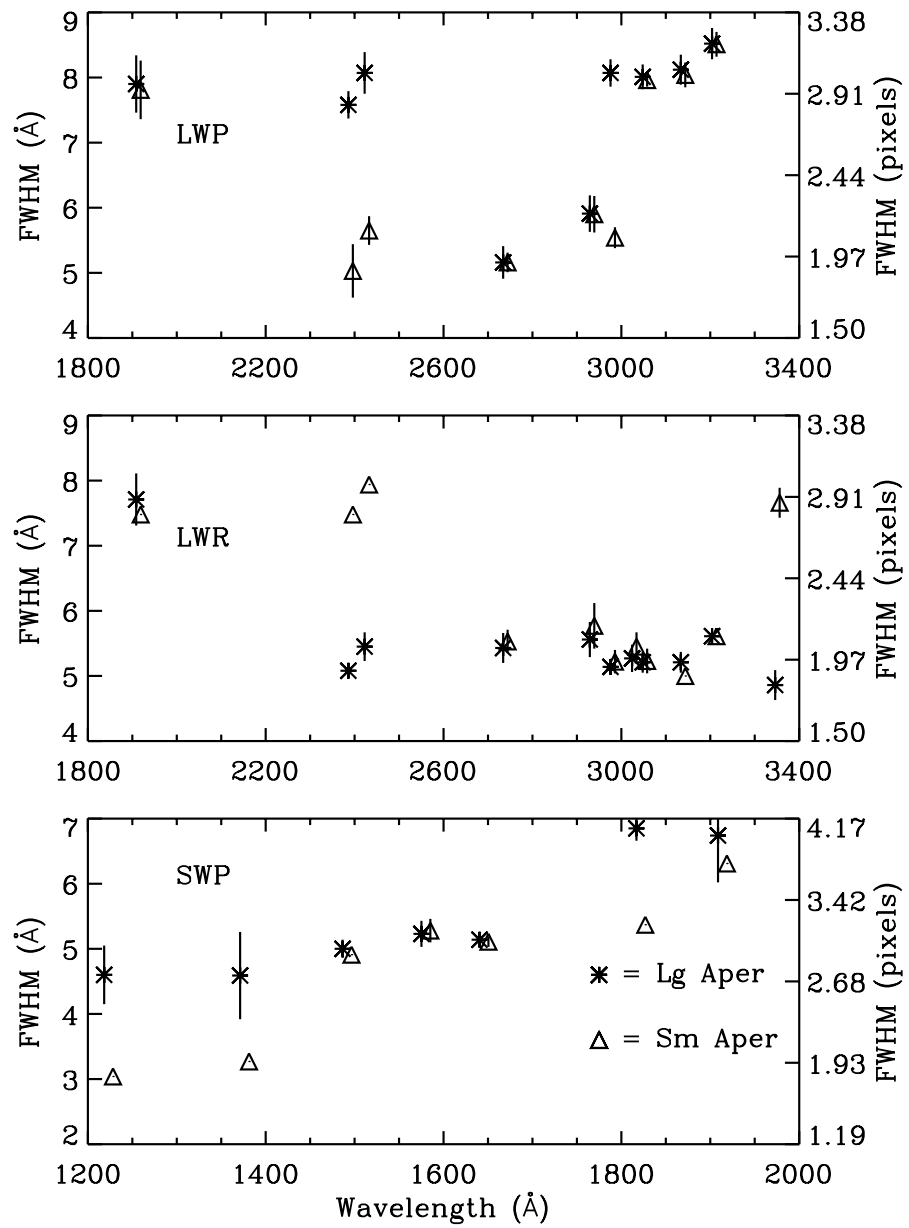


Figure 2.19: Low-dispersion spectral resolution.

### 2.3.1.2 Resolution Perpendicular to the Dispersion

The NEWSIPS spatial resolution has been determined by analyzing the spectra of several low-dispersion standard stars (*viz.*, HD 60753, HD 93521, BD+33° 2642, and BD+75° 325). The FWHM of large- and small-aperture spectra were measured at several wavelengths and plotted (see Figure 2.20). As is the case with the spectral resolution studies, the NEWSIPS values show, in general, an improvement over IUESIPS. As is the case with the spectral resolution plots, the small-aperture data are slightly offset from the large-aperture data.

**LWP** – The spatial resolution for the LWP is best near 3000Å where the FWHM for the large aperture is 2.4 pixels (3.6 arcsec), and decreases to values of around 3.0 pixels at the short- and long-wavelength ends of the spectrum. There is no significant difference between the large- and small-aperture spatial resolutions.

**LWR** – The behavior of the LWR camera as a function of wavelength is similar to the LWP, with the smallest FWHM values for the large aperture of 2.6 pixels (3.9 arcsec) occurring near 3000Å, and increasing to 3.6 and 3.0 pixels at the wavelength extremes. The small aperture, unlike the other two cameras, shows a dramatic *decrease* in resolution of approximately 10%.

**SWP** – The SWP camera shows the best spatial resolution near 1400Å with mean FWHM values for the large aperture of 2.7 pixels (4.1 arcsec), increasing slightly to 2.8 pixels at 1250Å, and 3.7 pixels at 1950Å. The SWP small-aperture resolution response is approximately the same as the large-aperture resolution.

## 2.3.2 High-Dispersion Mode

### 2.3.2.1 Resolution Along the Dispersion

A study of the spectral resolution in the high-dispersion mode was performed utilizing several methods. The first measured emission lines from small-aperture wavelength calibration (WAVECAL) images obtained using the on-board hollow cathode platinum-neon (Pt-Ne) calibration lamp. The second measured several features from the emission line sources V1016 Cyg and RR Tel and interstellar absorption line features from the calibration standard BD+75° 325. The third method measured absorption features from the calibration standard HD 149757 (Zeta Oph). The WAVECAL images are useful in determining the spectral resolution as they are not affected by the telescope focus nor are they subject to astrophysical broadening. The Zeta Oph spectra are characterized by very narrow interstellar absorption features so they are also useful for measuring spectral resolution. Therefore, the measurements taken from WAVECAL and Zeta Oph images represent the best possible spectral resolution obtainable.

**LWP** – The WAVECAL and large-aperture Zeta Oph resolution data are displayed in Figures 2.21 and 2.24, respectively. The results, along with the associated one-sigma error bars and linear fits (dashed line), are plotted as a function of order number in both wavelength and pixel space. The dotted line in the pixel space plots is the average of the resolution data over all orders. No small-aperture high-dispersion data of Zeta Oph is available. In addition,

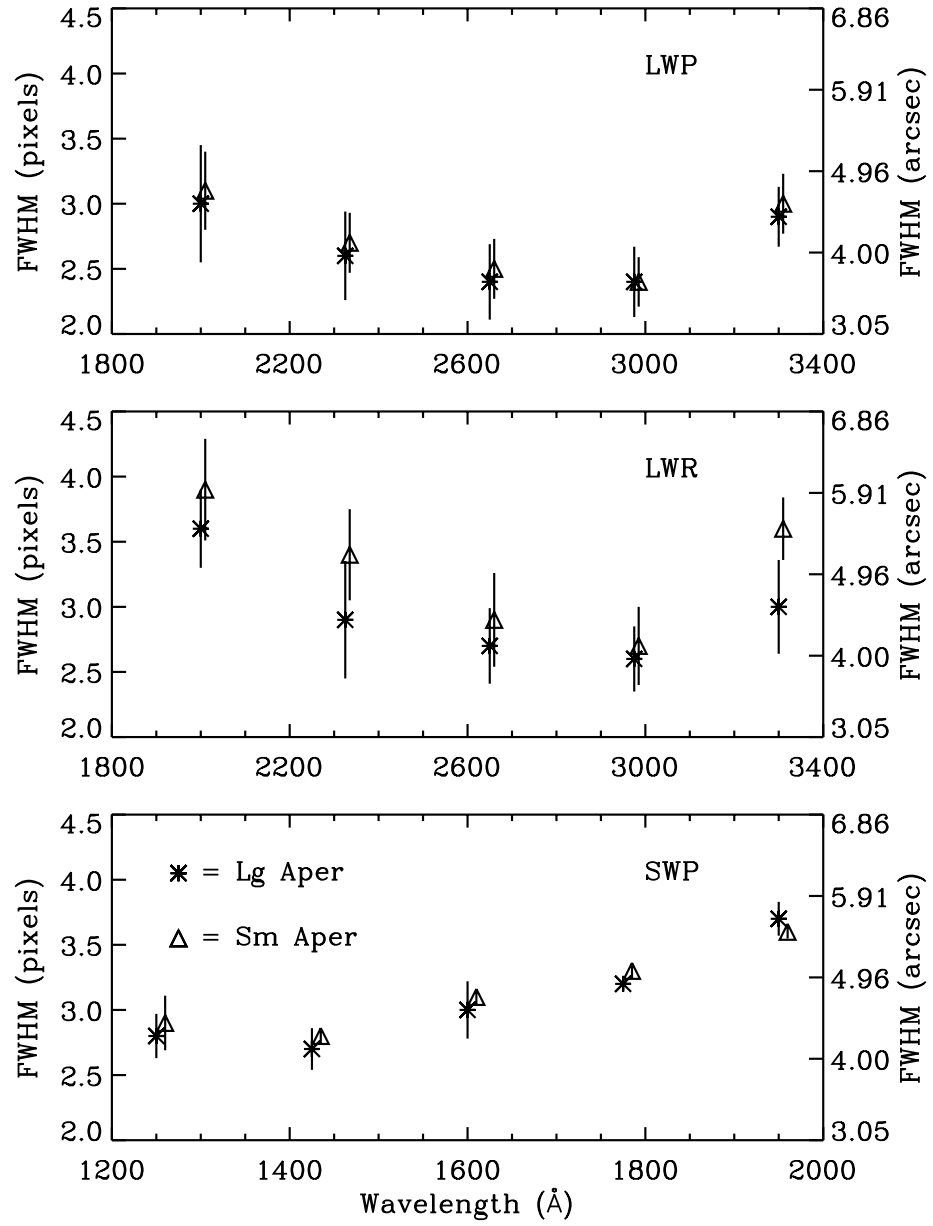


Figure 2.20: Low-dispersion spatial resolution.

the standard star, RR Tel, and V1016 Cyg data were too noisy to yield suitable results. The large-aperture Zeta Oph measurements are quite similar to the small-aperture WAVECAL analysis. The spectral resolution in wavelength space is approximately  $0.18\text{\AA}$  FWHM at order 75 and linearly decreases (roughly) to  $0.11\text{\AA}$  at order 117. The pixel space data for both WAVECALs and Zeta Oph show the same improvement in resolution between orders 95 and 110.

The IUE Systems Design Report (GSFC 1976) lists  $15,000 (\lambda/\Delta\lambda)$  as the high-dispersion resolution for the long-wavelength cameras. This yields  $0.22\text{\AA}$  for order 69,  $0.17\text{\AA}$  for order 90, and  $0.13\text{\AA}$  for order 123. These numbers are comparable to the NEWSIPS results of  $0.24\text{\AA}$ ,  $0.15\text{\AA}$ , and  $0.12\text{\AA}$  for these same orders. An analysis of IUESIPS spectral resolution was performed by Evans and Imhoff (1985) using FWHM measurements obtained from WAVECAL images. The results are as follows:  $0.22\text{\AA}$  for order 75,  $0.17\text{\AA}$  for order 83,  $0.13\text{\AA}$  for order 96, and  $0.13\text{\AA}$  for order 116. These figures are very similar to the NEWSIPS results of  $0.20\text{\AA}$ ,  $0.14\text{\AA}$ ,  $0.15\text{\AA}$ , and  $0.13\text{\AA}$ .

**LWR** – The WAVECAL spectral resolution measurements are shown in Figure 2.22 along with the corresponding linear fit (dashed line) and average (dotted line). The FWHM trends (wavelength space) below order 80 are quite similar to the LWP figures (i.e., a linear dependence of FWHM on order number). The camera resolution in wavelength space is nearly constant for orders 80 through 115, with a slight degradation in LWR resolution above order 115. This trend is easily visible in the the pixel space resolution plot and is evident from the deviation of the FWHM measurements from the mean (dotted line).

Cassatella et al. (1981) and Cassatella and Martin (1982) report a nearly constant FWHM (wavelength space) as a function of order number for WAVECAL images processed through IUESIPS. The average FWHM from their analysis is approximately  $0.18\text{\AA}$  above order 81; a value which is higher than the corresponding NEWSIPS FWHM of  $0.14\text{\AA}$ . They report a FWHM of  $0.22\text{\AA}$  for order 72, which again is much higher than the NEWSIPS results of  $0.19\text{\AA}$ . Evans and Imhoff (1985) also measured spectral resolution using IUESIPS processed WAVECAL images. They present FWHM values of  $0.19\text{\AA}$ ,  $0.17\text{\AA}$ ,  $0.16\text{\AA}$ , and  $0.15\text{\AA}$  for orders 75, 83, 96, and 116, respectively. The corresponding NEWSIPS values for these same orders are:  $0.19\text{\AA}$ ,  $0.14\text{\AA}$ ,  $0.15\text{\AA}$ , and  $0.14\text{\AA}$ . Boggess et al. (1978) quote a constant FWHM of  $0.19\text{\AA}$  for WAVECAL images, regardless of order number. This contradicts all subsequent reports written on this subject as well as the NEWSIPS results shown here. Their analysis was performed early in the life of IUE; perhaps the camera characteristics had not yet stabilized at this period in time.

**SWP** – The WAVECAL, Zeta Oph, and large- and small-aperture stellar source spectral resolution data are displayed in Figures 2.23, 2.25, 2.26, and 2.27. As is the case with the LWP and LWR, the plots include one-sigma error bars and linear (dashed line) and mean (dotted line) fits to the data. In Figures 2.26 and 2.27, the emission line measurements for orders 111 and above were excluded from the analysis when performing the linear fit to the stellar data because they were highly discrepant. The spectral resolution in wavelength space for the WAVECAL, Zeta Oph, and stellar source images shows no dependence on wavelength within an order and a roughly linear dependence on order number. Unlike the

LWP, the SWP resolution from the Zeta Oph analysis (Figure 2.25) is much worse than the corresponding WAVECAL data (Figure 2.23). The stellar source results are somewhat inconclusive for orders 111 and above. The emission line widths are dramatically higher than the corresponding absorption line measurements. This trend was also seen in the analysis by Grady (1985). The IUE Systems Design Report (GSFC 1976) quotes a figure of 10,000 ( $\lambda/\Delta\lambda$ ) for the spectral resolution in high-dispersion mode. This corresponds to a FWHM of approximately  $0.2\text{\AA}$  for order 66 and  $0.1\text{\AA}$  for order 125. This same trend is seen in the top plot (Figure 2.23) of the WAVECAL resolution analysis; the spectral resolution is essentially a constant value in pixel space (bottom plot). The stellar source resolution measurements in pixel space (bottom plot of Figures 2.26 and 2.27) show some degradation towards higher order numbers. In addition, the small-aperture data (Figure 2.27) indicates an 8% improvement in resolution over the large-aperture counterpart (Figure 2.26).

The general trend of the wavelength-space resolution for the WAVECAL images is approximately the same for every IUESIPS study that has been reviewed (i.e., Boggess et al. 1978, Cassatella et al. 1981, Cassatella and Martin 1982, and Evans and Imhoff 1985). That is, the camera resolution in wavelength space varies roughly linearly with order number and improves towards shorter wavelengths ( $0.19\text{\AA}$  for order 69 and  $0.09\text{\AA}$  for order 106). The results from analysis of WAVECAL images processed through NEWSIPS are almost identical to these figures. Penston (1979) reported SWP large-aperture FWHM values of  $0.20\text{\AA}$  for absorption lines and  $0.24\text{\AA}$  for emission lines. These figures are comparable with the average NEWSIPS results of  $0.21\text{\AA}$  and  $0.23\text{\AA}$  respectively. However, Penston's (1979) measurements for the small-aperture resolution are no better than the large aperture. This result could be supported by the NEWSIPS analysis as the apparent improvement in small-aperture resolution is less than the one-sigma error of the FWHM average for any given order. Grady (1985) assessed the effects of the two-gyro control mode on high-dispersion data using large-aperture RR Tel spectra. The mean resolution (averaged over all orders) from the Grady analysis ( $0.22\text{\AA}$ ) agrees with the average NEWSIPS resolution result.

### 2.3.2.2 Resolution Perpendicular to the Dispersion

The spatial resolution has been determined by analyzing the spectra of high-dispersion standard stars. The FWHM of several pairs of large and small-aperture line-by-line images were measured at five sample positions (*viz.*, 134, 258, 384, 507, and 615). For each sample position, a three pixel wide average cross-cut perpendicular to the dispersion was taken and the widths of the orders measured using the gaussian fitting routine. The results for each image were in good agreement, so we averaged the results to yield a set of spectral widths for each aperture as a function of order number and sample position. The differences in telescope focus between the images were kept small so as to minimize the effect of focus on the resolution measurements (Pérez et al. 1990). The database of spectra used for each camera contains a combination of optimally exposed images for the central orders and overexposed (in the central orders only) images for the extreme orders. The spatial resolution data and the one-sigma error bars for each sample position are plotted as a function of order number.

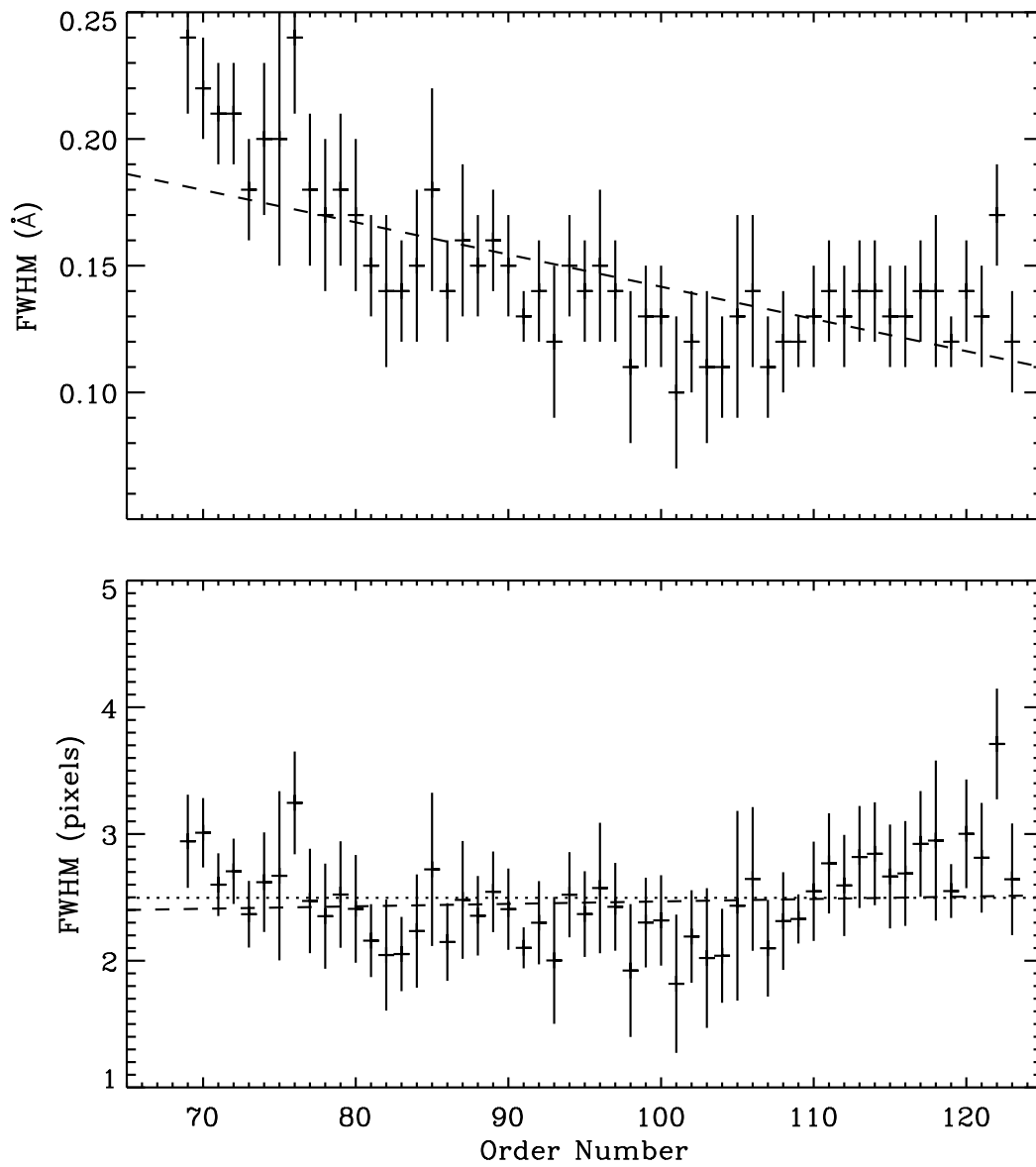


Figure 2.21: LWP high-dispersion spectral resolution from WAVECAL analysis.

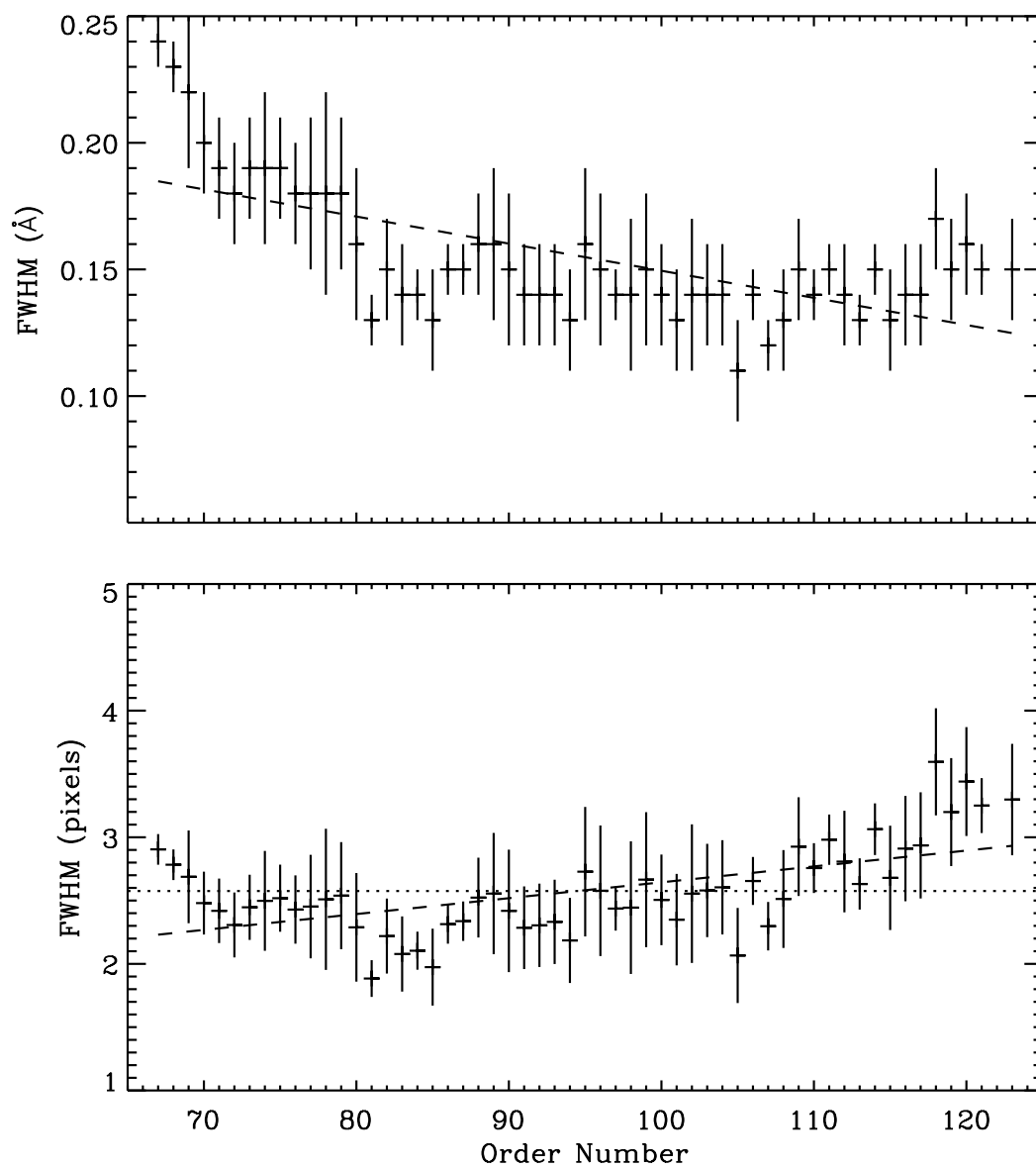


Figure 2.22: LWR high-dispersion spectral resolution from WAVECAL analysis.



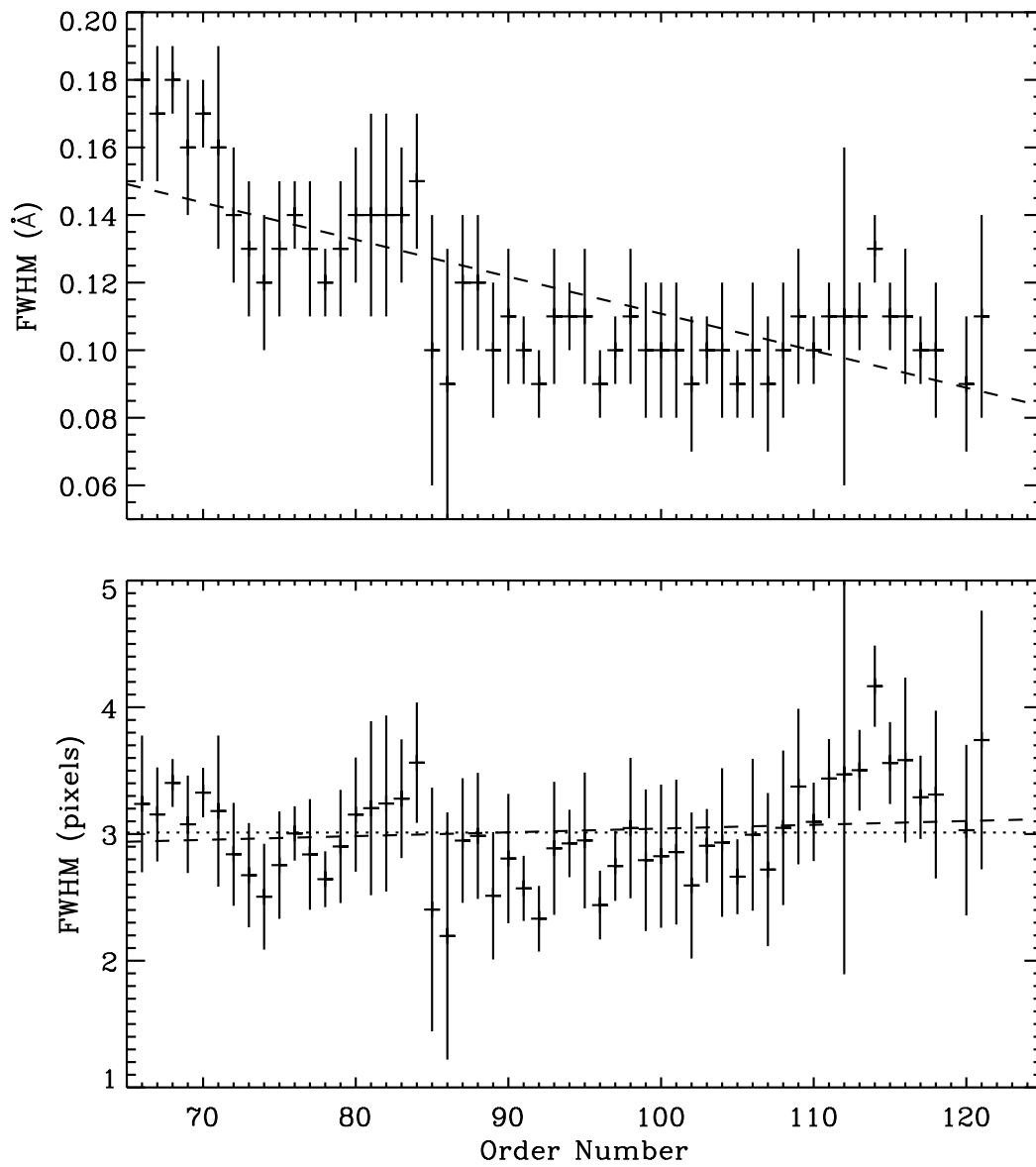


Figure 2.23: SWP high-dispersion spectral resolution from WAVECAL analysis.

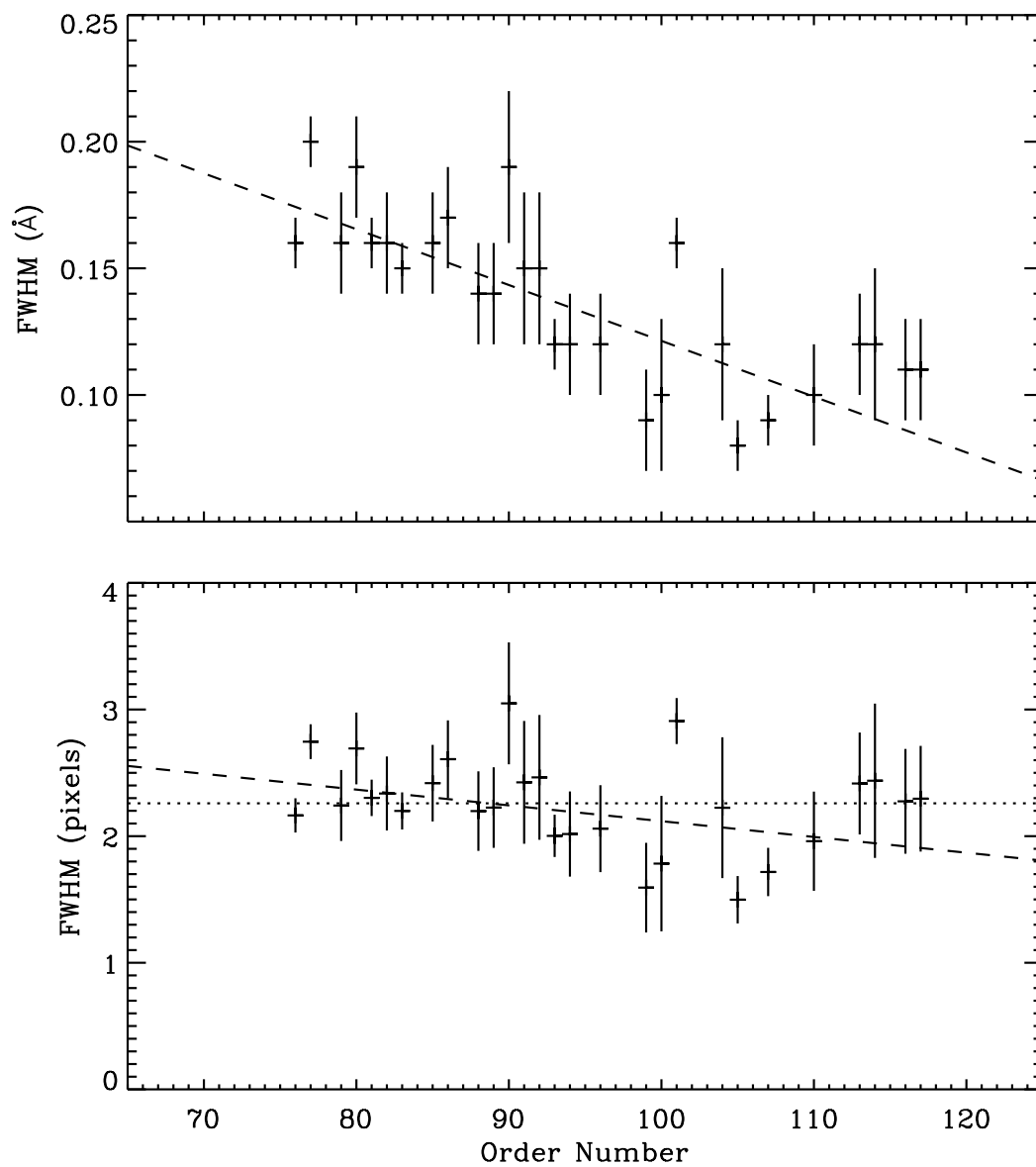


Figure 2.24: LWP high-dispersion spectral resolution from analysis of large-aperture Zeta Oph data.

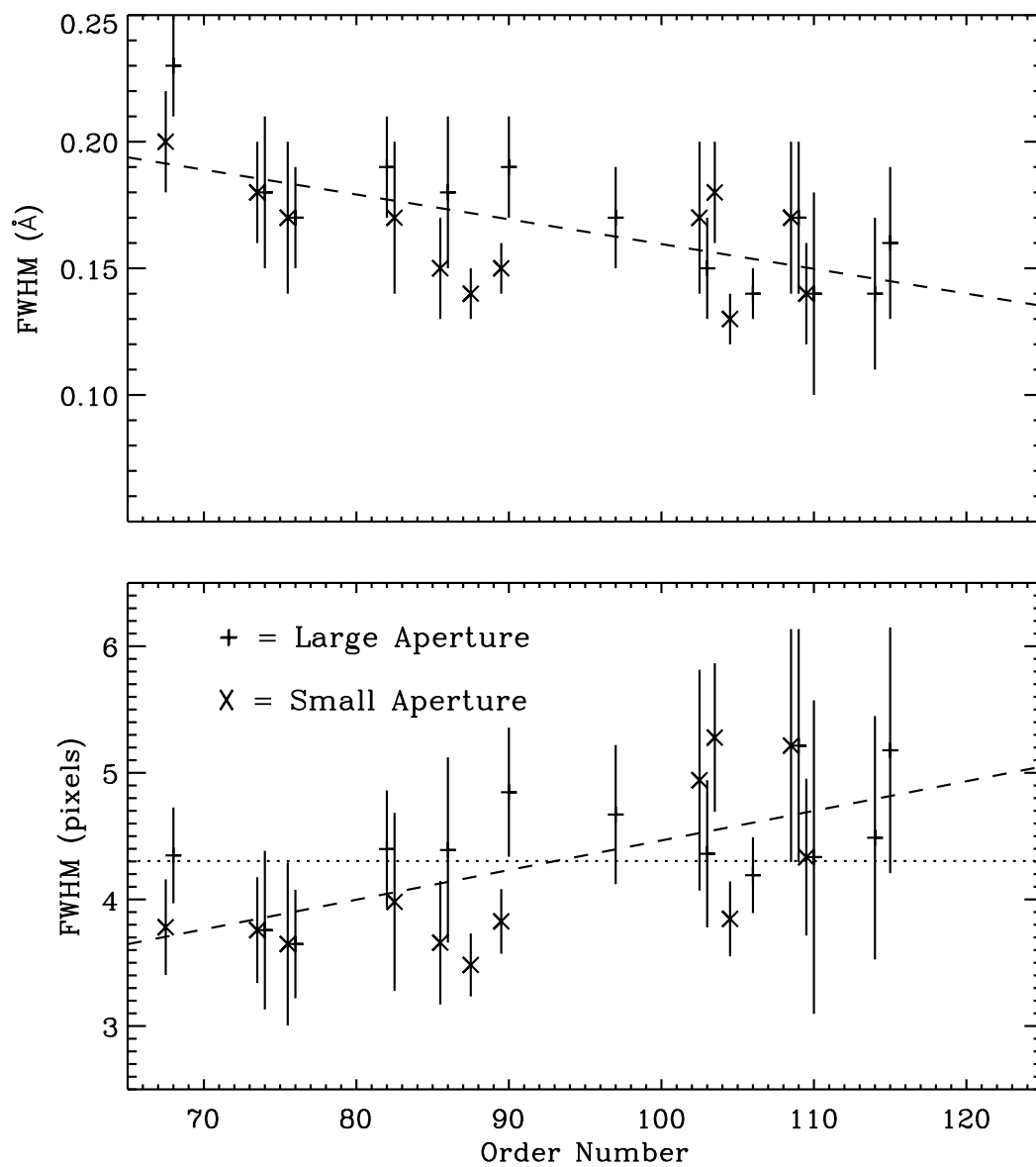


Figure 2.25: SWP high-dispersion spectral resolution from analysis of large- and small-aperture Zeta Oph data. Small-aperture data is horizontally offset to the left of the large-aperture data by half an order.

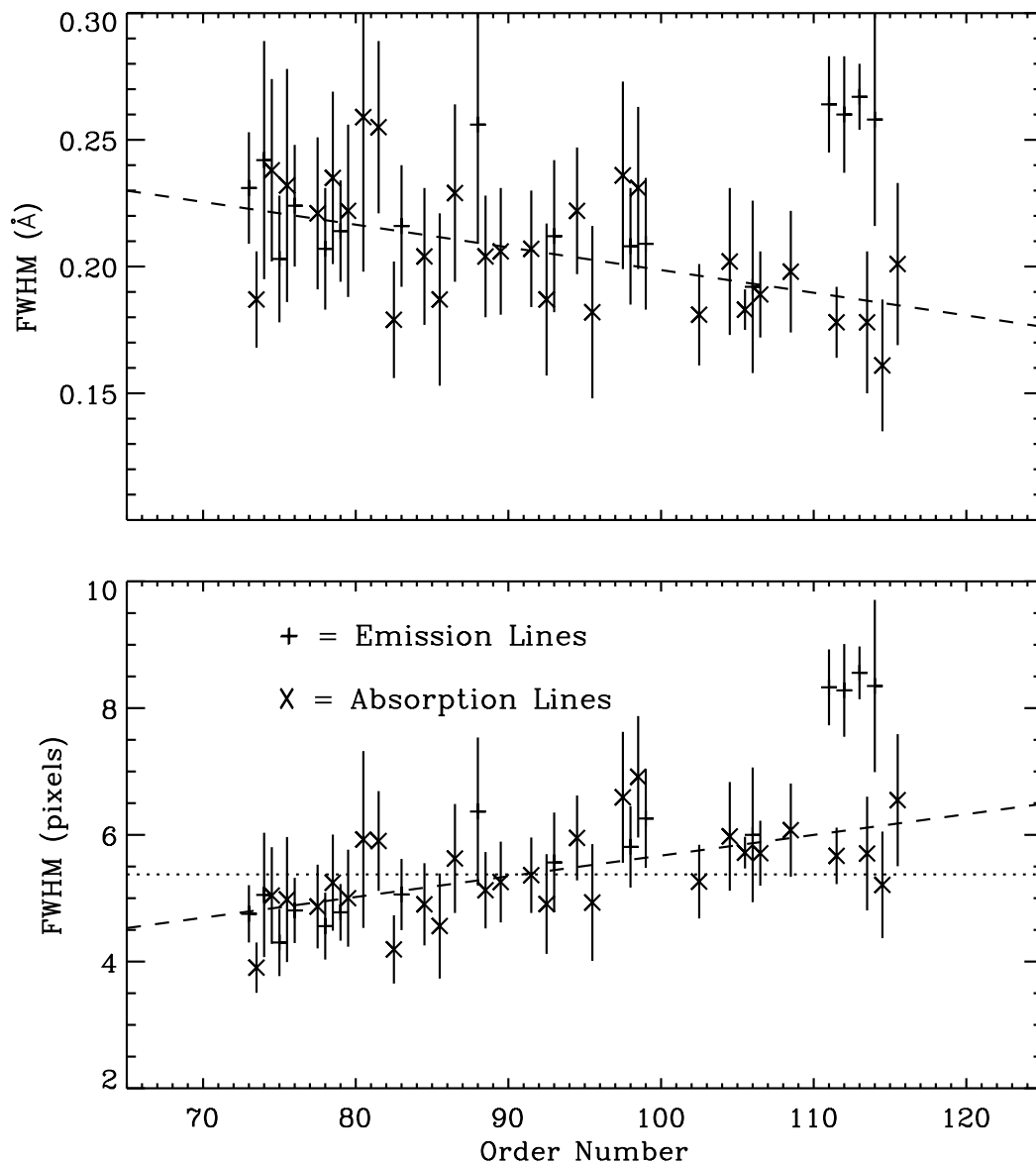


Figure 2.26: SWP high-dispersion spectral resolution from large-aperture stellar source analysis. Absorption line data is horizontally offset to the left of the emission line data by half an order.

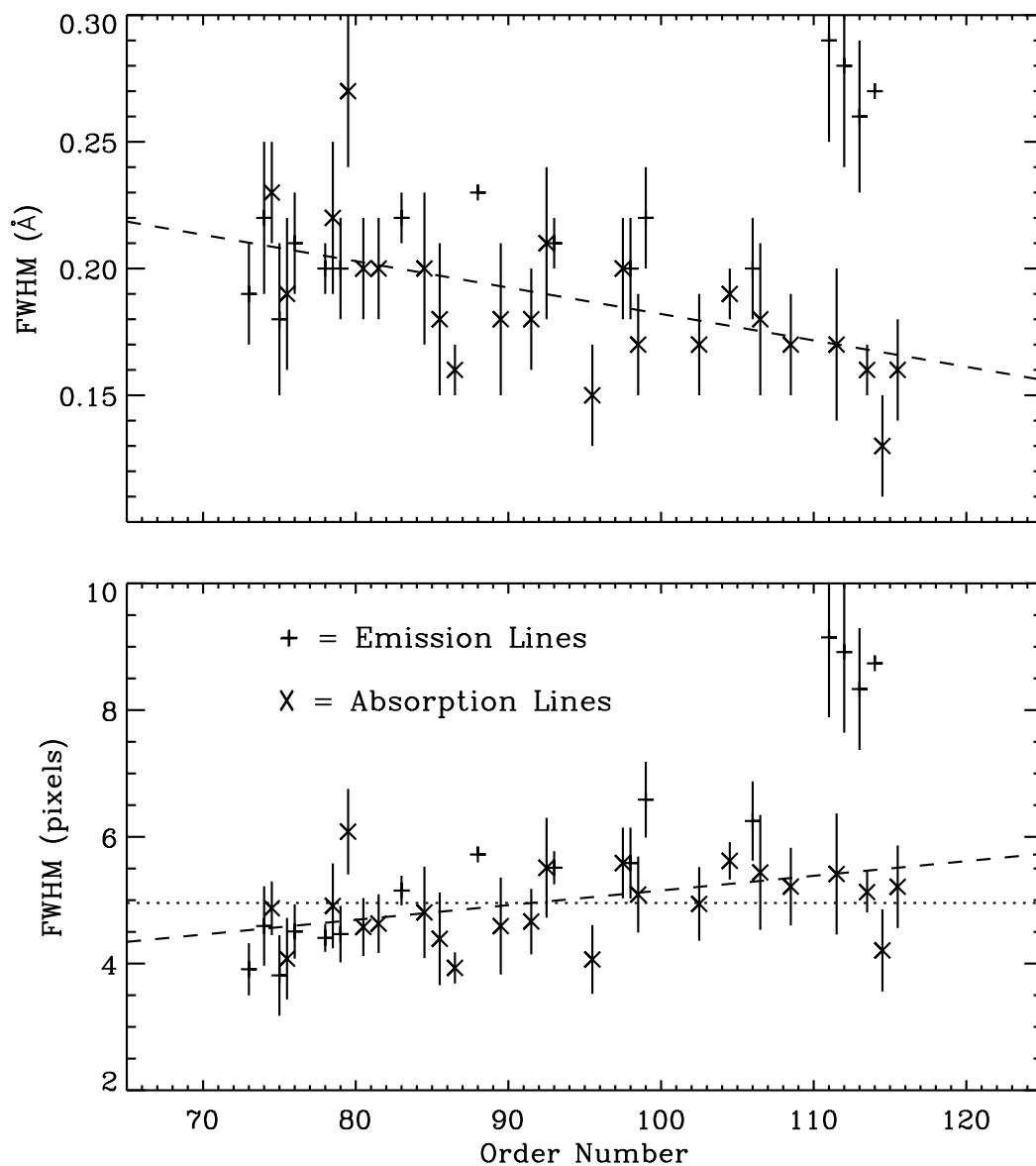


Figure 2.27: SWP high-dispersion spectral resolution from small-aperture stellar source analysis. Absorption line data is horizontally offset to the left of the emission line data by half an order.

The small-aperture data are horizontally offset to the left of the large-aperture data by half an order for clarity. A seventh-order polynomial fit to the data is also provided.

**LWP** – Spatial resolution measurements of the FWHM are plotted in Figures 2.28–2.32. The spatial resolution for sample position 384 is approximately 3.5 pixels FWHM at order 69 and decreases to 2.3 pixels at order 80 where it is roughly constant for the remaining orders. The spatial resolution degrades as one moves towards smaller sample positions and improves slightly (as compared with sample position 384) above order 90 for sample position 507. Small-aperture resolution shows an average improvement (over all orders and sample positions) of 4.6% over the large aperture. This difference is most apparent between orders 80 through 100 and at the smaller sample positions where it is as much as 8% for sample position 134. Unfortunately, no LWP high-dispersion spatial resolution studies could be found for IUESIPS data to compare against the NEWSIPS results.

**LWR** – Figures 2.33–2.37 show spatial resolution measurements of the FWHM plotted as a function of order number. The resolution trends for sample positions 134 through 384 are quite similar. The FWHM is approximately 3.0 pixels for order 69 and linearly decreases to 2.4 pixels at order 80 where it remains fairly constant for the remaining orders. For sample position 507, the FWHM is around 3.2 pixels for order 69 and linearly decreases to 2.6 pixels at order 80 where it then gradually decreases to 2.3 pixels at order 123. The behavior for sample position 615 demonstrates a rapid decrease in FWHM from 3.8 pixels at order 69 to 2.7 pixels at order 95 where it then gradually decreases to 2.3 pixels at order 120. The small-aperture resolution shows an improvement of approximately 4.7% over the large aperture.

The IUESIPS FWHM measurements obtained by Cassatella et al. (1981) using WAVE-CAL images are somewhat inconclusive. Their data only includes 5 orders (71, 73, 77, 81, and 90) and no mention was made of the sample positions at which these measurements were taken. Their numbers range from 3.5 pixels at order 71 to 2.7 pixels at order 90; values which are around 10% higher than the corresponding NEWSIPS FWHM measurements. The trends seen in the 2-D contour plots made by de Boer et al. (1983) are in good agreement with the NEWSIPS results. They show that for the central sample positions (i.e., 384) the FWHM starts out at 3.1 pixels at low order numbers and decreases to 2.8 pixels towards the center of the camera (e.g., order 90). The slight degradation in resolution seen in the central orders of Figure 2.35 is also apparent in the de Boer plots.

**SWP** – Spatial resolution measurements of the FWHM are plotted in Figures 2.38–2.42. The resolution trends as a function of order number are, in general, the same for every sample position. The FWHM is around 4 pixels at order 66 (long wavelengths) and decreases to approximately 2 pixels near order 100 (short wavelengths). Unlike the indications from previous IUESIPS studies (e.g., Bianchi (1980), Schiffer (1980), and Cassatella et al. (1981)), this decrease is not linear with order number. A plateau of around 3.0 pixels FWHM occurs between orders 75 and 85. This trend is confirmed by the analysis of de Boer et al. (1983), which displayed the order widths using 2-D contour plots. The FWHM remains fairly constant above order 100 for sample positions 258 and 384. At these sample positions, the higher orders (100 and above) are well away from the edge of the camera. The more

extreme sample positions (i.e., 134 and 507) show an edge effect as the resolution dramatically worsens above order 100. The best spatial resolution occurs near sample position 384 and worsens slightly as one moves towards smaller sample positions (i.e., shorter wavelengths within an order). Differences in resolution between the large and small apertures are small. The small aperture shows an average improvement (over all orders) of 2.4% in resolution over the large aperture.

As is the case with the low-dispersion resolution studies, the NEWSIPS values show an improvement over IUESIPS measurements. Schiffer (1980) quoted FWHM values of 3.5 pixels for order 75 and 2.4 pixels for order 105. The NEWSIPS results for those orders are 3.3 pixels and 2.1 pixels, respectively. Analysis by de Boer et al. (1983) showed the best resolution of 2.4 pixels FWHM occurring near the center of the camera. The NEWSIPS results indicate a FWHM of 2.0 pixels in this same area (sample position 384). Also, Bianchi (1980) expressed FWHM as a function of order number, regardless of camera, according to the following formula:  $FWHM = 7.23 - 0.04 \times m$  where  $m$  is order number and the FWHM is in pixels. Thus, for order 71, this indicates a FWHM of 4.4 pixels, a figure that is almost 20% higher than the NEWSIPS average measurement for that order.

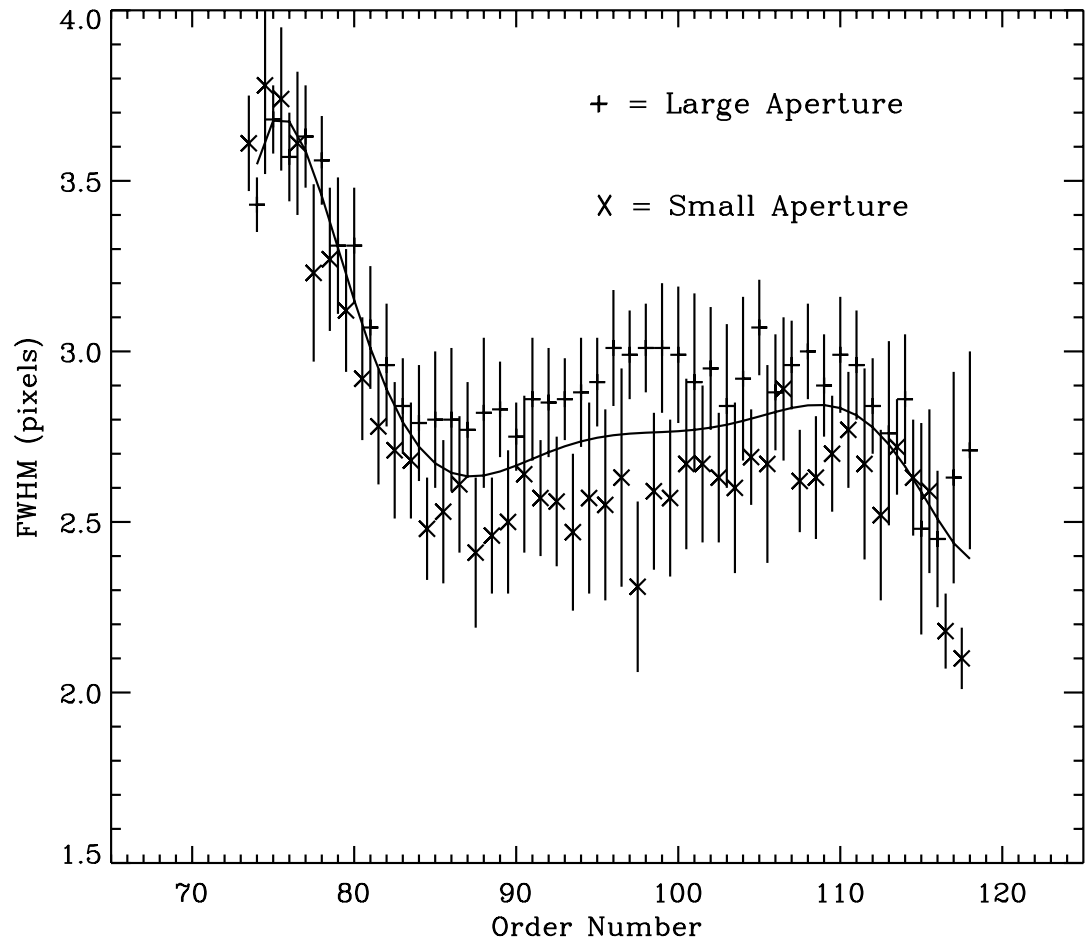


Figure 2.28: LWP high-dispersion spatial resolution for sample position 134. Small-aperture data is horizontally offset to the left of the large-aperture data by half an order.



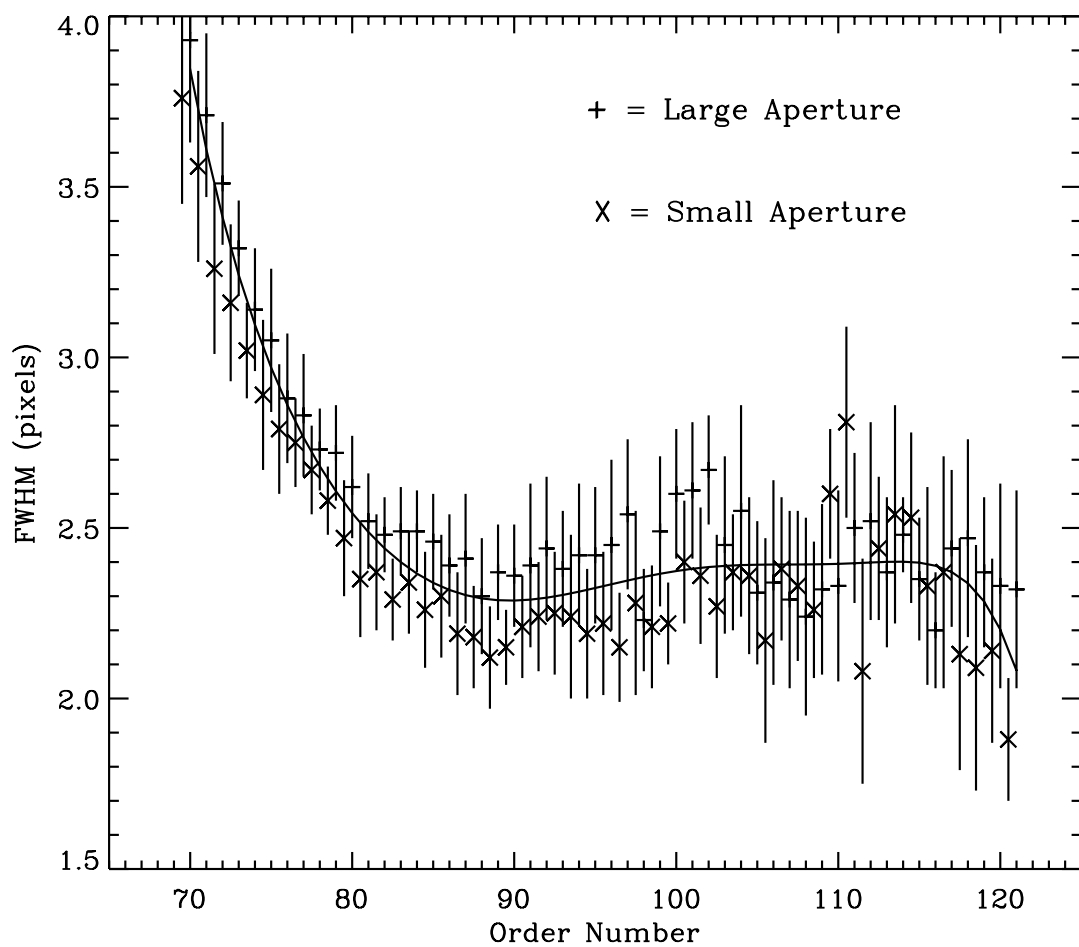


Figure 2.29: LWP high-dispersion spatial resolution for sample position 258. Small-aperture data is horizontally offset to the left of the large-aperture data by half an order.

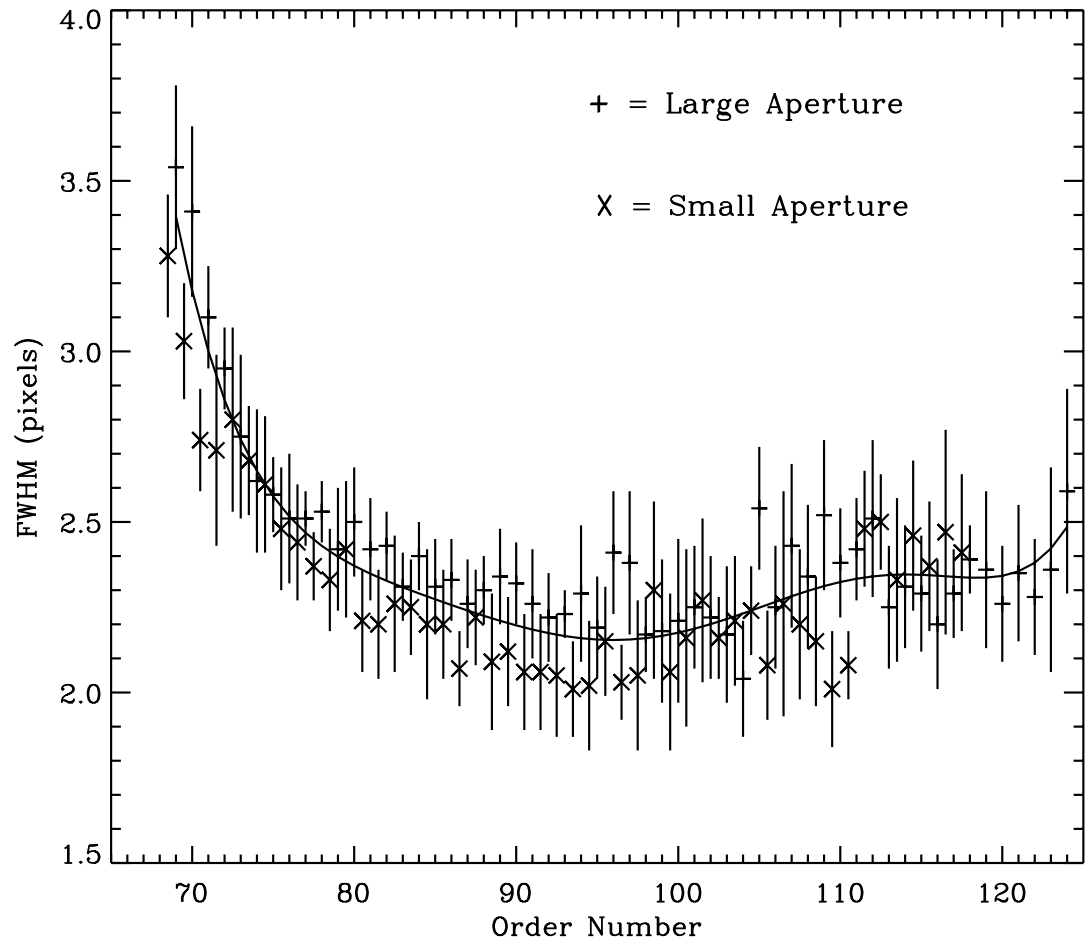


Figure 2.30: LWP high-dispersion spatial resolution for sample position 384. Small-aperture data is horizontally offset to the left of the large-aperture data by half an order.

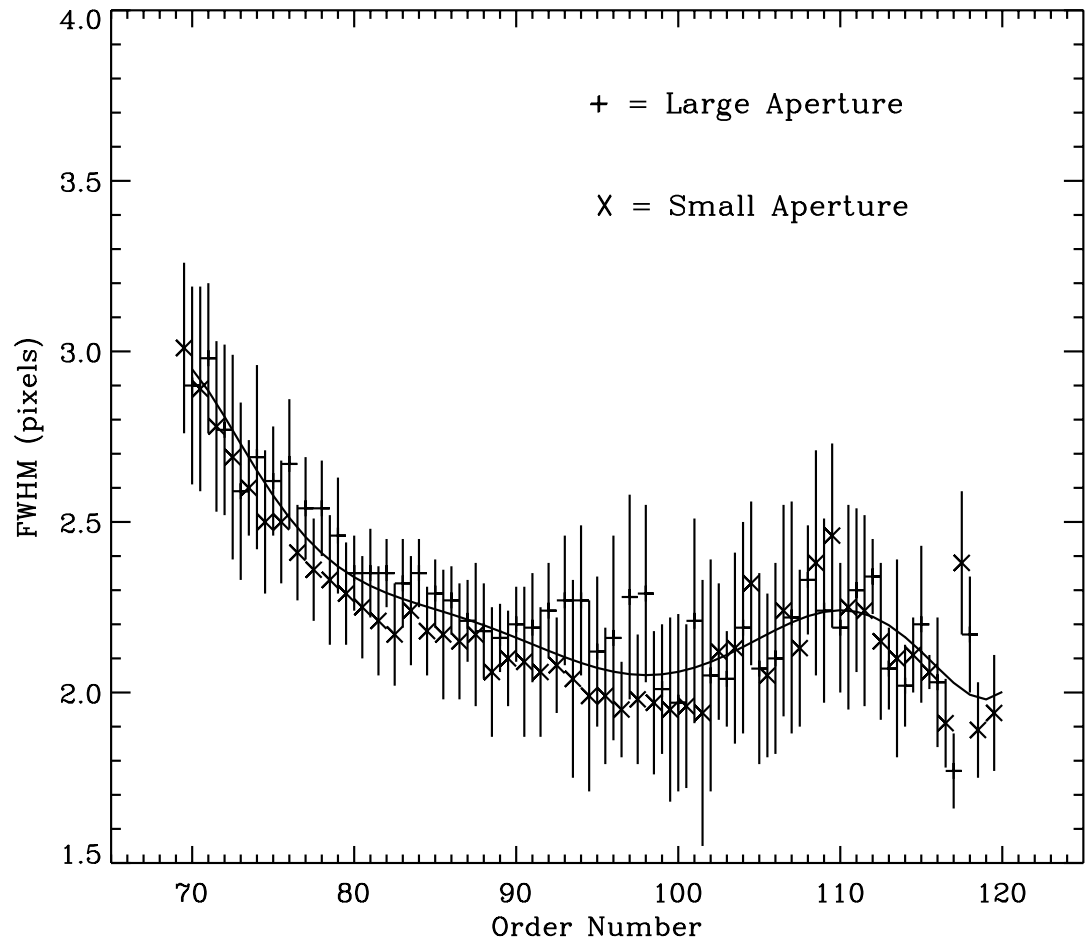


Figure 2.31: LWP high-dispersion spatial resolution for sample position 507. Small-aperture data is horizontally offset to the left of the large-aperture data by half an order.

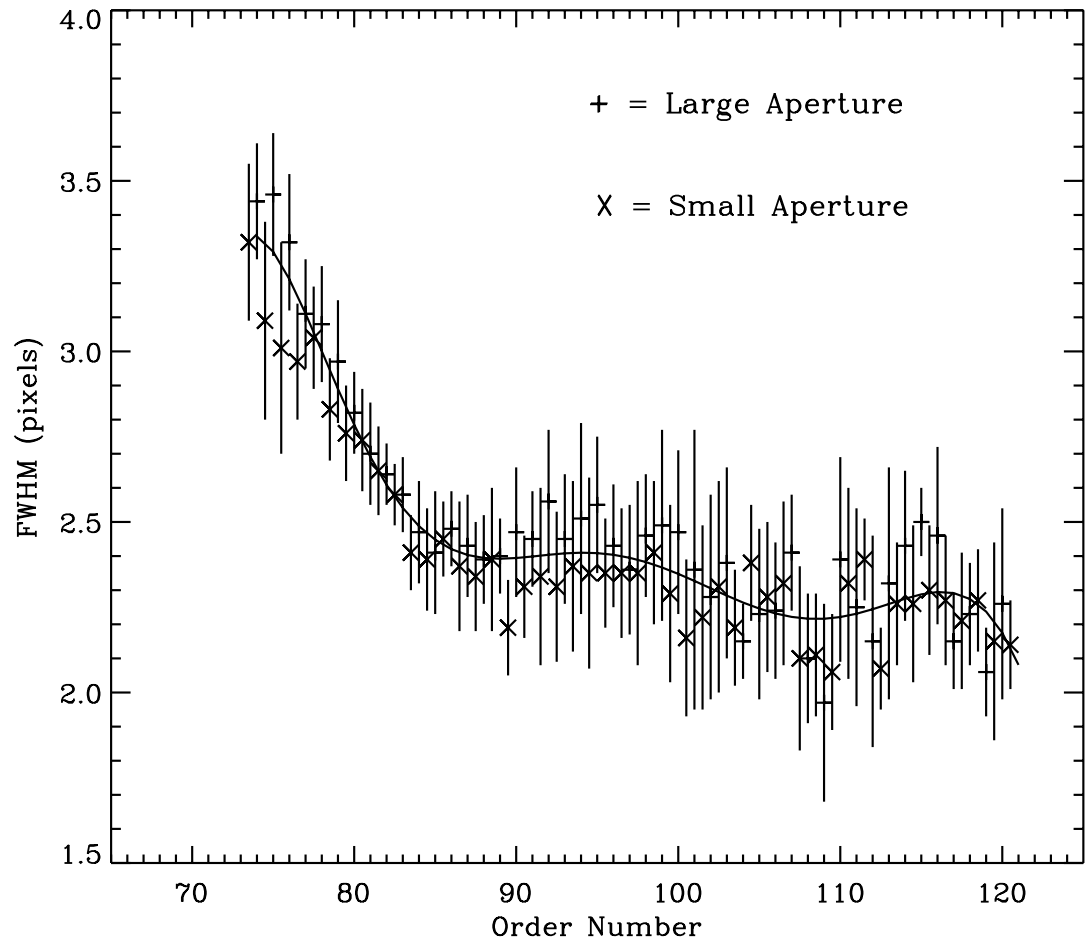


Figure 2.32: LWP high-dispersion spatial resolution for sample position 615. Small-aperture data is horizontally offset to the left of the large-aperture data by half an order.

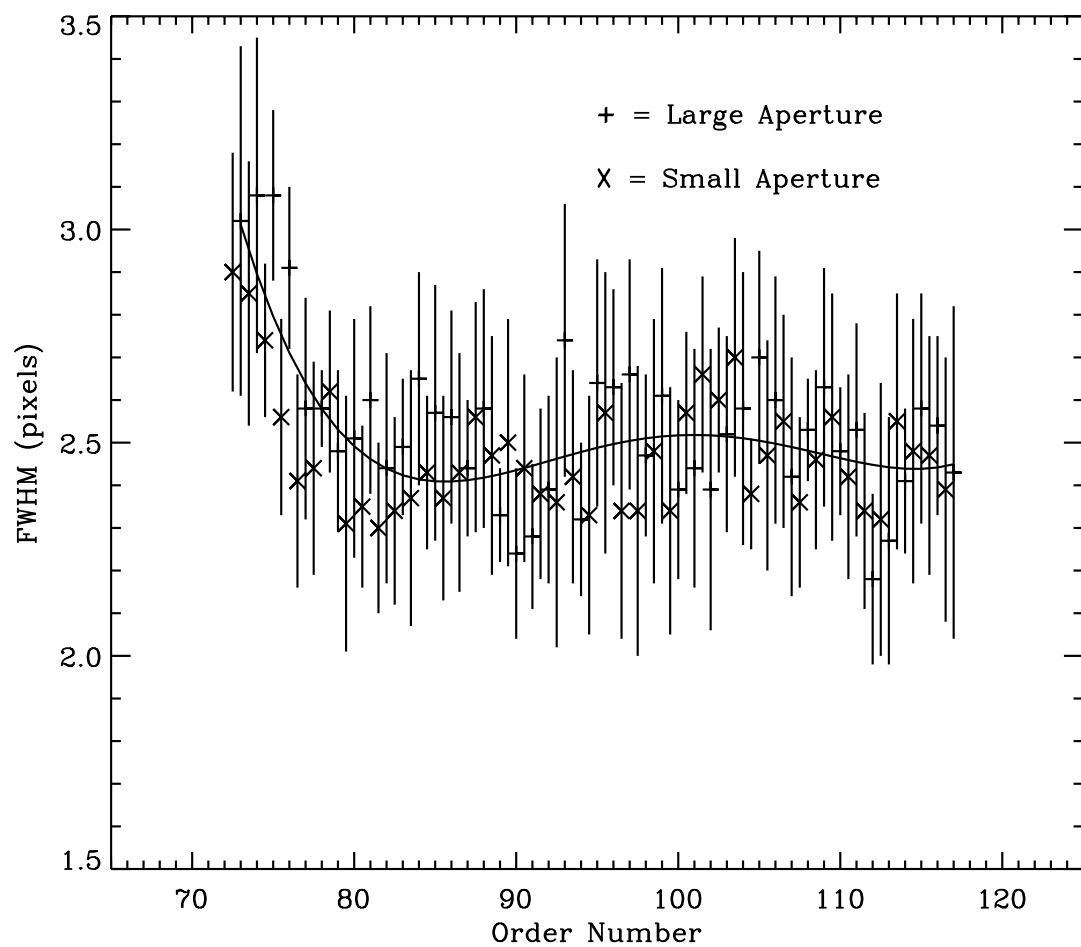


Figure 2.33: LWR high-dispersion spatial resolution for sample position 134. Small-aperture data is horizontally offset to the left of the large-aperture data by half an order.

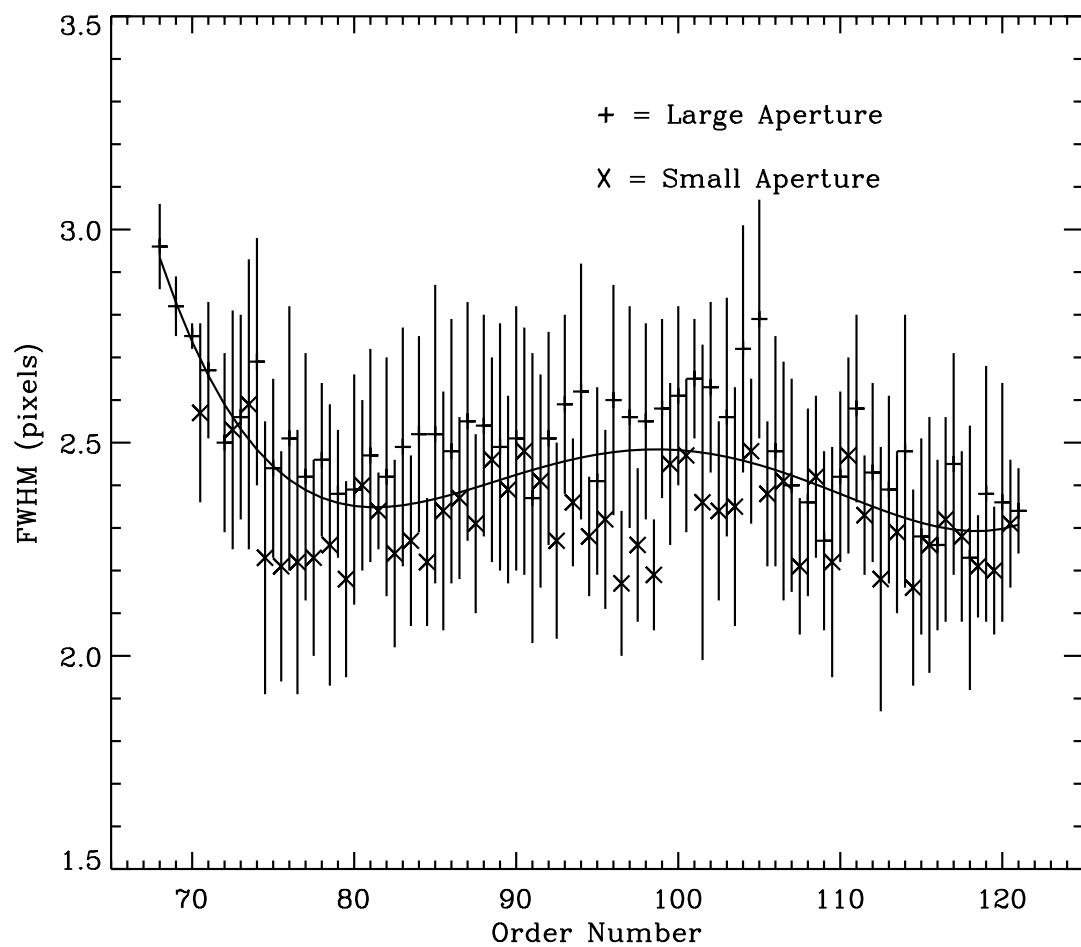


Figure 2.34: LWR high-dispersion spatial resolution for sample position 258. Small-aperture data is horizontally offset to the left of the large-aperture data by half an order.

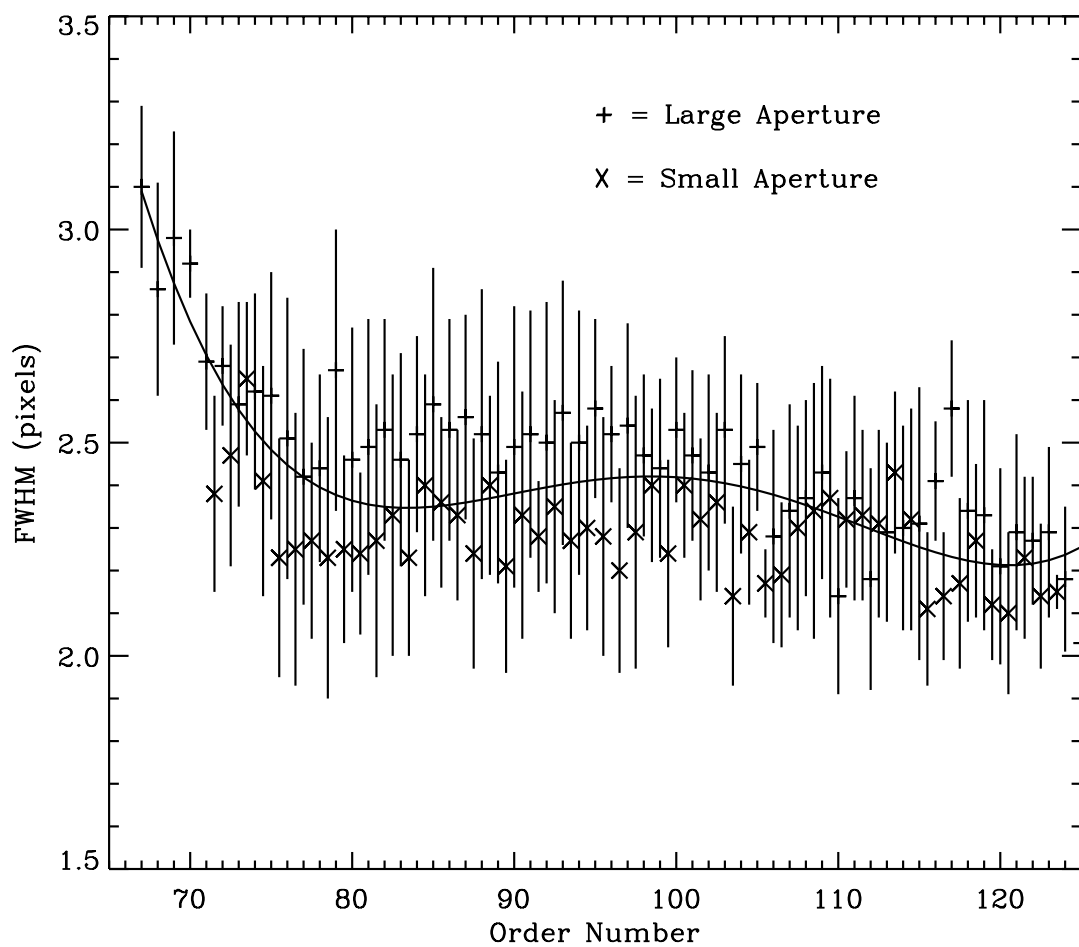


Figure 2.35: LWR high-dispersion spatial resolution for sample position 384. Small-aperture data is horizontally offset to the left of the large-aperture data by half an order.

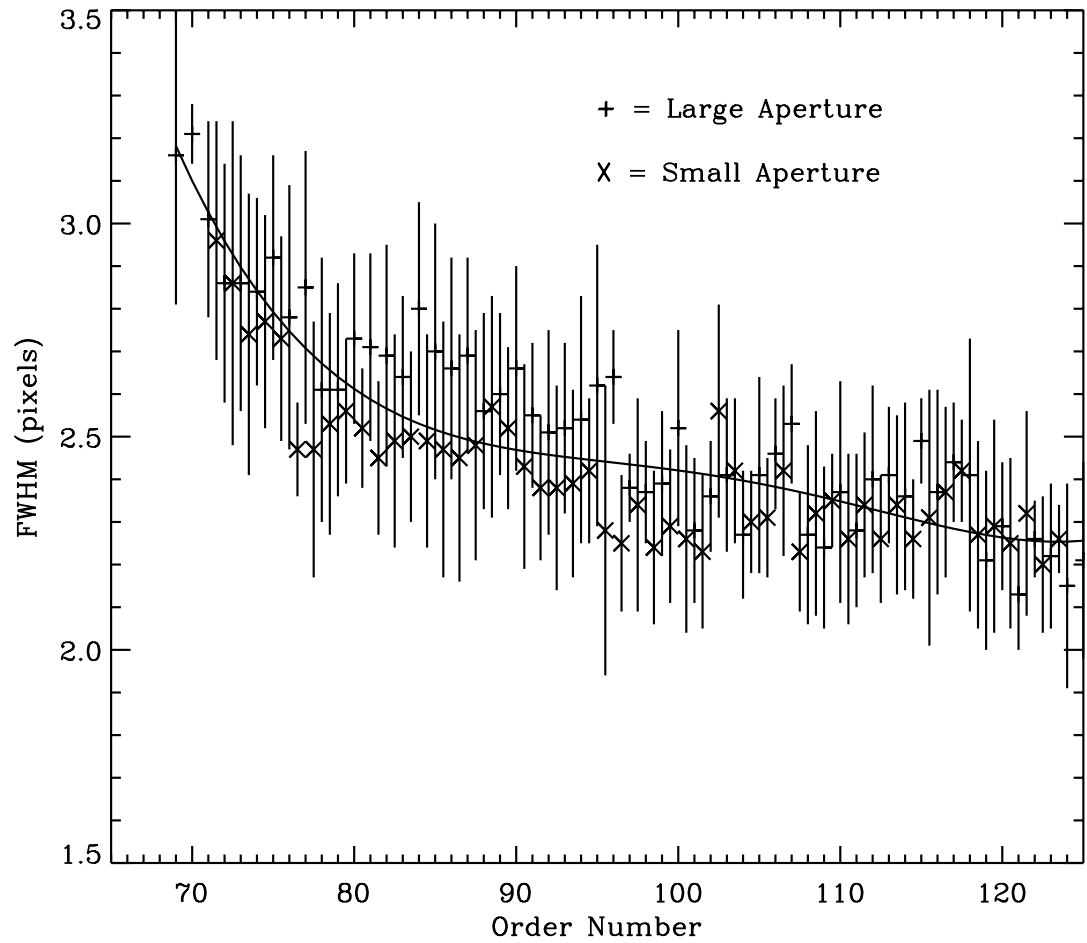


Figure 2.36: LWR high-dispersion spatial resolution for sample position 507. Small-aperture data is horizontally offset to the left of the large-aperture data by half an order.



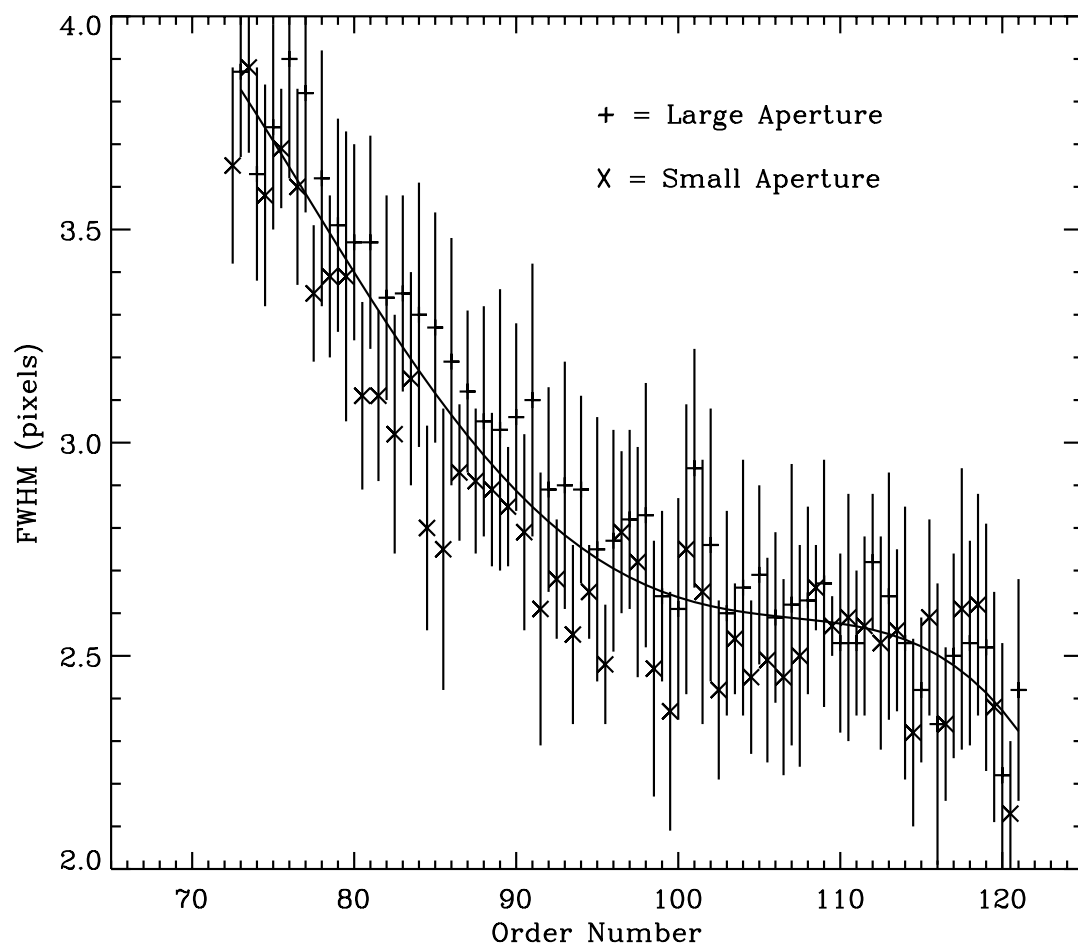


Figure 2.37: LWR high-dispersion spatial resolution for sample position 615. Small-aperture data is horizontally offset to the left of the large-aperture data by half an order.

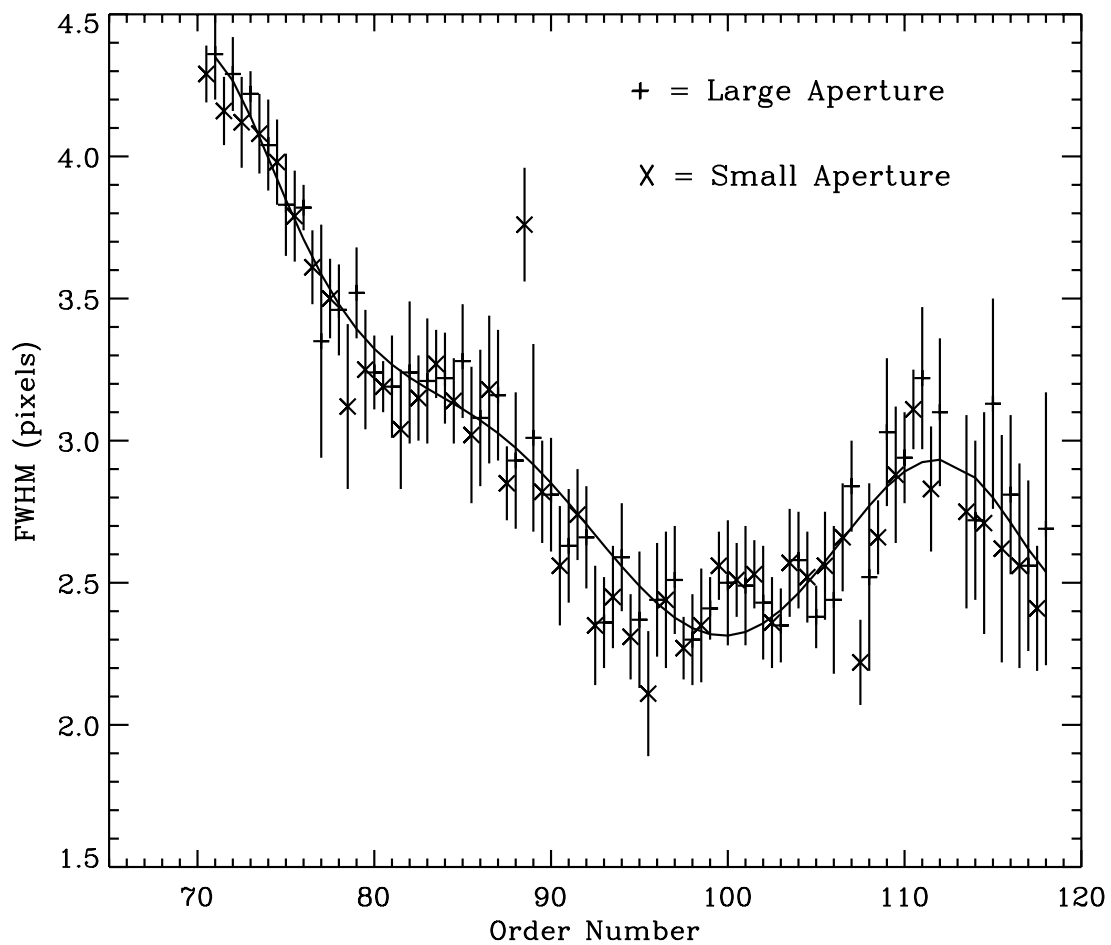


Figure 2.38: SWP high-dispersion spatial resolution for sample position 134. Small-aperture data is horizontally offset to the left of the large-aperture data by half an order.

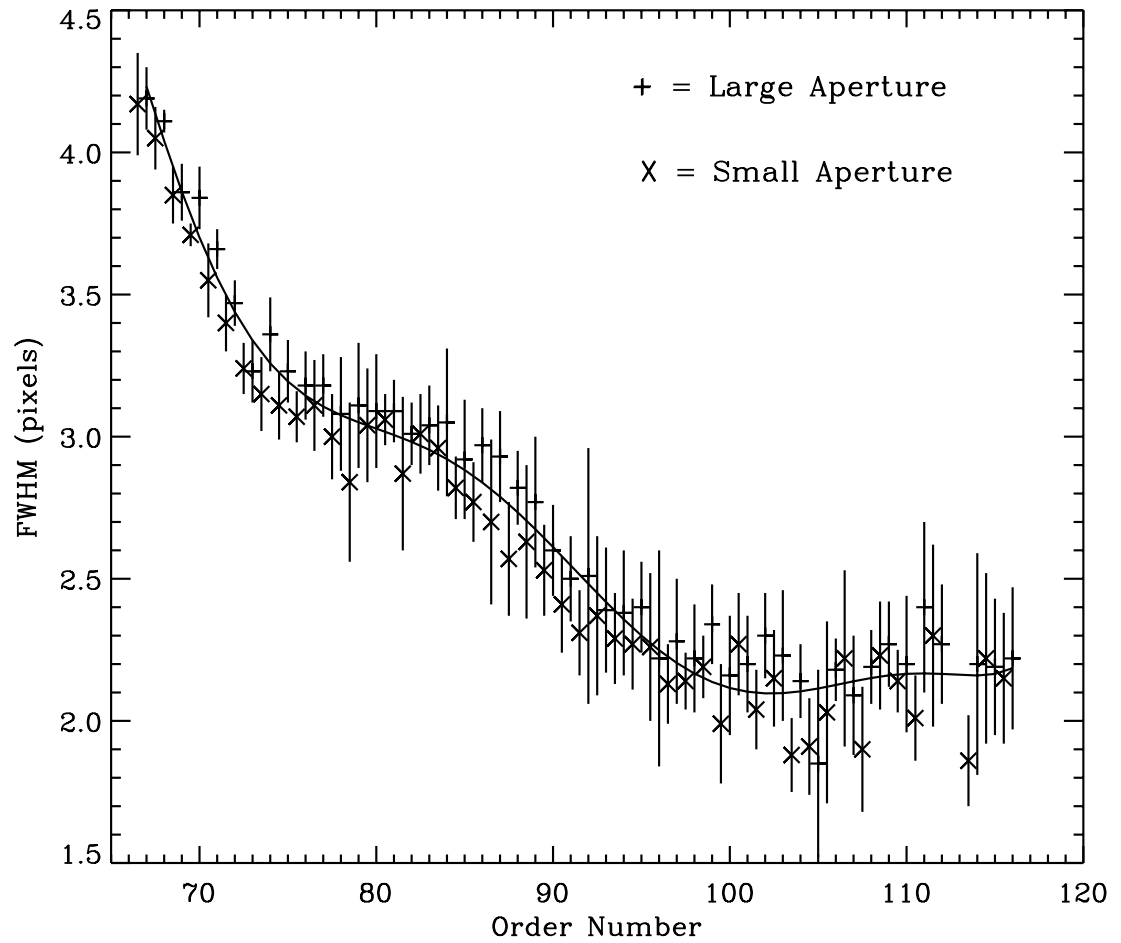


Figure 2.39: SWP high-dispersion spatial resolution for sample position 258. Small-aperture data is horizontally offset to the left of the large-aperture data by half an order.

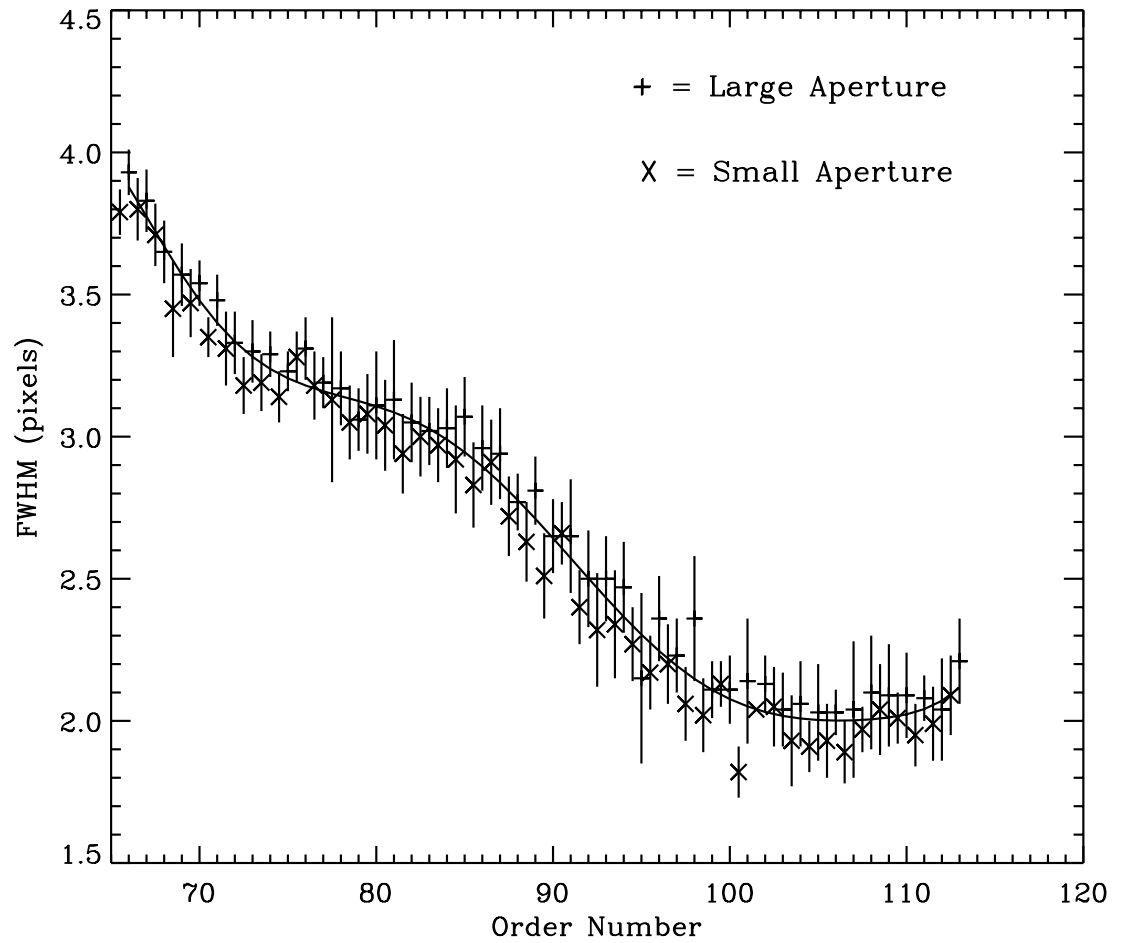


Figure 2.40: SWP high-dispersion spatial resolution for sample position 384. Small-aperture data is horizontally offset to the left of the large-aperture data by half an order.

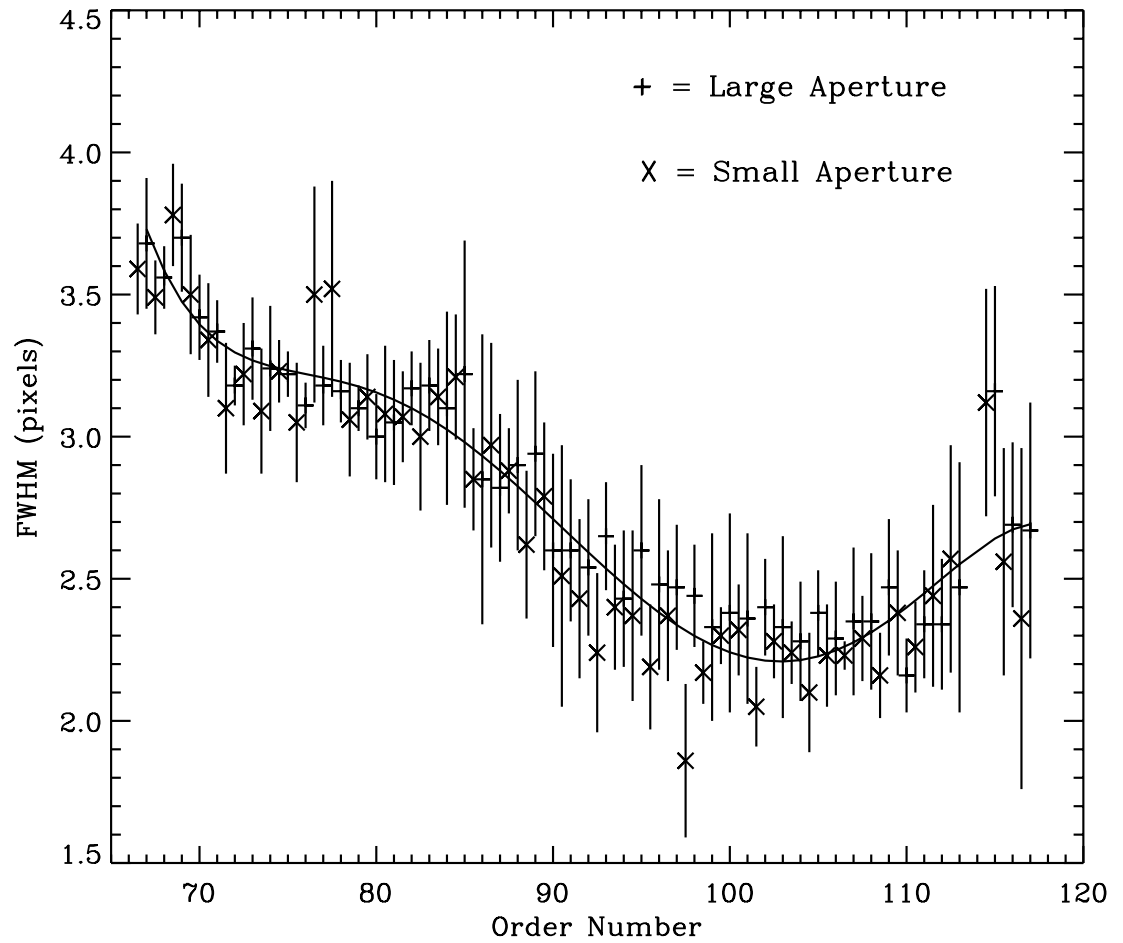


Figure 2.41: SWP high-dispersion spatial resolution for sample position 507. Small-aperture data is horizontally offset to the left of the large-aperture data by half an order.

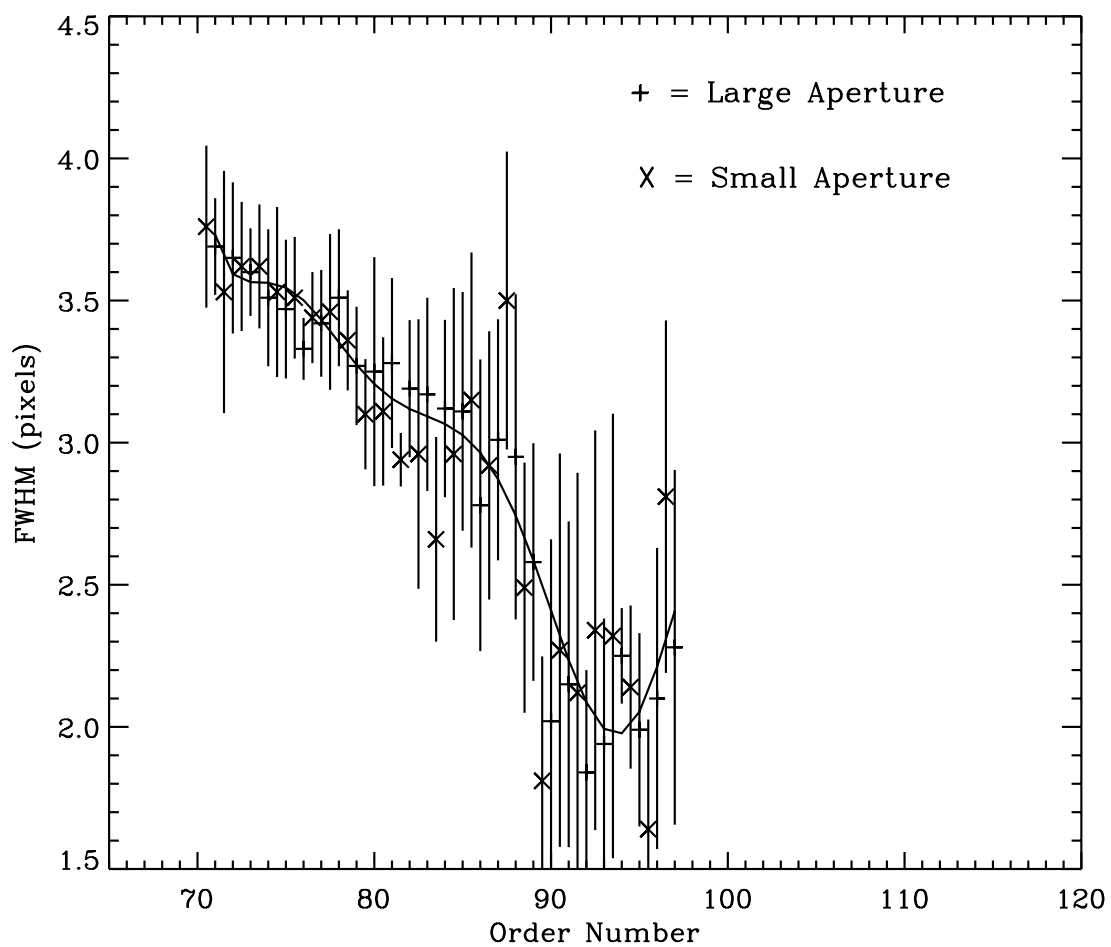


Figure 2.42: SWP high-dispersion spatial resolution for sample position 615. Small-aperture data is horizontally offset to the left of the large-aperture data by half an order.

# Chapter 3

## Data Quality Flag Description

For the creation of the IUE Final Archive, data quality ( $\nu$ ) flags are provided on a pixel-by-pixel basis for the two-dimensional (2-D) photometrically corrected (LI) and geometrically resampled (SI) output files, and as a function of wavelength in the one-dimensional merged extracted image (MX) file. These quality flags denote exceptional conditions in the data which can range from fairly minor situations of telemetry dropouts in the background regions to quite serious conditions of telemetry dropouts in extracted spectral regions. The  $\nu$  flag values have been apportioned such that the more serious conditions have more negative values in order to provide an immediate indication as to the severity of the problem condition. In contrast to the method of “epsilon” flagging as implemented in IUESIPS, where only one problem condition is noted (i.e., the most severe), the  $\nu$  flags are encoded to indicate all problem conditions associated with each pixel or wavelength bin.

The flexibility of the  $\nu$  flags is derived from the bit-encoding of the individual problem conditions. Using a total of 16 bits, the flags are stored as negative values in two’s complement form (bit 16 contains the sign), and the remaining 15 bits are utilized to represent each defined problem condition. Table 3.1 describes the problem conditions and defines the corresponding  $\nu$  flag values. Once all problem conditions are identified for each pixel or wavelength bin, the individual flag values are added together to produce a total value which is a unique combination of its components. Since additional  $\nu$  flags are available for the Final Archive dataset, and some problem conditions may have an altered definition when compared to the IUESIPS  $\epsilon$  flags, a more detailed definition of the  $\nu$  flags is in order. The descriptions of the  $\nu$  flags in this chapter are ordered according to their generation in NEWSIPS processing rather than by severity. Flags produced by the raw image screening process (*RAW\_SCREEN*) are mentioned first, while the flags introduced during the extraction phase (i.e., *SWET* or *BOXCAR*) are discussed last.

The *RAW\_SCREEN* cosmic ray/bright spot detection algorithm (Chapter 4.1) is an application of a median filtering technique and identification of the spots is based upon their limited spatial extent and unusual brightness. This flag ( $-64$ ) is differentiated from the low-dispersion extraction (*SWET*) cosmic ray flag ( $-32$ ) which is generated by a sigma rejection criterion discussed below.

Table 3.1:  $\nu$  Flag Values

Condition	$\nu$ Flag Value	BIT
Pixels not photometrically corrected	−16384	15
Missing minor frame in extracted spectrum	−8192	14
Reseau (in the ITF)	−4096	13
Permanent ITF artifact	−2048	12
Saturated pixel (w.r.t. ITF pixel DN)	−1024	11
Warning track (near edge of <i>PHOTOM</i> region)	−512	10
Positively extrapolated ITF	−256	9
Negatively extrapolated ITF - far below ITF level 1	−128	8
<i>RAW_SCREEN</i> cosmic ray/bright spot	−64	7
<i>SWET</i> cosmic ray (low disp. only)	−32	6
Microphonics (LWR only)	−16	5
Potential DMU corrupted pixel	−8	4
Missing minor frame in extracted background	−4	3
Uncalibrated data point (MX data only)	−2	2
No known problem condition	0	1



While the NEWSIPS algorithms used to detect cosmic rays/bright spots and microphonics ( $-16$ ) are similar to the IUESIPS versions, the flagging of missing minor frames (MMFs) is a new implementation. Clearly, it is important to know of the existence of a MMF in the vicinity of spectral information in order to evaluate the extent to which the MMF will affect the data. All telemetry dropouts are flagged in 2-D images as MMFs, but it is important to translate this information into how these dropouts affect the extracted spectral data and background. As a result, MMF pixels can be assigned either of two  $\nu$  flag values depending on their proximity to the spectral data. The first flag ( $-8192$ ) is utilized to label missing pixels in the spectral data. The second flag ( $-4$ ) denotes missing pixels in the extracted background. Since the background is fit with a Chebyshev polynomial, missing pixels in the extracted background potentially play a very small role in the computation of the net flux. The much smaller absolute value of the second flag reflects the less crucial nature of the condition. The MMF detection algorithm is described in Chapter 4.4.

A recent addition to the  $\nu$  flags is the one that specifies pixels which are most likely affected by DMU corruption. This flag ( $-8$ ) is allotted to pixels via a statistical process in *RAW\_SCREEN* and only applies to images taken after October of 1994. Information related to the detection of DMU corrupted pixels can be found in Chapter 4.5.

During the photometric correction (*PHOTOM*) stage of processing, extrapolations required for the conversion from data number (DN) to flux number (FN) are appropriately flagged as being either positive (DN above ITF Level 12) or negative (DN far below ITF Level 1). Positively extrapolated pixels are flagged with  $-256$  while pixels with excessive negative extrapolations are given a flag of  $-128$ . Refer to Chapter 6.3.2 for details concerning the definition of what constitutes extrapolated data.

Some of the flags, or more properly, the pixel locations of the flags, have been pre-defined based upon the location of the condition in the ITF images. For example, the positions of all permanent artifacts ( $-2048$ ) and reseaux ( $-4096$ ) are defined according to their positions in the ITF images and are flagged after the science image and the ITF are properly registered. The *PHOTOM* region is based upon the shape of the illuminated target region of the ITF; this region is nearly a circle for the SWP camera, but resembles more of a flattened circle for the long wavelength cameras. Pixels located outside the *PHOTOM* region are given a  $\nu$  flag value of  $-16384$ . The low-dispersion *PHOTOM* swath is a band contained within this pseudo-circular region, optimally positioned about the low-dispersion spectrum. In most instances, the photometric correction of an individual pixel depends somewhat upon its neighbors. As the edge of the *PHOTOM* region is approached, there can be wild fluctuations in the DN (and hence the resulting FN) values, so that the photometric correction may be less reliable in these regions. Therefore, a warning track flag ( $-512$ ) is defined to designate these less reliable flux values. The warning track is an approximately five-pixel-deep buffer zone on the inside edge of the *PHOTOM* region.

The saturation level for each pixel within the *PHOTOM* region has been obtained by examining the ITF curve of each pixel and determining the DN associated with any substantial leveling off of the ITF curve (DN vs. exposure time) with increased intensity. According to the analysis of the ITF images, there are a number of pixels which “saturate” at values much

less than 255 DN. *Ergo, many more pixels may be considered saturated by the NEWSIPS system than IUESIPS*, since in IUESIPS only pixels with a DN of more than 250 are deemed to be saturated. Saturated pixels are issued a  $\nu$  flag value of  $-1024$ .

*SWET* examines the fitted profile values in the cross-dispersion direction in each wavelength bin and compares the actual data to the profile, rejecting those values deviating by more than “N” sigma and assigning a flag value of  $-32$ . The *SWET* cosmic ray detection is not applicable for high-dispersion data, as a boxcar extraction is applied in that case. A description of the *SWET* cosmic ray removal process is given in Chapter 9.5.

The uncalibrated data flag ( $-2$ ) is found only in the final extracted spectrum and indicates wavelength regions which have been extracted from the resampled image, but whose absolute flux calibration has not been defined.

Because the  $\nu$  flags are stored as negative integers, a warning on the correct interpretation of these data is necessary. Negative integers are stored in two’s complement form by most computer systems. This means that the internal bit settings for negative values are calculated by subtracting the desired value from  $2^{15}$  or  $2^{31}$ , for 2 or 4 byte integers respectively. Accordingly, many more bits are turned on (set to 1) to represent the negative integer than just the bits for the actual digit. Consequently, if intrinsic bit decoding functions are used to decode the  $\nu$  flag values as is, the wrong answer will be derived. It is most straightforward to first take the absolute value of the  $\nu$  flag image or vector before attempting to interpret the data.

# Chapter 4

## Raw Image Screening (*RAW\_SCREEN*)

Certain operations performed by NEWSIPS may be categorized as screening or preprocessing operations which prepare the data for subsequent processing. The procedures of this nature which are performed on IUE data are described in this chapter.

### 4.1 Bright-Spot Detection

Long IUE exposures characteristically contain “bright spots”, i.e., pixels with unusually high data number (DN) values which are comprised of discrete impulse noise often reaching the saturation level. Such bright spots are thought to be caused either by permanent blemishes in the target surface, by extraordinarily sensitive (“hot”) pixels which result in recurrent bright spots at fixed locations, or by radiation-induced events within the UV converter which result in randomly placed, nonrecurrent bright spots (Ponz, 1980).

Ponz (1980) has described an algorithm for detecting in raw images bright spots of either kind on the basis of their limited spatial extent and unusual brightness values, primarily through a median filtering technique. The NEWSIPS bright-spot detection algorithm is based on the procedure used in standard IUESIPS processing, which incorporates this method to flag bright spots as described below.

Let  $DN(i,j)$  be the DN value of the pixel at line  $i$ , sample  $j$ . Further, let AVE and MED represent operators which return the weighted average and median values of their argument, respectively. Then the pixel at  $(i,j)$  is detected as a bright spot if:

$$DN(i,j) > AVE\{DN(k,l)\} + \Delta \quad \text{and} \quad DN(i,j) > MED\{DN(k,l)\} + \Delta$$

where  $\Delta$  is a DN threshold value, and  $(k,l)$  are positional elements of a 7-pixel spatial window centered on the pixel at  $(i,j)$  and oriented on a diagonal (i.e., nearly along the dispersion direction). The condition in the first equation is included to reduce the number of times the median operation in the second equation is performed.

In practice, the spatial windows are weighted according to the weights (0, 0, 1, 0, 1, 0, 0), and a threshold value of  $\Delta = 90$  DN is employed. The area of the image searched for bright

spots corresponds to the entire camera faceplate regardless of dispersion. This differs from the IUESIPS approach, which only examined the regions containing spectral information. Pixel locations detected as bright spots are written to an output flag file (Chapter 3) subsequently read by the spectral extraction routines (Chapters 9 and 10) so that extracted fluxes derived from bright spot pixels may be flagged appropriately.

Several reports have been written that list the permanent or recurrent bright spots for the three cameras. These bright spots are not automatically flagged like the permanent ITF artifacts (see Chapter 6.4.3.1), but rather only if they trigger the bright-spot detection algorithm. Ponz (1980) has published partial listings of recurrent bright spots in the LWR and SWP cameras which are listed in Tables 4.1 and 4.2. The table entries include the line and sample positions in the raw frame of reference and the approximate corresponding wavelengths for the various dispersion modes and apertures. The “B” notation means the background spectrum is affected. This work has been supplemented by Imhoff (1984a), who provided positions of additional permanent blemishes in the LWP and LWR cameras, given in Table 4.3. Several publications by Crenshaw et al. detail the recurrent bright spots, which are labeled “camera artifacts”, in low-dispersion (Crenshaw et al. 1990) and high-dispersion (Crenshaw et al. 1996) spectra. These features appear at fixed locations in spectra with long exposure times yet are not detectable in spectra with exposure times shorter than an hour. They also determined that the artifacts appear to scale in intensity with the total background exposure level. Artifact positions of the more prominent features are listed in Table 4.4 (low dispersion) and Table 4.5 (high dispersion) as a function of wavelength.

## 4.2 Microphonic Noise Detection

LWR images are preprocessed in order to detect the presence of periodic noise interference (“microphonic noise”). In the SWP camera, this interference often covers all of the image and its amplitude is generally low (often only 1–3 DN) compared to random background noise (Northover, 1980), making detection difficult. Microphonic noise is also present in LWP images and is similar in appearance and amplitude to SWP microphonic noise. In the LWR, however, the microphonic noise has different characteristics, being localized chiefly in a small number of image lines, well-modeled by an exponentially dampened sinusoid, and with a peak amplitude typically in excess of 20 DN (Northover, 1980; Panek and Schiffer, 1981). The LWR microphonic noise is descriptively referred to as a “ping” because of its sudden onset and rapid decay. Unless an extended heater warm-up prior to image read is used as a ping avoidance technique, a given LWR image has about an 85% probability of suffering a ping, generally in the lower one-third of the image (Holm and Panek, 1982). If the heater warmup procedure is used, the ping is typically displaced to the top of the image where it does not impact the useful data.

Utilizing techniques developed by K. Northover (1980), the microphonics screening done by NEWSIPS for all LWR images is based on the characteristics of the image data in the last 32 samples of each image line. This area is outside of the target region, and pixel values are zero except for noise. Image lines affected by the microphonics are initially identified

Table 4.1: Hot Pixels in the LWR Camera  
(Ponz, 1980)

Raw Image		Low Dispersion (Å)		High Dispersion (Å)	
Line	Sample	Lg. Ap.	Sm. Ap.	Lg. Ap.	Sm. Ap.
126	291	1780	1775 B	1919.3	1904.8 B/1920.5
170	200				
175	369			2172.5	2153.6 B/2173.9
178	610			2732.0	2733.8
208	391			2258.5 B/2280.0	2282.4 B
215	326	2190	2130	2135.3	2117.0 B/2136.7
257	323			2198.2	2199.7 B/2178.8
333	317			2288.9	2290.3/2268.0 B
412	385			2570.2	2543.8 B/2572.0 B
434	479			2818.7	2786.3 B/2820.5 B
518	545			3084.0	3086.0
532	307			2550.8/2579.2 B	2552.3
680	332			2838.0	2839.8

Table 4.2: Hot Pixels in the SWP Camera  
(Ponz, 1980)

Raw Image		Low Dispersion (Å)		High Dispersion (Å)	
Line	Sample	Lg. Ap.	Sm. Ap.	Lg. Ap.	Sm. Ap.
292	413	1795 B		1379.6 B/1393.6	1378.7 B/1392.6
352	501			1330.2 B/1343.0	1342.2
392	127			1859.1	1857.8
398	521			1357.9 B/1371.4	1357.0 B/1370.4
410	535			1358.5/1372.0 B	1357.6/1371.0 B
482	342			1686.7	1685.6
568	127			2060.2	2058.9
611	387			1779.0 B/1756.5 B	1778.0 B/1755.3 B

Table 4.3: Permanent Blemishes in the LWP and LWR Cameras  
(Imhoff, 1984a)

Camera	Raw Image		Comments
	Line	Sample	
LWP	101	525	Fuzzy Patch at $\lambda \sim 2482\text{\AA}$ in order 93 Hole at $\lambda \sim 2880\text{\AA}$ in order 80
	205	319	
	396	384	
	409	208	
	426	435	
	455	35	
LWR	169	499	
	364	60	

Table 4.4: Low-Dispersion Camera Artifacts ( $\text{\AA}$ )  
(Crenshaw et al. 1990)

Camera	Source Type	
	Point	Extended
LWP	None	None
LWR	2256	2256
	3087	3087
SWP	1279	1279
	1288	1288
		1491
		1535
	1663	1750

Table 4.5: High-Dispersion Camera Artifacts  
(Crenshaw et al., 1996)

LWP		LWR		SWP			
Order Number	$\lambda$ ( $\text{\AA}$ )	Order Number	$\lambda$ ( $\text{\AA}$ )	Order Number	$\lambda$ ( $\text{\AA}$ )	Order Number	$\lambda$ ( $\text{\AA}$ )
93	2483.3	122	1888.3	119	1154.9	78	1757.7
80	2880.4	112	2067.3	119	1160.0	78	1762.4
		112	2074.4	118	1165.9	77	1790.1
		107	2167.1	118	1172.8	77	1795.5
		106	2171.7	116	1195.5	76	1810.1
		100	2303.2	116	1195.8	72	1914.3
		100	2322.3	115	1205.9	72	1916.0
		94	2450.1	108	1281.7	70	1975.0
		93	2501.1	106	1298.6	70	1980.6
		87	2670.1	104	1320.8	69	2005.0
		86	2694.4	103	1337.8	69	2009.5
		84	2756.2	101	1369.8	67	2059.1
		82	2808.4	95	1453.6	67	2059.5
		82	2829.0	93	1474.3		
		80	2900.6	93	1481.8		
		77	3010.7	93	1483.0		
		76	3029.6	93	1487.7		
		75	3066.4	92	1500.9		
		75	3083.1	92	1504.8		
		75	3100.0	92	1505.5		
		72	3194.3	90	1540.0		
		72	3195.2	89	1549.3		
				89	1552.0		
				88	1566.5		
				88	1573.0		
				87	1577.9		
				87	1583.9		
				87	1593.2		
				87	1593.5		
				86	1598.5		
				86	1603.6		
				82	1691.1		
				80	1725.9		
				79	1755.5		

by thresholding the variance of the last 32 samples; the interference amplitude is then estimated on the basis of the power spectrum of the sampled data, with successive image lines processed in pairs. Pixels in image lines with estimated noise amplitudes in excess of the chosen threshold (corresponding to a peak-to-peak noise amplitude of approximately 10 DN) are flagged in the data quality ( $\nu$ ) flag image with a value of  $-16$ . This condition, which is documented by a notation in the image processing history portion of the label (Chapter 12) and noted in the core data item ABNMICRO, is subsequently used by the spectral extraction routine (Chapters 9 and 10) to flag extracted fluxes derived from lines affected by the microphonic interference.

### 4.3 Partial-Read Image Preprocessing

“Partial-read” images are those for which only a portion of the target has been read. By not having a full  $768 \times 768$  array readout, a substantial fraction of the operations overhead time associated with the camera readout and subsequent preparation for the next exposure is reduced. Partial-read images are used only in the low-dispersion mode and are read out such that a camera-dependent rectangular partial image, sufficient to encompass the entire region normally extracted in low-dispersion processing (Chapter 9), is generated. The partial-read images are preprocessed to imbed the partial-read area into a full  $768 \times 768$  array for which DN values outside of the partial-read area are zero. This is done to enable the normal NEWSIPS processing, which works on  $768 \times 768$  images, to occur without further special consideration of the partial-read nature of the images.

In order to prepare an image file in which to place the partial data, a zero filled blank image of 768 lines by 768 samples is generated. The partial-read data are inserted into the blank image using the positions tabulated by Imhoff (1991).

### 4.4 Missing Minor Frame Detection

Missing minor frames (MMFs) or “data dropouts” are flagged and recorded in the  $\nu$  flag image, as well as noted in the output core data item keyword ABNMINFR. A minor frame consists of 96 consecutive pixel values read down in batch from the satellite. Minor frames are used to reconstruct the image, beginning at line 1, sample 1 by assigning values for incremental samples. Occasionally, one or more minor frames are corrupted or missing from the telemetry stream resulting in consecutive values of zero in the image. Such missing minor frames are detected automatically in the NEWSIPS system by screening the data for 96 consecutive values of zero. Only the target region is screened for missing minor frames; therefore, any MMFs outside the target area will not be detected or flagged. These 96 pixels are then flagged with a  $\nu$  flag value of  $-8192$ . No attempt is made to interpolate across or correct for such data loss. A more detailed description of the IUE telemetry system can be found in *IUE Technical Note No. 30*.



## 4.5 DMU Corrupted Pixel Detection

A recent addition to the *RAW\_SCREEN* process is the module that flags pixels which are potentially affected by the Data Multiplexer Unit (DMU) corruption which arose in late 1994. The DMU corruption of the raw image is such that pixels between a certain DN range may be assigned erroneously a DN value of 159. A raw image screening algorithm using statistical methods was developed by VILSPA which singles out images that have abnormally high numbers of pixels at DN's of 159 and thus are likely to have been affected by the DMU problem. This image screening process is only run on images taken after October of 1994. There is no way to tell which specific pixels with DN= 159 have been affected by the DMU corruption. As a result, in images which the screening process has identified as suspect, *all* pixels with DN values of 159 are flagged (with  $\nu$  flag=  $-8$ ) as possibly being corrupted.

## 4.6 Source-Type Determination

This preprocessing algorithm determines if large-aperture spectral data should be extracted either as a point or an extended source, as such information is needed in order to define certain extraction parameters. A quick rotation of the image to align the spectrum with the horizontal direction is performed using a nearest neighbor resampling algorithm and a two-dimensional (2-D) portion of the spectral/background region is sampled. Starting and ending at a point several pixels above and below the center of the spectrum, the DN values for every pixel along each line of the rotated image are averaged together. The resultant one-dimensional array of numbers represents an average cross-cut of the spectrum and by counting the number of pixels that are above the average background, NEWSIPS determines whether the spectrum is a point or extended source. If the number of such pixels exceeds a certain value (Table 4.6), then the spectrum is considered to be extended; otherwise it is

Table 4.6: Source Type Determination Values (number of pixels)

Camera	Dispersion	
	Low	High
LWP	15	8
LWR	15	9
SWP	15	11

considered a point source. The determination of point or extended source for low-dispersion large-aperture data is used to activate the detilting algorithm (see Chapter 7.2.3) in the geometric correction step for certain images and to set the width of the spectral extraction swath. If no flux is detected in the large aperture, the source type is set by default using an object class look-up table. Object classes 1–3 and 6–8 default to extended-source extraction.

All other object classes default to point source extraction, with one notable exception. If a low-dispersion large-aperture spectrum is designated a multiple or trailed exposure, it will always be extracted as extended, regardless of the results of the automated spectral width determination.

The source-type determination algorithm only sets a flux/no-flux flag for small-aperture data, as all exposures acquired in this aperture are considered to be a point source for the purposes of flux extraction.

## 4.7 Serendipitous Spectrum Recognition

Using the algorithm described in the previous section, the NEWSIPS software searches for low-dispersion spectral flux in both apertures, regardless of the information recorded on the original observing script as to which apertures were exposed. If flux is detected in an aperture that was not originally documented as having been exposed, the FITS keyword **SERENDAP** will appear in the output files for that image indicating that a serendipitous exposure was found and in which aperture.

When a serendipitous spectrum is detected with the NEWSIPS software, the aperture-dependent Core Data Items (CDIs) for the primary spectrum will be copied to the CDIs for the serendipitous spectrum. The coordinates for the serendipitous exposure will be calculated from the primary coordinates using the following algorithms:

$$RA(s) = RA(t) + \Delta RA \quad \text{and} \quad DEC(s) = DEC(t) + \Delta DEC$$

where  $RA(s)$  and  $DEC(s)$  are the coordinates of the serendipitous pointing, and  $RA(t)$  and  $DEC(t)$  are the coordinates of the target.  $\Delta RA$  and  $\Delta DEC$  are computed in units of arcseconds as follows:

$$\Delta RA = -0.2680(FESX(s) - FESX(t)) \cos \Psi + 0.2617(FESY(s) - FESY(t)) \sin \Psi$$

$$\Delta DEC = -0.2680(FESX(s) - FESX(t)) \sin \Psi - 0.2617(FESY(s) - FESY(t)) \cos \Psi$$

where  $\Psi$  = spacecraft roll angle + 28.31 deg,  $FESX(s)$  and  $FESY(s)$  are the FES x and y coordinates of the serendipitous aperture, and  $FESX(t)$  and  $FESY(t)$  are the FES x and y coordinates of the target aperture. The FES coordinates of the apertures are given in Table 4.7.

The target name for the serendipitous exposure will be NEAR XXX. The HISTORY portion of the label will reflect that the main object is in the other aperture and the **APERTURE** keyword will be changed to BOTH. In the case that the serendipitous exposure is in the small aperture and the large-aperture spectrum is trailed, the serendipitous exposure is considered a trailed overshoot. The large-aperture coordinates and object name are copied exactly to the appropriate entries for the small aperture, as well as the aperture-dependent CDIs. In this instance, the coordinates are not recalculated and the object name is not preceded by “NEAR”.

Table 4.7: FES Coordinates of the Apertures

Aperture	FES x, y
SWSA	243, -89
SWLA	94, -90
LWSA	47, 65
LWLA	-106, 52

The NEWSIPS system also searches for unexpected spectral data in images classified as sky background. These images are usually acquired simultaneously with a pointed spectral exposure in another camera. If an image has an object class of 07 (sky background) and spectral data are detected with the algorithm described above, processing is terminated and the IUE staff attempts to identify the pointed observation obtained in another camera contemporaneously with the image. Assuming the associated image can be identified, the coordinates will be derived from those of the main object and the object class changed to that of the main object. The target name is “NEAR XXX”. If the associated image cannot be identified, then the object class is changed to “UNKNOWN”. A COMMENT line in the FITS header will say, “SERENDIPITY WITH CAMXXXXX”. If no spectral flux is detected in the image, processing continues as for a large-aperture extended source.

## 4.8 Background and Continuum Intensity Estimation

This section of code determines the maximum continuum and average background DN levels for data utilizing the same rotated raw image as described in Chapter 4.6. This information is stored in the FITS header and history portion of the label as keywords. Although this information is not used in subsequent portions of image processing, it provides the user with a consistent quick-look estimate of the exposure level for a given image. The continuum levels for low- and high-dispersion wavelength calibration and flat-field exposures are set to zero, regardless of the output from the code.

The continuum level is determined in the following manner. Several predefined 2-D regions along the dispersion direction, encompassing both background and spectrum, are sampled. The sample areas are placed so as to avoid most emission lines and were carefully chosen after examining a variety of exposures of stars with different spectral types. The brightest pixels within each zone are averaged together to derive a peak continuum level for that region. The DN averages for each region are compared, and the maximum is chosen as representative of the continuum level. An image is considered to be overexposed (i.e., continuum level set to 255 DN) if 5 or more pixels in any single region are saturated. The approximate low-dispersion wavelengths for each sample area are listed in Table 4.8. A measurement of the high-dispersion continuum level is taken in a similar fashion. In this

Table 4.8: Low-Dispersion Wavelength Regions for DN Measurements ( $\text{\AA}$ )

Continuum		
LWP	LWR	SWP
2120–2285	2405–2480	1255–1300
2595–2685	2565–2710	1310–1365
2850–2910	2850–2925	1830–1880
3070–3120	2985–3035	1925–1975

Background		
LWP	LWR	SWP
2120–3120	2405–3035	1255–1975

case, the samples correspond to areas centered about the peak of the echelle blaze and span several orders.

Low-dispersion background levels are calculated by averaging the DN values for a line of pixels (see Table 4.8 for the wavelength boundaries) sampled parallel to the dispersion and midway between the large- and small-apertures. For high-dispersion, a swath of interorder pixels adjacent to the respective continuum section is averaged. The background level corresponding to the maximum continuum region is recorded.

## 4.9 High-Dispersion Order Registration (*ORDERG*)

The extraction of high-dispersion spectral and background fluxes requires a precise knowledge of the placement of the echelle orders. Target centering errors and camera temperature (THDA) variations can shift an image potentially by several pixels. The *ORDERG* module in *RAW\_SCREEN* computes an estimated shift that corresponds to the spatial direction in the high-dispersion resampled image (SI) geometry. Because *ORDERG* reckons this shift from the raw image, it uses raw DN values as the unit of flux. In addition, the computations are made from a simple rotation of the raw image (identical to the one described in Chapter 4.6) which is meant to approximate the high-dispersion SI geometry.

Studies of high-dispersion echellograms show that the order locations for individual images can differ not only by simple translational offsets but also by an expansion and contraction term (differential order shifts) as well. Because attempts to correlate such distortions with instrumental variables have been unsuccessful, *ORDERG* was designed to determine both the mean global shift of each image and, if possible, the differential order shifts, which can be as large as  $\pm 0.6$  pixels. Note that similar shifts in the dispersion (spectral) direction cannot be corrected for in this manner because they are indistinguishable from wavelength shifts due to target centering errors or the radial velocity of the source. Shifts in the disper-

sion direction are addressed in Chapter 8, which deals with the wavelength calibration.

### 4.9.1 Order Registration Process

For images with high-signal continua, the derivation of spatial order shifts occurs in a two-step process. The first step figures an average global shift, while the second step determines the much smaller differential shifts.

#### 4.9.1.1 Step 1: Global Shifts

This step generates a global spatial shift, which is an average of the individual shifts for each order that can be located successfully. The calculations are based on an 11-pixel-wide swath in the spatial direction of the crudely rotated raw image. Initially, the maximum and minimum DN values are computed in a predefined search window, which is expected to include the first (long-wavelength) order. These maxima and minima are assumed to be the “peak” flux of the order and the local “background” level, respectively. The local background (interpolated from pixels on either side of the order) is subtracted from the spatial profile, resulting in a “net-flux” profile. If the peak of the net-flux profile exceeds 5 DN, the algorithm proceeds to compute the centroid position of the order.

The centroid position of the order is computed using a least-squares gaussian fit to the net-flux profile within the preselected search window limits. Following the determination of an order centroid, *ORDERG* steps to the search window for the next order. This window is computed from the found positions of the preceding three orders (except for the first two orders). If an order does not have sufficient net flux for explicit centroid-finding, *ORDERG* steps to the estimated position for the next order, and an attempt is made to find that order. This process continues from the long-wavelength orders to the short-wavelength orders.

Following the determination of the order centroid positions, relative weights are assigned to each position according to the peak net flux. Found-minus-expected centroid position differences are computed for these orders and compared to the corresponding differences computed for orders from a fiducial image unique to each camera (LWP06316, LWR14996, and SWP13589). The order positions for these special images were calculated during the initial development of the *ORDERG* algorithm. A weighted least-squares solution of these pixel differences computes both a mean global shift and an rms statistic. The mean shift is the final value output from Step 1 and is the value applied to all lines in the image if any test in Step 2 fails (see below). However, two tests must first be passed before Step 1 is completed. The first is that a minimum number of orders (five for SWP, three for LWP/LWR) must be found with sufficient flux for order-centroiding. The second is that the rms statistic referred to above must be below a threshold (1.5 pixels). If either of these tests fails, a default value is adopted for the global spatial shift based on statistical predictions using time- and THDA-dependent spatial motions. Also, for either of these failure conditions, the noncontinuum keyword for the appropriate aperture is also set to “YES” in the HISTORY portion of the FITS header. Note that the setting of this keyword to “NO” (i.e., all tests in Step 1 are

passed) denotes that the image is considered to have continuum flux and is treated as such by the background-extraction algorithm described in Chapter 10.

#### 4.9.1.2 Step 2: Differential Shifts

Following the successful completion of Step 1, an attempt is made to refine the order shifts by determining systematic differential shifts across the image, e.g., due to an expansion/contraction term. A failure in the Step 2 tests described below results in the adoption of the global fit determined from Step 1. Differential shifts cannot be computed for these cases.

Order centroid positions and weights found above are used in Step 2. This step differs from Step 1 in two important respects. First, a sufficient number of orders containing flux must be found both in the short- and long-wavelength (spatial) ends of the camera. If this distribution test fails, the global shift from Step 1 is adopted and applied to all lines in the image. A second difference from Step 1 is that Step 2 computes order spacings from the found centroids. A least-squares solution is then determined from the differences of the logarithms of these spacings versus echelle order number (because of the expected  $1/m^2$ -dependence in order separation) and the logarithms of the corresponding order spacings for the fiducial image. A quadratic least-squares solution is attempted for SWP images because a curvature term is sometimes necessary. For LWP images the least-squares solution is linear, while for LWR images the solution is two joined line segments across the camera. As a quality-control check, *ORDERG* makes a test on the derived shifts at the end of Step 2. If any of the shifts exceed a threshold value of 4.0 pixels, Step 2 reverts to the solution from Step 1.

The found shifts resulting from Step 2 are defined literally only for the order centroid positions. As a practical matter, the final shift for a given order is applied uniformly to all lines associated with that order, including the adjacent lines containing background fluxes. Note that this can produce small shift discontinuities for lines located midway between the orders.

### 4.9.2 Potential Problem Areas

Because *ORDERG* operates by bootstrapping positions of previously located orders, a potential problem in finding the first order can occur. The SWP camera circumvents this problem by ignoring the first order ( $m = 66$ ), as it describes a sinuous path on the raw image. As a result, *ORDERG* begins with order 67 for the SWP. The situation is more complex for the long-wavelength cameras because the gradient in camera sensitivity with increasing wavelength near the camera edge causes the identification of the first order to be sensitive to exposure level. If this identification is wrong, the window limits will be misassigned and large errors introduced into the mean global shift. This problem has been addressed for the long-wavelength cameras by starting the search at the (normally) third visible order.

A second type of problem involving order misidentification occurs for images having broad P-Cygni features with weak continuum (e.g., Wolf-Rayet spectra). If such broad features are common and distributed throughout the image, the true continuum orders may be too

weak for *ORDERG* to use for registration. If the search for several such orders in a row is unsuccessful, errors in the search windows for new orders may become large enough to cause a misregistration of the next orders by an order. This problem was addressed by specifying that the search window positions be computed from the average of the positions of the previous three orders (per Step 1 discussion). A very large number of test images for these problems were checked, but there is no guarantee that the solutions for every image in the NEWSIPS archive will be accurate.

## 4.10 *RAW\_SCREEN* Output

The *RAW\_SCREEN* module does not generate any output data products (i.e., FITS file). Instead it produces a temporary (internal only) file which contains various  $\nu$  flag conditions that are used by subsequent processing modules (e.g., *PHOTOM*).

The *RAW\_SCREEN* module outputs the following information to the HISTORY portion of the image label:

- number of bright spots detected,
- number of missing minor frames (telemetry dropouts) detected,
- large-aperture extraction mode (if applicable),
- serendipitous-exposure information (if applicable),
- large- and/or small-aperture continuum DN levels,
- background DN level (An error was discovered in the reporting of this parameter, ie. a value of 0 DN was recorded, which affects all SWP high-dispersion small-aperture images processed prior to June 14, 1997.)
- *ORDERG* global offset (high dispersion only), and
- *ORDERG* processing information (high dispersion only).

# Chapter 5

## Raw Image Registration (*CROSS-CORR*)

The NEWSIPS system relies upon an explicit determination of the registration between the raw science image and the raw space Intensity Transfer Function (ITF) to apply an accurate photometric correction (discussion of the ITF is deferred until Chapter 6). The image registration is derived using a linear cross-correlation algorithm with the fixed pattern found in all IUE raw images as the registration fiducial. In this context the fixed pattern is a manifestation of systematic variations in sensitivity from pixel-to-pixel over the entire image.

### 5.1 Registration Fiducial

Although the reseaux have traditionally been used for *CROSS-CORR* purposes, using the fixed pattern as the registration fiducial has several advantages over the reseaux; one being that fiducials can be found anywhere on the exposed part of the image, so that many more such fiducials are available than reseaux. Also, the fixed pattern can be detected at even the lowest exposure levels, which eliminates the need for predicted information. Finally, the presence of the exposed spectrum can be excluded from the cross-correlation region, and therefore, does not inhibit the use of the fixed pattern in the surrounding background (De La Peña et al., 1989, 1990). A consistent fixed pattern has been shown to be present in the literally thousands of raw IUE images tested; however, it is known that the character of the fixed pattern is modulated to some degree by observation date and camera temperature (Bushouse 1991b).

### 5.2 General Method

*CROSS-CORR* employs a pattern-matching technique which depends heavily upon the linear cross-correlation function to identify similar patterns between a raw science image and the



raw-space ITF. A rectangular grid of fiducial positions (centered 28 pixels apart) has been defined for each camera and dispersion. At each defined position, a cross correlation is performed to determine the displacement between the raw image and the ITF at that locale. Specifically, at each locale an array (*template*) of  $23 \times 23$  pixels of the raw science image is used for comparison to a corresponding array (*window*) of  $29 \times 29$  pixels of the raw-space ITF image. The window is larger than the template in both dimensions such that the template can be moved about the window to “search” for the best correlation location. It is known from a number of analyses that the maximum extent to the motion of the fixed pattern in most raw images is only a few pixels. Therefore, the window size is ordinarily set in the NEWSIPS processing to accommodate motion of only a few pixels, but the size can be varied, if necessary.

Once a pattern match location is found to whole pixel accuracy at a defined fiducial locale, the match location is evaluated via a series of statistical tests to validate the result. Upon validation, further computations refine this determination to the sub-pixel accuracy required for an accurate photometric correction.

After all the valid pattern match locations for a camera and dispersion have been derived to sub-pixel accuracy for the raw science image, the determinations are viewed as spatial deviations and examined as an ensemble for consistency. Displacements which do not conform in a general sense to a smoothly varying function are adjusted to conform. Finally, after all the fine tuning has been completed, a full three-dimensional (3-D) displacement image ( $768 \times 768 \times 2$ ) is created for  $\Delta$ Sample and  $\Delta$ Line using a bi-cubic spline interpolation scheme.

### 5.3 Pattern Matching Algorithm – Step by Step

The following elaborates the procedures incorporated into *CROSS-CORR*. Fiducial locations which have been pre-defined for each camera and dispersion are accessed; these are hereafter referred to as the sampling locations. For each sampling location, the following steps are performed.

1. The raw science image template is classified by its computed median Data Number (DN), and the ITF level possessing a comparable DN value at that location is chosen for correlation purposes.
2. Any reseaux, hot spots, cosmic ray hits, and spectral information are ignored in the template during the correlation analysis. These artifacts contaminate the science template with features not present in the ITF window and are temporarily masked during the correlation procedure.
3. The template is sequentially positioned throughout the window, and at each position a linear cross correlation is performed. For each position a correlation coefficient is computed and the corresponding coordinates (pixel accuracy only) are saved. By virtue of

the sizes of the template and search windows, a total of forty-nine correlation coefficients are computed to determine the best pattern match location to pixel accuracy for each sampling location. These forty-nine coefficients are actually in the form of a  $7 \times 7$  matrix which corresponds to the overlap positions of the template upon the window. The maximum coefficient in this sample is assumed to be the best representation for a true match.

The cross-correlation coefficient is defined as

$$r(m, n) = \frac{\sum_x \sum_y (w(x, y) - \overline{w(x, y)})(t(x - m, y - n) - \bar{t})}{(\sum_x \sum_y (w(x, y) - \overline{w(x, y)})^2 \sum_x \sum_y (t(x - m, y - n) - \bar{t})^2)^{1/2}} \quad (5.1)$$

where  $-1.0 \leq r \leq +1.0$ . In this equation,  $\bar{t}$  is the average value of the template,  $\overline{w(x, y)}$  is the average value of the portion of the window which is currently coincident with the template  $t(x, y)$ , the line coordinate  $m = 0, 1, 2, \dots, (L - 1)$ , and the sample coordinate  $n = 0, 1, 2, \dots, (S - 1)$ . For the purposes of this implementation,  $L = 29$  and  $S = 29$  which are the nominal dimensions of the correlation window; the template dimensions are  $23 \times 23$  pixels. Summations are performed over the coordinates common to both  $w$  and  $t$ .

4. The maximum correlation coefficient must pass several statistical tests to be considered a valid correlation:
  - There must be a minimum of 139 ( $13 \times 13$ ) non-rejected pixels in the template for the correlation to be performed at all (see Item 2);
  - The maximum correlation coefficient cannot reside on the edge of the correlation matrix;
  - The probability distribution criterion of less than 1% must be satisfied;
  - There can be no other “local” maxima in the correlation matrix within 0.25 sigma of the absolute maximum coefficient. Sigma is the standard deviation of the correlation coefficient matrix.
  - The maximum correlation coefficient must be at least two sigma greater than the rest of the coefficients in the matrix.
5. If the coefficient is deemed valid, the position of the pattern match is then determined to sub-pixel accuracy. The original ITF window data is resampled into successively finer and finer sub-pixel increments and the cross correlation with the template is repeated until 0.125 sub-pixel accuracy is achieved.

If the coefficient is not validated by the tests described in Item 4, the sampling position is considered a bad location, and the algorithm passes onto the next sampling position.

### 5.3.1 Intermediate *CROSS-CORR* Output

The intermediate results from *CROSS-CORR* can be used to monitor the geometric/photometric state of the raw science image. In the vector displacements (VD) file, these intermediate results are stored in a binary table extension containing the following output for each sampling position:

1. science image x-position (sample),
2. science image y-position (line),
3. ITF x-position of best match (sub-pixel accuracy),
4. ITF y-position of best match (sub-pixel accuracy),
5. maximum cross-correlation coefficient (computed for pixel location accuracy),
6. number of pixels used to calculate the correlation, and
7. the ITF level used for *CROSS-CORR*

Items 1 and 2 are the pre-defined fiducial locations about which *CROSS-CORR* performs its search. Items 3 and 4 are the best match positions between the raw science image and the ITF image. Note that these final positions are in quantized units of  $1/8$  pixel, which is a consequence of the design of *CROSS-CORR*. Item 5 is the maximum correlation coefficient which can range between 0.0 and 1.0. In practice the correlations range between  $-1.0$  and  $+1.0$ , but negative correlations have been deemed invalid. Item 6 is the number of points used to compute the correlation; this will range from 139–529 pixels for a  $23 \times 23$  pixel template. Item 7 is the ITF level used for the correction and will range in value from 1 to 12.

The total number of entries in the binary table extension is both camera and dispersion dependent. Table 5.1 contains the number of fiducial locations used in *CROSS-CORR*.

Table 5.1: Number of Fiducial Locations

Camera	Number of Locations Low Dispersion	Number of Locations High Dispersion
LWP	150	490
LWR	151	511
SWP	139	510

The data contained in the binary table extension can be used to produce diagnostic plots for *CROSS-CORR*. Panel *a* of Figure 5.1 shows the displacements computed between an

SWP low-dispersion image and the SWP ITF. The small boxes denote the fiducial locations where a successful correlation was determined. The associated vector represents the computed displacement between the raw science image and the ITF; the vector displacements have been magnified for visual clarity. Single points mark the locations of fiducials with unsuccessful correlations. Panel *b* of Figure 5.1 shows the magnitude of the correlation coefficients corresponding to the results in Panel *a*. Larger plus signs denote stronger correlations. The dashed lines represent the region of the image that is photometrically corrected. Recall that all of these correlations have passed the 1% probability distribution test which means that there is less than a 1% probability any of these correlations could have arisen by random chance. The corresponding example for high-dispersion data is illustrated in Figure 5.2.

## 5.4 Evaluation of the Raw Correlations

After all of the pre-defined fiducial locations have been investigated as individual entities, the computed results are examined as an ensemble of information. The goal is to create an idealized or smoothed version of the actual displacements and then compare the smoothed values to the actual values, making adjustments to the actual displacements if necessary.

The creation of the smoothed displacement image is done in two major stages. First, an averaging procedure is invoked for each successful correlation sample. The closest fiducial locations to the sample in question which also have successful correlations are weighted according to their “distance” from the sample in question and if there is deemed to be enough data, the displacements from all of these successful locations are averaged to yield a mean displacement for the smoothed image at the sample location in question. If enough data are not acquired in the pre-defined search region, the data point must be an isolated or semi-isolated correlation. Isolated or semi-isolated correlations which cannot adequately be compared to the immediate surroundings for spatial trends are considered invalid correlations after-the-fact and are permanently removed from consideration.

Once the averaged image is created, the displacements for the “missing” fiducial locations are filled in by an interpolation/extrapolation scheme. The search for missing data is performed in a radial sense, starting at the center of the low- or high-dispersion photometric correction region. An extrapolation of the mean displacements is performed well outside the photometric correction limits to ensure that the bi-cubic spline fit done during the last stage of *CROSS-CORR* is well-behaved for all pertinent data regimes.

The actual displacements are then compared to the smoothed interpretation and any displacements that differ by 0.25 pixel from the smoothed array are modified to conform to the smoothed displacements. These final vector displacements are then expanded into a full 3-D ( $768 \times 768 \times 2$ ) floating point displacement image ( $\Delta\text{Sample}$  and  $\Delta\text{Line}$ ) using a bi-cubic spline interpolation algorithm. The  $\Delta\text{Sample}$  values are located in the first level of the final image; the  $\Delta\text{Line}$  values are located in the second level of the image.

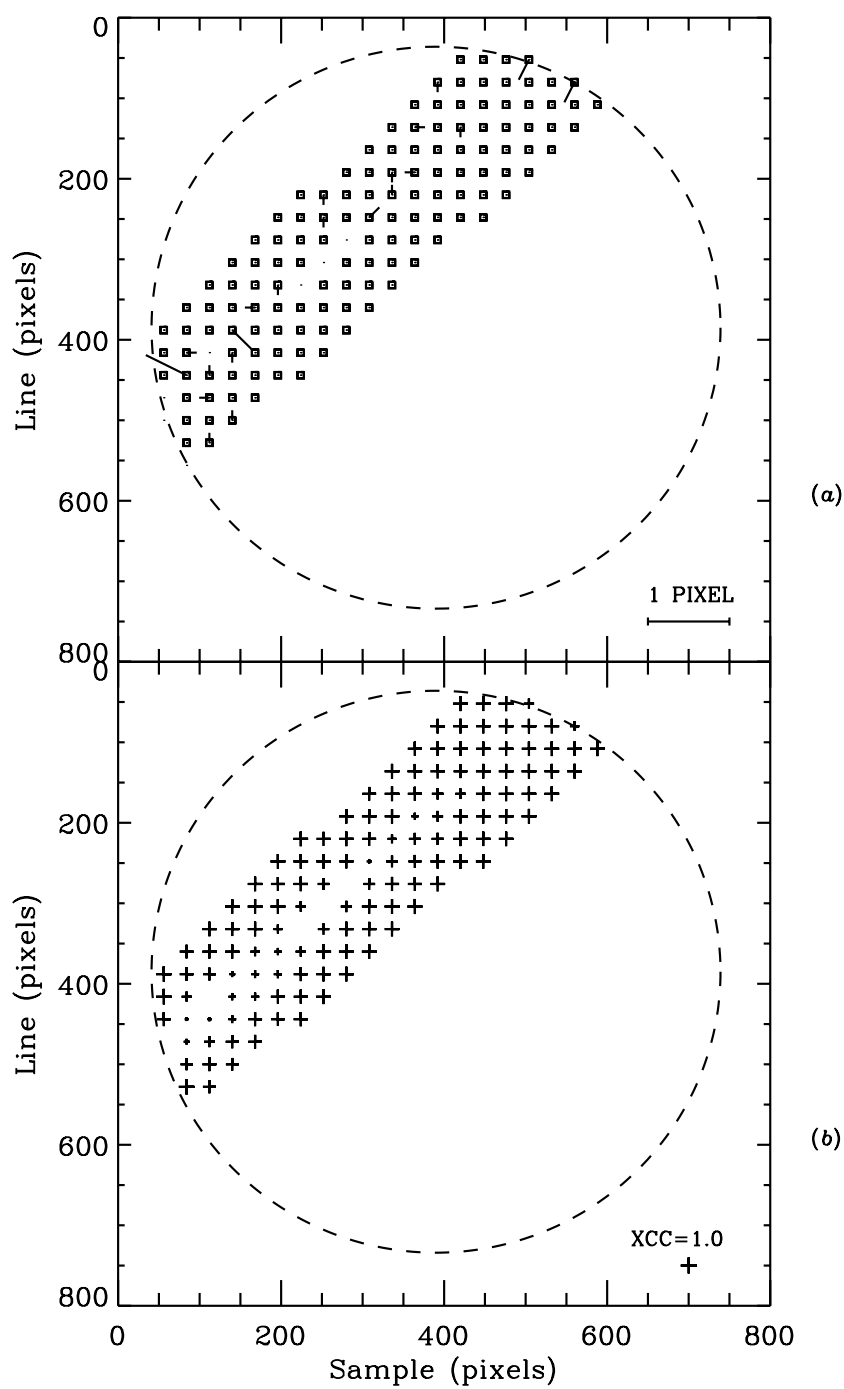


Figure 5.1: (a) Displacements computed between an SWP low-dispersion image and the SWP ITF. (b) Magnitude of the correlation coefficients corresponding to the results shown in Panel (a).

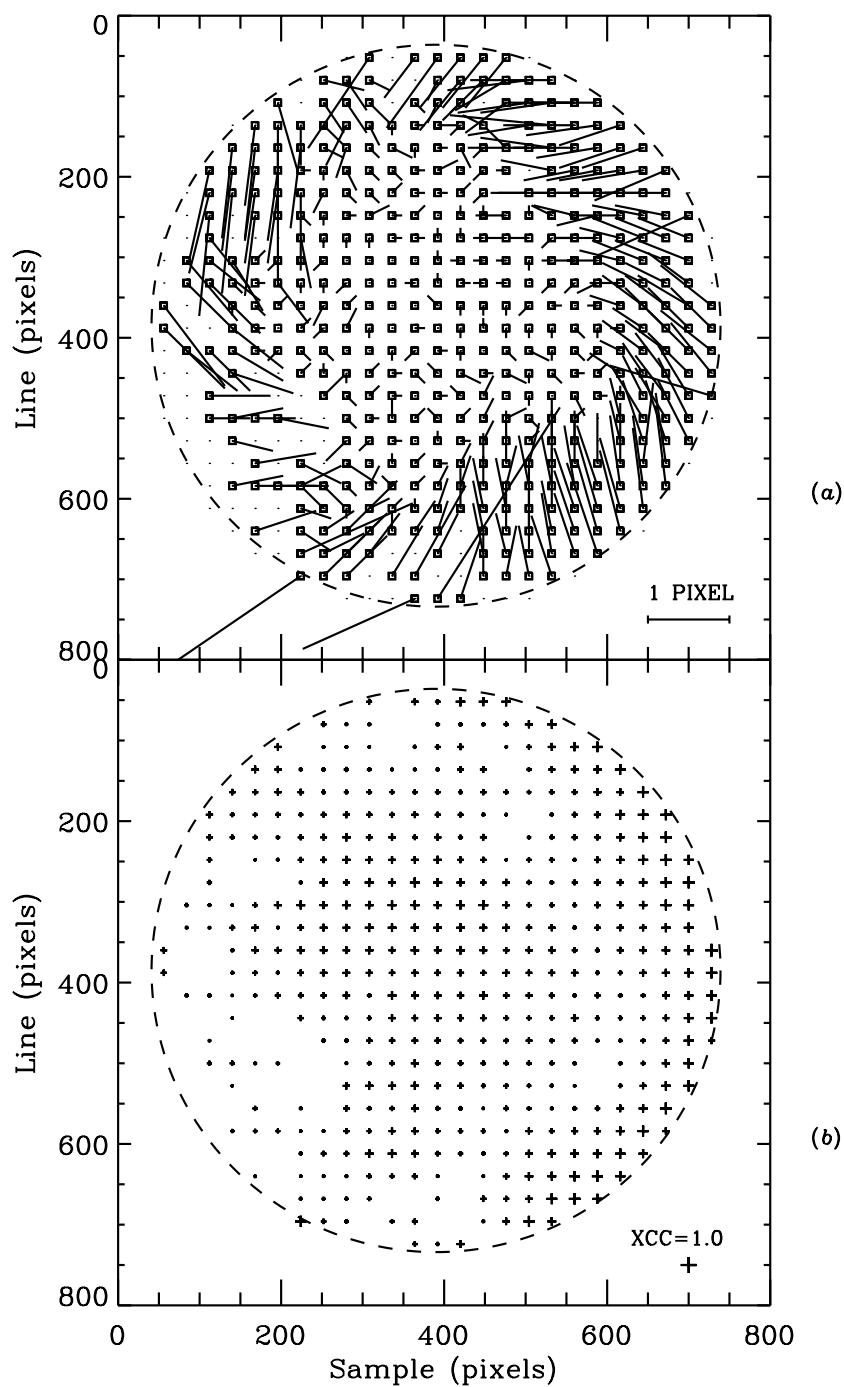


Figure 5.2: (a) Displacements computed between an SWP high-dispersion image and the SWP ITF. (b) Magnitude of the correlation coefficients corresponding to the results shown in Panel a.

## 5.5 *CROSS-CORR* Output

The VD data output by *CROSS-CORR* are an essential component for NEWSIPS processing. The information it carries is used as input to the photometric correction scheme to align properly the raw science image to the raw-space ITF image (Chapter 6) and by the geometric correction scheme as one of the vector components to the geometric resampling stage (Chapter 7). These specific data, however, are not retained directly in an IUE Final Archive output data product. As is discussed in Chapter 7, the VD FITS file (VDLO/VDHI) produced during the geometric correction procedure contains the summation of all the geometric corrections implemented to perform the single image resampling. The raw cross-correlation information can be retrieved indirectly from the binary table extension to the VDLO/VDHI. *CROSS-CORR* does not generate any  $\nu$  flag values.

The *CROSS-CORR* module writes the following information to the HISTORY portion of the image label:

- window size,
- template size,
- ITF identification,
- percent successful correlations,
- median cross-correlation coefficient,
- standard deviation of the cross-correlation coefficient,
- mean computed displacement in pixels,
- maximum computed displacement in pixels, and
- number of isolated or semi-isolated displacements filtered.

# Chapter 6

## Photometric Correction (*PHOTOM*)

Non-linear photometric response and spatial sensitivity variations in the detectors are present in all raw data and must be taken into consideration before the data can be utilized for scientific purposes. In accounting for the detector response, the *PHOTOM* procedure converts raw data numbers (DN) into normalized flux numbers (FN) which are linearly related to the incident photon flux. *PHOTOM* is performed on a pixel-by-pixel basis in the two-dimensional raw image.

The *PHOTOM* procedure in NEWSIPS differs in two fundamental ways from the correction performed in IUESIPS. The Intensity Transfer Functions (ITFs) (i.e., graded ultraviolet floodlamp exposures used to linearize and normalize the camera response) are constructed in a manner which eliminates the necessity to resample, and consequently degrade, the data and preserves the inherent characteristics of the detector. In addition, a more precise image registration technique (Chapter 5) is used to align accurately the raw science data with the ITFs (Shaw 1990, De La Peña et al., 1990).

### 6.1 Construction of the ITFs

The modern epoch ITF series used for the Final Archive (LWP:1992, LWR:1983, and SWP:1985) were obtained in a closely monitored and stable satellite configuration such that any parameters known to affect the image quality (e.g., camera temperature) were carefully controlled. These improved acquisition procedures ensured that the constituent ITF images at each exposure level have little geometric distortion relative to each other. The ITFs for the Final Archive have been constructed in raw space with no attempt to align geometrically the images, because some smoothing of the ITF data is inherent in such an alignment. The raw images for each level were averaged on a pixel-by-pixel basis to form a mean level. If the intensity level of a pixel from one of the component images varied from the mean intensity value for that pixel by more than 2.5 sigma for the SWP and LWR ITFs and 1.4 sigma for the LWP 1992 ITF, the deviant pixel was excluded from the sum. In this way it was possible to use images with missing minor frames in the construction of the ITF. Each level of the ITF is constructed with at least 4 images; the null level was typically constructed with many



more images. The resulting ITF for each camera is a three-dimensional file of dimensions  $768 \times 768 \times 12$  pixels.

The lowest level of the ITF is a zero exposure or null level which is the background left by the standard camera flood/erase preparation procedure. Correspondingly, the highest level of the ITF has a long enough exposure time to allow the detector to achieve its saturation limit of 255 DN over a majority of the image. The intermediate ITF levels map the camera response through the mid-range of DN values. The 12 level ITF provides sufficient granularity in intensity to allow linear interpolation between the levels.

### 6.1.1 LWP ITF

The ITF originally acquired for the LWP camera in 1978–1980 was a “mini-ITF” with one image for most of the levels. These images were taken under widely varying spacecraft conditions, with some images taken during optimization testing when camera parameters were deliberately modified. The ITF taken in 1984 was taken under controlled conditions and the images are geometrically similar, allowing the construction of a raw space ITF. However, it was discovered during testing of this ITF that the LWP dataset of science images divide generally into two subgroups. Images taken before 1984 tend to have similar geometric distortions to one another, and images taken after 1984 tend to have similar geometric distortions, but the two subgroups are not geometrically similar to each other. Clearly, there was a discrete change in the camera operating parameters in 1984, possibly in the voltages set in the camera, but the information available via telemetry is not sufficient to identify the exact nature of the change. Unfortunately, images taken before the 1984 ITF (a very small percentage of the total LWP dataset) are geometrically similar to the LWP ITF (Epoch 1984). Images taken after the 1984 ITF are not well aligned with the 1984 ITF. This situation prompted the acquisition of a new ITF for the LWP camera in 1992.

The LWP ITF acquired in 1992 is virtually always better aligned in raw space with the science images acquired since 1984 than the 1984 ITF. However, the bimodal nature of the image distortion for the LWP camera manifested itself in the null images acquired for the 1992 ITF. The null level images formed two discrete groups. Approximately half the null images are geometrically similar to each other and form an internally consistent group (Null A). The other group of null images (Null B) are geometrically similar to each other in raw space, but the two groups are not sufficiently aligned geometrically to be co-added without loss of accuracy in *PHOTOM*. While somewhat more than half of the science images acquired with the LWP camera are better aligned with Null B than Null A, the intensity level of Null B is higher than that of Null A, resulting in the science data not being fully bracketed by the calibration ITF data in intensity when Null B is used. The Final Archive processing uses the 1992 LWP ITF constructed with Null A.

### 6.1.2 LWR ITF

As is the case with the LWP camera, two ITFs were acquired for the LWR. The first ITF (1978 epoch) was acquired with no constraints placed on camera temperature (THDA). Hence, a viable raw space ITF could not be constructed from the 1978-epoch dataset (i.e., the individual UV-Flood images in a given ITF level did not align geometrically with one another). The second ITF (1983 epoch) was taken under more controlled spacecraft conditions; however, an ITF constructed purely using the 1983-epoch images (LWR83R94A or ITF A) did not correlate well with pre-1984 science images. As a result, a “hybrid” 1983-epoch ITF (LWR83R96A or ITF B) was generated where all levels (except the null) of the ITF were constructed from UV-Flood images taken during the 1983 ITF acquisition and the null level is composed of six null images taken during the 1978–1983 time period. LWR science images show a marked bimodality as far as ITF preference is concerned. For the most part, the majority of low-dispersion images taken prior to 1984 tend to correlate well with ITF B; while images taken after this date register well with the ITF A.

LWR ITF selection in NEWSIPS low-dispersion processing is made on an image-by-image basis. Each low-dispersion LWR image is processed twice through the image registration (*CROSS-CORR*) step; once using ITF A and another time utilizing ITF B. NEWSIPS then chooses the ITF which yields a higher median cross-correlation coefficient for subsequent processing of the image. High-dispersion LWR images do not go through such a selection process; only ITF A is used. This is because no clear improvement in image quality was seen when using ITF B over ITF A in high dispersion.

### 6.1.3 SWP ITF

At the time of construction of the SWP ITF for use in the Final Archive, two ITF series had been acquired for that camera. The images that comprise the ITF acquired in 1978 were not acquired under stable spacecraft conditions and are geometrically dissimilar to each other. These images cannot be used to construct a raw space ITF, which requires minimal distortion among the images. The images acquired for the 1985 ITF comprise a geometrically homogeneous group. Therefore, the images acquired for the 1985 ITF were used to construct the raw space ITF for the Final Archive processing. In 1992, a new ITF for the SWP camera was acquired, but there are no current plans for use of this ITF in the Final Archive processing.

### 6.1.4 Periodic Noise

All raw IUE images suffer from periodic noise (Nichols-Bohlin 1988, Shaw 1989) which is constant in raw space. The noise has been found to be multiplicative in nature and ranging from 1% to 8% in amplitude; however, the particular periodicities present and the amplitude of the noise are camera specific. Due to geometric distortion, the periodic noise in the ITF will not, in general, align with the noise present in the science image, and therefore, the periodic noise has been filtered from the ITF images using a Fourier-filtering technique. For

the SWP camera, noise spikes were filtered every 192 points in the line direction and every 16 points in the sample direction in frequency space. For the LWP camera, noise spikes were filtered every 12 points in the line direction and every 16 points in the sample direction. The noise features in the LWR camera are much larger (8%) than the other cameras; noise spikes every 192 points are filtered in both the line and sample directions.

## 6.2 Determination of the Effective Exposure Times

The effective exposure times for the 1983–1985 Epoch ITFs were derived by Imhoff (1984b and 1986), by De La Peña and Coulter (1996) for the 1992 Epoch LWP ITF, and by De La Peña for the LWR ITFs. During the creation of the 1983–1985 ITFs in their own geometric space for the NEWSIPS system, if additional images were deemed usable in contrast to those originally chosen by Imhoff, the effective exposure times were modified to reflect the use of additional images.

Table 6.1 lists the effective exposure times (FN exposure values) for each level of the ITFs used in the Final Archive. These exposure values have been normalized to an arbitrary scale such that the FN associated with the lowest level of an ITF is 0.0.

Table 6.1: ITF Effective Exposure Times (seconds)

ITF Level	SWP Epoch 1985	LWP Epoch 1992	LWR ITFA Epoch 1983	LWR ITFB Epoch 1983
1	0.000	0.000	0.000	0.000
2	32.919	38.750	35.880	35.607
3	67.946	78.737	72.974	72.425
4	104.147	121.868	91.067	89.708
5	131.397	168.958	125.213	125.621
6	166.296	200.756	156.510	162.627
7	223.034	237.941	193.275	198.780
8	269.680	278.107	245.053	254.362
9	340.471	341.073	283.705	288.706
10	408.490	396.582	320.355	325.599
11	473.749	483.497	385.554	401.720
12	575.995	561.518	471.557	490.480

## 6.3 Description of the Photometric Correction

The actual pixels *PHOTOM*ed in high dispersion reside within a region defined by edge-detection algorithms on raw, well-exposed UV Flood images. These pseudo-circular regions coincide with the target boundary. For low dispersion, only a diagonal swath of data encompassing both the large and small apertures, as well as a generous portion of the background, is *PHOTOM*ed.

The *PHOTOM* procedure accesses *explicitly* determined displacements between the raw science image and the ITF to align the two images and to convert the DN to FN. These displacements have been derived using the image registration technique as described in Chapter 5.

### 6.3.1 Determination of the ITF Pixels

Displacement vectors calculated in the *CROSS-CORR* step map each pixel in the raw science image to the geometric space of the ITF, where the final displacement coordinates are floating point coordinates. If the final coordinates for the science pixel are within 0.125 pixel (in either the line or sample direction) of the integer coordinates of an ITF pixel, the science image pixel is assumed to be coincident with the ITF pixel and the FN computed will be based upon data contributed only from the single ITF pixel. If the science image pixel is displaced by more than 0.125 pixel from the integer coordinates of any ITF pixel, the FN computed will be based upon data contributed from a  $4 \times 4$  matrix of ITF pixels surrounding the final position in question. Both of these scenarios are described in further detail in the next section.

### 6.3.2 Determination of the Flux Values

In contrast to the original IUESIPS *PHOTOM*, the raw DN values are converted to linearized (i.e., photometrically corrected) FN values directly from the effective exposure time associated with each level of the ITF. For a given pixel the FN associated with level  $i$  of the ITF is:

$$FN_i = T(i)$$

where  $T(i)$  is the effective exposure time in seconds for level  $i$ .

There are four basic methods for the determination of the FN of a raw science image pixel from a single ITF pixel (for the case where the displacement coordinates of the science image are  $\leq 0.125$  pixel from the ITF pixel coordinate). In the following discussion, let  $DN(ITF_1)$  represent the DN level of the relevant pixel in the first ITF level; let  $DN(ITF_{12})$  represent the DN level of the relevant pixel in the twelfth ITF level; let  $DN_{raw}$  represent the DN level of the science image pixel; and let  $DN_{sat}$  represent the DN level of saturation for the relevant pixel. Then the four alternatives are:

- **Fully calibrated data:** When  $DN(ITF_1) \leq DN_{raw} \leq DN(ITF_{12})$ , the FN is determined with a linear interpolation algorithm. The interpolation is performed between the two ITF levels that bound the input DN in intensity.
- **Saturated data:** When  $DN_{raw} \geq DN(ITF_{12})$  and  $DN_{raw} \geq DN_{sat}$ , the pixel is considered to be saturated and the FN is set to a constant (the FN value for the top level of the ITF; see Table 6.1).  $DN_{sat}$  has been determined on a pixel-by-pixel basis through analysis of the individual ITF curves and is defined to be the DN at which the slope of the ITF curve (DN versus exposure level) approaches zero. Since ITF curves vary considerably from pixel to pixel, the DN level corresponding to saturation varies from pixel to pixel. The flagging of saturated data is broken down into two separate cases; in either case, the FN for the pixel in question is set to the FN of the top level of the ITF:

**Case 1:**  $DN_{raw} = DN(ITF_{12})$ . These pixels are flagged with the saturation flag of  $-1024$ .

**Case 2:**  $DN_{raw} > DN(ITF_{12})$ . These pixels are flagged with both the saturation flag of  $-1024$  and a positive extrapolation flag of  $-256$ . In this instance, the assignment of an extrapolation flag serves only to identify the fact that the DN exceeds that of the top level of the ITF; no extrapolation of the FN data is performed.

- **Positively extrapolated data:** When  $DN_{raw} > DN(ITF_{12})$  and  $DN_{raw} < DN_{sat}$ , the FN is computed by a two-point extrapolation from the top two levels of the ITF. These pixels are flagged with the positive extrapolation flag of  $-256$ .
- **Negatively extrapolated data:** When  $DN_{raw} < DN(ITF_1)$ , the FN is computed with a two-point extrapolation from the bottom two levels of the ITF. However, the pixel is only flagged with an indication of negative extrapolation if the extrapolation is considered excessive. For this purpose, a “negative extrapolation reference image” has been created by determining the 50% intensity level of the ITF null image, and smoothing these data with a 5-point boxcar in two-dimensions. Consequently, negative extrapolations are only considered excessive and flagged if  $DN_{raw} < DN_{neg. ext. ref. image}$ . Excessive negative extrapolations are flagged with a value of  $-128$ .

When there is significant misalignment ( $>0.125$  pixel) between the raw science image and the ITF, a  $4 \times 4$  matrix of ITF pixels surrounding the location in question is used to compute the relevant FN. Using the raw science image DN, an FN value is computed at each of the  $4 \times 4$  locations in the matrix, using the above described single-pixel scenarios. The median FN in the matrix is computed, and then deviant values are eliminated from the FN matrix and replaced with the median FN. FN values are considered to be deviant if they are different from the median by more than 100 FN. Once the FN matrix has been defined and deviant values replaced, the matrix is fit with a spline surface which is evaluated at the final coordinate location desired for the final FN value.

The FNs determined during the *PHOTOM* procedure have values which range between  $\pm 1024$ . Any FN values originally exceeding these limits are clipped and set to the respective limit value.

## 6.4 Associated $\nu$ Flags and Reference Images

### 6.4.1 Non-photometrically Corrected Image Regions

As discussed in Chapter 6.3, the regions defined for *PHOTOM* either reside within an approximately circular boundary for high dispersion, or a diagonal swath encompassing the location of both apertures and a large area of background for low dispersion. All pixel locations which do not reside within these defined boundaries are not *PHOTOM*ed and are flagged as  $-16384$ .

### 6.4.2 Warning Track

In order to alert the user that data being analyzed are spatially close to the edge of the *PHOTOM* region and/or near the target ring, a warning zone approximately five pixels deep has been established on the *PHOTOM*ed data side of the boundary. Pixel locations determined to be in the warning track are flagged as  $-512$ .

### 6.4.3 ITF Artifacts

#### 6.4.3.1 Permanent Artifacts and Reseaux

The permanent ITF artifacts have been cataloged and both the artifacts and reseaux have been removed from the ITF images with a bi-linear interpolation scheme. The location of the specific pixels affected by either an artifact or reseau mark have been preserved in an ITF-dependent “permanent blemish” reference image. This image is used in the pipeline processing during the *PHOTOM* step to flag pixels in the science image whose location is coincident to those of the ITF blemishes. The  $\nu$  flag values corresponding to permanent ITF artifacts and reseaux are  $-2048$  and  $-4096$ , respectively. Because the ITF has been spatially interpolated in these regions, the accuracy of *PHOTOM* is somewhat degraded in the vicinity of the pertinent artifacts and reseaux.

#### 6.4.3.2 The 1515Å Artifact

Analyses of presumably featureless SWP spectral data of white dwarfs have revealed a distinctive absorption artifact at 1515Å. Although this “feature” is now known to be present in a variety of the SWP spectra, its presence in the featureless white dwarf spectra analyzed for flux calibration studies was the catalyst for further investigation and allowed the absolute determination of this “feature” as an artifact (De La Peña 1992).

Figure 6.1 is a plot of the SWP spectrum of the white dwarf, G191-B2B, a featureless continuum source. The spectra were produced with the standard extraction method of the NEWSIPS image processing system, a Signal Weighted Extraction Technique (*SWET*).

Upon further investigation, the 1515Å feature was found to be present in both NEWSIPS and IUESIPS data. Recall that NEWSIPS is using a *SWET* extraction and the SWP ITF (Epoch 1985) was constructed in raw space. IUESIPS uses a standard boxcar extraction and the SWP ITF (Epoch 1978) was constructed in geometrically corrected space. Therefore, this artifact is independent of the extraction method, and both the ITF epoch and creation method. Despite the major differences in the image processing techniques employed by the two systems, the feature is apparent in both datasets. In addition, not only is this artifact found in these recently obtained white dwarf observations (1991), but it also can be found in extracted spectra acquired as early as 1978.

Using the data from a specific SWP image in which this absorption feature is present, the vector displacement information was used to trace the pixels in the extracted/resampled (MX/SI) images back to the linearized and raw images (LI and RI, respectively), and ultimately back to the ITF. There appears to be a group of “lazy” pixels in the ITF at the computed location. These pixels lack sensitivity in the lowest levels of the ITF in that they require more illumination than their neighbors before they “react.” Unfortunately, there are several adjacent pixels along the edge of the low-dispersion spectral swath which appear to be less sensitive than the neighboring pixels at low illumination levels. It is simply an unfortunate circumstance that these pixels reside along the edge of the spectral swath, and therefore, manifest themselves as a flux deficit in the extracted data. Because of the difficulty in accurately identifying the pixels contributing to the 1515Å artifact due to the variable placement of the spectrum on the image, this artifact is not flagged.

## 6.5 *PHOTOM* Output

The low-/high-dispersion LI FITS files (LILO/LIHI) are the main output data product produced during the *PHOTOM* stage of image processing. This file contains the LI and associated  $\nu$  flag (LF) data. For both low and high dispersion, the LI and LF arrays are full  $768 \times 768$  images. The LI contains FN values in RI space for the data which have been *PHOTOM*ed. Since the LI was created by overwriting a copy of the RI, the remainder of the data in the LI frame outside the *PHOTOM* region are the raw data scaled down by a factor of 32. The LF contains the *PHOTOM*  $\nu$  flag error conditions which have been combined with the conditions determined during the raw image screening portion of image processing. The intensity data (LI) are output as the FITS primary array, and the associated  $\nu$  flags (LF) are output as the corresponding FITS image extension to the LILO/LIHI.

The *PHOTOM* module writes the following information to the HISTORY portion of the image label:

- ITF used by *PHOTOM* (camera and ITF acquisition epoch),
- mean THDA of ITF,

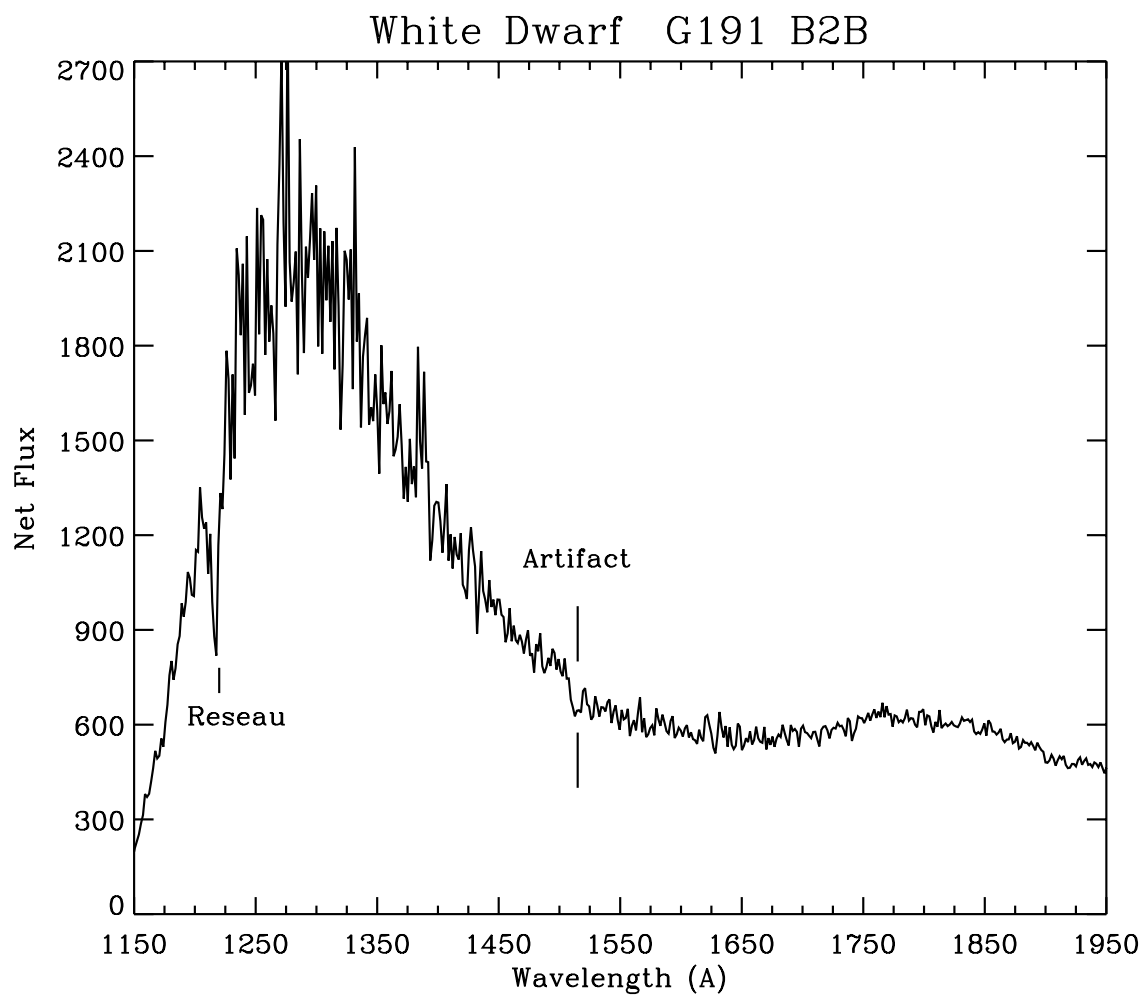


Figure 6.1: White Dwarf SWP spectra showing the 1515Å artifact.



- ITF UVC voltage, UV flood wavelength, ITF SEC voltage, and
- ITF characteristics and construction date.

# Chapter 7

## Image Resampling (*GEOM*)

Raw IUE images suffer from spatial distortions introduced by the SEC Vidicon cameras. The electrostatically-focused imaging section of the camera produces a pincushion distortion, while the magnetically-focused readout section produces an S-distortion. Furthermore, the dispersion direction lies at an angle of approximately 45 degrees relative to the image axes and the dispersion function is not linear within the spectral orders. The combination of these effects make the task of spectral extraction and subsequent analysis very difficult. The goal of the *GEOM* module is to create a geometrically-resampled and spatially-rotated image in which the spectral orders are horizontally aligned and the dispersion is linear within each order thus providing an image format that is best suited for scientific analysis. The *GEOM* step operates on the linearized (i.e., photometrically corrected) image (LI).

The NEWSIPS approach to producing a geometrically resampled image (SI) is to construct a vector field that maps each pixel from its instrumental raw space to a geometrically rectified space. For both low- and high-dispersion images, these vectors include corrections for the following effects:

- the displacements between the raw science image and the Intensity Transfer Function (ITF),
- the displacement of the reseau pattern (camera fiducials) in the ITF from its original square grid,
- the rotation of the spectral format to lie along image rows, and
- the small change of scale needed to linearize the dispersion.

In addition to the above corrections common to both dispersions, the vectors applied to low-dispersion SI data include:

- the shift to align the two spectrograph apertures in wavelength space,
- corrections for the spatial deviations (cross-dispersion “wiggles”) in the long-wavelength cameras,

- a correction (detilting) for extended sources to account for the fact that the major axis of the large aperture is not exactly perpendicular to the dispersion direction, and
- shifts in both the wavelength and spatial directions to maintain a fixed starting wavelength and spatial position in the image,
- an adjustment to the LWP data to put the large-aperture data at the top, and
- an adjustment so that both long wavelength cameras provide coverage of the same spectral range.

In addition to the corrections common to both dispersions, the vectors applied to high-dispersion SI data include:

- corrections for the echelle order splaying,
- spatial shifts for proper alignment of the orders to a fiducial location (order registration), and
- corrections for the cross-dispersion wiggles.

Both the corrections common to both dispersions and the dispersion-specific corrections are discussed in more detail in the sections which follow.

## 7.1 Corrections Common to Both Dispersions

### 7.1.1 Measurement of Distortions

#### 7.1.1.1 Mapping of Raw Science Image to ITF Space

The first correction for image distortion maps the science image to the geometric space of the relevant ITF. This correction utilizes the vector displacements (VD) determined for each pixel during the raw image registration step (Chapter 5). These vectors are unique for each science image and can be recovered from the information in the binary table extension to the final VD FITS file.

#### 7.1.1.2 Mapping of ITF Space to Geometrically Rectified Space

Laboratory measured positions of the fiducial marks (reseau) are used to map the distortion of the null-subtracted 20% level of the ITF in order to compensate for the geometric distortions in the ITF images. The faceplate of each camera is etched with a square-grid pattern of 169 reseau marks arranged in 13 rows and 13 columns. The reseau appear on images as occulted areas approximately 2–3 pixels wide, spaced approximately 55 pixels apart for LWP and LWR and 56 pixels apart for SWP. Of the 169 reseau marks embedded in the fiber-optic coupling, approximately 129 fall within the camera target area. According to the

design specifications of the scientific instrument (GSFC System Design Report for the IUE, 1976), the placement of the reseau marks in a true square grid is accurate to within  $\pm 0.005$  mm, which corresponds to  $\pm 0.138$  pixels for LWP/LWR and  $\pm 0.14$  pixels for SWP.

In order to refine the true locations of the reseau marks, laboratory measurements were made of the reseau grid on an SEC Vidicon camera which was manufactured about the same time as the IUE cameras; therefore, the same deposition mask was used for the reseaux. The work was performed by the Metrology Department at Rutherford Appleton Laboratory (Didcot, U.K.) in late 1990. The measurements were obtained in an X/Y reference frame in millimeters with a demonstrated repeatability of  $\pm 0.003$  millimeters. As a result, it was necessary to derive a scale factor to convert the millimeter measurements to “true” pixel locations for the reseaux. Note that the NEWSIPS true reseau positions may be very different from the positions quoted for IUESIPS. The IUESIPS reseau positions are *not* laboratory measurements, but rather a square grid construct based upon the definitions of a central reseau mark and mean reseau spacing. The NEWSIPS true reseau positions are listed in Tables 7.1–7.6.

The observed positions of the reseau marks are determined per ITF, and the departures of the observed positions from their true locations are used to characterize the geometric distortion of the camera system. A vector field defining the displacement of each pixel in the null-subtracted 20% level of the ITF from geometrically rectified space is derived using a bi-cubic spline interpolation between the reseau marks.

### 7.1.2 Image Rotation

The image rotation is not, strictly speaking, a distortion correction, but rather is an image remapping performed to simplify the extraction of spectral data from the SI. The purpose of the rotation is to align the spectral order(s) horizontally along the geometrically rectified image.

### 7.1.3 Wavelength Linearization

As discussed in Chapter 8.1, the dispersion solutions for the SI are not precisely linear; significant second- and third-order terms are present in both dispersion modes. The nonlinearities which exist in the dispersion solutions for the SI can, if not accounted for, lead to wavelength errors on the order of several Ångströms (low dispersion) or several kilometers per second (high dispersion) in some regions of the spectrum. Therefore, a remapping of the SI data is necessary to force the dispersion solution onto a linear scale. In low dispersion, the high-order terms for a given camera are quite stable over time and camera temperature (THDA) so that a single third-order correction can be applied to all of the data for a given camera. The same holds true for high dispersion except that individual solutions are applied independently to each echelle order. The derivation of the corrections is discussed in detail in Chapter 8.1.

The form of the low-dispersion linearization correction for each camera is displayed in

Table 7.1: LWP True Reseau Positions in X Direction

	1	2	3	4	5	6	7
1	80.39	135.37	190.32	245.29	300.11	355.10	410.15
2	80.39	135.35	190.26	245.25	300.17	355.11	410.18
3	80.33	135.32	190.32	245.25	300.17	355.10	410.20
4	80.39	135.39	190.33	245.24	300.20	355.18	410.18
5	80.39	135.40	190.32	245.25	300.20	355.15	410.21
6	80.39	135.30	190.26	245.20	300.17	355.09	410.18
7	80.41	135.33	190.33	245.22	300.20	355.15	410.21
8	80.39	135.24	190.26	245.13	300.13	355.07	410.18
9	80.39	135.25	190.25	245.13	300.09	355.09	410.20
10	80.37	135.22	190.22	245.11	300.09	355.10	410.14
11	80.36	135.20	190.18	245.03	300.02	355.00	410.09
12	80.33	135.26	190.24	245.18	300.10	355.13	410.15
13	80.36	135.26	190.22	245.13	300.07	355.10	410.14

	8	9	10	11	12	13
1	465.00	520.00	574.88	629.81	684.67	738.86
2	465.04	520.06	574.88	629.88	684.73	738.93
3	465.04	520.04	574.92	629.84	684.77	739.14
4	465.06	520.06	574.93	629.71	684.76	739.15
5	465.07	520.06	574.99	629.78	684.76	739.25
6	465.03	520.02	574.92	629.70	684.73	739.32
7	465.10	520.10	574.95	629.76	684.67	739.36
8	465.04	520.09	574.91	629.70	684.56	739.29
9	465.03	520.04	574.93	629.70	684.55	739.34
10	465.00	520.04	574.93	629.63	684.52	739.34
11	464.96	519.92	574.81	629.54	684.38	739.32
12	465.04	520.03	574.88	629.70	684.36	739.45
13	465.03	520.03	574.89	629.74	684.51	739.54

Table 7.2: LWP True Reseau Positions in Y Direction

	1	2	3	4	5	6	7
1	60.40	60.32	60.29	60.39	60.32	60.33	60.29
2	115.35	115.22	115.44	115.44	115.39	115.40	115.33
3	170.20	170.21	170.30	170.50	170.30	170.36	170.18
4	225.21	225.22	225.41	225.46	225.41	225.30	225.24
5	280.18	280.13	280.36	280.43	280.32	280.36	280.21
6	335.20	335.13	335.32	335.32	335.30	335.21	335.11
7	390.14	390.07	390.24	390.32	390.22	390.14	390.04
8	445.04	445.09	445.18	445.35	445.29	445.28	445.07
9	500.21	500.09	500.18	500.33	500.17	500.21	500.10
10	555.10	555.13	555.22	555.30	555.25	555.15	554.98
11	610.00	610.07	610.04	610.29	610.15	610.09	609.93
12	664.93	665.05	665.03	665.30	665.14	665.13	664.98
13	719.96	720.15	720.13	720.20	720.04	720.11	719.98

	8	9	10	11	12	13
1	60.36	60.26	60.32	60.30	60.29	60.29
2	115.26	115.29	115.32	115.25	115.22	115.22
3	170.33	170.30	170.33	170.13	170.24	170.17
4	225.30	225.20	225.26	225.17	225.11	225.32
5	280.29	280.20	280.24	280.18	280.25	280.33
6	335.29	335.22	335.21	335.14	335.17	335.29
7	390.18	390.11	390.17	390.06	390.15	390.24
8	445.22	445.11	445.18	445.17	445.14	445.29
9	500.15	500.13	500.25	500.13	500.09	500.22
10	554.98	555.04	555.18	555.03	555.06	555.29
11	610.09	609.99	610.03	609.99	609.92	610.17
12	665.04	665.00	664.93	664.89	664.92	665.13
13	720.04	719.93	719.87	719.93	719.98	720.20

Table 7.3: LWR True Reseau Positions in X Direction

	1	2	3	4	5	6	7
1	80.39	135.37	190.32	245.29	300.11	355.10	410.15
2	80.39	135.35	190.26	245.25	300.17	355.11	410.18
3	80.33	135.32	190.32	245.25	300.17	355.10	410.20
4	80.39	135.39	190.33	245.24	300.20	355.18	410.18
5	80.39	135.40	190.32	245.25	300.20	355.15	410.21
6	80.39	135.30	190.26	245.20	300.17	355.09	410.18
7	80.41	135.33	190.33	245.22	300.20	355.15	410.21
8	80.39	135.24	190.26	245.13	300.13	355.07	410.18
9	80.39	135.25	190.25	245.13	300.09	355.09	410.20
10	80.37	135.22	190.22	245.11	300.09	355.10	410.14
11	80.36	135.20	190.18	245.03	300.02	355.00	410.09
12	80.33	135.26	190.24	245.18	300.10	355.13	410.15
13	80.36	135.26	190.22	245.13	300.07	355.10	410.14

	8	9	10	11	12	13
1	465.00	520.00	574.88	629.81	684.67	738.86
2	465.04	520.06	574.88	629.88	684.73	738.93
3	465.04	520.04	574.92	629.84	684.77	739.14
4	465.06	520.06	574.93	629.71	684.76	739.15
5	465.07	520.06	574.99	629.78	684.76	739.25
6	465.03	520.02	574.92	629.70	684.73	739.32
7	465.10	520.10	574.95	629.76	684.67	739.36
8	465.04	520.09	574.91	629.70	684.56	739.29
9	465.03	520.04	574.93	629.70	684.55	739.34
10	465.00	520.04	574.93	629.63	684.52	739.34
11	464.96	519.92	574.81	629.54	684.38	739.32
12	465.04	520.03	574.88	629.70	684.36	739.45
13	465.03	520.03	574.89	629.74	684.51	739.54

Table 7.4: LWR True Reseau Positions in Y Direction

	1	2	3	4	5	6	7
1	60.40	60.32	60.29	60.39	60.32	60.33	60.29
2	115.35	115.22	115.44	115.44	115.39	115.40	115.33
3	170.20	170.21	170.30	170.50	170.30	170.36	170.18
4	225.19	225.22	225.41	225.46	225.41	225.30	225.24
5	280.18	280.13	280.36	280.43	280.32	280.36	280.21
6	335.20	335.13	335.32	335.32	335.30	335.21	335.11
7	390.14	390.07	390.24	390.32	390.22	390.14	390.04
8	445.04	445.09	445.18	445.35	445.29	445.28	445.07
9	500.21	500.09	500.18	500.33	500.17	500.21	500.10
10	555.10	555.13	555.22	555.30	555.25	555.15	554.98
11	610.00	610.07	610.04	610.29	610.15	610.09	609.93
12	664.93	665.05	665.03	665.30	665.14	665.13	664.98
13	719.96	720.15	720.13	720.20	720.04	720.11	719.98

	8	9	10	11	12	13
1	60.36	60.26	60.32	60.30	60.29	60.29
2	115.26	115.29	115.32	115.25	115.22	115.22
3	170.33	170.30	170.33	170.13	170.24	170.17
4	225.30	225.20	225.26	225.17	225.11	225.32
5	280.29	280.20	280.24	280.18	280.25	280.33
6	335.29	335.22	335.21	335.14	335.17	335.29
7	390.18	390.11	390.17	390.06	390.15	390.24
8	445.22	445.11	445.18	445.17	445.14	445.29
9	500.15	500.13	500.25	500.13	500.09	500.22
10	554.98	555.04	555.18	555.03	555.06	555.29
11	610.09	609.99	610.03	609.99	609.92	610.17
12	665.04	665.00	664.93	664.89	664.92	665.13
13	720.04	719.93	719.87	719.93	719.98	720.20

Table 7.5: SWP True Reseau Positions in X Direction

	1	2	3	4	5	6	7
1	74.41	130.48	186.50	242.55	298.45	354.51	410.65
2	74.41	130.45	186.45	242.51	298.50	354.53	410.68
3	74.36	130.42	186.50	242.51	298.50	354.51	410.69
4	74.41	130.49	186.52	242.50	298.53	354.60	410.68
5	74.41	130.51	186.50	242.51	298.53	354.57	410.70
6	74.41	130.41	186.45	242.45	298.50	354.50	410.68
7	74.44	130.44	186.52	242.48	298.53	354.57	410.70
8	74.41	130.34	186.45	242.38	298.46	354.48	410.68
9	74.41	130.35	186.43	242.38	298.42	354.50	410.69
10	74.40	130.32	186.40	242.37	298.42	354.51	410.63
11	74.39	130.30	186.36	242.29	298.35	354.41	410.58
12	74.36	130.36	186.42	242.44	298.43	354.54	410.65
13	74.39	130.37	186.40	242.38	298.41	354.51	410.63

	8	9	10	11	12	13
1	466.57	522.65	578.60	634.61	690.55	745.80
2	466.61	522.71	578.60	634.68	690.61	745.87
3	466.61	522.69	578.64	634.64	690.65	746.08
4	466.63	522.71	578.66	634.51	690.63	746.10
5	466.64	522.71	578.71	634.58	690.63	746.19
6	466.60	522.66	578.64	634.50	690.61	746.26
7	466.67	522.75	578.67	634.55	690.55	746.31
8	466.61	522.73	578.63	634.50	690.44	746.24
9	466.60	522.69	578.66	634.50	690.42	746.29
10	466.57	522.69	578.66	634.43	690.39	746.29
11	466.53	522.57	578.53	634.33	690.25	746.26
12	466.61	522.68	578.60	634.50	690.23	746.40
13	466.60	522.68	578.62	634.54	690.38	746.49

Table 7.6: SWP True Reseau Positions in Y Direction

	1	2	3	4	5	6	7
1	54.43	54.34	54.32	54.41	54.34	54.36	54.32
2	110.45	110.32	110.55	110.55	110.49	110.51	110.44
3	166.38	166.39	166.49	166.68	166.49	166.54	166.36
4	222.47	222.48	222.68	222.72	222.68	222.57	222.50
5	278.52	278.46	278.70	278.77	278.66	278.70	278.55
6	334.61	334.54	334.74	334.74	334.72	334.62	334.53
7	390.63	390.56	390.73	390.82	390.72	390.63	390.54
8	446.61	446.66	446.75	446.92	446.87	446.85	446.64
9	502.86	502.73	502.83	502.99	502.82	502.86	502.75
10	558.83	558.85	558.95	559.04	558.98	558.88	558.70
11	614.81	614.88	614.85	615.10	614.96	614.89	614.74
12	670.82	670.93	670.91	671.19	671.03	671.01	670.86
13	726.92	727.12	727.09	727.16	727.01	727.08	726.94

	8	9	10	11	12	13
1	54.39	54.29	54.34	54.33	54.32	54.32
2	110.37	110.39	110.42	110.35	110.32	110.32
3	166.52	166.49	166.52	166.31	166.42	166.35
4	222.57	222.45	222.52	222.43	222.37	222.58
5	278.63	278.53	278.57	278.52	278.59	278.67
6	334.71	334.64	334.62	334.55	334.58	334.71
7	390.68	390.61	390.66	390.55	390.65	390.73
8	446.80	446.68	446.75	446.74	446.71	446.87
9	502.80	502.78	502.90	502.78	502.73	502.87
10	558.70	558.77	558.91	558.76	558.78	559.02
11	614.89	614.79	614.83	614.79	614.72	614.97
12	670.93	670.89	670.82	670.77	670.80	671.01
13	727.01	726.89	726.82	726.89	726.94	727.16

Figure 7.1. This figure shows the amount by which each pixel in the low-dispersion SI must be shifted along the dispersion direction from its original uncorrected position in order to achieve a linear dispersion solution. This correction is applied uniformly throughout the spatial direction of the image so that entire image columns (i.e., lines of constant wavelength) are shifted by the same amount.

In high dispersion, since the vectors which correct for wavelength nonlinearities are determined separately for each order, the corrections for each order are applied in a “block-like” fashion. That is, each pixel in a line of constant wavelength for a given order is shifted by the same amount. The starting and ending spatial positions for each “block” about an order are set halfway between the adjacent orders.

## 7.2 Additional Corrections for Low Dispersion

### 7.2.1 Aperture Alignment

The low-dispersion SI includes the spectral data for both the large and small apertures. Because the centers of the two apertures are not aligned along a line of constant wavelength in the rotated image space, it would be impossible to have a single dispersion solution apply to the entire image. Therefore, a shift along the dispersion direction is introduced for the small-aperture spectra so that both apertures are on a common wavelength scale. The small-aperture data for SWP are shifted by 0.8 pixels in the dispersion direction towards longer wavelengths, and for LWP and LWR the small-aperture data are shifted by 2.3 pixels towards shorter wavelengths. The shift is applied uniformly to all pixels within the small-aperture region of the low-dispersion SI, which is defined to extend from row 1 through row 33 of the image.

### 7.2.2 Wiggle Corrections

The LWP and LWR cameras are known to exhibit localized discontinuities in the spectral format which are believed to be due to slight misalignments between neighboring fiber optic bundles in the output stage of the ultraviolet converter (UVC) portion of the cameras. These misalignments are seen as abrupt changes in the spatial centroid of the spectrum of up to 1 pixel. In addition to these abrupt changes, there also exist more slowly varying “wiggles” in the spectral format. These wiggles can have peak-to-peak amplitudes of 1 pixel or more within the space of a few dozen pixels along the dispersion direction. Figures 7.2 and 7.3 show the locations of the spectral centroid as a function of wavelength for the LWP and LWR cameras, respectively. Note the sharp discontinuities at  $\sim 3290\text{\AA}$  in the large aperture (the feature at  $\sim 3100\text{\AA}$  is a *reseau*) and at  $\sim 2780\text{\AA}$  and  $\sim 3290\text{\AA}$  in the small aperture for the LWP. The LWR shows similar discontinuities at  $\sim 2450\text{\AA}$  and  $\sim 2830\text{\AA}$  in the large aperture. The existence of these wiggles complicates the task of spectral extraction since it is necessary to have the extraction slit follow the changing spectral centroid in order to ensure that all of the spectral flux is extracted at a given wavelength.



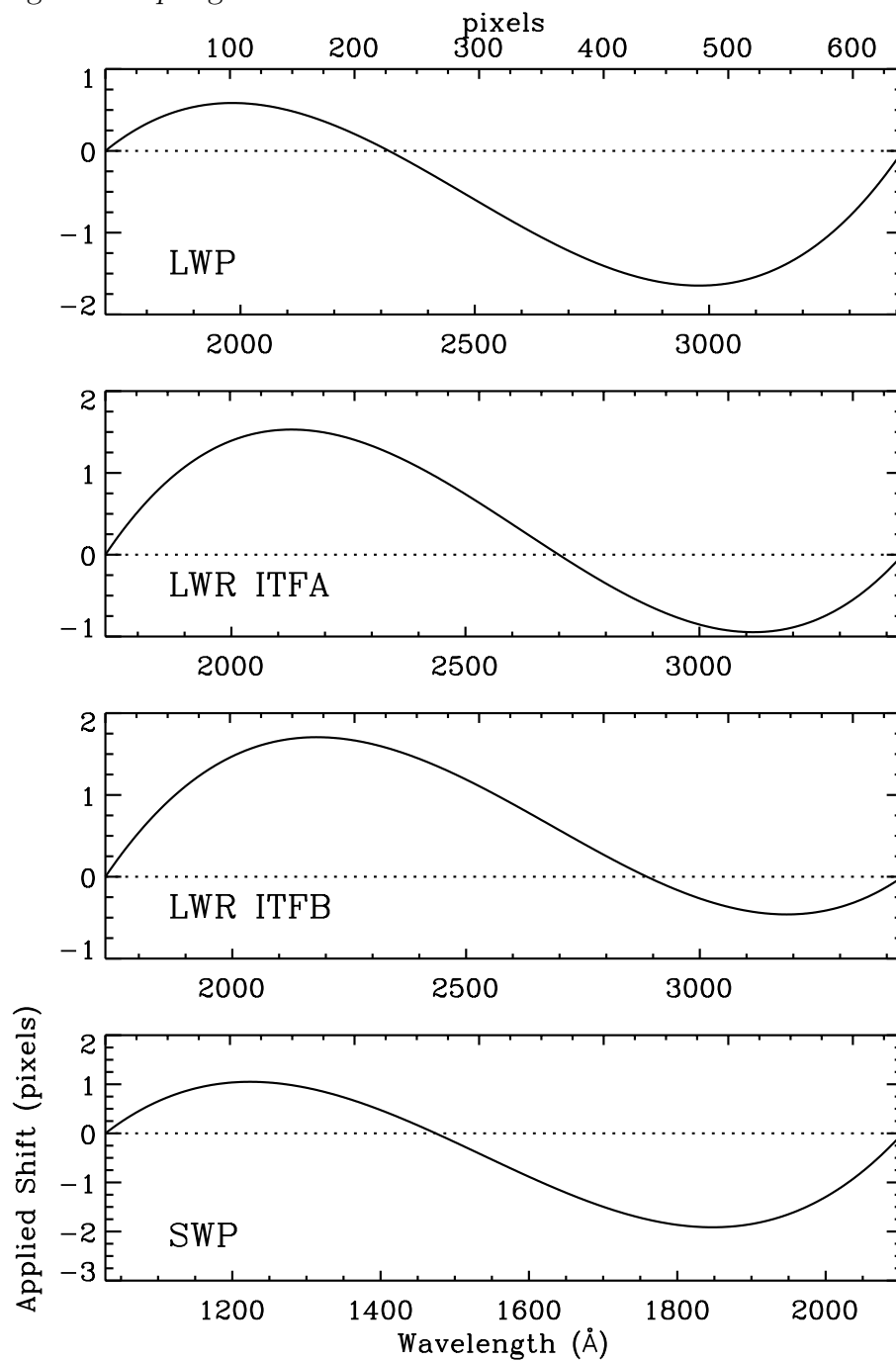


Figure 7.1: Low-dispersion wavelength linearization correction vectors.

To compensate for these wiggles, the spectral centroid as a function of wavelength has been measured from approximately 30 low-dispersion SI for each of the LWP and LWR cameras and the average deviations have been incorporated into the resampling step of the image processing system as an additional geometric correction vector. These corrections affect only the spatial dimension of the low-dispersion SI. Separate deviation vectors are applied for the large- and small-aperture regions of the LWP and LWR low-dispersion SI. As Figures 7.2 and 7.3 show, the deviation vectors for the two apertures are qualitatively similar, but differ in detail, due to the fact that they are imaged onto different portions of the camera faceplate. Figures 7.4 and 7.5 show examples of the measured centroid locations for “dewiggled” versions of LWP and LWR images.

### 7.2.3 Large-Aperture Tilt Correction

The major axis of the large aperture in low-dispersion data is not precisely perpendicular to the direction of dispersion. The major axis is at an angle, called the  $\omega$  angle, with the dispersion direction, which is slightly different for each of the three cameras. The geometry of the entrance apertures in relation to the image scan lines and dispersion directions as they appear in the low-dispersion SI is shown in Figure 7.6. The left side of each figure shows the intrinsic geometry with no corrections applied, the middle portion shows the resulting geometry after applying the aperture alignment correction only, and the right side shows the results after applying both alignment and tilt corrections. Note that the major axis of the large aperture in high-dispersion data is very nearly coincident with the direction of dispersion so no tilt correction is necessary.

The error introduced by extracting extended spectral data (data that fills the large aperture) which has not been tilt corrected, by summing the flux perpendicular to the dispersion can be estimated as follows. The maximum tilt of the large aperture with respect to the dispersion direction occurs in the SWP camera, with an  $\omega$  angle of  $81^\circ$ . If the length of the large aperture is taken to be 14.2 pixels (based on a plate scale factor of 1.53 arcsec/pixel), then the displacement from the line perpendicular to the dispersion direction is 1.1 pixels at each end of the aperture, or approximately  $1.9\text{\AA}$ . Spectral features will show some broadening if extracted perpendicular to the dispersion ( $\omega = 90^\circ$ ), which will amount to a broadening of the base of the point spread function by  $3.8\text{\AA}$ . The overall effect is in reality not as severe as a simple convolution of the data with a  $3.8\text{\AA}$  wide slit, because the part of the signal extracted near the slit center is not really being degraded. A more precise approximation to the error is to think of the  $10\text{\AA}$  slit width as being convolved with a triangular function with FWHM of  $2\text{\AA}$  and a base width of  $4\text{\AA}$ , which will result in a degradation in resolution of 20–25%.

Since this is a significant effect, a correction is made to “detilt” the large-aperture data for observations that result in the detection of spatially extended spectra. This correction is obviously not necessary for point source spectra, nor is it appropriate for most trailed or multiple observations because in these types of observations the source is moved along the FES x-axis which is nearly perpendicular to the dispersion direction. Multiple spectra acquired

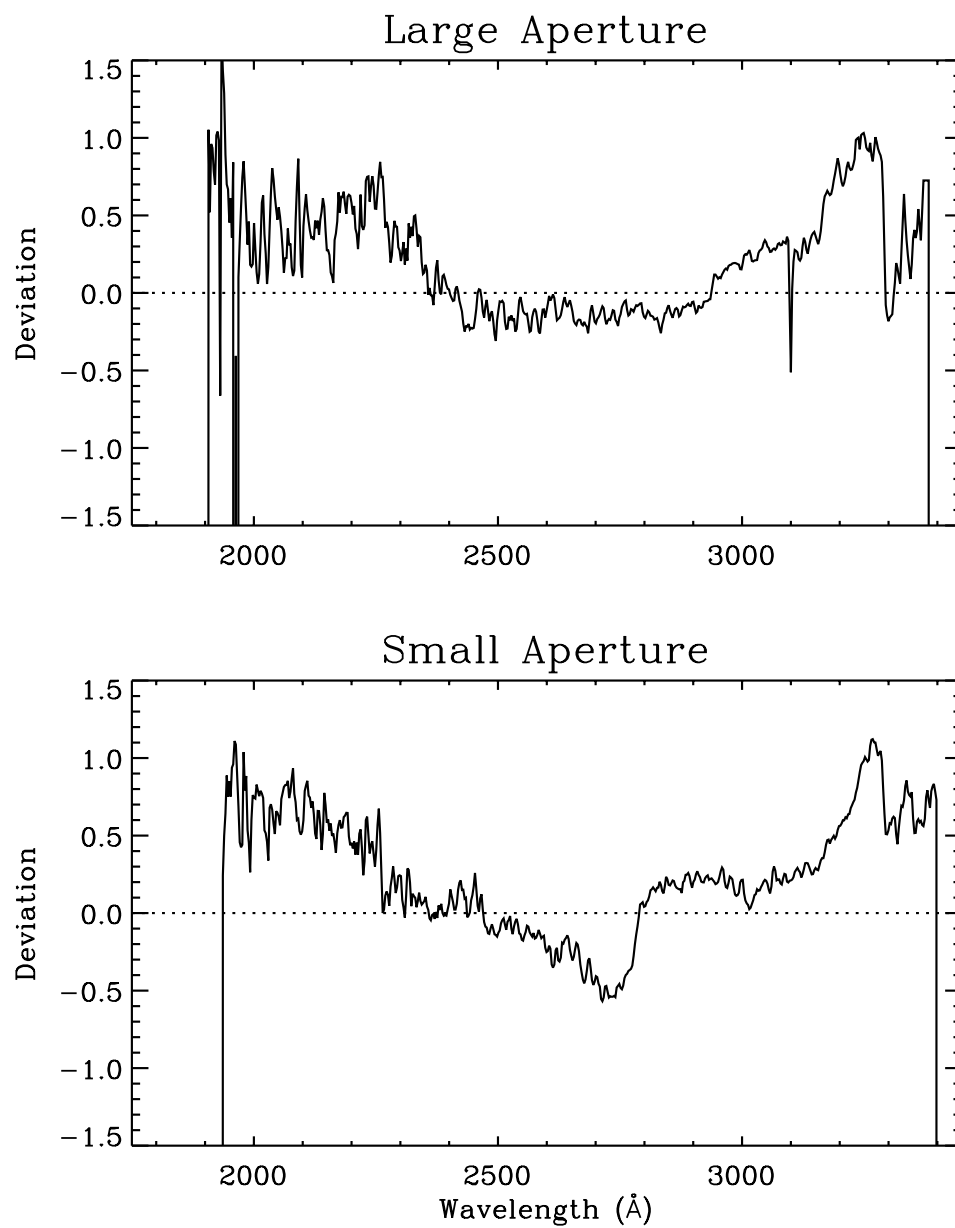


Figure 7.2: Spectrum centroid location in LWP low-dispersion SI data.

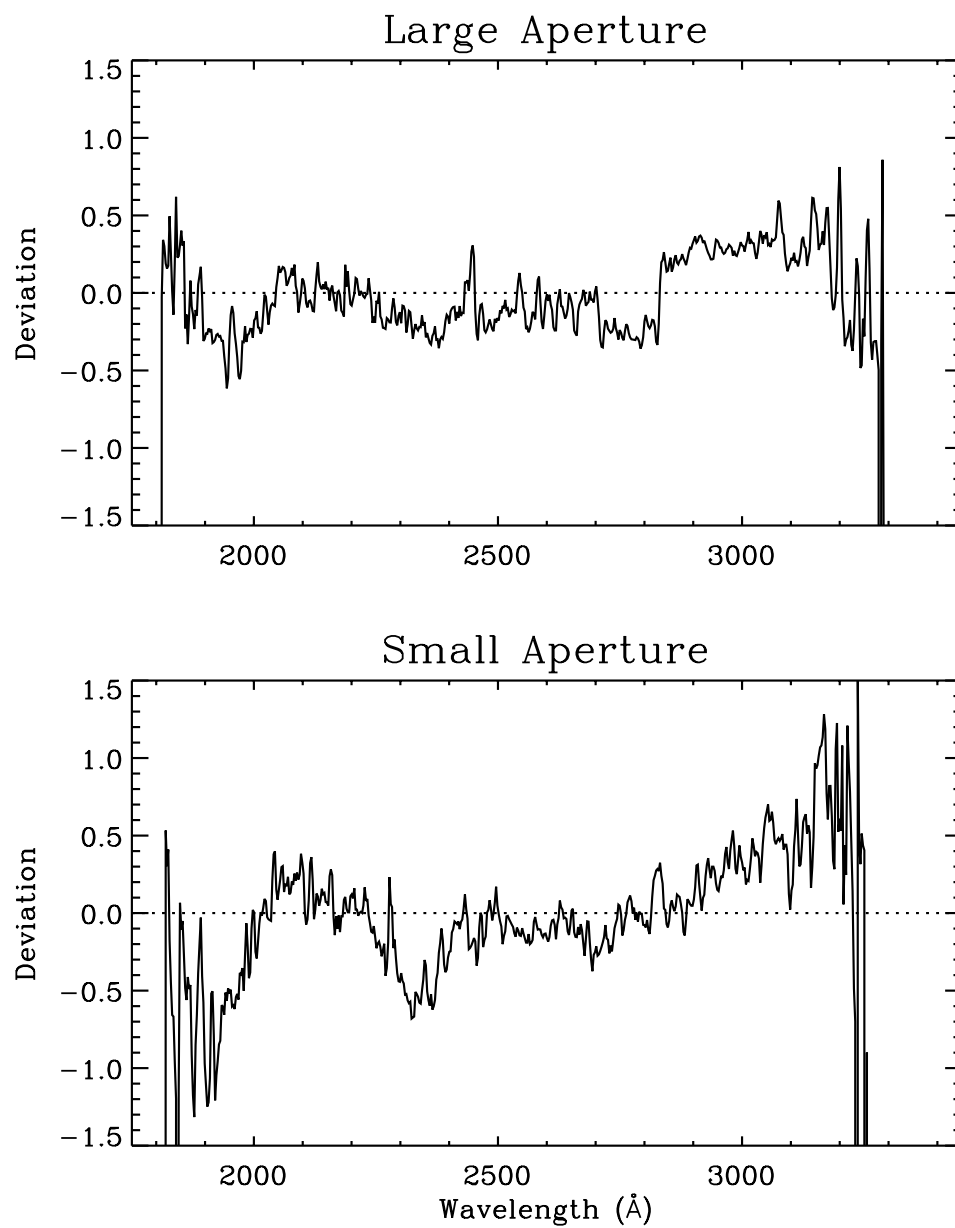


Figure 7.3: Spectrum centroid location in LWR low-dispersion SI data.

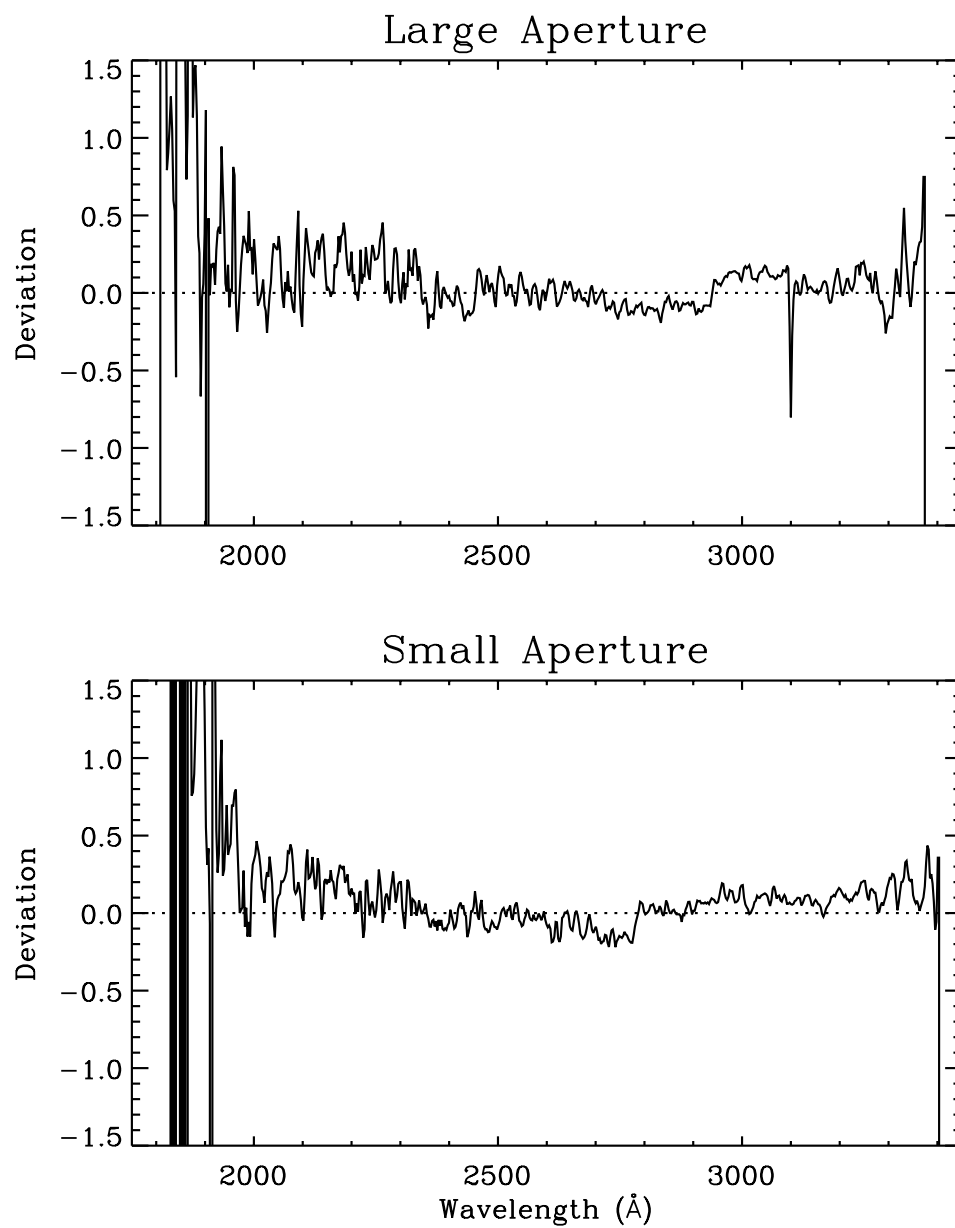


Figure 7.4: Spectrum centroid location in “dewiggled” LWP low-dispersion SI data.

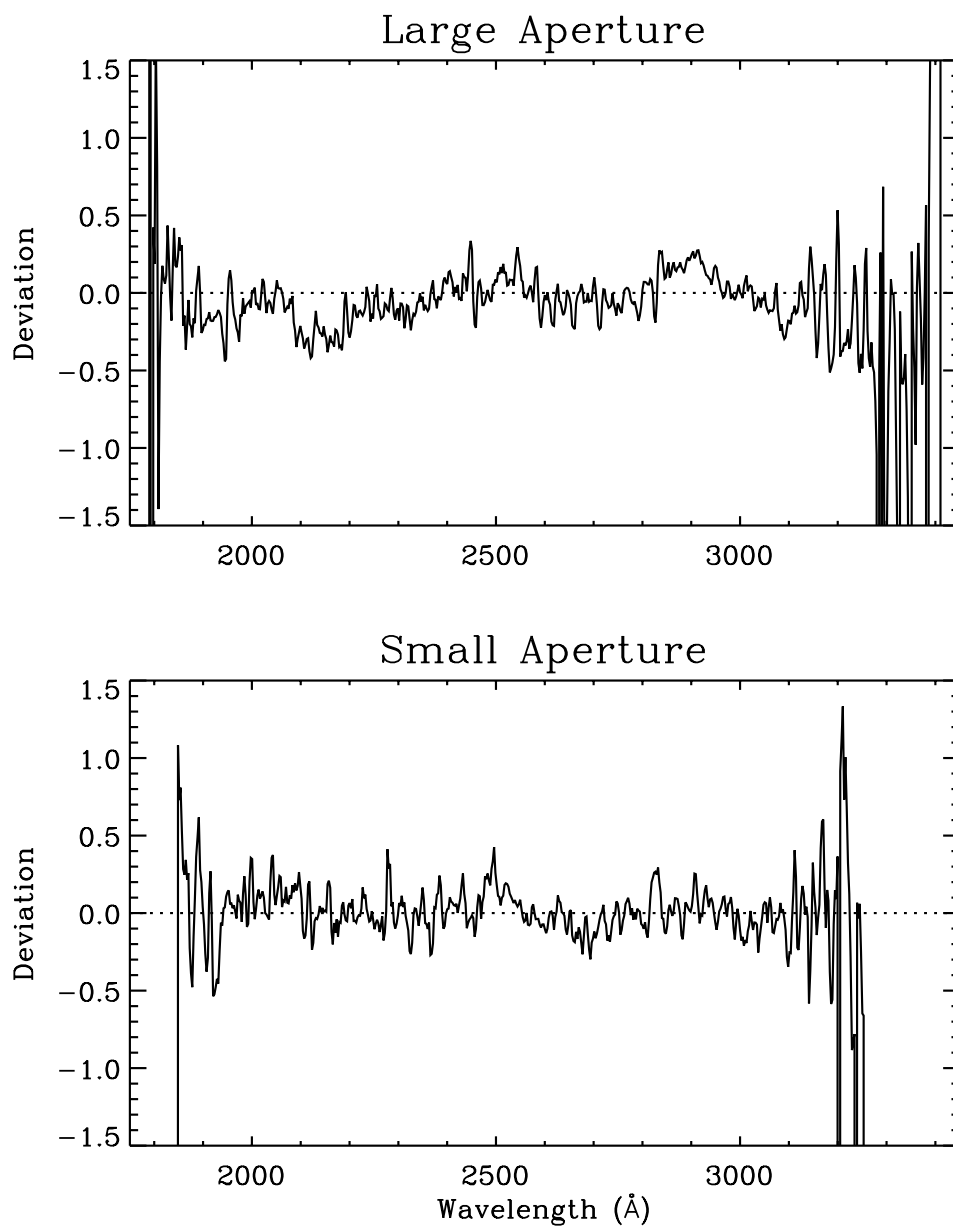


Figure 7.5: Spectrum centroid location in “dewiggled” LWR low-dispersion SI data.

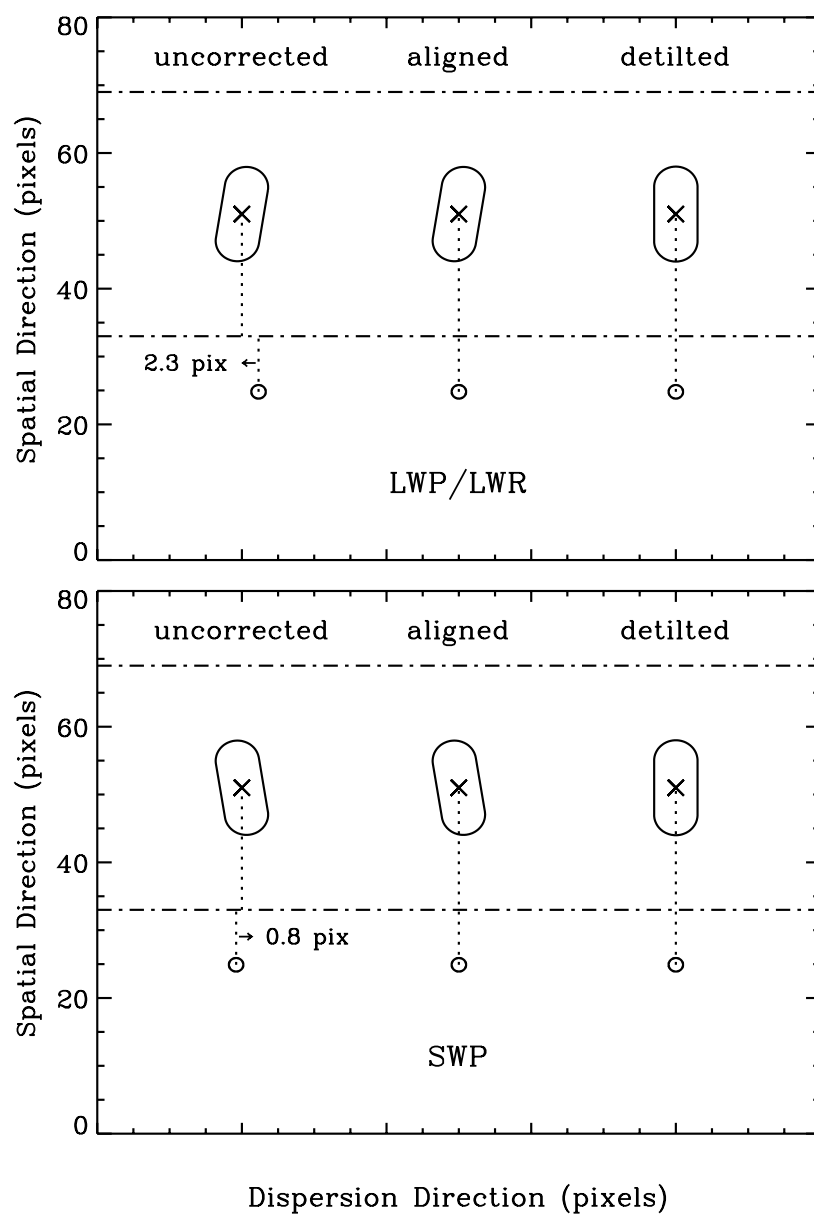


Figure 7.6: Geometry of the spectrograph apertures as they appear in the low-dispersion SI.

along the major axis of the aperture, however, are tilt corrected. The tilt correction is not applied to any non-multiple spectrum having object class designation 10–57 (stellar sources), regardless of whether the spectrum is determined to be point or extended. Presumably a stellar spectrum measured to be extended is saturated.

The tilt correction is only applied to a region of the low-dispersion SI that extends for 18 image lines on either side of the predicted center of the large aperture, thus leaving the small-aperture data intact. The extent of the correction region was chosen so as to include the areas on either side of the aperture which are used for background subtraction in the subsequent extraction step of the image processing. The actual correction is accomplished by simply shifting each image line in the dispersion direction by an amount given by:

$$\Delta x = \Delta y \times \tan(\omega_t)$$

where  $\Delta y$  is the number of spatial image lines between the center of the large aperture and the image line under consideration, and  $\omega_t$  is the tilt angle of the aperture. Note that this correction is a projection of the aperture onto the spatial axis of the image, as opposed to a rotation about the center of the aperture, since the latter would result in a slight remapping of the spatial character of the data.

### 7.2.4 Wavelength and Spatial Normalization

As discussed in Chapter 8.1, global shifts in the location of the spectral format occur as a function of time and camera temperature. These global movements of the spectral format appear as displacements of the spectrum in both the spatial and dispersion directions of the low-dispersion SI. The resulting change in the starting wavelength (i.e., the wavelength value assigned to column 1 of the low-dispersion SI) can be compensated for through the application of zeropoint corrections derived from wavelength calibration (WAVECAL) images (Chapter 8.1). While this would result in the assignment of the correct wavelength zeropoint for each low-dispersion SI, it would also result in the assignment of a *different* starting wavelength for each image. Having spectra with offset wavelength scales would affect subsequent data analysis.

To alleviate this effect in low dispersion, zeropoint shifts in both the spatial and dispersion directions are applied to the image resampling vectors so that all spectra for a given camera have the same starting wavelength and the same spatial location within the low-dispersion SI. Furthermore, additional shifts are applied to the image resampling vectors so that both long wavelength cameras provide coverage of the same spectral range. The spatial centroid of large-aperture spectra is chosen to lie on or about line 51 of the low-dispersion SI for all cameras. The resulting centroid of small-aperture spectra is approximately at line 25. Due to the nature of the LWP geometry, this requires an additional adjustment to the LWP data in order to place the large-aperture spectrum at the top of the file. The common wavelength starting values are 1050Å and 1750Å for the short and long wavelength cameras, respectively. The amount of the zeropoint shift to be applied to each image is computed from the difference between the desired starting wavelengths and those predicted from the time-



and temperature-corrected dispersion constants (Chapter 8.1). Image-to-image scatter in the precise location of the spectral format leads to 1-sigma errors in the predicted wavelength and spatial zeropoints of  $\sim 0.3\text{\AA}$  and 0.26 pixels, respectively, for the SWP and  $\sim 0.6\text{\AA}$  and 0.35 pixels, respectively, for the LWP.

## 7.3 Additional Corrections for High Dispersion

### 7.3.1 Order De-splaying

The differential rotation (“splaying”) of individual echelle orders results from the combined effects of the echelle and cross-dispersing elements. The ratio of these two components of dispersion is proportional to the ratio of the grating orders and can be expressed as  $1/m_{echelle}$  times a constant. The change in this ratio from one order to the next causes the orders to be differentially rotated (“splayed”) on the detector. The de-splaying angle for each camera was determined after first rotating the raw space image in the *GEOM* module and recognizing conceptually that the  $y$  coordinate of the rotated image may be replaced with the parameter  $1/m_{ech}$ . Since the  $y$  positions of the orders are distributed as  $1/m_{ech}$ , this axis may be thought as mapping a continuous (floating-point) parameter,  $1/m_{ech}$  (Smith 1990a, 1990b). A single differential rotation constant may then be incorporated which is used ultimately to detilt each of the  $y$  pixel-lines with respect to a reference (“horizontal”) line position. This detilting is in fact a de-splaying of each of the lines in the image with respect to a reference order: a single constant which properly takes into account the variation of the splaying-tilt with  $m_{ech}$  across the image field. The de-splaying angle is determined empirically and by means of a virtual-coordinate artifice rather than from grating parameters of the spectrograph because *NEWSIPS* does not yet “know” what  $m_{ech}$  value will correspond to each  $y$  line in the rotated raw-image space in which the de-splaying corrections are computed. The de-splaying correction performed in *NEWSIPS* processing is such that pixels which lie along “central”  $x$ - $y$  axes (positioned about the center of the target area) have no correction applied. Pixels which lie off of the “central” axes have a de-splaying correction applied that is directly proportional to the displacement of the pixel’s position from the origin of the “central” axes. The de-splaying correction corresponds to a shift in the  $y$  (i.e., line) direction only.

Determination of the splaying constants was done iteratively for a collection of continuum images for each camera until values were found which forced all the orders to fall along constant pixel lines. In practice, the “wiggles” of the orders (Chapter 7.3.3) limited the accuracy to which the de-splaying constants could be determined. However, small residual errors in these constants were presumed to be incorporated as residual slopes in the wiggle vectors.

### 7.3.2 Wavelength and Spatial Normalization

Displacement vectors that adjust for the spatial shifting of the orders with respect to a fiducial image are generated during the raw image screening process and applied to science

images during the *GEOM* stage. These vectors include a global shift of each image and, if needed, differential order shifts. A detailed discussion of the order registration process can be found in Chapter 4.9.

Note that unlike the low-dispersion counterpart, no starting wavelength normalization correction is applied to high-dispersion data. As a result, a resampling of individual spectra to a common wavelength scale is in general required to coadd properly multiple high-dispersion images of a given source.

### 7.3.3 Wiggle Corrections

Localized discontinuities (wiggles) in the spatial direction are also detectable in high-dispersion images for all three cameras. Corrections, similar to those developed in low dispersion for the long-wavelength cameras, have been derived which map out these distortions present in every order. The SWP wiggles demonstrate a time dependency in patchy areas on the camera surface. Therefore, two SWP correction templates have been derived: one for early-epoch (before 1988 January 02) images, the other for late-epoch (after 1990 January 02) data. Wiggle corrections are interpolated linearly for SWP high-dispersion images obtained between these two dates. The LWP and LWR cameras have only single-epoch correction templates. The wiggles among the SWP images correlate well enough that a mean-wiggle template removes at least half the amplitude of the excursions in an individual image. The wiggles present in long-wavelength images are not as well correlated.

## 7.4 Flux Resampling Algorithm

The final coordinate mapping is derived by adding the individual geometric corrections in a vectorial fashion. Consequently, the transformation from raw image space to geometrically rectified space necessitates the use of a sophisticated resampling algorithm because the raw image pixels must be resampled from the irregular grid resulting from the vector mapping to a regular grid to produce the SI. This type of two-dimensional interpolation is mathematically challenging and particularly difficult to solve satisfactorily. The intensity values (FNs) in the LI are resampled to the geometrically corrected space of the SI using a modified Shepard method, an algorithm found in the NAG (1990) library. The interpolant for the modified Shepard method is continuous and also possesses first derivative continuity. The method is local in that the output flux value is dependent only upon data in a surrounding neighborhood.

## 7.5 Data Quality ( $\nu$ ) Flag Resampling

Since the intensity values are resampled in the mapping from the raw space of the LI to the geometrically rectified space of the SI, the  $\nu$  flag values must also be appropriately mapped into this new space. In order to map the flag values from raw space to the new geometric

space, a “resampling” algorithm is clearly *not* desired as the  $\nu$  flags have a very specific discrete meaning which must be maintained. The flag values need to be mapped to their new coordinates such that they retain their initial values, but also are appropriately assigned to additional locations in the remapped space in accordance to the distribution of intensities.

The residuals from integer coordinates are computed for the sample and line final floating-point geometric coordinates. These residuals are then evaluated in combination against a pre-defined threshold of 0.25. This threshold represents an “in-between” region which determines if the  $\nu$  flags should be mapped to 1, 2, 3, or 4 pixels in the final geometric space.

## 7.6 High-Dispersion Cosmic Ray Detection Algorithm (*COSMIC\_RAY*)

This algorithm initially was developed to flag off-order (i.e., background) pixels that are potentially affected by a cosmic ray event. The cosmic ray flagging procedure was conceived for application by the high-dispersion background determination (*BCKGRD*) module.

The flagging by the *COSMIC\_RAY* module is done by dividing the non-illuminated regions of the target into  $57 \times 57$ -pixel boxes and computing local means and rms statistics for each box (see Fahey, Bogert, and Smith 1994). A flagging-threshold was determined empirically as a function of a normalized rms parameter (rms/mean) for each camera. The choice of this criterion was driven by a trade-off between requirements of detecting the “coma” of cosmic rays and not triggering on high points in the background regions when the rms is large.

The sensitivity of the *BCKGRD* solutions to cosmic rays actually is caused by the surrounding low-level coma regions of these central “hit” areas. This can cause ringing over a larger spatial scale across the image. In practice it was difficult to discriminate against the background-flux granularity without sacrificing the *COSMIC\_RAY* module’s ability to detect coma regions. An optimization of the trade-off between detecting low-level coma and not flagging isolated high pixels was such that the flagging still occurred frequently enough that instabilities, resulting from pixel-undersampling, occurred in many background extractions for all three cameras. As a result, the cosmic ray image extension to the high-dispersion SI (CRHI) is not used by *BCKGRD* but is retained as an output product for informational purposes only. The contents of the CRHI are encoded as follows. Pixels which are masked out by the *COSMIC\_RAY* module (e.g., on-order pixels and regions outside the target area) are denoted in the CRHI with a value of +64. Non-condition pixels (i.e., those that are not flagged as cosmic rays) are signified in the CRHI by a value of +32. Pixels that are determined to be affected by cosmic rays are indicated with a value of +160.

## 7.7 GEOM Output

### 7.7.1 Low-Dispersion

The low-dispersion SI and VD FITS files (SILO and VDLO, respectively) are the main output data products produced during the image resampling stage. The SILO contains the geometrically resampled intensity data and the resampled  $\nu$ -flag image corresponding to the intensity data. The intensity data are output as a FITS primary array, and the associated  $\nu$  flags are output as the corresponding FITS image extension. The VDLO contains the summation of all the geometric corrections implemented to perform the single image resampling and gives, for each pixel in LI space, the final  $x$  and  $y$  coordinate in SI space stored in a FITS primary array. As discussed in Chapter 5, the raw cross correlation data are retained in a FITS binary table extension of the VDLO.

The *GEOM* module writes the following information to the HISTORY portion of the low-dispersion image label:

- four Chebyshev coefficients used to define the wavelength linearization,
- tilt angle (applied only to extended sources),
- wavelength zeropoint and spatial shifts,
- final time/temperature corrected dispersion constants, and
- predicted center line of the large and small apertures.

### 7.7.2 High-Dispersion

The high-dispersion SI and VD FITS files (SIHI and VDHI, respectively) are the main output data products produced during the image resampling stage. The SIHI contains the geometrically resampled intensity values stored in a FITS primary array, the resampled  $\nu$ -flag image corresponding to the intensity data stored as a FITS image extension, the associated starting wavelength, wavelength increment, and predicted and found line positions for every order stored in a FITS binary table extension, and an array of pixels which have been flagged as cosmic rays by the high-dispersion *COSMIC\_RAY* module stored as a FITS image extension. The VDHI contains the summation of all the geometric corrections implemented to perform the single image resampling and gives, for each pixel in LI space, the final  $x$  and  $y$  coordinate in SI space stored in a FITS primary array. As discussed in Chapter 5, the raw cross correlation data are retained in a FITS binary table extension of the VDHI.

The following information is written to the HISTORY portion of the high-dispersion image label by the *GEOM* module:

- epoch of the spatial deviation (wiggle) file,
- de-splaying angle in radians, and

- predicted line center of a representative “checkpoint” echelle order (order 100 for SWP or order 90 for the LWP and LWR). The LWP processing HISTORY initially reported the line position for order 100. This was subsequently changed to order 90 after the start of the processing effort, as this order is in a region of higher sensitivity than order 100 for the LWP and LWR. This change only affects LWP and LWR high-dispersion images processed after July 28, 1997.

## 7.8 *COSMIC\_RAY* Output

The following information is written to the HISTORY portion of the high-dispersion image label by the *COSMIC\_RAY* module:

- mean FN of interorder background and
- number of flagged pixels.

# Chapter 8

## Wavelength Calibration (*TTDC*)

High- and low-dispersion small-aperture spectra of the on-board hollow cathode platinum-neon (Pt-Ne) calibration lamp are used to determine wavelength as a function of position in IUE images. These wavelength calibration (WAVECAL) exposures were obtained once a month for each camera and are usually a combination of the calibration spectrum and a tungsten flood lamp (TFLOOD) exposure. The TFLOOD exposure was originally added to raise the DN level of the fainter emission lines and was also used to allow reseau marks to be located on the low-dispersion WAVECAL images; these reseau positions were used by IUE-SIPS to perform geometric corrections, but are not needed in the NEWSIPS system. Since approximately mid-1992 WAVECAL images have been obtained without the superimposed TFLOOD exposures, as it was found that the NEWSIPS wavelength calibration analysis was more accurate without them. Instead, the TFLOOD was taken as a separate exposure.

### 8.1 Image Field-Distortions

Due to residual small-scale geometric distortions introduced by the IUE SEC Vidicon cameras, the dispersion solutions for low and high dispersion are not precisely linear in nature. Residuals from a linear fit to the emission-line positions in WAVECAL spectra show significant second- and third-order terms. These distortions lead to wavelength errors on the order of several Ångströms (low dispersion) or several kilometers per second (high dispersion) in some regions of the camera if left uncorrected. A remapping (along the dispersion direction) of the geometrically-corrected, rotated, linearized, and resampled image (SI) data is necessary to eliminate these distortions and allow the use of a linear dispersion relation. This remapping has been incorporated into the resampling (*GEOM*) step of the image processing system as another vector field that is added to the existing vector fields that describe the image rotation (Chapter 7.1.2) and geometric rectification (Chapter 7.1.3). Higher-order terms, associated with fine scale shifts in the dispersion direction analogous to the fine-scale shifts shown in Figures 7.2 and 7.3, are probably also present but cannot be corrected because of the paucity of WAVECAL Pt-Ne features.

Analysis of many WAVECAL spectra has shown that the first-, second-, and third-order

dispersion terms for low-dispersion SI which have not been linearized are very uniform over time and THDA. This allows the use of a single third-order remapping vector for all low-dispersion images from a given camera. In high dispersion, a similar condition exists except that the remapping vectors are determined separately for each order. The exact form of the correction for each camera is derived as follows. First, a representative sample of WAVECAL images covering the extremes in both observation date and THDA is chosen for analysis. The number of images is typically on the order of 80–90. This sample of images is initially processed without any attempt to apply the (as yet unknown) linearization correction in the *GEOM* step. Third-order Chebyshev dispersion solutions are derived for each of these uncorrected images (using IRAF routines that are described in the next section) and the mean dispersion coefficients for the entire sample are calculated on a term-by-term basis. The mean dispersion coefficients are converted into equivalent pixel-space coefficients, at which point they can be used to compute the appropriate linearization correction vector to apply to all subsequent images within the *GEOM* processing step. The resulting low-dispersion linearization correction displacements for each camera are shown graphically in Figure 7.1. These are included in the *GEOM* processing of every low-dispersion image, so that the SI reflects a linearized wavelength scale. Similar corrections are applied to every order in high dispersion, yielding comparable results.

After the linearization correction is determined for a given camera, all WAVECAL images for that camera are processed with the correction applied (which is the normal processing mode) so that mean linear dispersion solutions and corresponding zeropoint dependencies with time and THDA can be derived as described in the following sections.

## 8.2 Low-Dispersion Wavelength Calibration

### 8.2.1 Parameterization of the Dispersion Relations

Each set of calibration images is processed to provide analytic relations between wavelength and pixel position in low-dispersion SI space. The derivation of these dispersion relations is a multi-step process. First, the pixel locations of the Pt-Ne emission lines in a reference low-dispersion WAVECAL image are measured interactively and combined with laboratory values for the wavelength of each emission line (stored in a line library). This analysis is performed using the IRAF task *identify* which generates a dispersion solution that is a one-dimensional fitted function (Chebyshev polynomial) of wavelength versus pixel number. The next step involves the use of the IRAF task *reidentify* which maps the reference-image Chebyshev solution derived from the *identify* step to an ensemble of images. The final dispersion solution is averaged from several hundred individual solutions output from *reidentify* and consists of a starting wavelength and wavelength increment per pixel. The line libraries are based on the Pt-Ne line positions measured by Reader et al., (1990) at the National Institute of Standards and Technology (NIST). Figure 8.1 shows low-dispersion WAVECAL spectra for the LWP/LWR and SWP cameras and indicates the features included in the low-dispersion libraries. Table 8.1 contains listings of the low-dispersion line libraries. The line positions for all cameras, and therefore the dispersion solutions, are expressed in *vacuum* wavelengths.

Because the geometric correction and resampling step of the image processing rotates the low-dispersion images so that the dispersion direction is parallel to the horizontal or  $x$ -axis of the low-dispersion SI, the terms of the dispersion solutions for the two image dimensions are completely decoupled. The parameterization of the dispersion solutions is as follows:

$$x = A_1 + A_2\lambda$$

$$y = B_1$$

where  $x$  and  $y$  are the image pixel locations and  $A_1$ ,  $A_2$ , and  $B_1$  are the dispersion constants. For a low-dispersion SI, the  $y$  dimension of the image contains spatial information only. In this case the  $B_1$  coefficient simply gives the image line number at which the spectrum centroid is located.

### 8.2.2 Application of the Dispersion Relations

The dispersion solutions derived from individual WAVECAL images display variations from the averaged dispersion solutions discussed above. These variations arise from two sources, the first of which is simply the measurement uncertainties involved in locating the Pt-Ne emission features in the WAVECAL images and the corresponding uncertainties in the coefficients of the derived dispersion solutions. Second, global shifts in the location of the spectral format within individual images are known to occur as a function of camera temperature (THDA) and time (see e.g., Thompson 1988 and Garhart 1993). These shifts occur both parallel and perpendicular to the dispersion direction and consequently result in changes



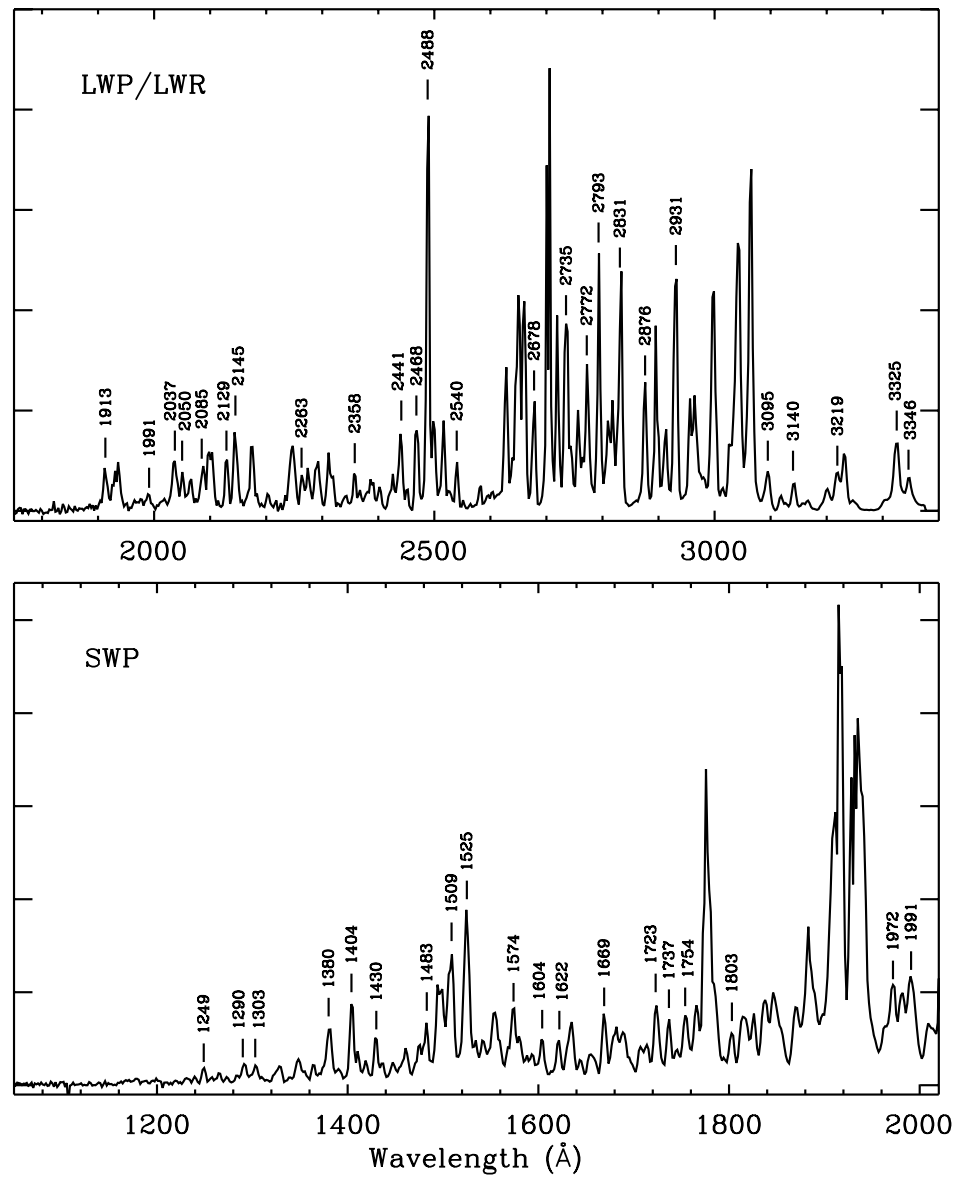


Figure 8.1: Short and long wavelength low-dispersion WAVECAL spectra. Pt-Ne features included in the low-dispersion line libraries are marked.

Table 8.1: Low-Dispersion Pt-Ne Line Libraries

Short Wavelength Camera ( $\text{\AA}$ )	Long Wavelength Cameras ( $\text{\AA}$ )
1248.61	1913.23
1289.95	1990.58
1302.79	2037.12
1380.49	2050.05
1403.90	2085.26
1429.52	2129.31
1482.83	2144.92
1509.29	2263.42
1524.73	2357.83
1574.31	2440.80
1604.01	2468.15
1621.65	2487.92
1669.23	2539.97
1723.13	2677.94
1736.52	2734.77
1753.83	2772.48
1802.94	2792.84
1971.54	2831.13
1990.58	2876.48
	2930.65
	3094.90
	3140.30
	3219.12
	3324.69
	3346.42

to the wavelength zeropoint ( $A_1$ ) as well as the spatial location ( $B_1$ ) of spectra within the low-dispersion SI. These format shifts appear to be a translational shift only, with no change in image scale. As a result, the higher order dispersion term ( $A_2$ ) remains constant.

The dispersion coefficients as actually applied to science images are determined by adding to the mean zeropoint terms corrections appropriate for the observation date and THDA of the particular image. The correction terms  $W_\lambda$  and  $W_s$ , which represent the offset that is added to the mean wavelength and spatial zeropoints, are defined by the following general expressions:

$$W_\lambda = W_{1\lambda} + W_{2\lambda}t + W_{3\lambda}T + W_{4\lambda}t^2 + W_{5\lambda}t^3$$

$$W_s = W_{1s} + W_{2s}t + W_{3s}T + W_{4s}t^2 + W_{5s}t^3$$

where  $W_\lambda$  and  $W_s$  are the corrections to be added to the  $A_1$  and  $B_1$  terms of the mean dispersion relation, respectively,  $T$  is the THDA at the end of exposure, and  $t$  is time expressed as the total number of elapsed days since 1 January 1978.

A first-order (i.e., linear) fit is sufficient to characterize the correlation between THDA and zeropoint for all cameras. The correlation between time and zeropoint, however, has second- and third-order dependencies for some cameras. The  $W_\lambda$  and  $W_s$  coefficients in use for the low-dispersion mode for pre-1990 LWP and SWP images are listed in Table 8.2. Coefficients appropriate for more recent LWP and SWP images are discussed in Chapter 8.2.3. The database of exposures used to generate the coefficients in Table 8.2 include WAVECAL images obtained through mid-1993 for the LWP and mid-1991 for the SWP. The respective coefficients for the LWR camera are listed in Table 8.3. In the case of the LWR, a separate set of coefficients are tabulated for the ITF A and ITF B calibrations. In addition, each ITF has an early and late epoch. This is due to the fact that the wavelength zeropoint shift was dramatically different between these two epochs. The cutoff date for the early and late epochs is 1980.1 for ITF A and 1979.9 for ITF B. The shift of the spectrum center does not exhibit this trend, so the spatial coefficients are identical for each epoch. The zeropoint shifts and corresponding polynomial fits are illustrated graphically for each camera in Figures 8.2–8.5.

### 8.2.3 1995 Wavelength Calibration Updates

In early 1995, concerns were raised about the accuracy of the extrapolations of the low-dispersion wavelength calibrations (i.e., the time and THDA wavelength and spatial zeropoint dependencies) to times beyond the original database of observations. While no errors due to the extrapolated corrections were seen in NEWSIPS data, the IUE Project felt that updating the old wavelength calibration analysis would result in more accurate wavelengths for recent LWP and SWP images. As a result of these concerns, the LWP and SWP wavelength calibration analysis was updated in 1995 using data taken through the beginning of 1995. These new corrections were applied to post-01 January 1990 images while the old corrections were used for pre-1990 images. No calibration update was required for the LWR camera, as it comprised a closed data set. The updated coefficients are listed in Table 8.4.

Table 8.2: LWP and SWP Low-Dispersion Time and THDA Coefficients (pre-1990)

	LWP	SWP
$A_1$ (Å)	1711.6597	1032.4392
$A_2$ (Å/pix)	2.6626680	1.6763376
$B_1$ (pix)	23.61	21.97
$W_{1\lambda}$	4.4345033	-2.3252555
$W_{2\lambda}$	4.0537516e-4	3.5285037e-3
$W_{3\lambda}$	-6.0635105e-1	-2.6882430e-1
$W_{4\lambda}$	0.0	-6.1677609e-7
$W_{5\lambda}$	0.0	4.2678509e-11
$W_{1s}$	-4.3763553	4.3991865
$W_{2s}$	2.8160580e-4	-3.2833262e-3
$W_{3s}$	3.6686645e-1	-1.0900706e-1
$W_{4s}$	0.0	8.2522805e-7
$W_{5s}$	0.0	-7.1718122e-11

Table 8.3: LWR Low-Dispersion Time and THDA Coefficients

	LWR ITF A		LWR ITF B	
	Pre-1980.1	Post-1980.1	Pre-1979.9	Post-1979.9
$A_1$ (Å)	1730.1170	1730.7719	1727.5143	1728.2415
$A_2$ (Å/pix)	2.6658213	2.6657266	2.6692838	2.6688933
$B_1$ (pix)	24.78	24.78	25.04	25.04
$W_{1\lambda}$	10.1020149	-4.7995158e-1	9.2690908	-2.0569484e-1
$W_{2\lambda}$	-1.6612805e-2	2.9549095e-3	-1.5753037e-2	2.5944874e-3
$W_{3\lambda}$	-4.5748750e-1	-2.4267995e-1	-4.1245027e-1	-2.2761587e-1
$W_{4\lambda}$	1.6308716e-5	-6.2727972e-7	1.5803093e-5	-6.0699193e-7
$W_{5\lambda}$	-4.5832944e-9	4.2171131e-11	-4.5624765e-9	5.1719073e-11
$W_{1s}$	-11.6908924	-11.6908924	-11.5273270	-11.5273270
$W_{2s}$	2.9216646e-3	2.9216646e-3	3.0038018e-3	3.0038018e-3
$W_{3s}$	6.1467118e-1	6.1467118e-1	5.9936489e-1	5.9936489e-1
$W_{4s}$	-5.9403908e-7	-5.9403908e-7	-6.2260391e-7	-6.2260391e-7
$W_{5s}$	4.1402462e-11	4.1402462e-11	4.3818172e-11	4.3818172e-11

Table 8.4: LWP and SWP Low-Dispersion Time and THDA Coefficients (post-1990)

	LWP	SWP
$A_1$ (Å)	1711.7219	1032.7897
$A_2$ (Å/pix)	2.6627994	1.6763867
$B_1$ (pix)	23.66	21.97
$W_{1\lambda}$	3.1902447	-2.6142797
$W_{2\lambda}$	1.2511673e-3	3.4473210e-3
$W_{3\lambda}$	-6.2114623e-1	-2.7509139e-1
$W_{4\lambda}$	-1.2237954e-7	-5.6468763e-7
$W_{5\lambda}$	0.0	3.43165905-11
$W_{1s}$	-4.4882965	4.6596390
$W_{2s}$	2.7621062e-4	-3.2043927e-3
$W_{3s}$	3.7540199e-1	-1.1149894e-1
$W_{4s}$	0.0	8.0137016e-7
$W_{5s}$	0.0	-7.1156480e-11

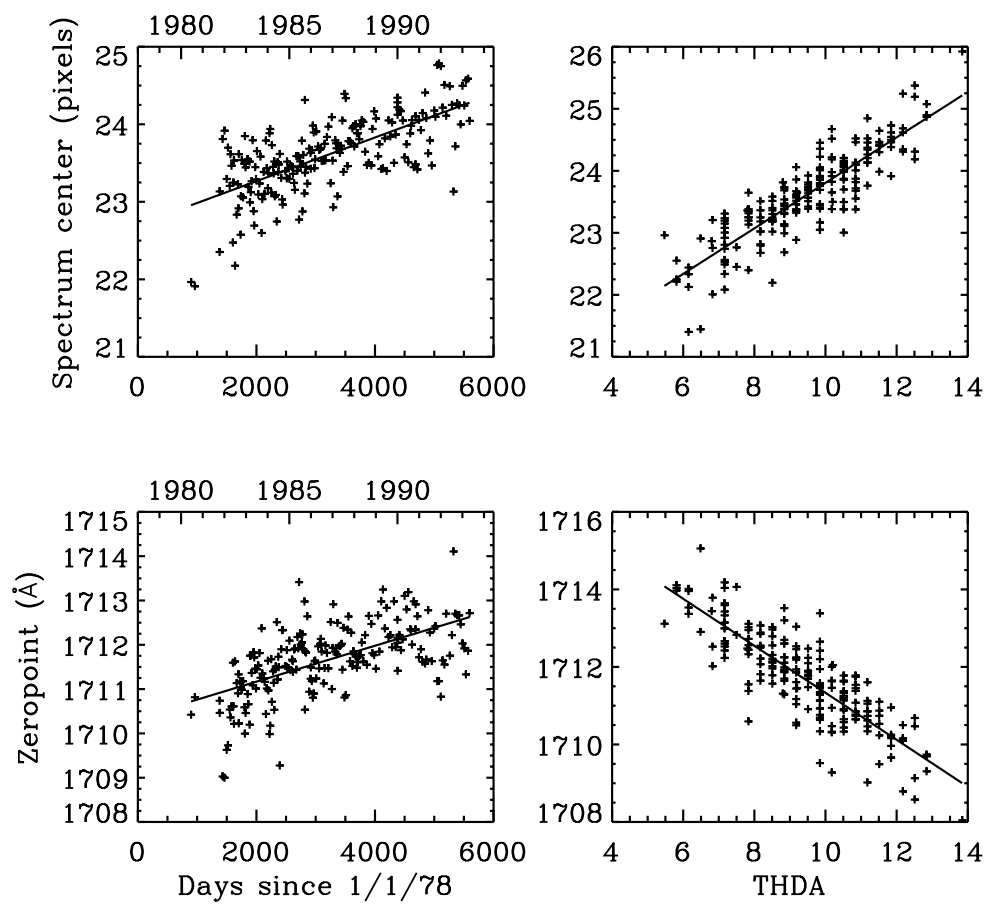


Figure 8.2: Low-dispersion time and temperature correlations with wavelength and spatial zeropoints for the LWP camera.

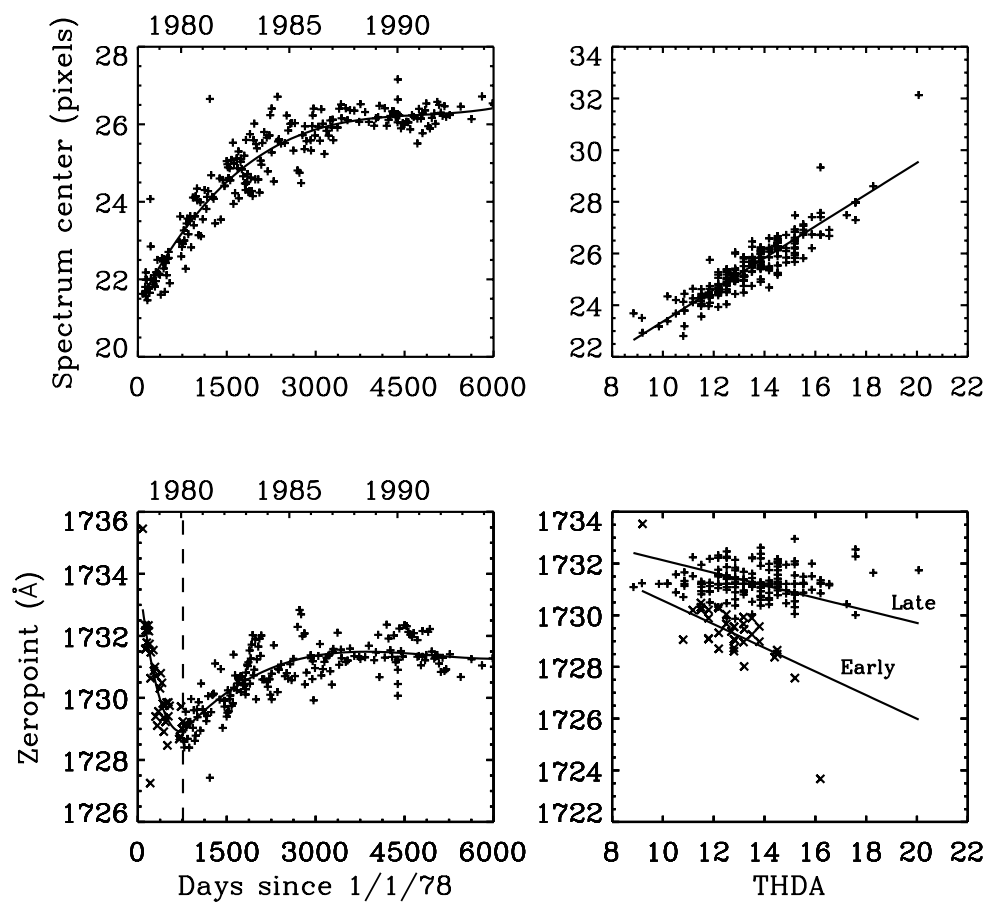


Figure 8.3: Low-dispersion time and temperature correlations with wavelength and spatial zeropoints for the LWR camera (ITF A).

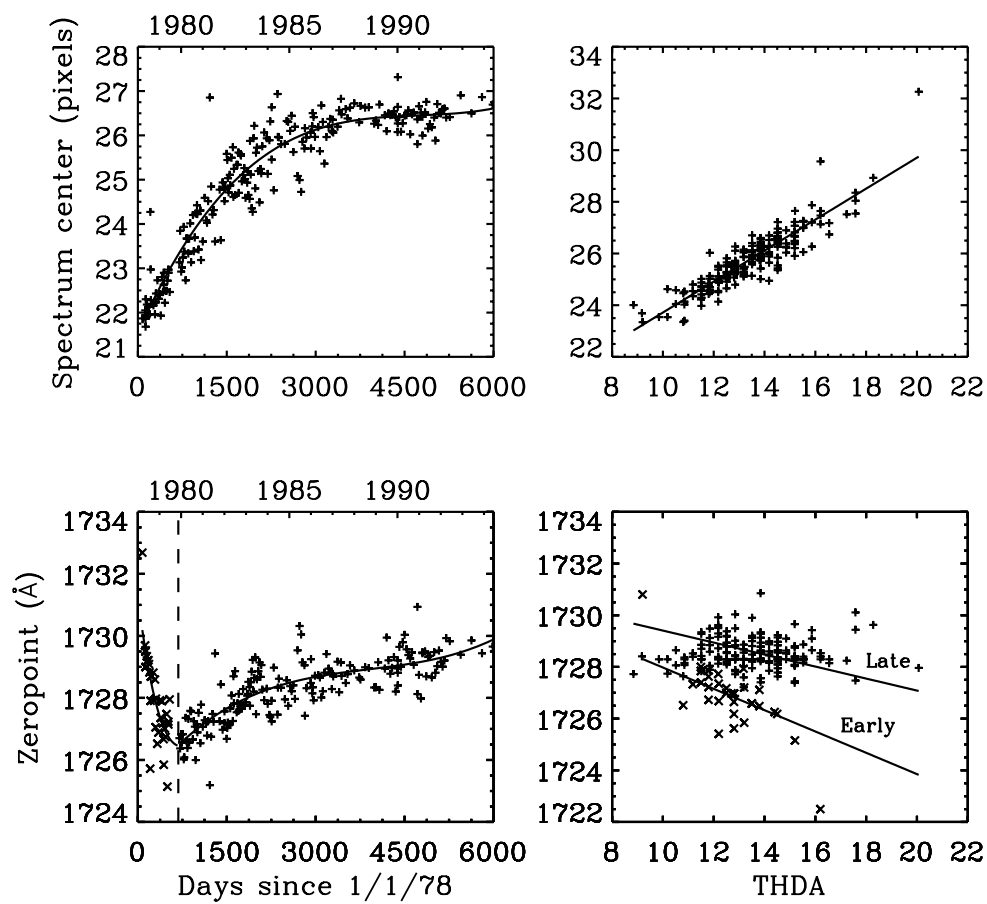


Figure 8.4: Low-dispersion time and temperature correlations with wavelength and spatial zeropoints for the LWR camera (ITF B).



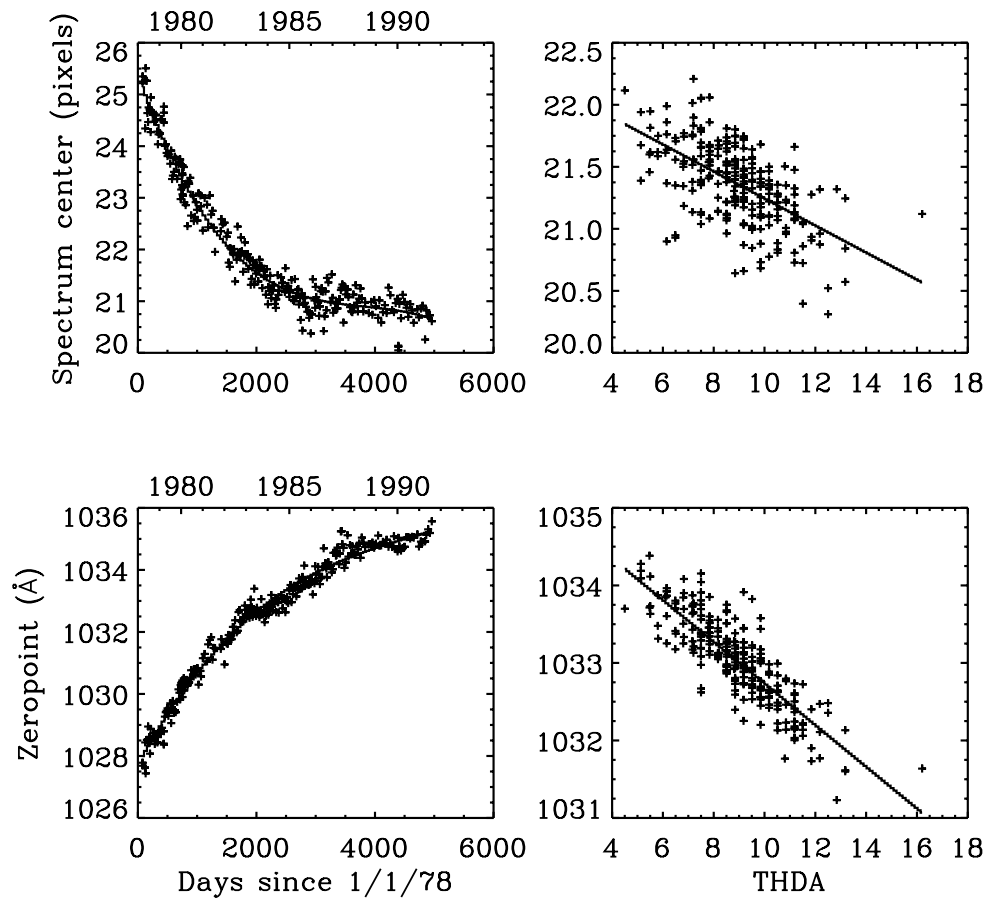


Figure 8.5: Low-dispersion time and temperature correlations with wavelength and spatial zeropoints for the SWP camera.

## 8.3 High-Dispersion Wavelength Calibration

### 8.3.1 Parameterization of Dispersion Relations

The separation of the echelle orders in the spatial direction by the cross-disperser complicates the calculation of the wavelength parameterization of high-dispersion IUE spectra. NEWSIPS departs from IUESIPS in seeking a 1:1 correspondence between dispersion parameters and physical properties of the spectro-optical system. The goal of such a representation is to identify each term with optical properties of the spectrograph and to prevent these physical effects from introducing cross-terms that could complicate the estimate of errors in the wavelength solution (for a full discussion of this concept, see Smith 1990a, 1990b). In the raw geometry this is not possible because the rotation of the order produces a correlation of the line and sample positions for a wavelength. For low-dispersion images this problem is largely solved by de-rotating the image. In the high-dispersion geometry the dispersion axis is also dependent on the echelle order: the precise angle is equal to the tangent of the dispersing powers of the echelle and cross-dispersing grating. Because this factor varies as  $1/m_{ech}$ , the dispersion axis slowly rotates and produces a splaying of the orders (see Chapter 7.3.1). In order to place all echelle orders along a common pseudo-dispersion axis, the order-splaying is removed as part of a single resampling step in the *GEOM* module. This removes the second and last of the important cross-coupling terms between the two axes in the original raw space. Thus the *GEOM* resampling forces the echelle orders to fall along a common *sample* axis ( $s$ ) and to be separated by a difference in *line* positions ( $l$ ) on the high-dispersion SI. This operation produces a small tilt of a monochromatic image on an order which is usually ignored because its effect on the spectral instrumental profile is small.

The representation of the dispersion parameters in the rectilinear ( $s, l$ ) high-dispersion SI geometry can be expressed as a Taylor expansion of the grating equation in terms of the quantity  $m_{ech}\lambda$ . The equations for the dispersion solution for sample and line positions are:

$$s = A_1 + A_2(\lambda m_{ech}/m_{Xdisp}) + A_3(\lambda m_{ech}/m_{Xdisp})^2 + \dots, \quad (8.1)$$

$$l = B_1 + B_2(\lambda m_{Xdisp}/m_{ech}) + B_3(\lambda m_{Xdisp}/m_{ech})^2 + \dots, \quad (8.2)$$

where the  $m$ 's refer to the order numbers for the echelle and cross-dispersing gratings ( $m_{Xdisp} = 1$ ) and the  $A$ 's and the  $B$ 's are constants to be determined empirically. The relations in Equations 8.1 and 8.2 represent an orthogonal system (i.e., each of the factors is decoupled from the others).

In practice higher-order terms in the Taylor expansion of the dispersion solution are small for the IUE gratings and need not be considered. However, the quadratic term is still significant for the IUE grating geometry (Smith 1990a, 1990b). Furthermore, although the cubic and quartic terms are not significant in the Taylor expansion of the grating equation, such terms *do* arise from the electro-optical distortions within the IUE cameras. These high-order terms (quadratic, cubic, and quartic) have been determined empirically as a function of echelle order and incorporated within the *GEOM* module as additional terms, as in the linearization process performed in low dispersion (Chapter 8.1). The result of these *GEOM*

corrections is an SI with very nearly linear relation between wavelength and sample position in each order.

### 8.3.2 Calculation of the Dispersion Coefficients

As is the case in low dispersion, each set of high-dispersion WAVECAL images is processed to provide the relation between wavelength and pixel position. The analytic method is also the same multi-step process as used in low dispersion; it simply has been expanded to include a group of echelle orders rather than one single order. The high-dispersion line libraries are based on an updated set of Pt-Ne line positions measured by Sansonetti et al., (1992) at the NIST. The line positions for all cameras, and therefore the dispersion solutions, are expressed in *vacuum* wavelengths.

The linear mapping of high-dispersion images from pixel space to Ångströms was carried out with the *IRAF* routine *identify*. This task identifies the emission lines for a single order in a reference WAVECAL spectrum and generates a dispersion solution which is a one-dimensional fitted function (Chebyshev polynomial) of wavelength versus pixel number. The next step involves the use of the *IRAF* task *reidentify* which maps the reference-image Chebyshev solution derived from the *identify* step to an ensemble of images. The final dispersion solution for a given order is averaged from several hundred individual solutions output from *reidentify* and consists of a starting wavelength and wavelength increment per pixel. This process is repeated for every order to yield a set of order-by-order solutions.

Some orders, particularly those at the shorter wavelengths, have too few Pt-Ne lines in the WAVECAL spectra for valid individual dispersion solutions. In these cases the *IRAF* tasks *ecidentify* and *ecreidentify* were used to determine two-dimensional dispersion solutions (as a function of wavelength and order number versus pixel) for a specified block of orders; thus the Chebyshev solutions for these orders are coupled. The types of *IRAF* solutions used for the wavelength linearization and the time and temperature correlation steps are listed in Tables 8.5 and 8.6. The block solution simultaneously solves for three contiguous orders and is applied only to the central order of the block. The global solution solves for all orders and usually is utilized only (with the exception of the LWR) for the higher orders.

Table 8.5: *IRAF* Solutions Used for the Wavelength Linearization Step

Method	LWP	LWR	SWP
Order by Order	69,70,72, 73,75–102	67,72,73,75–82, 85–96,98	66–101
Block	71,74	71,97,99	
Global	103–127	68–70,74,83, 84,100–127	102–125

Table 8.6: IRAF Solutions Used for Time and Temperature Correlation Step

Method	LWP	LWR	SWP
Order by Order	69,70,72 73,75–109	67,68,71,73, 75,76,78–82	66–101
Block	71,74	72,77,93–99	
Global	110–127	69,70,74,83, 84,90,100–127	102–105

### 8.3.3 Time and THDA Dependence of the Wavelength Zeropoint

Once the mean dispersion solutions were derived from typically several hundred images, the wavelength zeropoint motion was determined as a function of time and THDA. Mean time- and THDA-dependent coefficients were determined, as in low-dispersion, permitting predicted zeropoint shifts (one value for each order of an image) to be evaluated from these relations. Typically fourth-order polynomials are used to represent the variation in the wavelength system as a function of time, while the THDA dependence is represented by a linear function. The time- and THDA-predicted zeropoint shifts in the wavelength direction are applied to every image. The time- and THDA-predicted zeropoint shifts in the spatial direction are applied *only* in cases where empirically-measured registration shifts cannot be successfully determined by the order registration algorithm within the *RAW\_SCREEN* function (see Chapter 4.9).

### 8.3.4 Checks Against Other Calibrations

A check of the SWP high-dispersion wavelength calibration was made against the *Copernicus* satellite wavelength system for the standard B0.2  $\tau$  Scorpii with representative large-aperture images. This check showed a zeropoint offset of  $-4$  km/s with respect to the *Copernicus* system for typical images; no trend with wavelength was found. The estimated errors in the IUE wavelengths as measured from these  $\tau$  Scorpii observations were  $\pm 5$  km/s per line.

### 8.3.5 Pertinent Spectrograph Parameters

Table 8.7 contains further spectrographic lay-out and design information which has bearing on spectroscopic behavior for the three *IUE* cameras. The echelle grating and cross-disperser parameters are taken from Boggess et al. (1978), Evans (1975), and the IUE System Design Report (1976). These values are believed to be accurate, except that there is evidence that the effective focal lengths of the cameras were modified by several percent during the instrument assembly and testing stages.

The approximate wavelength ranges for each order are listed in Table 8.8. These values

Table 8.7: IUE Spectrograph Parameters

Parameter	LWP	LWR	SWP
Wavelength Range ( $\text{\AA}$ )	1808–3359	1810–3456	1097–2097
Order Range	69–127	67–127	66–125
Abs. Calib. Wavelength Range ( $\text{\AA}$ )	1850–3350	1850–3350	1150–1980
Abs. Calib. Order Range	69–125	69–125	70–120
Coll. Focal Length (mm)	950	950	950
Cam. Focal Length (mm)	684	684	684
Coll.-to-Cam. Angle (deg.)	20.42	20.42	20.37
Image Scale ( $\mu\text{m pix}^{-1}$ )	36.4	36.4	35.7
X-Disp. Ruling Freq. ( $\text{gr mm}^{-1}$ )	241.50	241.50	369.233
X-Disp. Order	1	1	1
Ech. Ruling Freq. ( $\text{gr mm}^{-1}$ )	63.207	63.207	101.947
Ech. Blaze Wavel. ( $\mu\text{m}$ )	23.19	23.19	13.76
Ech. Blaze Angle $\beta$ (deg.)	48.126	48.126	45.449
Ech. Grating Angle $\phi$ (deg.)	0	0	0

will vary by several tenths of an Ångstrom due to the global shifts in the location of the spectral format as a function of time and THDA.

A few remarks concerning the spectrographic elements:

- the collimator mirror is an off-axis paraboloid,
- the camera mirror is ruled as the cross-dispersing element,
- the echelle grating operates in a Littrow mode,
- the separation of the incoming and outgoing rays at the grating is achieved in the direction perpendicular to the dispersion (i.e, the echelle operates in an “over-under Littrow mode”),
- differences in the dispersion caused by the angular separation between the large and small entrance apertures are  $<0.1\%$  and are not detectable.

Note finally that the wavelength coverage for the long wavelength cameras, particularly for the LWR, extends into the accessible range of ground-based instruments. The long-wavelength limits for absolutely calibrated fluxes for all three cameras is limited by the low-dispersion spectra impinging on the camera target ring.

Table 8.8: Approximate Wavelength Ranges for the Echelle Orders - continued on next page

Order No.	LWP		LWR		SWP	
	Large	Small	Large	Small	Large	Small
127	1808.9–1830.6	1809.9–1831.9	1811.6–1830.5	1811.5–1831.7		
126	1823.1–1845.2	1824.0–1846.7	1824.4–1845.4	1825.6–1846.7		
125	1850.0–1860.2	1850.0–1861.3	1850.2–1860.4	1850.0–1861.8	1098.1–1112.6	1097.3–1112.0
124	1852.0–1875.1	1853.1–1876.9	1853.3–1875.8	1854.5–1877.1	1106.8–1121.6	1106.0–1121.0
123	1866.8–1891.0	1867.9–1892.4	1868.3–1891.2	1869.3–1892.6	1115.7–1130.9	1114.9–1130.3
122	1881.9–1906.7	1883.0–1908.0	1883.2–1906.9	1884.4–1908.9	1124.7–1140.3	1123.9–1139.7
121	1897.3–1922.7	1898.3–1924.0	1900.0–1923.0	1901.2–1924.3	1133.8–1149.8	1133.1–1149.2
120	1912.8–1938.9	1913.9–1940.3	1915.8–1939.2	1915.4–1940.5	1150.0–1157.8	1150.0–1158.0
119	1928.7–1955.4	1929.7–1956.8	1930.0–1955.5	1931.3–1957.1	1152.6–1167.6	1151.7–1167.7
118	1944.7–1972.2	1946.3–1973.5	1946.2–1972.6	1947.4–1974.0	1162.2–1177.6	1161.4–1177.7
117	1961.7–1989.2	1962.3–1990.6	1962.6–1989.6	1963.9–1991.0	1172.0–1187.7	1171.2–1187.8
116	1977.9–2006.6	1979.1–2008.0	1979.3–2007.0	1980.6–2008.4	1181.9–1197.8	1181.2–1198.1
115	1994.9–2024.2	1996.1–2025.6	1996.3–2023.9	1997.6–2026.1	1192.0–1208.5	1191.3–1208.6
114	2012.2–2042.1	2013.4–2043.5	2015.0–2041.7	2016.1–2044.0	1202.3–1219.1	1201.6–1219.2
113	2029.8–2060.4	2031.0–2061.8	2032.8–2060.8	2032.6–2062.2	1213.7–1230.1	1212.1–1230.1
112	2047.7–2079.0	2049.0–2080.4	2049.2–2079.4	2050.5–2080.9	1224.5–1241.0	1222.8–1241.1
111	2065.0–2097.9	2067.3–2099.3	2067.5–2098.4	2068.8–2099.8	1234.5–1252.3	1233.7–1252.4
110	2084.7–2117.1	2085.9–2118.5	2086.1–2117.6	2087.5–2119.1	1245.6–1263.7	1244.8–1263.8
109	2103.6–2136.7	2104.8–2138.1	2105.1–2137.2	2106.4–2138.7	1256.9–1275.4	1256.1–1275.5
108	2122.9–2155.5	2124.2–2156.7	2124.4–2157.2	2126.7–2158.8	1268.4–1287.3	1267.6–1287.4
107	2142.6–2175.6	2143.9–2178.3	2145.2–2177.5	2146.4–2179.0	1280.1–1299.4	1279.8–1299.5
106	2162.4–2197.6	2163.9–2198.9	2164.2–2198.2	2165.6–2199.7	1292.7–1311.7	1291.3–1311.8
105	2183.0–2218.7	2184.4–2220.0	2184.6–2219.4	2186.0–2220.6	1304.3–1323.6	1303.5–1324.4
104	2203.9–2239.9	2205.2–2241.5	2205.5–2240.9	2206.9–2242.3	1316.7–1337.1	1316.0–1337.2
103	2225.2–2261.8	2226.6–2263.5	2226.7–2262.8	2228.2–2264.2	1329.4–1350.2	1328.7–1350.3
102	2246.9–2284.0	2248.1–2285.4	2248.4–2285.1	2249.9–2286.6	1342.4–1363.5	1341.6–1363.6
101	2269.0–2306.6	2270.4–2308.0	2270.6–2307.5	2272.0–2309.0	1355.6–1377.1	1354.8–1376.8
100	2291.4–2329.8	2292.9–2331.3	2293.2–2330.6	2294.7–2332.6	1369.1–1391.0	1368.3–1391.1
99	2314.5–2353.4	2316.0–2353.2	2316.2–2353.5	2317.7–2355.0	1382.8–1405.0	1382.0–1405.3
98	2338.0–2375.6	2339.4–2379.0	2339.7–2378.9	2341.8–2380.5	1396.9–1418.9	1396.1–1419.7
97	2362.0–2402.1	2363.4–2403.7	2363.9–2403.5	2365.4–2405.1	1411.2–1434.3	1410.4–1434.4

Table 8.8: Approximate Wavelength Ranges for the Echelle Orders - continued

Order No.	LWP		LWR		SWP	
	Large	Small	Large	Small	Large	Small
96	2387.0–2427.2	2388.5–2428.7	2388.3–2428.6	2389.9–2430.3	1425.8–1449.4	1425.0–1449.5
95	2411.5–2452.7	2412.9–2454.3	2413.6–2454.3	2415.1–2455.9	1440.8–1463.2	1440.0–1464.9
94	2437.2–2478.8	2438.7–2480.4	2439.0–2480.5	2440.6–2482.1	1456.1–1480.5	1455.3–1480.6
93	2463.4–2505.4	2464.9–2507.0	2466.7–2507.2	2466.9–2508.3	1471.7–1496.5	1470.9–1496.6
92	2490.0–2532.6	2491.6–2534.2	2492.0–2533.6	2493.6–2536.0	1488.3–1512.7	1487.5–1511.9
91	2517.3–2560.5	2518.9–2560.5	2519.3–2562.2	2521.0–2563.5	1504.0–1529.7	1503.2–1529.8
90	2545.4–2588.8	2547.0–2590.4	2547.4–2590.5	2549.1–2592.3	1520.7–1546.8	1519.9–1546.9
89	2574.1–2617.8	2576.6–2619.4	2576.0–2619.8	2577.7–2621.4	1537.8–1564.4	1536.9–1564.5
88	2604.3–2647.4	2605.0–2649.0	2605.4–2649.5	2607.1–2651.2	1555.3–1582.3	1554.4–1582.4
87	2633.5–2677.7	2635.1–2679.3	2635.4–2680.0	2637.1–2681.5	1573.2–1600.6	1572.3–1600.8
86	2664.2–2708.6	2666.0–2710.2	2668.3–2711.0	2669.8–2712.6	1591.6–1619.4	1590.7–1619.5
85	2695.7–2740.6	2697.5–2742.0	2697.8–2742.9	2699.5–2744.5	1610.4–1638.6	1610.6–1636.7
84	2727.9–2772.5	2729.8–2774.1	2731.8–2775.3	2733.5–2777.0	1630.4–1657.0	1628.7–1658.0
83	2761.1–2805.8	2762.9–2807.5	2763.2–2808.4	2765.0–2810.2	1649.3–1678.5	1648.4–1677.8
82	2795.5–2839.3	2797.3–2841.3	2797.3–2842.3	2799.1–2843.0	1669.6–1699.0	1668.6–1669.5
81	2830.1–2874.2	2831.9–2875.9	2832.0–2877.3	2833.9–2879.1	1690.5–1719.8	1689.6–1718.9
80	2865.8–2909.7	2867.7–2911.3	2869.1–2912.9	2870.9–2914.6	1711.8–1741.2	1710.9–1740.3
79	2902.6–2946.0	2904.5–2947.6	2904.5–2949.2	2906.4–2950.7	1733.7–1763.0	1732.8–1762.0
78	2940.3–2982.9	2942.3–2984.6	2942.2–2986.3	2944.1–2988.0	1756.4–1784.9	1755.4–1784.3
77	2979.2–3020.7	2981.3–3022.3	2980.9–3024.6	2982.9–3026.5	1779.3–1808.2	1778.3–1807.1
76	3019.2–3059.5	3021.3–3061.2	3020.9–3063.6	3022.8–3065.4	1803.0–1831.6	1803.5–1830.5
75	3060.3–3099.4	3062.6–3101.2	3061.9–3103.7	3066.4–3105.7	1827.4–1854.6	1826.5–1853.7
74	3102.5–3140.3	3105.0–3142.1	3104.3–3144.9	3106.8–3146.8	1852.6–1880.2	1851.7–1879.2
73	3146.7–3182.0	3148.9–3183.4	3148.8–3187.4	3150.6–3189.3	1878.5–1905.4	1877.6–1904.2
72	3191.9–3224.6	3194.2–3225.5	3193.0–3230.0	3195.3–3232.1	1905.3–1931.2	1904.4–1930.0
71	3237.4–3267.0	3239.5–3268.9	3240.8–3273.4	3242.8–3275.8	1932.9–1957.7	1931.9–1956.5
70	3287.8–3311.7	3290.2–3312.6	3287.9–3318.3	3290.2–3320.4	1961.5–1980.0	1960.5–1980.0
69	3338.8–3348.2	3342.2–3349.9	3338.3–3350.0	3340.7–3349.9	1990.9–2012.4	1989.9–2011.2
68			3390.7–3410.0	3393.5–3411.4	2021.5–2040.7	2020.6–2039.3
67			3444.3–3456.5	3446.5–3458.7	2053.5–2069.2	2052.6–2067.6
66					2087.4–2097.7	2086.3–2096.1

## 8.4 *TTDC* Output

The *TTDC* module does not generate any output data products (i.e., FITS file). Instead it produces a temporary (internal only) file which contains various spatial- (in the case of low dispersion) and wavelength-dependent parameters that are used by subsequent processing modules (e.g., *GEOM*).

### 8.4.1 Low-Dispersion

The *TTDC* module writes the following information to the HISTORY portion of the low-dispersion image label:

- THDA used for correcting dispersion constants,
- date of observation used for correcting dispersion constants,
- degree of time-dependent polynomial fit,
- degree of THDA-dependent polynomial fit,
- zeropoint correction in Ångstroms, and
- spatial correction in pixels.

### 8.4.2 High-Dispersion

The *TTDC* module writes the following information to the HISTORY portion of the high-dispersion image label:

- THDA used for correcting dispersion constants,
- date of observation used for correcting dispersion constants,
- zeropoint correction in Ångstroms for each order,
- spacecraft velocity vector,
- Earth velocity vector,
- net (spacecraft + Earth) correction vector to heliocentric velocity, and
- heliocentric velocity correction in kilometers per second.



## Chapter 9

# Low-Dispersion Flux Extraction (*SWET*)

Spectral data are extracted from the two-dimensional (2-D) low-dispersion resampled images (SI) using a signal weighted extraction technique (*SWET*). This technique provides an increase in the signal-to-noise ratio (S/N) of the extracted spectrum, as compared to simple “boxcar” extractions, by utilizing information on the cross-dispersion spectral profile, while preserving the total flux. The output of this technique also includes an error estimate associated with each point in the extracted spectrum and cosmic ray hits are, in many cases, automatically rejected from the calculation of extracted fluxes. The technique, which has been developed for low-dispersion IUE data, is based on the weighted slit extraction code originally developed by Horne (1986) for use with optical CCD data. A detailed explanation of the adaptation of this software for use with IUE data processed using IUESIPS is given by Kinney et al., (1991) who supplied the software to the IUE Project. Various threshold values in the code were modified by the IUE Project to account for the very different flux scales of NEWSIPS and IUESIPS.

Briefly, the processing steps involved in the weighted extraction of a one-dimensional (1-D) spectrum from the low-dispersion SI are as follows:

- The background flux as a function of wavelength in the low-dispersion SI is characterized by a sixth-order Chebyshev polynomial.
- The spectral signal is located within the image and the average signal strength is evaluated in order to determine whether or not a spectral profile can be computed empirically.
- If there is sufficient signal strength, the cross-dispersion instrumental flux profile is derived for each wavelength sample. A default profile shape is used for spectra that are too faint to allow an empirical determination.
- The cross-dispersion profile is used in combination with a model of the detector noise characteristics to identify anomalous data points which are to be excluded from the

computation of extracted fluxes.

- The good data points are weighted according to their positions on the cross-dispersion profile and according to their relative noise in order to calculate the total net flux and its associated one-sigma uncertainty at each wavelength sample.
- A 1-D  $\nu$  flag spectrum is calculated to show where flagged pixels may have precluded the calculation of a reasonable flux value.

## 9.1 Noise Models

Two portions of the low-dispersion extraction procedure rely upon an estimate of the detector noise in order to perform their functions. First, the cross-dispersion profile fitting routine utilizes the estimated S/N of each wavelength sample in order to calculate appropriately weighted spline fits to the data. Second, the extraction procedure uses the noise model information to derive an error estimate for each point in the extracted spectrum. The noise models are derived empirically for each camera by measuring the scatter in the flux numbers (FN) around the mean FN in the background regions of several hundred science and flat-field images taken at a variety of exposure levels. Since the sigma as a function of FN is wavelength-dependent, the analysis is performed within 20 equal-sized wavelength bins ( $\sim 54\text{\AA}$  wide for the SWP and  $\sim 85\text{\AA}$  wide for the long-wavelength cameras) in the low-dispersion SI. For each wavelength bin the standard deviation in FN versus mean FN is represented by a third-order polynomial. The wavelength-dependence of the four coefficients of this polynomial are then each represented with a third-order polynomial to allow a determination of the expected standard deviation of any pixel given its wavelength and observed FN.

## 9.2 Background Flux Extraction

The background flux that is present in IUE images is composed of contributions from several sources, including the null pedestal, particle radiation, radioactive decays within the detector phosphor, halation within the UV converter, background skylight, and scattered light. The integrated effect of the last three sources varies in a complicated manner across the target depending on the spectral flux distribution of the object observed, whereas the general radiation and null components vary slowly across the vidicon tube. In practice, the average background flux in the low-dispersion SI is computed within two regions on either side of the spectrum and this average flux as a function of wavelength is fitted with a sixth-order Chebyshev polynomial.

The two background regions that are examined are each 7 pixels wide and, for large-aperture data, begin at a distance of 13 pixels from the predicted center location of the spectrum. For small-aperture data the two regions begin at a distance of 8 pixels from the center of the spectrum (see Figure 9.1). The narrow large-aperture extraction region

corresponds to the 13-pixel point source slit height, while the broad region is the 23-pixel extended, trailed, multiple, and flat-field source slit height. The entire wavelength space of the low-dispersion SI is included in the analysis. Before calculating the average flux as a function of wavelength for each of the two regions, each spatial image line within the two regions is examined individually in order to identify flagged pixels. The FN values of flagged pixels are temporarily replaced with the FN value of the closest unflagged pixel. Telemetry dropouts in the background regions are identified during this process and  $\nu$  flag values of  $-4$  are set in the output 1-D flag spectrum as well as retroactively set in the 2-D low-dispersion resampled flag image. This flag replaces the original value of  $-8192$ .

At this point a difference spectrum is computed from the average FN as a function of wavelength for each of the two background regions. This difference spectrum is used to detect the presence of cosmic ray hits that may occur in either of the two regions. The Chebyshev polynomial that will be fitted to the background data is sensitive to broad features such as grazing cosmic ray hits. Since we are only concerned with relatively broad features, the difference spectrum is smoothed with a 7 pixel wide boxcar function. The mean and standard deviation of the smoothed difference spectrum is then computed and any pixel locations that deviate by more than  $2\sigma$  from the mean have their weights for the polynomial fitting step set to zero. All remaining good pixel locations are given equal non-zero weights in the polynomial fit. Pixel locations that are beyond the long-wavelength edge of the camera target area are also excluded from the polynomial fit. Once the Chebyshev fit has been calculated, the values in the 1-D background spectrum that correspond to locations outside the camera target area are replaced with the fitted value of the last valid pixel.

### 9.3 Spectrum Location and Signal Level

The location of the spectrum in the low-dispersion SI (in the cross-dispersion direction) is found by computing the wavelength-averaged flux-weighted centroid of the background-subtracted flux levels within a search region that is centered on the predicted spectrum location. For SWP images the region of the low-dispersion SI below  $1233\text{\AA}$  is excluded from this calculation so as to avoid contamination from geocoronal  $\text{Ly}\alpha$ . If insufficient signal exists from which to determine reliably a location for the spectrum, the predicted center position is used instead and a warning message to this effect appears in the processing history log.

If the spectrum centroid can be determined empirically, then the dispersion line that contains the maximum net flux (summed over wavelength) is also determined and is referred to as the spectrum peak location. The wavelength-averaged net flux of this dispersion line is computed and compared against the threshold value of 5 FN in order to determine whether the spectral signal is strong enough to attempt an empirical profile fit. For the SWP camera, the region below  $1233\text{\AA}$  is excluded from this computation so as to avoid contamination from geocoronal  $\text{Ly}\alpha$ . If the image is processed as a point source, then a warning message appears if the location of the spectrum peak is found to be more than one image line away from the spectrum centroid, since this may indicate that the spectrum is not characteristic of a point source but rather may be spatially extended.

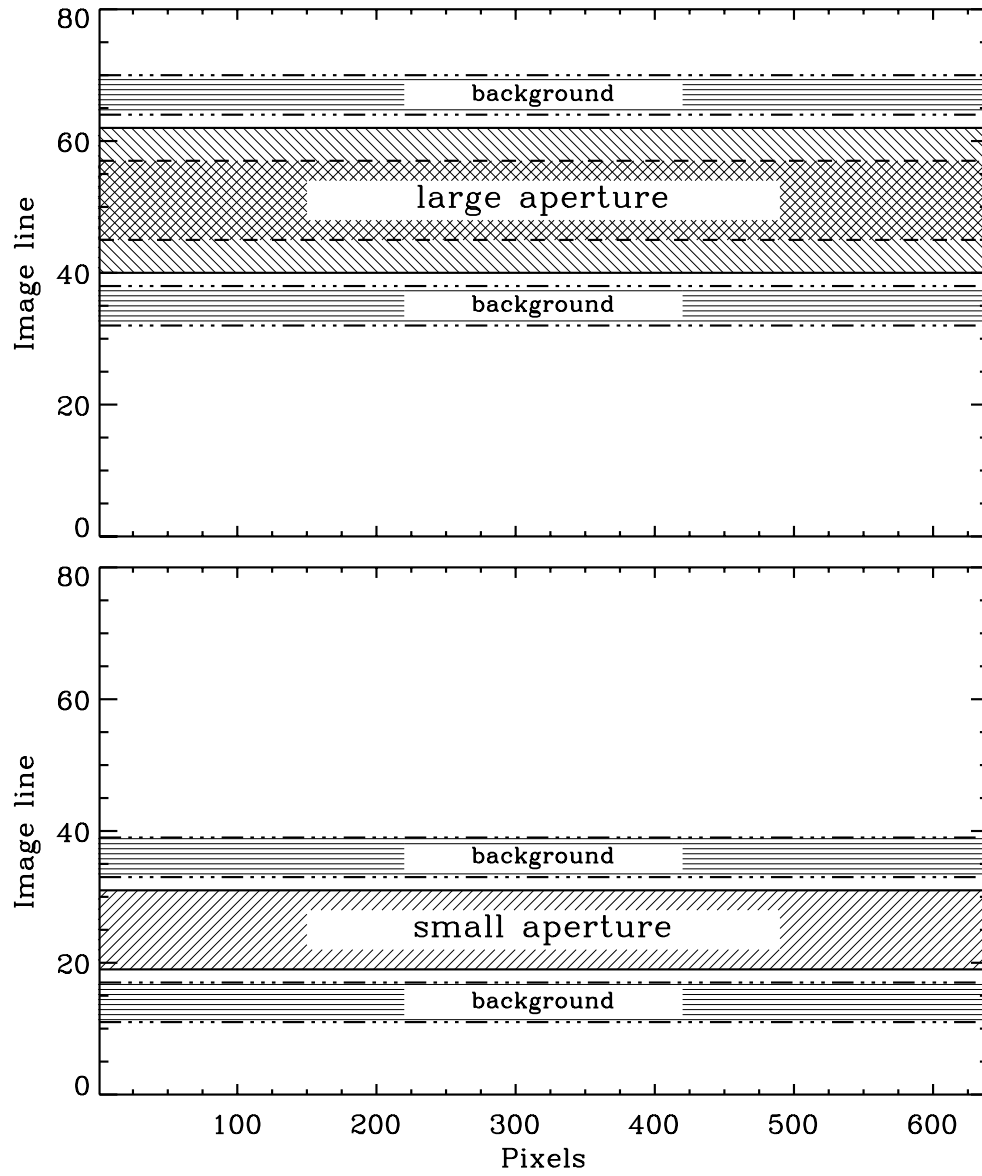


Figure 9.1: Locations of the extraction and background fitting regions within the low-dispersion SI.

If the average FN of the peak line of the spectrum is below the threshold value, then an empirical fit is not attempted. Instead, a default profile shape is used to compute the extracted fluxes. There are three default profiles for point sources, one for each camera. Each default profile has been derived from well-exposed observations of IUE standard stars, by averaging the profile fits for these observations over wavelength and renormalizing, thus producing a profile that is constant in wavelength. Since the spectral profile for IUE data is not repeatable from image to image, this average profile provides a rough weighting that is useful in very low signal images and provides a lower noise spectrum than attempting to fit the profile from the image. For extended and trailed sources, the default profile has a boxcar-like shape where all spatial image lines receive equal weights. Warning messages appear in the processing history log when a default profile is used.

A warning message is also issued if the location of the spectrum centroid is found to be more than two image lines away from the predicted spectrum center. This situation may arise if the location of the spectral format within the raw image space does not follow, for whatever reason, the normal behavior of the spectral format as a function of time (observation date) and camera temperature (THDA) as may be the case for objects poorly centered in the aperture. If this is the case, then the time and temperature-corrected dispersion constants that are computed for this particular image may be called into question. Note, however, that this warning only indicates that the location of the spectrum in the cross-dispersion (i.e., spatial) direction has been found to be unusual. We have no information as to whether or not a similar shift may have occurred in the dispersion direction of the image.

The search for the spectrum center and the determination of the average peak FN is skipped entirely for images classified as flat-field (i.e., nulls and other floodlamp only images), since they contain no spectral data. In this case the predicted spectrum center location and the default profile for extended/trailed sources are used to perform the computation of extracted fluxes.

## 9.4 Profile Fitting

The cross-dispersion profile is determined from the background-subtracted net flux data. Each line of data in the low-dispersion SI that is contained within the spatial limits of the extraction slit (13 lines for point sources, 23 lines for extended, trailed, multiple, and flat-field sources) is temporarily binned in wavelength according to the S/N, with bin sizes typically ranging from 1 to 10 pixels. A warning is issued if the bin size exceeds 4 pixels since this may indicate either weak or noisy spectral data or that a large fraction of the data is unusable due to conditions such as saturation or telemetry dropouts. The area under the cross-dispersion profile at each wavelength bin is then normalized to one to divide out the spectral information. After normalizing, the fraction of flux in each line of data (relative to the total flux in each wavelength bin) is smoothed by fitting splines with anywhere from 2 to 15 nodes in each line.

The number of spline nodes is determined dynamically based on the total of the square of the S/N of the spectral data. The placement of the nodes in wavelength space is also

determined dynamically so that the data located between each pair of nodes have an equal total of  $(S/N)^2$ . Thus regions of higher S/N have more spline nodes placed more closely together than regions with lower S/N. All lines of data in the cross-dispersion direction use the same number and placement of spline nodes and there is always a minimum of two nodes placed at either end of the spectrum. However, when only two spline nodes are used, the spectral data is fitted with a default extraction profile. The spline fits for each line of data are computed iteratively, rejecting data bins that have residuals to the fit greater than  $3.5\sigma$ . The iteration cycle ends when no new bins are rejected.

In the procedure outlined above, those wavelength bins that have negative or zero total flux are rejected from the computation of the spline fits. If bins on either end of the spectrum are rejected, they are replaced by the average fraction of light values for the last 10 good bins closest to the end. This is done to avoid extrapolation of the high order spline fits into wavelength regions that have no constraining data. Rejected bins that are not at either end of the spectrum but are located in the interior of spectrum are simply excluded from the computation of the spline fit and are therefore essentially interpolated over. This extrapolation/interpolation process provides a means of dealing with discontinuous data.

The cross-dispersion profile at each wavelength sample is constructed by evaluating the spline fits, clipping the negative values that may occur in the wings of the profile, and renormalizing to ensure a sum of unity at each wavelength. Thirteen spline fits (one for each of the 13 lines of the low-dispersion SI containing source flux) are used to specify the cross-dispersion profile for point source data, and likewise 23 are used for extended, trailed, or multiple sources. This profile is used when computing the extracted fluxes to weight the data so that the pixels with the largest fraction of light are given the most weight. Because the profile is derived by spline fitting each spatial line of data independently of other lines, a wide variety of profiles can be accommodated. Specifically, the algorithm is very capable of handling spectra obtained through either the large or small spectrograph apertures, trailed sources, and extended objects with complicated source structures which may cause the profile to vary dramatically as a function of wavelength. However, because the algorithm produces a single output spectrum, spectra of several sources in the aperture (multiple spectra) will not be separated. Such images will require custom extraction.

## 9.5 Extraction of Flux and Cosmic Ray Removal

The computation of the extracted flux and corresponding identification and rejection of bad pixels is performed iteratively. The total flux at each wavelength is found by performing a weighted sum of all “good” (see next paragraph) pixels at the given wavelength according to:

$$FN_{total} = \frac{\sum FN(i) \times p(i)/\sigma(i)^2}{\sum p(i)^2/\sigma(i)^2}$$

where  $FN(i)$  is the net flux of the  $i^{th}$  spatial pixel at this wavelength, and  $p(i)$  and  $\sigma(i)$  are the corresponding profile and estimated noise values for that pixel. Similarly, the estimated

error in the extracted flux is:

$$error(i) = \sqrt{\frac{1}{\sum p(i)^2 / \sigma(i)^2}}$$

which is hereafter referred to as the “sigma” spectrum. Because the sum of the profile values is involved in the calculation of the total flux, individual bad pixels can be excluded from the sum so that a reliable estimate of the total flux can be obtained based on only the remaining good pixels.

At the outset of the extraction process, “good” pixels are those with  $\nu$  flags greater than  $-256$ . Hence, pixels which have been assigned  $\nu$  flags of  $-256$  or more negative by the earlier processing stages are excluded from the extracted flux computation. However, pixels which were not flagged previously but which are found during the course of the extraction to have anomalously high FN values (hereafter referred to generically as *SWET* cosmic ray pixels) are also identified and excluded during calculation of extracted fluxes. This is accomplished by rejecting the most extreme outlying pixel at each wavelength sample if the value of that pixel is greater than a predetermined sigma level from the scaled profile at that wavelength. The threshold values for this rejection are  $6\sigma$ ,  $5\sigma$ , and  $4\sigma$  for the LWP, LWR, and SWP cameras, respectively. The rejection thresholds for each camera were determined empirically so that most cosmic ray pixels are removed without removing good data points. When such a pixel is identified, it is assigned a  $\nu$  flag value of  $-32$  which is written back into the low-dispersion  $\nu$  flag image (SF). Each time a new cosmic ray pixel is identified and excluded, an updated value for the total flux at that wavelength is computed. This process is repeated until no more pixels are rejected or until less than 30% of the flux in the profile at that wavelength sample remains.

The total numbers of pixels excluded as bad because they had already been assigned  $\nu$  flags of  $-256$  or more negative before the extraction procedure and those excluded as cosmic ray pixels by this routine are reported to the processing history log. In the event that either of these values exceeds 10% of the total number of pixels available to the extraction process, a warning message is issued in the processing history log.

## 9.6 One-Dimensional $\nu$ Flag Spectrum

In deriving the 1-D  $\nu$  flag spectrum, the cross-dispersion profile and the flag values in the low-dispersion SF are examined. For each wavelength sample the contribution to the spectral profile from unflagged pixels is calculated. If this contribution amounts to at least 45% of the total flux (as represented by the associated profile values), the wavelength sample will contain no flags in the output spectrum. If less than 45% of the total flux in the profile is from unflagged pixels, then each flag value is examined individually to determine what fraction of the total contribution from all pixels is due to one particular flag condition. For each flag condition that affects pixels representing more than 15% of the spectral profile, that flag value will appear in the output flag spectrum.

Situations can exist in which the contribution by pixels with one particular flag condition account for 45% of the flux at a given wavelength, for example, and a second flag condition is associated with pixels that account for only 11%. Here the total contribution from flagged pixels exceeds the 55% threshold, but only the flag value corresponding to the first condition will appear in the output flag spectrum. The threshold values were determined empirically so that problem conditions that definitely have an adverse affect on the computation of extracted fluxes are always flagged in the output spectrum, while, at the same time, conditions that only have a marginal impact are not flagged. Note that in marginal cases where only one or perhaps a few pixels that contribute in a relatively minor way to the total flux at a given wavelength are flagged and hence excluded from the computation of the extracted flux, the associated error estimate for that extracted flux value will be increased accordingly even though no flags will appear in the output spectrum. Thus the sigma spectrum serves as an additional indicator of the relative accuracy of the extracted fluxes.

## 9.7 *SWET* Output

The main output data product produced during *SWET* is the low-dispersion merged extracted image FITS file (MXLO). The MXLO contains the net (background-subtracted) integrated flux spectrum, the Chebyshev characterized background spectrum, the  $\nu$  flag spectrum, the absolutely calibrated net flux spectrum, and the calibrated sigma spectrum stored in a FITS binary table extension. The net flux and background spectra are in units of FN, the flag spectrum is in the normal bit-encoded unitless values, and the calibrated flux and sigma spectra are in physical units of  $\text{ergs sec}^{-1} \text{cm}^{-2} \text{\AA}^{-1}$ . The sigma spectrum, originally computed in FN units, undergoes identical calibration steps (including all corrections for sensitivity degradation, etc.) as the net flux spectrum. Chapter 11 details the process of absolute flux calibration and camera degradation correction.

The background flux spectrum is scaled to the same integrated slit length as the net flux spectrum and is evaluated over the entire wavelength space of the camera target region contained in the low-dispersion SI (1050Å to ~2000Å for SWP and 1750Å to ~3400Å for LWP and LWR). The background values for pixel locations past the long-wavelength end of the camera target are replications of the last valid background value. The net flux and sigma spectra are computed over the entire wavelength space of the low-dispersion SI, but locations that are outside the camera target area will have net fluxes equal to zero because these regions do not contain any valid image data. The edge of the camera target areas are encountered at wavelengths greater than (approximately) 3395, 3425, and 2000Å for the LWP, LWR, and SWP cameras, respectively, for large-aperture spectra. Due to the curvature of the target boundary, small-aperture spectra reach the target edge at different wavelengths: 3380, 3400, and 2015Å for the LWP, LWR, and SWP cameras. The absolute calibrations are valid over wavelength limits of 1150–1980Å for SWP and 1850–3350Å for LWP and LWR. Beyond these limits the calibrated net flux and sigma spectra are set to values of 0 and  $-1$ , respectively and have a  $\nu$  flag value of  $-2$ . The valid wavelength limits of the calibrated spectra are consequently somewhat truncated as compared to the net flux



spectrum.

The *SWET* module writes the following information to the HISTORY portion of the image label:

- noise model version number,
- aperture-dependent extraction/calibration information:
  - predicted and found line positions of spectrum center, line position of the peak flux, and average peak FN,
  - cross-dispersion profile information (blocksize, total number of blocks, and number of rejected blocks),
  - number profile nodes and sigma rejection,
  - line position of profile centroid,
  - line numbers of flux extraction window,
  - pixel rejection threshold,
  - total number of extracted pixels, number of pixels rejected as cosmic rays, and number of pixels rejected as bad,
  - absolute flux calibration version number,
  - absolute calibration mode (i.e, point or trailed),
  - absolute calibration epoch,
  - camera rise time,
  - effective exposure time,
  - THDA of image,
  - reference THDA,
  - temperature-dependent sensitivity correction coefficient,
  - temperature correction factor,
  - time-dependent sensitivity degradation correction version number,
  - time-dependent sensitivity degradation correction mode,
  - sensitivity degradation calibration epoch, and
  - observation date.

# Chapter 10

## High-Dispersion Flux Extraction

### 10.1 Background Flux Determination (*BCKGRD*)

The determination of smoothed background fluxes is made using the high-dispersion resampled image (SI). A representative high-dispersion SI given in Figure 10.1 shows the echelle orders running horizontally and the spatial (cross-dispersion) direction running vertically. We will refer hereafter to the image sectors at the top and bottom as the “ends” of the image. The background extraction module (*BCKGRD*) produces smoothed background flux spectra which, together with the gross spectra, form the net spectra. The background model is created by computing continuous Chebyshev polynomial functions from pixels that sample valid background fluxes. *BCKGRD* models the backgrounds of images having continuum flux in two one-dimensional passes. For images with no continuum, the algorithm proceeds straightforwardly by sampling the neighboring interorder fluxes for each spectral order and fitting the result to a Chebyshev polynomial. In the sections below, the salient features of *BCKGRD* are described; this process is presented in greater detail in Appendix A.

#### 10.1.1 Pass 1: Cross-Dispersion Swaths

##### 10.1.1.1 Overview

For continuum source images, a series of 25 or 26 nearly equally spaced extraction swaths (slit height of 5 pixels) is made in the spatial direction of the high-dispersion SI, with a starting position at small spatial pixel numbers (short-wavelength end). Except for the first and last few Pass 1 swaths, which form short chords along the left and right edges of the camera image, each swath samples fluxes for nearly the entire range of sample positions; that is to say that they include pixels at the spatial ends of the camera which are not affected by contaminated interorder-overlap flux. The “interorder overlap” flux is described by a Point Spread Function (PSF) model described below. The accumulated effects of overlapping PSFs increase as the orders become more closely spaced. The accumulation causes the interorder overlap to become increasingly severe until the camera sensitivity falls off at short wavelengths. It is this overlap which causes local background extractions in IUESIPS to

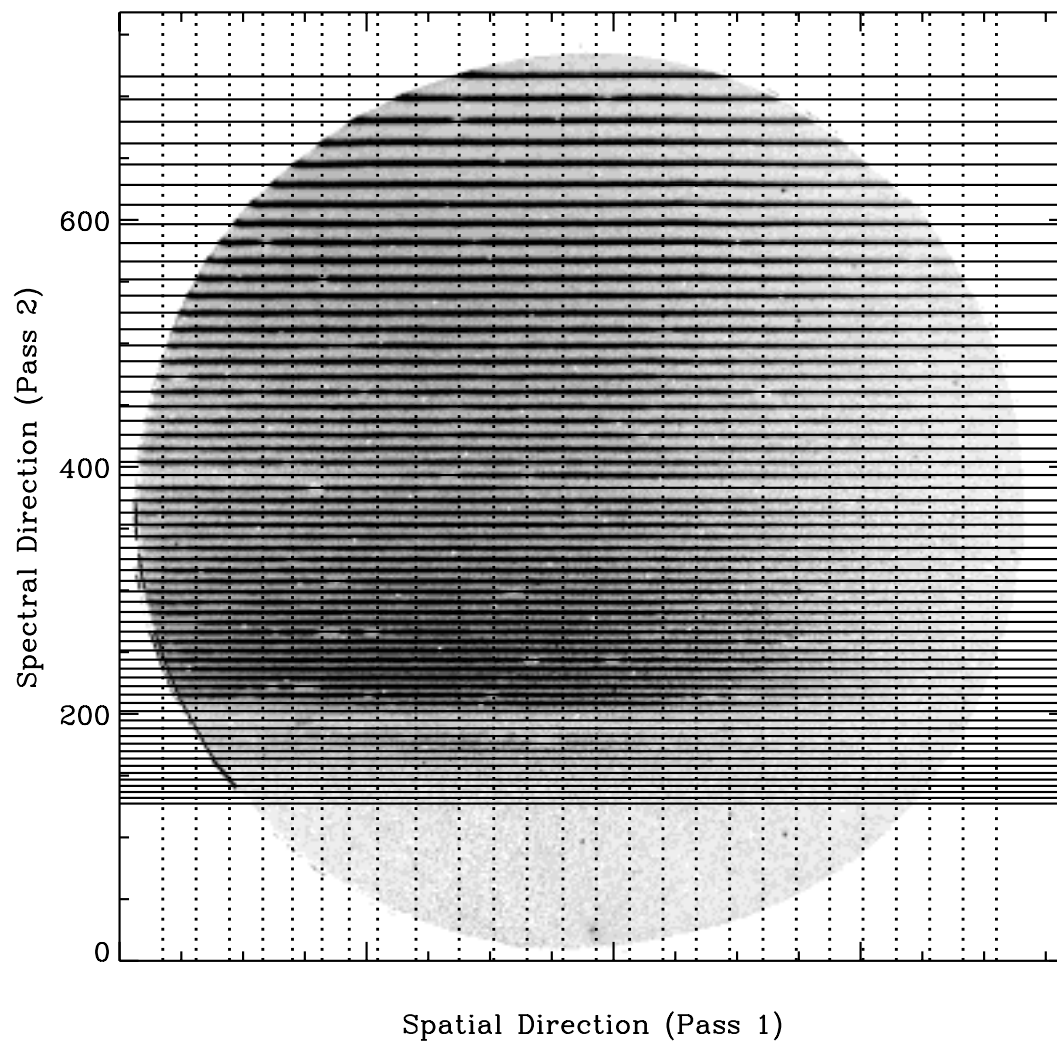


Figure 10.1: Layout of the background extraction swaths on a sample SWP high-dispersion image. Lines running in the vertical (spatial) direction are the Pass 1 extractions. The reconstructed background solutions created in Pass 2 are placed in the positions of the echelle orders (horizontal lines).

be systematically high for short-wavelength orders and which necessitated a strategy for *BCKGRD* to sample background fluxes from distant uncontaminated regions as well as local contaminated ones.

The fluxes sampled from interorder pixels in Pass 1 are modified if they are affected by contamination from neighboring orders. A model PSF provides an initial estimate of how much the fluxes should be offset before the Chebyshev fit is made. The PSF model itself consists of two components, first, a monotonically decreasing function out to about four pixels and, second, a “halation ramp” which extends from four to about seven pixels from the center of each order profile. Each of these components is responsible for order overlap in a particular range of echelle orders. We will refer to the image area where the monotonic portion dominates as the “Interorder-Overlap Region” (IOR). The halation component is actually an extension of the IOR. However, *BCKGRD* treats it separately because, unlike the IOR, its characterization is independent of the order profiles.

The IOR and halation-dominated portions of a Pass 1 swath are indicated in Figure 10.2 for an SWP image. The initially sampled interorder fluxes in both the IOR and the halation regions are revised downward during the course of the calculations. The original and revised “working” fluxes are shown in this plot as squares and small crosses, respectively, and the flux revision for one point is shown as a downward pointing arrow. The final Chebyshev solution for Pass 1 is shown in our example in Figure 10.2 as a continuous undulating line.

### 10.1.1.2 PSF Modeling Details

The estimate of the contamination of IOR and halation-ramp region fluxes by illumination from the spectral orders proceeds in two steps. Information from the PSF model and from the echelle order fluxes is not used in the first step, nor is a halation overlap region defined. The solution in this “Step 1” of Pass 1 is determined entirely from a Chebyshev interpolation from points in the end (non-IOR) regions of the swath. In the presence of certain image pathologies (described below), as well as for the first and last few Pass 1 swaths, this Step 1 is the only step; it becomes the final solution for the Pass 1 phase.

For the great majority of Pass 1 swaths (i.e., those passing through the middle of the camera image and not encountering poor statistical solutions) *BCKGRD* continues with a Step 2. This step uses the solution from Step 1 as a starting point to compute a PSF-compensated solution in which we attempt to subtract from the measured interorder fluxes the contamination from adjacent orders. Note particularly that there is no adjustment made to correct the *on-order* (gross) fluxes for such contamination.

*BCKGRD* uses the same trial spatial PSF model for all types of continuum source types in a given camera. The algorithm also assumes that the PSF is global over the image. The model was determined by replicating the accumulation of flux overlap toward short-wavelength orders from a large number of actual images.

The PSF may actually change from image to image. The algorithm attempts to accommodate such changes by using on-the-fly order information to refine the PSF model – specifically the slope of the  $\overline{nf\ nd}$  leg of the IOR triangle (see Figure 10.2). This is ac-

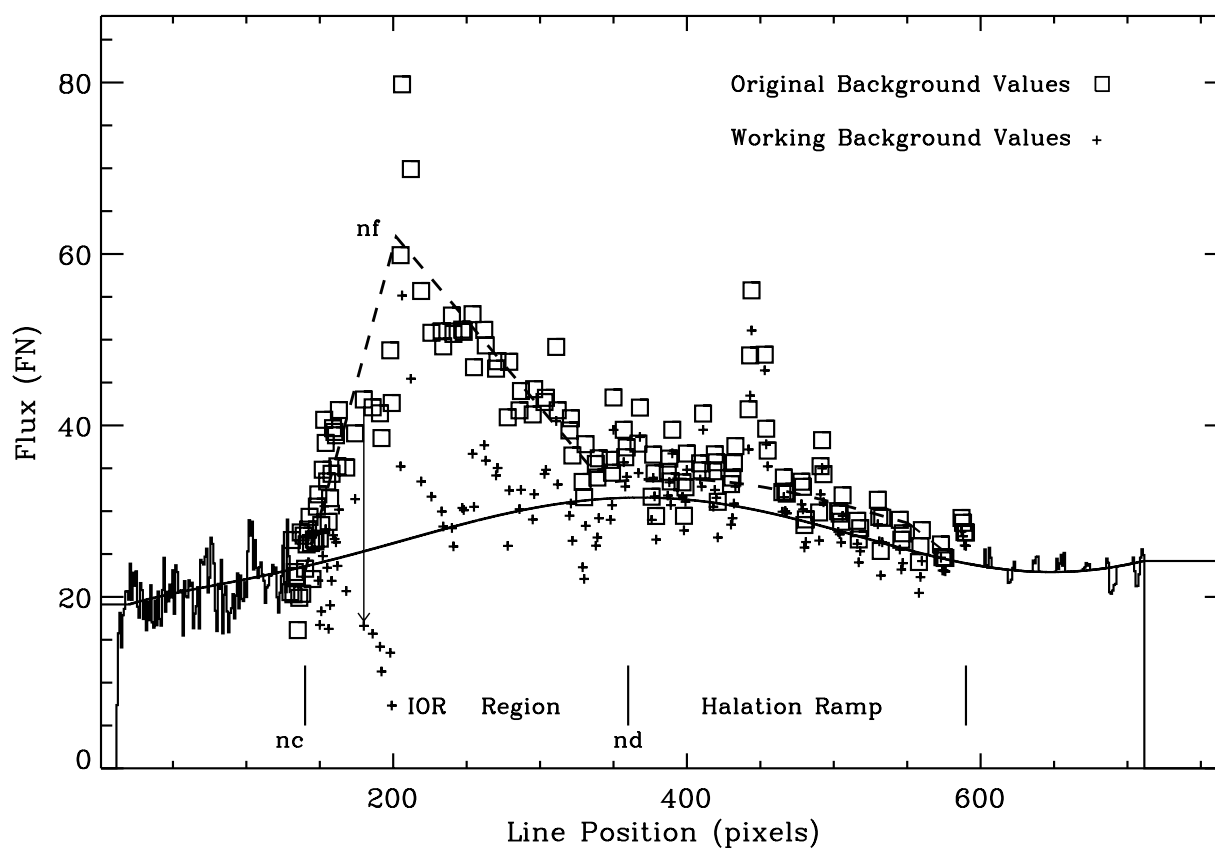


Figure 10.2: Crosscut of background fluxes from a central “Pass 1” swath through an SWP image. Stellar fluxes are off-scale in this diagram. The triangular area describes the local raw background fluxes in the Interorder-Overlap Region where order crowding is severe; the halation region is shown to the right. Small crosses denote the raw fluxes corrected for overlap by the PSF model. The solid line is the Pass 1 solution, a Chebyshev, degree-7 polynomial.

complished by comparing the observed fractional flux overlap with the model result for a reference order within the IOR, that is by comparing the increase in overlap for this order to the overlap found at the start of the IOR (pixel  $nd$ ). If the measured and model slopes agree within a tolerance factor ( $1.5\times$ ), the program adopts the measured slope and scales the model PSF accordingly. Otherwise, the model PSF is used. Tests show that various Pass 1 swaths for a given image can either pass or fail this tolerance test independently.

### 10.1.2 Pass 2: Dispersion Direction Swaths

In the second operation (Pass 2), inferred background fluxes at the order positions are sampled and assembled as arrays in the spectral direction: the fluxes from the Pass 1 solutions are used to compute a continuous Chebyshev solution for the background at each echelle order position. The generation of a fit along the positions of the echelle orders proceeds with the computation of a 7th-degree Chebyshev function interpolated for all wavelength positions. The Pass 2 operation tends to dilute the effects of poor solutions from a single Pass 1 swath. However, it also introduces a second smoothing into the final background surface.

Figure 10.3 shows a final solution obtained for Order 95 of image SWP20931 on the B0 star HD93222. This order contains a strong Lyman- $\alpha$  feature. The spike pattern indicates samplings from the 26 swaths in Pass 1. A comparison of the residuals (comb pattern in the figure) shows that the solution for the Ly $\alpha$  order is less certain than those for long-wavelength orders where uncontaminated background pixels are common.

### 10.1.3 Non-continuum images

The existence or absence of continuum flux in an IUE echellogram is determined by the order registration module (*ORDERG*). Because interorder-overlap flux can affect background determinations only for continuum images, in the noncontinuum case *BCKGRD* does not go through a Pass 1 step. The background estimates for these images are determined by sampling the interorder background on the long-wavelength side (spatial) of a given order with a one-pixel slit. A 7th-degree Chebyshev solution is then computed for this array of interorder pixels. Note that tests show that some minor contamination from strongly saturated emission lines has been detected in neighboring orders.

### 10.1.4 Data Pathology Assessments

Occasionally circumstances in the interorder fluxes lead to solutions that are slightly unstable, producing wiggles in an interpolated region that go beyond the flux range of sampled pixels at the two spatial ends of the camera. Such occurrences may be caused by abnormal conditions affecting the image (eg., target-ring glow, cosmic ray hits, LWR flare, and flux down-turns at camera edge). A series of eight “pathology tests” has been added to *BCKGRD* to protect against blind solutions at the end of Pass 1 which do not agree with simple and often correct interpolations (see Appendix A for full details). These checks generally rely on

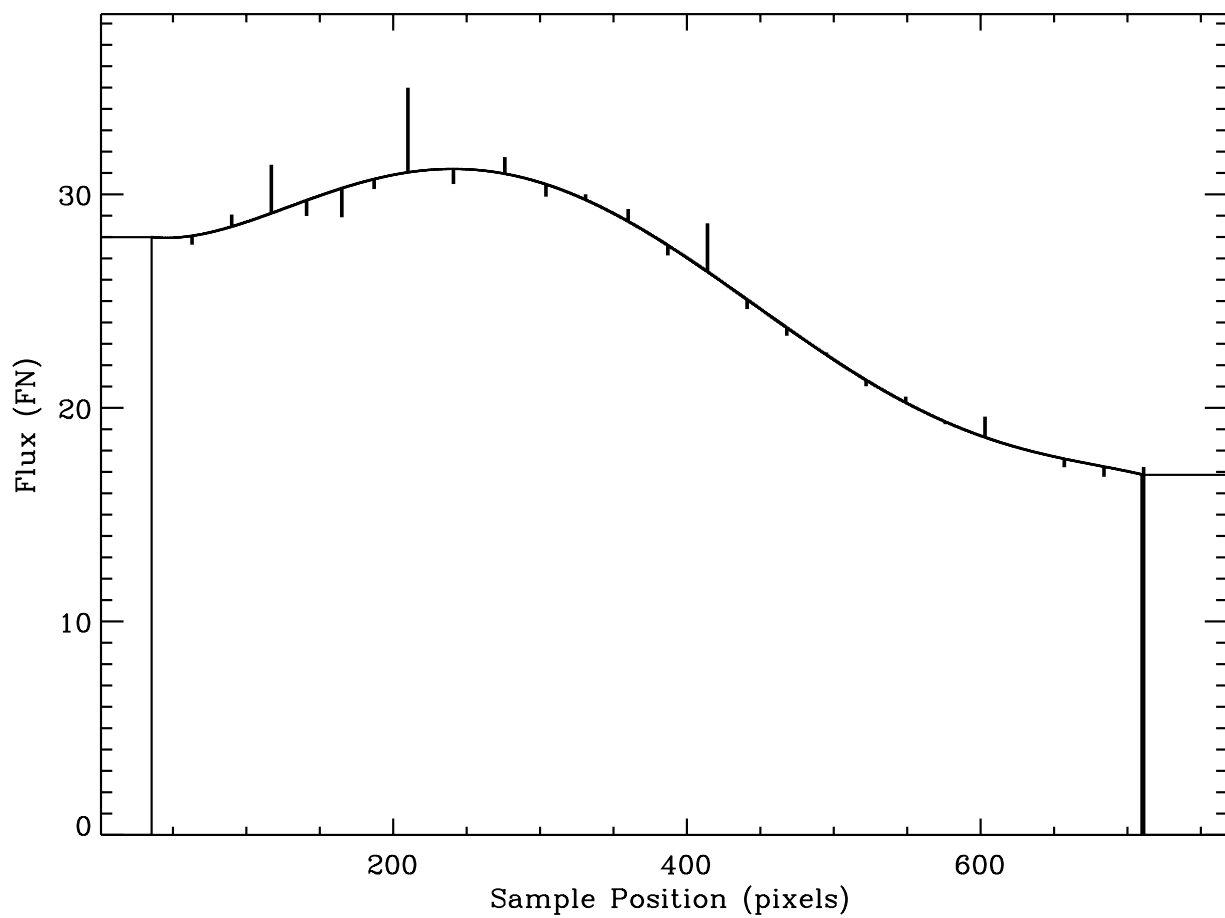


Figure 10.3: Final background solution for SWP20931, Order 95 (smooth solid line). The comb structure connected to the solution reflects the solutions for the various Pass 1 swaths sampled at the line position of this order.

a comparison of fluxes at two or more pixels along the swath or on a ratio of smoothed flux ranges. The rms statistic computed from local raw background fluxes is a convenient unit of measure for flux ranges because it does not rely upon source brightness, exposure time, or an arbitrary flux level. In most cases a failure of a solution in a pathology test causes either the PSF information not to be used in Pass 1, the degree of the polynomial fit to the interorder data to be reduced, or both. Lowering the fitting degree has the effect of removing extra wiggles in the solution; however, the degree of the Chebyshev fit is never reduced below 3. In those cases where superfluous wiggles in the IOR region persist stubbornly after a few trials, a simple linear interpolation is adopted between “good” regions. This may occur for spatial positions toward the short-wavelength (spatial) end of the IOR for certain swaths having reliable background samplings at the target edge. These tests are used only for continuum source images in Pass 1. Therefore, the final output background vectors from Pass 2 are still guaranteed to be pure continuous Chebyshev functions.

### 10.1.5 Failure Modes

The background swath fitting process is considered to fail if certain conditions apply pertaining to Pass 1 swaths (Appendix A). When this solution fails, the background solution is set to zero for the entire swath. If this occurs for an isolated swath, an interpolated solution from the two neighboring Pass 1 swaths is substituted for the original solution. If two consecutive Pass 1 swaths fail the background arrays for the entire image are set to zero and *BCKGRD* has “given up” on the image. This occurs for about 13 images in the GSFC high-dispersion archives, usually as a consequence of a major portion of the image being missing. This condition is documented in the processing history log.

### 10.1.6 Caveat

Tests have shown that high-dispersion spectra from each of the three IUE cameras have characteristics that impose unique challenges for automated background extraction algorithms. Examples of specific problems are given in Appendix A. The great diversity of image types in the archives prohibits implementing any strategy that makes assumptions about the behavior of source spectra in order to fix isolated background problems, particularly in an automated processing environment. Although the background-extraction algorithm generally provides a good background flux estimate, the results are not always optimal for particular regions of some images. A customized interactive determination of the background fluxes based on individual image characteristics may produce a more accurate estimate of the background in certain cases when data pathologies are present. If users wish to derive a customized background, they should first reconstitute the “gross” flux spectrum by adding the background vector to the net flux vector, multiply the customized vector by the conversion factor between the high-dispersion SI and merged extracted image (MX) fluxes ( $\text{slit\_length} \times 32.0$ ), and subtract this result from the gross spectrum. (In this example, the customized background vector is assumed to have been derived on the basis of a 1-pixel long slit.)



### 10.1.7 *BCKGRD* Output

The *BCKGRD* module writes the following information to the HISTORY portion of the image label:

- source type (i.e., point or extended) identification for interorder background points and
- background determination method (i.e., continuum or non-continuum) used.

## 10.2 Spectral Flux Extraction (*EXTRACT*)

The computation of high-dispersion net fluxes in NEWSIPS proceeds straightforwardly with a boxcar extraction. The input data consist of the high-dispersion SI, the high-dispersion resampled  $\nu$  flag image (SF), the background fluxes determined by *BCKGRD*, and the noise model file. The decision to extract the fluxes with a boxcar weighting scheme means that a rectangular extraction slit is used, giving equal weight to all included pixels except at the very ends of the slit, and that both flagged and non-flagged pixels are used. No attempt is made to exclude flagged pixels in the way that the *SWET* procedure does in low dispersion, because there is no modeling of the spatial profile in a boxcar extraction and hence no knowledge of the relative weight that a “bad” pixel ought to have within the extraction slit. To address the corruption of the flux at a given wavelength by a bad pixel(s) in the extraction slit, NEWSIPS provides a noise vector. This vector may be used as an inverse weight to evaluate the relative uncertainties of computed fluxes with wavelength.

Briefly, the processing steps involved in the boxcar extraction of a series of 1-D spectra (one for each order) from a high-dispersion SI are as follows:

- A 1-D cut across each order is made by extracting fluxes in the spatial direction with a broad swath.
- A centroid position is determined by fitting a gaussian profile to the spatial profile of each order above a locally-defined background level.
- Extraction slit limits are positioned around the centroid position of each order, with fractional begin- and end-line values defining the expected spatial (line-value) limits for capturing 98% of the total flux in the order. These slit heights are fixed functions of camera, source type (point or extended), and order number.
- For each wavelength in every order, the fluxes are summed between the begin- and end-line of the 98% integration limits.
- For each pixel summed across the order, a noise value is determined from the camera noise model.
- The procedure loops through all the echelle orders in this fashion.

### 10.2.1 Determination of Echelle-Order Locations

The key step in the extraction operation is the determination of the centroid of each echelle order to subpixel accuracy. In principle, the global shifting operation of *ORDERG*, the results of which are incorporated into the high-dispersion SI, accomplishes this same function, but this routine does not always provide the shifting accuracy needed (e.g., for images having weak continua and for extended sources). The input for this refined centroid operation is provided by the high-dispersion SI and SF, the high-dispersion noise model and a set of fiducial line positions for each order which are given in Table 10.1.

The centroid order positions in Table 10.1 were determined empirically for a collection of well-exposed images for each camera. In each case the separations of the initial determinations were compared with echelle grating theory (i.e., they should vary as  $1/m_{ech}^2$ ). The final positions show smooth undulating departures from this distribution amounting to a few tenths of a pixel in most cases.

For each of the echelle orders, fluxes are extracted from a cut in the spatial direction of the high-dispersion SI, summing the fluxes of all “good” (i.e., nonflagged) pixels in a swath between sample positions 150 and 450. The summed fluxes for each spatial line are normalized to a common number of contributing pixels to account for the exclusion of flagged pixels. Next, an rms scatter is computed after excluding points in the spatial profile with significant flux above an initial rms value calculated by including all profile points. A local background is also fit through the low-flux points and subtracted from the profile array. A gaussian model is then cross-correlated through the net-flux profile if there are at least two points with fluxes above the rms value. A default value (i.e., the appropriate fiducial value from Table 10.1) is assigned for the order’s centroid position according to any of the following conditions:

- fewer than two spatial profile points have fluxes above the local rms level,
- the centroiding cross-correlation coefficient is unsatisfactory,
- the centroid determined by cross-correlation is beyond a tolerance value (ranging from  $\pm 0.5$  to  $\pm 3.0$  pixels for short- and long-wavelength orders, respectively) away from the fiducial value.

The shift of the order centroid from the initial assumed value is applied to the end points of the extraction slit. The centroid of each echelle order is found independently with the above steps, effectively centering the boxcar slit on each order.

### 10.2.2 Description of Spectral Flux Extraction Process

A boxcar extraction slit running along each order is used to extract the spectral fluxes. The length of the extraction slit (listed in Table 10.2 for the various extraction modes) was chosen on the basis of tests with a large group of images to admit a fixed fraction ( $\sim 98\%$ ) of an order’s total flux. This fraction may fluctuate slightly for a given image according

Table 10.1: Fiducial Line Positions for the Echelle Orders

Order No.	LWP Line	LWR Line	SWP Line	Order No.	LWP Line	LWR Line	SWP Line
127	131.04	119.56		96	352.28	343.82	325.32
126	136.34	127.23		95	361.82	353.34	334.43
125	141.95	133.99	128.39	94	371.56	363.11	343.73
124	147.41	139.70	132.99	93	381.50	373.01	353.24
123	153.21	144.50	137.76	92	391.68	383.19	362.95
122	158.98	150.55	142.70	91	402.06	393.50	372.88
121	164.98	156.16	147.82	90	412.71	404.20	383.02
120	171.17	162.81	153.12	89	423.60	415.06	393.40
119	177.12	168.67	158.92	88	434.78	426.14	404.01
118	183.38	175.00	164.80	87	446.18	437.41	414.86
117	189.77	181.49	170.78	86	457.78	449.12	425.96
116	196.22	187.47	176.85	85	469.68	461.04	437.32
115	202.81	194.43	183.02	84	481.90	473.26	448.95
114	209.49	200.80	189.30	83	494.42	485.74	460.85
113	216.16	207.60	195.69	82	507.20	498.52	473.04
112	223.02	214.35	202.20	81	520.30	511.59	485.53
111	229.94	221.02	208.82	80	533.71	525.15	498.32
110	236.97	228.38	215.57	79	547.48	538.83	511.43
109	244.15	235.83	222.45	78	561.57	553.07	524.87
108	251.49	243.17	229.45	77	576.02	567.50	538.65
107	259.02	250.71	236.60	76	590.80	582.49	552.79
106	266.71	258.43	243.88	75	606.01	597.78	567.30
105	274.56	266.13	251.31	74	621.65	613.48	582.19
104	282.57	274.20	258.88	73	637.76	629.57	597.47
103	290.70	282.15	266.60	72	654.42	646.08	613.18
102	298.98	290.53	274.49	71	671.34	662.99	629.31
101	307.43	299.04	282.53	70	688.88	680.35	645.89
100	316.02	307.41	290.74	69	706.53	697.89	662.94
99	324.81	316.31	299.12	68		715.36	680.48
98	333.81	325.30	307.67	67		733.63	698.53
97	342.96	334.44	316.40	66			717.11

Table 10.2: Extraction Slit Lengths for the Echelle Orders - continued on next page

Order No.	LWP			LWR			SWP		
	Lg.	Ext.	Sm.	Lg.	Ext.	Sm.	Lg.	Ext.	Sm.
127	5.14	6.24	5.14	5.14	6.24	5.14			
126	5.14	6.24	5.14	5.14	6.24	5.14			
125	5.14	6.24	5.14	5.14	6.24	5.14	4.72	6.07	4.08
124	5.14	6.24	5.14	5.14	6.24	5.14	4.72	6.07	4.08
123	5.14	6.24	5.14	5.14	6.24	5.14	4.72	6.07	4.08
122	5.14	6.24	5.14	5.14	6.24	5.14	4.72	6.07	4.08
121	5.14	6.24	5.14	5.14	6.24	5.14	4.72	6.07	4.08
120	5.14	6.24	5.14	5.14	6.24	5.14	4.31	6.07	4.08
119	5.24	6.24	5.14	5.24	6.24	5.14	4.06	6.07	4.08
118	5.26	6.24	5.14	5.26	6.24	5.14	4.12	6.07	4.08
117	5.34	6.30	5.20	5.34	6.30	5.20	4.66	6.07	4.08
116	5.46	6.34	5.22	5.46	6.34	5.22	4.66	6.07	4.18
115	5.48	6.40	5.24	5.48	6.40	5.24	4.68	6.07	4.26
114	5.52	6.46	5.29	5.52	6.46	5.29	4.70	6.07	4.36
113	5.56	6.52	5.34	5.56	6.52	5.34	4.70	6.07	4.46
112	5.52	6.58	5.32	5.52	6.58	5.32	4.72	6.07	4.54
111	5.52	6.62	5.32	5.52	6.62	5.32	4.74	6.07	4.64
110	5.60	6.68	5.38	5.60	6.68	5.38	4.82	6.07	4.82
109	5.52	6.74	5.37	5.52	6.74	5.37	4.86	6.07	4.82
108	5.58	6.80	5.42	5.58	6.80	5.42	4.74	6.18	4.76
107	5.68	6.86	5.48	5.68	6.86	5.48	4.70	6.27	4.60
106	5.70	6.92	5.48	5.70	6.92	5.48	4.96	6.38	4.68
105	5.72	6.98	5.52	5.72	6.98	5.52	4.88	6.48	4.76
104	5.74	7.04	5.54	5.74	7.04	5.54	4.84	6.59	4.54
103	5.70	7.10	5.40	5.70	7.10	5.40	4.74	6.69	4.68
102	5.62	7.16	5.34	5.62	7.16	5.34	4.82	6.80	4.60
101	5.58	7.22	5.34	5.58	7.22	5.34	4.82	6.90	4.62
100	5.54	7.30	5.24	5.54	7.30	5.24	4.86	7.01	4.62
99	5.52	7.36	5.18	5.52	7.36	5.18	5.38	7.12	4.96
98	5.42	7.42	5.14	5.42	7.42	5.14	5.06	7.23	4.99
97	5.42	7.48	5.12	5.42	7.48	5.12	5.10	7.34	4.82

Table 10.2: Extraction Slit Lengths - continued

Order No.	LWP			LWR			SWP		
	Lg.	Ext.	Sm.	Lg.	Ext.	Sm.	Lg.	Ext.	Sm.
96	5.44	7.54	5.06	5.44	7.54	5.06	5.20	7.45	4.88
95	5.38	7.62	5.00	5.38	7.62	5.00	5.04	7.56	4.92
94	5.38	7.68	4.98	5.38	7.68	4.98	5.44	7.67	5.22
93	5.44	7.74	5.02	5.44	7.74	5.02	5.28	7.78	4.96
92	5.46	7.82	5.00	5.46	7.82	5.00	5.68	7.90	5.44
91	5.46	7.88	4.96	5.46	7.88	4.96	5.80	8.01	5.60
90	5.54	7.94	5.04	5.54	7.94	5.04	5.86	8.12	5.58
89	5.48	8.02	5.02	5.48	8.02	5.02	6.18	8.24	5.72
88	5.52	8.08	5.08	5.52	8.08	5.08	6.06	8.34	5.87
87	5.56	8.16	5.10	5.56	8.16	5.10	6.27	8.46	6.08
86	5.60	8.22	5.20	5.60	8.22	5.20	6.28	8.60	6.02
85	5.58	8.30	5.14	5.58	8.30	5.14	6.42	8.70	5.92
84	5.64	8.38	5.16	5.64	8.38	5.16	6.46	8.82	6.16
83	5.64	8.44	5.12	5.64	8.44	5.12	6.46	8.94	6.24
82	5.68	8.52	5.22	5.68	8.52	5.22	6.60	9.06	6.20
81	5.78	8.58	5.32	5.78	8.58	5.32	6.62	9.18	6.30
80	5.90	8.66	5.54	5.90	8.66	5.54	6.66	9.30	6.22
79	6.03	8.74	5.74	6.03	8.74	5.74	6.70	9.42	6.28
78	6.18	8.82	5.92	6.18	8.82	5.92	6.86	9.54	6.52
77	6.36	8.88	6.08	6.36	8.88	6.08	6.76	9.66	6.52
76	6.52	8.96	6.20	6.52	8.96	6.20	6.88	9.79	6.50
75	6.66	9.04	6.36	6.66	9.04	6.36	7.02	9.92	6.66
74	6.84	9.12	6.48	6.84	9.12	6.48	7.20	10.04	6.92
73	6.98	9.20	6.68	6.98	9.20	6.68	7.28	10.16	7.10
72	7.01	9.28	6.78	7.01	9.28	6.78	7.62	10.28	7.36
71	7.02	9.36	6.88	7.02	9.36	6.88	7.88	10.42	7.68
70	7.03	9.44	7.01	7.03	9.44	7.01	8.12	10.54	7.96
69	7.03	9.50	7.01	7.03	9.50	7.01	8.32	10.66	8.24
68				7.03	9.50	7.01	8.40	10.80	8.30
67				7.03	9.50	7.01	8.70	10.92	8.46
66							8.84	11.06	8.72

to the actual width of its spatial profile, but it is expected to be the same for orders of a given image. The weights of all pixels, including flagged ones, in the boxcar are the same, except for fractional weights of pixels at the ends of the extraction slit. Thus the fluxes are summed along the slit at each wavelength. To obtain the net fluxes, the background fluxes determined by the *BCKGRD* step are normalized to the extraction slit area and subtracted from the gross spectral flux.

### 10.2.3 Noise Models

Unlike the processing of low-dispersion images, the extraction of high-dispersion fluxes does not require a noise model. Nevertheless, NEWSIPS provides a noise vector at each wavelength as an indicator of its reliability. This vector is generated by using the camera-dependent high-dispersion noise model (discussed below) to estimate a noise value according to the fluxes along the extraction slit at each wavelength. The total noise amplitude for the wavelength is the sum of the individual noise values of all pixels along the slit, including flagged pixels. In this computation, pixels at the ends of the slit are given their corresponding fractional weights.

The noise models are derived empirically for each camera by measuring the scatter in the FNs around the mean FN in the background regions of several hundred science and flat-field images taken at a variety of exposure levels. These measurements are made in a  $21 \times 21$  grid of regions, each region being 35 pixels on a side. At each grid point (region), the relation between noise level and FN is fit with a fourth order polynomial. This polynomial is then sampled uniformly at 50 points from 0 to 588 FN, and these sampled noise values for each grid point comprise the “noise model”. This positional FN and noise-level information is stored as a static data cube for use in the processing of high-dispersion images. As a given image is processed, the noise level corresponding to a given pixel location and FN value is calculated by interpolation of the noise model data cube: bilinear spatial interpolation is done among the appropriate grid point locations, and linear interpolation in FN is done among the sampled noise values. Noise values for FNs below zero and above 588 FN are set to the noise values corresponding to these extrema, respectively.

Unlike the low-dispersion counterpart, the 1-D noise spectrum which is output to the high-dispersion MX is *not* in absolutely calibrated units. To achieve this, the user should multiply the noise spectrum for a given order by the ratio of the absolutely calibrated flux to the net flux. Although different in detail from the “sigma” vector produced by *SWET* in low dispersion, the high-dispersion noise vector is fundamentally analogous to the sigma vector in its origins from a “noise model” derived from rms measurements of flat fields and in the relationship of its construction to the spectral-flux extraction method used in each case.

### 10.2.4 One-Dimensional $\nu$ Flag Spectrum

The 1-D  $\nu$  flag spectrum is derived from the flag values in the high-dispersion SF. No attempt is made to screen out flags for pixels which do not contribute a significant enough fraction of the total flux. Consequently, in high-dispersion the final 1-D  $\nu$  flag value for a given wavelength sample is simply the sum of all unique individual flags for the pixels in the boxcar slit at that wavelength.

### 10.2.5 *EXTRACT* Output

The main output data product produced during *EXTRACT* is the high-dispersion MX FITS file (MXHI). The MXHI contains the net (background-subtracted) integrated flux spectrum, the Chebyshev-characterized background spectrum scaled up to the extraction slit area, the  $\nu$  flag spectrum, the ripple-corrected spectrum, the absolutely-calibrated and ripple-corrected net flux spectrum, and the noise spectrum stored in a FITS binary table extension. The net flux, background, ripple, and noise spectra are in units of FN, the flag spectrum is in bit-encoded unitless values, and the calibrated flux spectrum is in physical units of  $\text{ergs sec}^{-1} \text{cm}^{-2} \text{\AA}^{-1}$ . See Chapter 11 for details concerning the process of absolute flux calibration and ripple correction.

The background values for locations before the short-wavelength ends or past the long-wavelength ends of the orders are replications of the first (or last) valid background value. The net flux and noise spectra are computed over the entire wavelength space of the high-dispersion SI, but locations that are outside the camera target area will have net fluxes equal to zero because these regions do not contain any valid image data. The absolute calibrations are valid over wavelength limits of 1150–1980 $\text{\AA}$  for SWP and 1850–3350 $\text{\AA}$  for LWP and LWR. Beyond these limits the calibrated net fluxes are set to a value of 0 and have a  $\nu$  flag value of  $-2$ . The valid wavelength limits of the calibrated spectra are consequently somewhat truncated as compared to the net flux spectrum.

The *EXTRACT* module writes the following information to the HISTORY portion of the image label:

- noise model version number,
- aperture-dependent extraction/calibration information:
  - slit height information,
  - found line position for a representative “checkpoint” echelle order (i.e., order 100 for the SWP or order 90 for the LWP and LWR). The LWP processing HISTORY initially reported the line position for order 100. This was subsequently changed to order 90 after the start of the processing effort, as this order is a region of higher sensitivity than order 100 for the LWP and LWR. This change only affects LWP and LWR images processed after July 28, 1997.
  - order centroiding warnings (if applicable),

- ripple calibration version number,
- absolute flux calibration derivation information,
- absolute flux calibration version number,
- absolute calibration mode (i.e., point or trailed),
- absolute calibration epoch,
- camera rise time,
- effective exposure time,
- THDA of image,
- reference THDA,
- temperature-dependent sensitivity correction coefficient,
- temperature correction factor,
- time-dependent sensitivity degradation correction version number,
- time-dependent sensitivity degradation correction mode,
- sensitivity degradation calibration epoch, and
- observation date.



# Chapter 11

## Calibration of the Net Flux

### 11.1 Low-Dispersion Absolute Flux Calibration

#### 11.1.1 1985-Epoch Point Source Calibrations

Absolute flux calibrations have been derived for the low-dispersion modes of the IUE cameras through observations of ultraviolet photometric standard stars, as well as observations and models of the white dwarf star, G191-B2B. The wavelength-dependence of the inverse sensitivity function ( $S_\lambda^{-1}$ ) for each camera has been determined by comparison of IUE observations of the white dwarf star with model atmosphere calculations that were provided to the IUE project by D. Finley. The overall zeropoint of the calibration curves has been set by applying the white dwarf derived  $S_\lambda^{-1}$  values to IUE observations of ultraviolet photometric standard stars and comparing these results with OAO-2 measurements in the 2100–2300Å band (see González-Riestra, Cassatella, and de la Fuente 1992 for details regarding the calibration procedures).

The final  $S_\lambda^{-1}$  curves for the LWP, LWR (ITFs A and B), and SWP, defined in 15Å bins for the long-wavelength cameras and 10Å bins for the SWP and fit with spline curves, are listed in Tables 11.1–11.4. The absolute flux at a given wavelength,  $F_\lambda$  (ergs sec<sup>-1</sup> cm<sup>-2</sup> Å<sup>-1</sup>), is computed as follows:

$$F_\lambda = FN_\lambda \times S_\lambda^{-1} / t_{eff}$$

where  $FN_\lambda$  is the extracted net flux in FN units,  $S_\lambda^{-1}$  is the inverse sensitivity value at that wavelength, and  $t_{eff}$  is the effective exposure time in seconds. The inverse sensitivity value at a particular wavelength is determined by quadratic interpolation of the tabulated values for a given camera.

The effective exposure time for non-trailed (e.g., point, extended, flat-field) sources is derived from the original commanded exposure time,  $t_{com}$ , and takes into account the effects of On-Board Computer (OBC) tick rounding and the camera rise time,  $t_{rise}$ , as follows:

$$t_{eff} = 0.4096 \times INT(t_{com}/0.4096) - t_{rise}$$

where the values of  $t_{rise}$  for each camera are taken from González-Riestra (1991) and are 0.123, 0.126, and 0.130 for the LWP, LWR, and SWP cameras, respectively. Tick rounding results from the integer arithmetic used by the OBC in commanding exposures. Effective exposure times for large-aperture trailed observations are determined according to:

$$t_{TR} = Trail\ length / Trail\ rate \times Passes$$

where *Trail length* is the trail path length of the aperture in arcsec, *Trail rate* is the effective trail rate in arcsec/sec, and *Passes* is the number of passes across the aperture. Because the OBC uses integer arithmetic in calculating fixed rate slews, there is a truncation in the commanded trail rate. This “rounding off” is similar to the OBC quantization of non-trailed exposure times. The effective trail rate is calculated using the following equation:

$$TR = \sqrt{(LSB \times INT(0.4695 \times TR_{com}/LSB))^2 + (LSB \times INT(0.8829 \times TR_{com}/LSB))^2}$$

where *LSB* is the least significant bit (0.03001548/32 arcsec/sec) and  $TR_{com}$  is the commanded trail rate.

### 11.1.2 Aperture Response Corrections

The  $S_{\lambda}^{-1}$  functions described above apply only to point source observations acquired through the large aperture. The small-aperture and trailed observing modes are known to have different relative responses as compared to large-aperture point spectra (e.g., Harris and Cassatella 1985, Bohlin 1986, Crenshaw and Park 1989). This effect has been ascribed to several sources, including vignetting effects of the entrance apertures in trailed and small-aperture spectra and spatial inhomogeneities in the UVC efficiency (Cassatella 1990). Application of the large-aperture point source calibration to spectra obtained either in trail mode or through the small aperture will introduce photometric errors of at least 5–7% in the regions near the detector edge and of 1–2% in regions where the camera response is flatter.

Calibration corrections for small-aperture observations and for large-aperture trailed observations have been derived and are applied by the processing system when necessary. IUE standard-star observations from the 1984–1985 epoch have been used to calculate the wavelength-dependent flux ratios of small- and large-aperture point sources, and of large-aperture point source and trail mode observations. Observations from the 1984–1985 epoch were chosen so as to match the large-aperture point source calibration epoch. Also, by limiting the range of time over which the observations were obtained, effects due to sensitivity degradation in the cameras are minimized.

Optimal exposure level observations of the four TD1 standard stars BD+28° 4211, HD 93521, HD 60753, and BD+75° 325 were used to compute the small-to-large aperture (S/L) ratios and the large-aperture trailed-to-point source (T/L) ratios. The effective exposure times of the trailed observations were determined using a value of 21.48 arcseconds for the SWP major-axis trail path length (Garhart 1992b), 22.55 arcseconds for the LWR major-axis trail path length, and 21.84 arcseconds for the LWP major-axis trail path length. The ratios

of pairs of observations of the same object obtained through the small and large apertures, or in point and trail modes were averaged together to determine the mean S/L and T/L spectral ratios. Approximately 20 pairs of spectra were used to determine each of the two response ratios. The mean spectral ratios were resampled into the bin size of the appropriate inverse sensitivity function and a spline fit to the binned ratios was calculated. Tabulated values of the spline fits for each camera are listed in Tables 11.5–11.8.

Because centering errors in the small aperture can lead to large variations in the overall observed flux level for individual spectra, it is impossible to determine an absolute S/L ratio. Therefore, the average of S/L over all wavelengths is normalized to unity. *As a result, the small-aperture fluxes are known in a relative sense but not in an absolute one.* The relative small- and absolute large-aperture inverse sensitivities are related by

$$S_{\lambda}^{-1}(S) = S_{\lambda}^{-1}(L)/(S/L).$$

Investigators should be aware that absolute fluxes for small-aperture data are significantly less reliable than those of large-aperture data. For the ratio of trailed response to point sources in the large aperture, the absolute calibrations are related by

$$S_{\lambda}^{-1}(T) = S_{\lambda}^{-1}(L)/(T/L).$$

Only trailed large-aperture spectra are calibrated with the T/L ratio applied. Images processed as extended sources are calibrated as point source observations.

### 11.1.3 Gain Factors

The  $S_{\lambda}^{-1}$  function for the LWR camera was derived from observations obtained at a UVC voltage setting of  $-5.0$  kV. Therefore all LWR observations that have been obtained at the reduced voltage setting of  $-4.5$  kV have an absolute calibration gain correction factor of 1.37 applied by the processing system (Harris 1985) to compensate. A message to this effect is included in the processing history log. In the event that an observation for any camera has been obtained at non-standard settings of either the exposure gain (normally MAXIMUM) or the camera read gain (normally LOW), an additional absolute flux scaling factor is multiplicatively applied as follows (cf. Coleman et al., 1977):

- Exposure Gain Corrections

**Maximum:** Correction = 1.0

**Medium:** Correction = 3.0

**Minimum:** Correction = 10.0

- Read Gain Corrections

**High:** Correction = 0.33

**Low:** Correction = 1.0

Table 11.1: LWP Absolute Calibration

$\lambda$	$S^{-1}^a$	$\lambda$	$S^{-1}$	$\lambda$	$S^{-1}$
1850	93.736	2360	6.108	2870	2.823
1865	62.950	2375	5.855	2885	2.877
1880	45.372	2390	5.560	2900	2.925
1895	35.791	2405	5.221	2915	2.998
1910	30.233	2420	4.918	2930	3.135
1925	25.704	2435	4.699	2945	3.314
1940	21.886	2450	4.498	2960	3.414
1955	18.946	2465	4.221	2975	3.686
1970	16.467	2480	3.902	2990	3.911
1985	14.460	2495	3.892	3005	4.132
2000	13.095	2510	3.892	3020	4.465
2015	12.447	2525	3.650	3035	4.868
2030	12.234	2540	3.460	3050	5.326
2045	12.084	2555	3.222	3065	5.972
2060	11.730	2570	3.173	3080	6.614
2075	11.326	2585	3.162	3095	7.318
2090	11.123	2600	3.010	3110	8.075
2105	11.227	2615	2.904	3125	9.101
2120	11.355	2630	2.853	3140	10.060
2135	11.266	2645	2.801	3155	11.577
2150	11.174	2660	2.739	3170	13.041
2165	11.127	2675	2.673	3185	14.704
2180	11.095	2690	2.635	3200	16.832
2195	11.050	2705	2.666	3215	19.605
2210	10.963	2720	2.726	3230	23.110
2225	10.806	2735	2.633	3245	27.069
2240	10.533	2750	2.636	3260	31.107
2255	10.026	2765	2.618	3275	35.122
2270	9.261	2780	2.648	3290	40.094
2285	8.657	2795	2.759	3305	47.271
2300	8.456	2810	2.702	3320	57.623
2315	7.974	2825	2.705	3335	71.007
2330	7.225	2840	2.729	3350	87.001
2345	6.560	2855	2.769		

<sup>a</sup>Inverse sensitivity in units of  $10^{-13}$   
 $\text{ergs cm}^{-2} \text{ \AA}^{-1} \text{ FN}^{-1}$ .

Table 11.2: LWR ITFA Absolute Calibration

$\lambda$	$S^{-1}^a$	$\lambda$	$S^{-1}$	$\lambda$	$S^{-1}$
1850	150.815	2360	7.404	2870	2.962
1865	100.432	2375	7.082	2885	2.981
1880	67.875	2390	6.768	2900	3.059
1895	51.682	2405	6.422	2915	3.214
1910	43.664	2420	6.021	2930	3.408
1925	36.055	2435	5.564	2945	3.489
1940	29.671	2450	5.123	2960	3.571
1955	26.087	2465	4.791	2975	3.803
1970	21.773	2480	4.624	2990	4.141
1985	19.958	2495	4.545	3005	4.426
2000	18.914	2510	4.442	3020	4.668
2015	17.786	2525	4.236	3035	5.194
2030	16.714	2540	3.981	3050	5.378
2045	15.910	2555	3.765	3065	5.873
2060	15.509	2570	3.647	3080	6.553
2075	15.350	2585	3.569	3095	7.337
2090	15.195	2600	3.443	3110	8.238
2105	14.868	2615	3.227	3125	9.269
2120	14.438	2630	3.055	3140	10.442
2135	14.090	2645	3.045	3155	11.772
2150	14.099	2660	3.061	3170	13.527
2165	14.235	2675	2.951	3185	16.124
2180	14.129	2690	2.814	3200	18.375
2195	13.629	2705	2.907	3215	22.451
2210	13.475	2720	2.813	3230	25.421
2225	13.725	2735	2.654	3245	30.192
2240	12.470	2750	2.754	3260	38.728
2255	12.053	2765	2.812	3275	46.958
2270	11.348	2780	2.826	3290	51.385
2285	10.490	2795	2.871	3305	60.704
2300	10.036	2810	2.859	3320	70.023
2315	9.535	2825	2.857	3335	110.890
2330	8.595	2840	2.926	3350	151.761
2345	7.860	2855	2.959		

<sup>a</sup>Inverse sensitivity in units of  $10^{-13}$   
 $\text{ergs cm}^{-2} \text{ \AA}^{-1} \text{ FN}^{-1}$ .

Table 11.3: LWR ITFB Absolute Calibration

$\lambda$	$S^{-1}^a$	$\lambda$	$S^{-1}$	$\lambda$	$S^{-1}$
1850	149.533	2360	7.407	2870	2.929
1865	108.895	2375	7.025	2885	2.962
1880	71.052	2390	6.697	2900	3.014
1895	53.992	2405	6.369	2915	3.159
1910	45.698	2420	5.983	2930	3.390
1925	37.905	2435	5.513	2945	3.461
1940	31.051	2450	5.052	2960	3.573
1955	26.426	2465	4.723	2975	3.906
1970	22.927	2480	4.598	2990	4.149
1985	20.562	2495	4.540	3005	4.336
2000	19.567	2510	4.364	3020	4.620
2015	18.827	2525	4.085	3035	5.047
2030	16.966	2540	4.075	3050	5.382
2045	16.849	2555	3.633	3065	5.867
2060	16.174	2570	3.514	3080	6.509
2075	15.269	2585	3.543	3095	7.279
2090	15.296	2600	3.342	3110	8.172
2105	15.661	2615	3.133	3125	9.178
2120	14.869	2630	3.013	3140	10.290
2135	14.905	2645	2.987	3155	11.499
2150	14.822	2660	2.989	3170	12.880
2165	14.503	2675	2.917	3185	14.826
2180	14.337	2690	2.746	3200	17.627
2195	14.176	2705	2.794	3215	20.836
2210	13.233	2720	2.748	3230	23.865
2225	13.843	2735	2.653	3245	27.121
2240	12.606	2750	2.646	3260	33.308
2255	11.817	2765	2.672	3275	39.515
2270	11.317	2780	2.706	3290	43.614
2285	10.375	2795	2.745	3305	53.328
2300	10.228	2810	2.787	3320	63.042
2315	9.434	2825	2.829	3335	78.023
2330	8.562	2840	2.867	3350	93.004
2345	7.901	2855	2.899		

<sup>a</sup>Inverse sensitivity in units of  $10^{-13}$   
 $\text{ergs cm}^{-2} \text{ \AA}^{-1} \text{ FN}^{-1}$ .

Table 11.4: SWP Absolute Calibration

$\lambda$	$S^{-1}^a$	$\lambda$	$S^{-1}$	$\lambda$	$S^{-1}$
1150	10.60	1440	1.491	1730	1.269
1160	7.032	1450	1.535	1740	1.226
1170	4.666	1460	1.568	1750	1.185
1180	3.204	1470	1.593	1760	1.149
1190	2.377	1480	1.616	1770	1.117
1200	1.921	1490	1.642	1780	1.089
1210	1.614	1500	1.677	1790	1.067
1220	1.396	1510	1.721	1800	1.049
1230	1.249	1520	1.766	1810	1.035
1240	1.153	1530	1.798	1820	1.025
1250	1.090	1540	1.808	1830	1.019
1260	1.045	1550	1.805	1840	1.017
1270	1.012	1560	1.798	1850	1.019
1280	0.991	1570	1.789	1860	1.025
1290	0.980	1580	1.778	1870	1.034
1300	0.977	1590	1.764	1880	1.046
1310	0.981	1600	1.745	1890	1.059
1320	0.992	1610	1.729	1900	1.071
1330	1.008	1620	1.706	1910	1.081
1340	1.030	1630	1.681	1920	1.086
1350	1.057	1640	1.652	1930	1.084
1360	1.089	1650	1.620	1940	1.073
1370	1.125	1660	1.584	1950	1.054
1380	1.166	1670	1.544	1960	1.038
1390	1.213	1680	1.501	1970	1.040
1400	1.265	1690	1.456	1980	1.075
1410	1.322	1700	1.409		
1420	1.381	1710	1.362		
1430	1.439	1720	1.315		

<sup>a</sup>Inverse sensitivity in units of  $10^{-12}$   
 $\text{ergs cm}^{-2} \text{ \AA}^{-1} \text{ FN}^{-1}$ .

Table 11.5: LWP S/L and T/L Relative Sensitivities\*

$\lambda$	S/L	T/L	$\lambda$	S/L	T/L	$\lambda$	S/L	T/L
1850	1.048	0.989	2360	1.024	1.003	2870	0.998	0.995
1865	1.026	0.989	2375	1.021	1.000	2885	0.997	0.995
1880	1.005	0.989	2390	1.017	0.996	2900	0.996	0.994
1895	0.989	0.989	2405	1.013	0.993	2915	0.994	0.994
1910	0.978	0.989	2420	1.009	0.990	2930	0.990	0.994
1925	0.973	0.988	2435	1.006	0.988	2945	0.987	0.994
1940	0.972	0.987	2450	1.004	0.987	2960	0.983	0.994
1955	0.974	0.986	2465	1.003	0.985	2975	0.979	0.995
1970	0.978	0.986	2480	1.002	0.985	2990	0.976	0.996
1985	0.983	0.985	2495	1.003	0.984	3005	0.973	0.997
2000	0.986	0.984	2510	1.004	0.984	3020	0.971	0.999
2015	0.988	0.984	2525	1.005	0.984	3035	0.970	1.001
2030	0.989	0.984	2540	1.007	0.985	3050	0.971	1.004
2045	0.987	0.984	2555	1.008	0.985	3065	0.973	1.007
2060	0.985	0.985	2570	1.009	0.986	3080	0.977	1.011
2075	0.983	0.987	2585	1.010	0.987	3095	0.982	1.016
2090	0.980	0.988	2600	1.010	0.989	3110	0.988	1.022
2105	0.978	0.991	2615	1.009	0.990	3125	0.995	1.029
2120	0.977	0.994	2630	1.008	0.991	3140	1.002	1.036
2135	0.976	0.998	2645	1.006	0.993	3155	1.008	1.045
2150	0.977	1.002	2660	1.004	0.994	3170	1.015	1.054
2165	0.980	1.006	2675	1.001	0.995	3185	1.021	1.064
2180	0.984	1.010	2690	0.999	0.996	3200	1.027	1.073
2195	0.990	1.013	2705	0.997	0.997	3215	1.031	1.080
2210	0.996	1.016	2720	0.995	0.998	3230	1.034	1.084
2225	1.003	1.019	2735	0.993	0.998	3245	1.037	1.085
2240	1.009	1.020	2750	0.992	0.998	3260	1.038	1.082
2255	1.016	1.021	2765	0.992	0.998	3275	1.040	1.074
2270	1.021	1.020	2780	0.992	0.998	3290	1.040	1.060
2285	1.025	1.019	2795	0.993	0.998	3305	1.040	1.039
2300	1.028	1.017	2810	0.995	0.997	3320	1.040	1.012
2315	1.029	1.014	2825	0.996	0.997	3335	1.039	0.980
2330	1.029	1.010	2840	0.997	0.996	3350	1.039	0.946
2345	1.027	1.007	2855	0.997	0.996			

\*Normalized to an average value of unity over all wavelengths.



Table 11.6: LWR ITFA S/L and T/L Relative Sensitivities\*

$\lambda$	S/L	T/L	$\lambda$	S/L	T/L	$\lambda$	S/L	T/L
1850	1.014	0.986	2360	0.997	0.986	2870	1.023	0.954
1865	1.014	0.998	2375	0.995	0.982	2885	1.027	0.956
1880	1.014	1.008	2390	0.994	0.977	2900	1.030	0.958
1895	1.014	1.012	2405	0.992	0.973	2915	1.032	0.961
1910	1.014	1.006	2420	0.991	0.968	2930	1.032	0.963
1925	0.980	0.992	2435	0.990	0.963	2945	1.032	0.966
1940	0.960	0.977	2450	0.991	0.959	2960	1.031	0.968
1955	0.951	0.970	2465	0.992	0.955	2975	1.029	0.971
1970	0.951	0.972	2480	0.995	0.952	2990	1.026	0.974
1985	0.955	0.979	2495	0.997	0.949	3005	1.023	0.976
2000	0.960	0.988	2510	1.001	0.947	3020	1.019	0.975
2015	0.963	0.993	2525	1.004	0.945	3035	1.014	0.969
2030	0.964	0.995	2540	1.008	0.943	3050	1.010	0.960
2045	0.963	0.995	2555	1.011	0.942	3065	1.005	0.950
2060	0.962	0.994	2570	1.013	0.941	3080	0.999	0.942
2075	0.959	0.992	2585	1.014	0.940	3095	0.993	0.949
2090	0.956	0.990	2600	1.014	0.939	3110	0.985	0.964
2105	0.953	0.988	2615	1.013	0.938	3125	0.975	0.975
2120	0.951	0.988	2630	1.011	0.938	3140	0.963	0.981
2135	0.949	0.989	2645	1.008	0.938	3155	0.949	0.984
2150	0.949	0.990	2660	1.004	0.938	3170	1.000	0.992
2165	0.951	0.992	2675	1.001	0.938	3185	1.000	0.998
2180	0.955	0.994	2690	0.997	0.938	3200	1.000	1.012
2195	0.959	0.996	2705	0.994	0.939	3215	1.000	1.044
2210	0.964	0.998	2720	0.991	0.939	3230	1.000	1.053
2225	0.970	1.000	2735	0.990	0.940	3245	1.000	1.022
2240	0.976	1.001	2750	0.990	0.941	3260	1.000	1.000
2255	0.982	1.002	2765	0.991	0.942	3275	1.000	1.000
2270	0.988	1.002	2780	0.994	0.943	3290	1.000	1.000
2285	0.992	1.001	2795	0.998	0.945	3305	1.000	1.000
2300	0.995	0.999	2810	1.002	0.946	3320	1.000	1.000
2315	0.997	0.997	2825	1.007	0.948	3335	1.000	1.000
2330	0.998	0.993	2840	1.013	0.950	3350	1.000	1.000
2345	0.998	0.990	2855	1.018	0.952			

\*Normalized to an average value of unity over all wavelengths.

Table 11.7: LWR ITFB S/L and T/L Relative Sensitivities\*

$\lambda$	S/L	T/L	$\lambda$	S/L	T/L	$\lambda$	S/L	T/L
1850	1.015	1.008	2360	0.997	0.978	2870	1.047	0.956
1865	1.015	1.015	2375	0.997	0.975	2885	1.052	0.957
1880	1.015	1.020	2390	0.997	0.972	2900	1.054	0.959
1895	1.015	1.019	2405	0.996	0.969	2915	1.053	0.961
1910	1.015	1.010	2420	0.996	0.966	2930	1.050	0.963
1925	0.971	0.995	2435	0.996	0.962	2945	1.044	0.965
1940	0.946	0.981	2450	0.997	0.958	2960	1.036	0.967
1955	0.935	0.974	2465	0.999	0.954	2975	1.026	0.979
1970	0.935	0.977	2480	1.002	0.951	2990	1.016	0.991
1985	0.941	0.985	2495	1.005	0.949	3005	1.004	1.000
2000	0.948	0.994	2510	1.008	0.948	3020	0.992	1.000
2015	0.952	0.999	2525	1.011	0.947	3035	0.981	1.000
2030	0.953	1.000	2540	1.014	0.946	3050	0.969	1.000
2045	0.953	0.999	2555	1.017	0.946	3065	0.959	1.000
2060	0.950	0.996	2570	1.018	0.946	3080	1.000	1.000
2075	0.947	0.992	2585	1.019	0.945	3095	1.000	1.000
2090	0.943	0.988	2600	1.018	0.945	3110	1.000	1.000
2105	0.939	0.985	2615	1.015	0.945	3125	1.000	1.000
2120	0.935	0.982	2630	1.011	0.945	3140	1.000	1.000
2135	0.933	0.981	2645	1.006	0.945	3155	1.000	1.000
2150	0.933	0.980	2660	1.001	0.945	3170	1.000	1.000
2165	0.934	0.980	2675	0.996	0.945	3185	1.000	1.000
2180	0.938	0.981	2690	0.991	0.945	3200	1.000	1.000
2195	0.943	0.981	2705	0.987	0.946	3215	1.000	1.000
2210	0.950	0.982	2720	0.985	0.946	3230	1.000	1.000
2225	0.957	0.983	2735	0.985	0.947	3245	1.000	1.000
2240	0.964	0.984	2750	0.986	0.947	3260	1.000	1.000
2255	0.972	0.985	2765	0.991	0.948	3275	1.000	1.000
2270	0.979	0.985	2780	0.997	0.949	3290	1.000	1.000
2285	0.985	0.985	2795	1.005	0.950	3305	1.000	1.000
2300	0.990	0.984	2810	1.014	0.951	3320	1.000	1.000
2315	0.994	0.983	2825	1.023	0.952	3335	1.000	1.000
2330	0.996	0.982	2840	1.032	0.953	3350	1.000	1.000
2345	0.997	0.980	2855	1.040	0.954			

\*Normalized to an average value of unity over all wavelengths.

Table 11.8: SWP S/L and T/L Relative Sensitivities\*

$\lambda$	S/L	T/L	$\lambda$	S/L	T/L	$\lambda$	S/L	T/L
1150	0.970	1.000	1440	1.020	0.981	1730	0.997	0.994
1160	0.974	0.995	1450	1.020	0.984	1740	0.996	0.995
1170	0.977	0.991	1460	1.020	0.986	1750	0.995	0.995
1180	0.981	0.986	1470	1.020	0.988	1760	0.993	0.995
1190	0.984	0.982	1480	1.020	0.990	1770	0.992	0.995
1200	0.987	0.977	1490	1.019	0.991	1780	0.991	0.996
1210	0.990	0.973	1500	1.019	0.992	1790	0.990	0.996
1220	0.992	0.969	1510	1.019	0.992	1800	0.988	0.996
1230	0.995	0.965	1520	1.018	0.992	1810	0.987	0.996
1240	0.997	0.962	1530	1.018	0.992	1820	0.986	0.997
1250	1.000	0.959	1540	1.017	0.993	1830	0.984	0.997
1260	1.002	0.956	1550	1.016	0.992	1840	0.983	0.997
1270	1.004	0.953	1560	1.016	0.992	1850	0.982	0.998
1280	1.006	0.951	1570	1.015	0.993	1860	0.981	0.998
1290	1.007	0.949	1580	1.014	0.993	1870	0.980	0.998
1300	1.009	0.947	1590	1.013	0.993	1880	0.979	0.998
1310	1.010	0.947	1600	1.012	0.993	1890	0.977	0.999
1320	1.012	0.946	1610	1.011	0.993	1900	0.976	0.999
1330	1.013	0.947	1620	1.010	0.993	1910	0.975	0.999
1340	1.014	0.948	1630	1.009	0.993	1920	0.974	1.000
1350	1.015	0.949	1640	1.008	0.993	1930	0.973	1.000
1360	1.016	0.952	1650	1.007	0.993	1940	0.972	1.000
1370	1.017	0.955	1660	1.006	0.993	1950	0.971	1.001
1380	1.018	0.958	1670	1.005	0.993	1960	0.971	1.001
1390	1.018	0.962	1680	1.004	0.993	1970	0.970	1.001
1400	1.019	0.965	1690	1.003	0.994	1980	0.969	1.002
1410	1.019	0.970	1700	1.001	0.994			
1420	1.020	0.973	1710	1.000	0.994			
1430	1.020	0.977	1720	0.999	0.994			

\*Normalized to an average value of unity over all wavelengths.

Corrections are also applied to the absolute flux spectrum to take into account changes in camera sensitivity as a function of time (observation date) and camera temperature (THDA). The derivation and application of these corrections are detailed in the following sections.

#### 11.1.4 Time-Dependent Degradation Correction

The sensitivity of the SEC Vidicon camera is known to degrade with time, hence the need for a method to correct for this loss. One of the fundamental requirements of the IUE Final Archive is that the dataset be fully intercomparable. The sensitivity degradation correction is essential in satisfying this requirement and allowing full utilization of the remarkably long timeline of IUE observations. The broad-band sensitivity analysis (Garhart 1992a) that monitors the degradation effects on the optical coatings of the camera caused by exposure to radiation is of insufficient resolution to provide a proper correction algorithm. The analysis described herein was motivated as a result of this concern.

##### 11.1.4.1 Database

The database employed in the analysis contains the same images used for quick-look sensitivity monitoring and consists of several hundred low-dispersion point source and trailed observations distributed amongst the sensitivity monitoring standard stars. Each image was carefully examined for defects such as data dropouts, cosmic ray hits, etc. and any corrupted spectra were discarded. All of the data were uniformly reprocessed using the prototype final archive processing software (Nichols-Bohlin 1990) and the updated line library and wavelength calibration (Bushouse 1991a). The original databases include images taken through early 1992 for the SWP, mid-1993 for the LWP, and late 1994 for the LWR.

##### 11.1.4.2 Analysis

The analysis was done on the extracted net spectra, before application of the absolute calibration (i.e., in flux numbers), and the data sets for each standard star were treated separately. The spectra were corrected for camera head amplifier temperature (THDA) induced sensitivity variations (Garhart 1991) and sections of the spectra affected by camera reseaux were interpolated across using adjacent good data points. Several absorption features (e.g., Si IV, C IV, and geocoronal Ly  $\alpha$ , ) were also interpolated across by applying the same technique. Each spectrum was then normalized by dividing by an average of several spectra taken in a six-month time period centered on 1985. The normalized data were then binned in 5Å intervals and a set of degradation ratios was produced by performing a final binning of the data at six-month intervals. The ratios derived from each standard star were compared and found to be in good agreement, so the last step of the process was repeated using all the data and a combined set of degradation ratios was derived. The same analysis was performed on low-dispersion trailed data and a separate set of degradation ratios was produced. Subsequent testing of the trailed corrections showed that only the SWP solutions provided any improvement over use of point source corrections when applied to trailed data.

Therefore, the LWP and LWR cameras apply point source degradation corrections to the trailed data.

#### 11.1.4.3 Initial Fits to the Ratios

**LWP** - The LWP camera appears to have two behavioral trends in sensitivity degradation (Teays and Garhart 1990). The division occurs at approximately 1984.5, which corresponds to the time this camera became the default camera. Post-1984.5 data are corrected using a linear fit (Bevington 1969) to the ratios in that time period, while images taken prior to 1984.5 are corrected using a linear interpolation between each pre-1984.5 degradation ratio. The fluxes of corrected pre-1984.5 data will be less accurate than the fluxes of corrected post-1984.5 data due to the higher uncertainty in the degradation ratios for the early data. Fortunately little science data (except for calibration images) were taken using this camera during the pre-1984.5 time period, so the impact on the entire archive is minimal.

**LWR** - As is the case with the LWP camera, the LWR exhibits two trends with the dividing point occurring at approximately the same time. However, since the LWR is a closed data set, the binned degradation ratios were fit with a fourth-order polynomial covering the entire time period.

**SWP** - The SWP sensitivity degradation for the post-1979.5 epoch is represented by a linear relationship. The 1978.5 to 1979.5 epoch degradation ratios, which exhibit a behavior unlike the post-1979.5 epoch, were fit using a linear interpolation between each discrete point (Garhart 1992c).

#### 11.1.4.4 Calibration Updates

**1995 Update** - In early 1995, concerns were raised about the accuracy of the extrapolations of the sensitivity corrections to times beyond the original database of observations. While no errors due to the extrapolated corrections were seen in NEWSIPS data, the IUE Project felt that updating the old sensitivity degradation analysis would result in more accurate fluxes for post-1992 and 1993 images. As a result of these concerns, the LWP and SWP sensitivity degradation analysis was updated in 1995 using data taken though the beginning of 1995. These new corrections were applied to post-01 January 1990 images while the old corrections were used for pre-1990 images. This 1995 update represents the first sensitivity degradation calibration update. No calibration update was required for the LWR camera, as it comprised a closed data set.

**1996 Update** - Towards the end of 1996, a changing trend in the late-epoch sensitivity degradation of the SWP camera was seen. Absolutely calibrated fluxes of post-1994 data showed systematic errors of approximately  $-3\%$  (i.e., lower fluxes) when compared with images taken prior to 1994. This indicated that the 1995 updated calibration was under-correcting the post-1994 data and could occur if the rate of SWP camera degradation were increasing. In the case of the LWP camera, there was marginal evidence for a possible opposite effect, namely a slight overcorrection of post-1995 data, which could occur if the rate of camera degradation were tapering off. As a result, the SWP low-dispersion point

source sensitivity degradation correction analysis was updated to include data taken through August of 1996 (Garhart 1997). In order to join the new late-epoch correction smoothly to the existing linear fit, a new linear fit was computed, joined to the old linear fit at a specific time (1993.0) and extended through a point defined by the average of the last three time-binned fluxes (i.e., an average of 1995.5, 1996.0, and 1996.5 bins). This resulted in a set of segmented linear fits (one for each wavelength bin) which are splicings of the previous linear fits and the late-epoch linear fit. A similar approach was tried with both SWP trailed and LWP point source data. However, in both cases the use of a segmented correction was no better than using an extrapolation of the old sensitivity degradation correction. Therefore the IUE Project decided to continue to use an extrapolation of the 1995 sensitivity degradation correction update for these two cases.

#### 11.1.4.5 Application of Degradation Correction

The degradation ratio at 1985.0, which corresponds to the mean time of the ITFs, was calculated for each wavelength bin using the linear fits. A zeropoint correction was then applied to the y-intercepts in order to force the degradation ratios to be one. This ensures that no degradation correction will be applied to data near the 1985.0 fiducial date.

The ratios are applied to the net flux spectra using a nearest neighbor wavelength interpolation scheme along with the inverse sensitivity function so as to provide absolutely calibrated and degradation-corrected flux data. Extended source images are corrected using the point source ratios. The correction is performed in the following manner:

- The appropriate coefficients which correspond to the calibration epoch of the observation in question are identified. In the case of the LWR camera, there is only one calibration epoch.
- A correction ratio for each wavelength is calculated in the following manner:

$$R_t = R_0 + R_1 D + R_2 D^2 + R_3 D^3 + R_4 D^4$$

where  $D$  is the observation date expressed as either decimal years (e.g., 1984.3) for the LWP and SWP or decimal years minus 1978.0 (e.g., 6.3 for an observation date of 1984.3) for the LWR. In addition, the coefficients  $R_2$ ,  $R_3$ , and  $R_4$  are zero for the LWP and SWP.

- The correction ratio is applied as follows:

$$\text{Time Dependent Corrected Flux}_\lambda = FN_\lambda / R_t(\lambda)$$

where  $\lambda$  refers to the closest 5Å bin and  $R_t(\lambda)$  is the  $R_t$  value for that bin.

### 11.1.5 Temperature-Dependent Degradation Correction

IUE flux values are corrected for variations in camera sensitivity as a function of THDA using the temperature-dependent coefficients as derived from the sensitivity monitoring analysis (Garhart 1991). This correction is applied to the net flux along with the absolute calibration and sensitivity degradation corrections according to:

$$R_T = \frac{1}{(1 + C(THDA - ref. THDA))}$$

and

$$Temperature\ Dependent\ Corrected\ Flux = FN_\lambda \times R_T$$

where *Flux* is the net flux, *C* is the temperature coefficient and *ref. THDA* is the reference THDA. The reference THDA was calculated by taking an average of the THDAs for the sensitivity monitoring data which were used to derive the temperature coefficients. Table 11.9 contains the correction values, as used in the above equation.

Table 11.9: Temperature Coefficients and Reference THDAs

	LWP	LWR	SWP
Temp. Coef. <i>C</i>	$-0.0019 \pm 0.0003$	$-0.0088 \pm 0.0004$	$-0.0046 \pm 0.0003$
Ref. THDA (°C)	9.5	14.0	9.4

### 11.1.6 Application of Calibrations and Corrections

It is important to note that, as implemented in the image processing software, the interpolated inverse sensitivity values, time- and temperature-dependent sensitivity corrections, effective exposure time normalization, and any overall gain correction factor (for non-standard exposure or read gain or LWR UVC voltage settings) are computed as independent correction factors and then all applied simultaneously to the net flux and sigma spectra to result in fully calibrated and corrected spectra in absolute flux units. The net flux spectrum (in FN units), as determined by *SWET*, that is retained in the low-dispersion extracted spectrum does not have any of these correction factors applied to it. The calibrations and corrections are applied as follows:

$$F_{calib} = FN_\lambda \times S_\lambda^{-1} \times gain \times R_T/R_t/t_{eff}$$

$$\sigma_{calib} = \sigma_{FN_\lambda} \times S_\lambda^{-1} \times gain \times R_T/R_t/t_{eff}$$

where  $S_\lambda^{-1}$  is the inverse sensitivity (including any necessary S/L or T/L response corrections), *gain* is the cumulative UVC voltage and gain correction factor (if necessary),  $R_t$  and

$R_T$  are the time- and temperature-dependent sensitivity correction factors, respectively, and  $t_{eff}$  is the effective exposure time. The values for  $S_\lambda^{-1}$  and  $R_t$  are evaluated at the wavelength of each pixel through quadratic and nearest neighbor interpolation, respectively, of their tabulated values. The resulting absolutely calibrated units are  $\text{ergs}/\text{cm}^2/\text{\AA}/\text{sec}$ .

## 11.2 High-Dispersion Absolute Flux Calibration

### 11.2.1 Ripple Correction

A distinctive feature of echelle gratings is the variation in sensitivity as a function of wavelength within a spectral order, commonly known as the blaze function. The adjustment applied to eliminate this characteristic is referred to as a ripple correction. The use of the term “ripple” becomes apparent when the net fluxes in successive orders are plotted as a function of wavelength. A series of scalloped or ripple patterns appear which must be corrected for prior to the application of the absolute calibration.

The ripple correction and all associated equations are defined in Cassatella (1996, 1997a, 1997b). The basic form of the ripple correction as a function of order number and wavelength is:

$$R_m = \sin^2 x / x^2$$

where  $x$  is expressed as:

$$x = \pi m \alpha (1 - \lambda_c) / \lambda,$$

the  $\alpha$  parameter is given as a function of order number:

$$\alpha = A_0 + A_1 m + A_2 m^2,$$

and the central wavelength corresponding to the peak of the blaze is:

$$\lambda_c = W_0/m + W_1 T + W_2 D + W_3.$$

Note that unlike the SWP camera, the LWP and LWR ripple corrections do not exhibit a dependence of central wavelength on THDA; instead the observed central wavelengths vary linearly with time. In addition, the LWR  $\alpha$  parameter evinces a bimodal behavior which has been fit with two separate functions (i.e., a linear and a quadratic polynomial). Here,  $m$  is order number,  $\lambda$  is wavelength in  $\text{\AA}$ ,  $T$  is the THDA, and  $D$  is the observation date in decimal years. The ripple correction is applied to the net flux prior to the application of the heliocentric velocity correction to the wavelengths. The various ripple coefficients used in the above equations are given in Table 11.10 for each camera.

### 11.2.2 Absolute Flux Calibration Function

The high-dispersion inverse sensitivity curve is defined to be the product of the low-dispersion inverse sensitivity curve and a wavelength-dependent high-to-low absolute calibration function (Cassatella 1994, 1996, 1997a, 1997b):

$$C = n/N$$



Table 11.10: High-Dispersion Ripple Coefficients

Coefficients	LWP	LWR		SWP
		$m < 101$	$m \geq 101$	
$A_0$	0.406835	3.757863	1.360633	0.926208
$A_1$	0.01077191	-0.0640201	-4.252626e-3	0.0007890132
$A_2$	-5.945406e-5	3.5664390e-4	0.0	0.0
$W_0$	230868.177	230538.518		137508.316
$W_1$	0.0	0.0		0.0321729
$W_2$	-0.0263910	-0.0425003		0.0
$W_3$	56.433405	90.768579		2.111841

where  $C$  is the calibration function,  $n$  is the low-dispersion net flux normalized to the exposure time, and  $N$  is the high-dispersion ripple-corrected net flux also normalized to the exposure time. The calibration function represents the efficiency of high-dispersion spectra relative to low-dispersion and was determined empirically using pairs of high- and low-dispersion spectra obtained close in time so as to minimize the effects of the time-dependent sensitivity degradation.  $C$  is represented functionally as a polynomial in the following form:

$$C_\lambda = C_0 + C_1\lambda + C_2\lambda^2 + C_3\lambda^3$$

where  $\lambda$  is wavelength in Ångstroms. The coefficients used in the calibration function are given in Table 11.11.

Table 11.11: High-Dispersion Calibration Function Coefficients

Coefficients	LWP	LWR	SWP
$C_0$	251.383956	251.383956	1349.8538
$C_1$	-0.053935103	-0.053935103	-2.0078566
$C_2$	0.0	0.0	1.10252585e-3
$C_3$	0.0	0.0	-2.0939327e-7

### 11.2.3 Application of Calibrations and Corrections

High-dispersion absolutely-calibrated fluxes are obtained using a combination of the high-dispersion net fluxes, the ripple correction, the high-dispersion calibration function, the

low-dispersion inverse sensitivity function, time- and temperature-dependent sensitivity corrections, effective exposure time normalization, and any overall gain correction factor (for non-standard exposure or read gain or LWR UVC voltage settings). The calibrations and corrections are applied as follows:

$$F_{calib} = FN_{\lambda} \times S_{\lambda}^{-1} \times gain \times R_T \times C_{\lambda} / R_m / R_t / t_{eff}$$

where  $S_{\lambda}^{-1}$  is the low-dispersion inverse sensitivity including any necessary S/L response correction, *gain* is the cumulative UVC voltage and gain correction factor (if necessary),  $R_t$  and  $R_T$  are the time- and temperature-dependent sensitivity correction factors, respectively,  $C_{\lambda}$  is the high-dispersion calibration function,  $R_m$  is the ripple correction, and  $t_{eff}$  is the effective exposure time. Except for  $R_m$  and  $C_{\lambda}$ , all corrections are defined in the previous section concerning low-dispersion calibrations. No T/L response correction is used for high-dispersion trails, as they are obtained by slewing across the minor-axis (versus the major-axis for low-dispersion trails) of the aperture and therefore the low-dispersion T/L ratio is not applicable. The values for  $S_{\lambda}^{-1}$  and  $R_t$  are evaluated at the wavelength of each pixel through quadratic and nearest neighbor interpolation, respectively, of their tabulated values. The resulting absolutely calibrated units are ergs/cm<sup>2</sup>/Å/sec.

**Note:** an error in the application of the time-dependent sensitivity degradation correction for LWP and LWR high-dispersion images was detected after the majority of these images were processed by GSFC. The error is such that it applies an incorrect solution to fluxes longward of approximately 2712Å and is on the order of several percent shortward of 3000Å, but can increase to 20% or more beyond 3200Å. LWP and LWR images affected by this error can be identified by a NEWSIPS version number of 3.3.1 or 3.3.2 in the processing history portion of the FITS header. It is the project's intent to correct this error by re-archiving corrected high-dispersion merged extracted image FITS files (MXHIs). Such corrected files will be identifiable by notations in the NEWSIPS processing history. Corrected LWP and LWR MXHIs will carry NEWSIPS version numbers of 3.3.1\_A\_C and 3.3.2\_A\_C, respectively. Additionally, the version numbers in these corrected files will be appended with the following text: "(CORRECTED SENS. DEGRAD.)". Data processed with the corrected NEWSIPS high-dispersion image processing pipeline system will be identifiable by a NEWSIPS version number of 3.3.3.

# Chapter 12

## Final Archive Data Products

The output files for the IUE Final Archive are fundamentally different from those produced by IUESIPS, both in content and format. They are based on the Flexible Image Transport System (FITS) format (NOST 1995) and incorporate the FITS binary table extensions (NOST 1995) and FITS image extensions (Ponz, Thompson, and Muñoz 1994). Although some FITS reading routines may not yet support these new FITS extensions, it was felt that there was no convenient alternative FITS format available for storing IUE data. Note that only those features included in the basic binary table proposal (i.e., excluding the conventions described in the appendices of the proposal) have been used in the Final Archive file formats. The formats described below (as originally described in DCG 1995) have been approved by the IUE Three Agencies as well as the NOST FITS Support Office.

Because NEWSIPS data will be made available to the astronomical community via electronic transfer, the adopted FITS format is envisioned as both a disk file format and a tape file format. It should be pointed out, however, that disk file structures vary with operating systems. For this reason, users should consider the Final Archive data as being comprised of 2880-byte logical records which may or may not be identical to any physical record lengths. FITS files transferred to VAX VMS systems using FTP for example, typically have 512-byte rather than 2880-byte records.

### 12.1 FITS File Formats

The various files associated with each image represent the stages of NEWSIPS processing starting with the raw image (RI) file and ending with the merged extracted image (MX) file containing fluxes, wavelengths and data quality ( $\nu$ ) flags. The Final Archive FITS files produced for low-dispersion images include the following:

**RILO** The RI stored as a FITS primary array. If a partial read was used to obtain the image, an image extension is included containing the original unshifted RI (i.e., all corrections for registration errors are included in the primary array).

**LIL0** The linearized (i.e., photometrically corrected) image (LI) stored as a primary array with the associated array of  $\nu$  flags stored in a FITS image extension.

**VDLO** The vector displacements (VD) file contains the vector displacements, which map raw space into resampled space, and the cross-correlation coefficients (XC), which describe the mapping from raw space to the appropriate level of the raw space Intensity Transfer Function (ITF). The VD are stored as a three-dimensional (3-D) primary array, and the XC are stored in a FITS binary table extension.

**SILO** The resampled image (SI) stored as a primary array with the associated  $\nu$  flags in an image extension.

**MXLO** The MX stored in a binary table extension, with each row containing the data extracted from one aperture.

If the RILO contains spectra collected through both the large and small aperture, the VDLO, SILO, and MXLO will contain data from both apertures. This is a slight change from the IUESIPS processing in which separate files were created for each aperture.

In the case of a high-dispersion spectrum the following files are generated:

**RIHI** The RI (no partial-read image extensions are applicable).

**LIHI** The LI and associated  $\nu$  flags.

**VDHI** The VD and XC data.

**SIHI** The SI stored as a primary array, with wavelengths and predicted and found line positions stored in a binary table extension. The associated  $\nu$  and cosmic ray flags are contained in two image extensions.

**MXHI** The MX stored in a binary table extension with each row of the table representing data for one spectral order.

Some images may be processed as both high- and low-dispersion images and, consequently, will have both sets of files in the archive. In these cases, two copies of the RI file will appear in the archives, due to the dispersion-dependent keywords assigned during processing. All low- and high-dispersion Final Archive file formats are summarized in Tables 12.1 and 12.2. File sizes and formats summarized as “various” in these tables are explicitly described in the subsequent sections of this chapter.

## 12.2 FITS Header Format

The main source of information regarding the format and nature of IUE data contained in each FITS file is stored in the primary header. Each primary header includes the following sections:

Table 12.1: Low-Dispersion File Formats

File ID	Data Stored	Size	Format	FITS Type
RILO	Raw Image	768x768	8-bit	primary array
	Original Raw Image*	768x768	8-bit	image extension
LILO	Linearized Image	768x768	I*2	primary array
	Linearized Flag Image	768x768	I*2	image extension
SILO	Resampled Image	640x80	I*2	primary array
	Resampled Flag Image	640x80	I*2	image extension
VDLO	Vector Displacements	768x768x2	R*4	primary array
MXLO	Cross-correlation Parameters	various	various	binary table extension
	Extracted Spectra	various	various	binary table extension

\* In the case of partial-reads only.

Table 12.2: High-Dispersion File Formats

File ID	Data Stored	Size	Format	FITS Type
RIHI	Raw Image	768x768	8-bit	primary array
LIHI	Linearized Image	768x768	I*2	primary array
	Linearized Flag Image	768x768	I*2	image extension
VDHI	Vector Displacements	768x768x2	R*4	primary array
	Cross-correlation Parameters	various	various	binary table extension
SIHI	Resampled Image	768x768	I*2	primary array
	SIHI wavelengths and predicted and found line positions	various	various	binary table extension
	Resampled Flag Image	768x768	I*2	image extension
MXHI	SIHI Cosmic Ray Image	768x768	8-bit	image extension
	Extracted Spectra	various	various	binary table extension

- Basic FITS keywords,
- Core Data Items (CDIs),
- Original IUE VICAR label,
- NEWSIPS Image Processing History.

All of these items are contained solely in the primary header of each Final Archive file; the extension headers do not duplicate this information and contain only the basic FITS keywords needed to read the data stored in that extension (with the exception of the `FILENAME` keyword described below).

It should be noted that the structure of the FITS header is such that some information may appear in more than one form. For example, specific information may appear in multiple places in the original IUE label as well as in a CDI FITS keyword and/or the processing history. *In the instances where these entries disagree, the CDIs should always be considered the most reliable source.* The contents of each of these sections is described below. Examples

of complete low- and high-dispersion primary headers are also given at the conclusion of this section.

### 12.2.1 Basic FITS keywords

The basic FITS keywords define the structure and content of the files. These basic keywords include both the required FITS keywords and, when appropriate, certain optional reserved FITS keywords. Each line of the FITS header has the syntax **keyname** = **value** / **comments**, where **keyname** is the name of a FITS keyword conforming to the FITS keyword rules. The basic FITS keywords are itemized for each file type below. Although not shown, each FITS header must end with the required **END** keyword.

A project-defined keyword that needs to be mentioned is **FILENAME**. This keyword describes the camera image number and the type of data contained in the particular FITS header-and-data unit (HDU) and appears in every HDU containing data. For example, **FILENAME** would equal SWP09876.LILO in the LILO primary header and SWP09876.LFLO in the LILO extension header. In the corresponding MXLO, the **FILENAME** keyword appears in the binary table extension header with the value SWP09876.MXLO but does not appear in the primary header since the MXLO does not contain any primary array data.

One purpose of the **FILENAME** keyword is to provide users with a naming convention when separating FITS HDUs into separate disk files (e.g., when reading FITS files from tape). Since the primary header contains most or all of the information describing IUE images, it might be preferable to keep the files intact. In any event, the **FILENAME** keyword is useful for verifying the contents of the various data sets.

The value of the **FILENAME** keyword is formed by the concatenation of the following codes:

- Camera: 3 letter code (LWP, LWR, SWP).
- Image number: 5 digits.
- File type: 2 letter code as:

RI raw image

RO original RI (low dispersion only, in the case of partial-read images)

VD vector displacements

XC binary table extension of the VD file containing the cross correlation coefficients

LI linearized image

LF  $\nu$  flag image extension of the LI file

SI resampled image

WL binary table extension of the high-dispersion SI file containing spectral wavelengths and spatial centroid positions of the orders

SF  $\nu$  flag image extension of the high-dispersion SI file

**CR** cosmic ray image extension of the high-dispersion **SI** file

**MX** merged extracted image (large, small or both apertures)

- Dispersion: 2 letter code (**HI**, **LO**).

### 12.2.2 Core Data Items

The CDIs are defined to be the minimum set of parameters needed for image processing and scientific analysis. They include both input CDIs, which are verified before processing and used by NEWSIPS to determine the type of processing to be performed, and output CDIs, which are generated by NEWSIPS and verified during quality control after pipeline processing. The CDIs appear in the FITS header of each file, as well as in the IUE Final Observing Log. Each CDI is assigned a unique FITS keyword, although some CDIs may have multiple values and, therefore, require more than one FITS keyword. For example, low-dispersion double-aperture image files will contain the FITS keywords **LEXPTIME** and **SEXPTIME** to store the large- and small-aperture effective exposure times. For those cases in which the CDI is either unknown or undefined for a particular image, the related keyword will not be included in the header. This follows the standard convention for optional FITS keywords. A complete description of the CDIs is included in Chapter 14.

The portion of the header containing the CDIs may be divided into three sections:

- Common set (includes aperture-independent parameters),
- Large-aperture set,
- Small-aperture set.

Each set will be preceded by three **COMMENT** lines as indicated in the header examples given at the end of this section. Low-dispersion files corresponding to a single aperture exposure and all high-dispersion files will contain only the corresponding (large or small) CDI set.

### 12.2.3 Original IUE VICAR Label

Each image has an associated RI VICAR header, which was generated by the IUE Operations Control Center (IUEOCC) software during image acquisition and contains various scientific and engineering data pertinent to the image. This header, called the image label, consists of 72-byte lines containing EBCDIC and binary information as described in Table 12.3.

The image label, as well as any appendages which had been added by IUESIPS for database information or label corrections, is stored in the primary FITS header. Each line contains the original label information coded in ASCII, in bytes 9 to 80, with blanks in bytes 1 to 8. Lines originally coded in EBCDIC have been converted to ASCII, and lines containing binary data have been converted into 2 lines containing hexadecimal ASCII characters (e.g., the unsigned integer byte value 63 will become '3F'). The first line of hexadecimal ASCII characters contains bytes 1 through 33 of the original line of binary data and is stored in

Table 12.3: Summary of the IUE Raw Image VICAR Header

Line number	Description	Code
1-2	Image info. written by the system	EBCDIC
3-9	General comments	EBCDIC
10-32	Real-time command buffer	EBCDIC
33-35	Blanks	EBCDIC
36-37	GO information from POT tape	EBCDIC
38-50	Spares	EBCDIC
51-75	Data quality bits	Binary
76-82	S/C snapshot	Binary
83-85	Orbital elements and S/C info	EBCDIC
86-100	Camera snapshots	Binary
101-end	Databank parameters/IUESIPS Process History	EBCDIC

columns 9 through 74. The second line contains bytes 34 through 66 in columns 9 through 74. The traditional VICAR line number and continuation character are stored at the end of each line in bytes 75 through 80. In this format, the image label generally consists of approximately 150 lines in the FITS header. Four **COMMENT** lines precede the image label, and one **COMMENT** line flags the end of the label.

Note that lines 3–9 were entered by the Telescope Operator (TO) at the console and may occasionally contain errors. Lines 36–37, normally input from the Preplanned Observation Tape (POT), may be modified by the TO and, hence, are also subject to errors. The automatic entries on the other lines (10–32) are more accurate but can be affected, for instance, by ground computer problems. The binary-format portion of the image label (located in lines 51–82 and 86–100) is not usefully decoded when interpreted in hexadecimal ASCII characters and has been omitted from the header examples shown in the following subsection. Further information concerning the contents of the image label can be found in the IUESIPS Information Manual, Version 2.0 (Turnrose and Thompson 1984) and the IUE Image Header Document (GSFC 1986). For a guide to the translation of the event round robin in the image label, see Van Steenberg (1989).

#### 12.2.4 NEWSIPS Image Processing History

The image processing history includes the cumulative processing information generated by NEWSIPS. This history documents the processing system (software identification, version (if required), and hardware platform) and the individual application modules with the corresponding time stamps. Relevant variables used or computed by the various processing routines (e.g., median cross-correlation coefficient, dispersion constants, shifts used during the extraction, etc.) are also reported in the history. A complete processing history is in-



Each line of the history contains the keyword **HISTORY** in bytes 1 to 8, with processing information stored in bytes 9 to 74. Time stamps that designate the GMT times at which the individual application modules were executed are stored in bytes 65 to 72. Separate lines containing the processing date point out the start and end of the log. Examples of the processing history are outlined in the following subsections.

The following example shows the complete primary FITS header corresponding to an LWR, low-dispersion, double aperture RILO. In the case of a single aperture spectral image, the header includes only the corresponding large- or small-aperture set of CDIs.

	1	2	3	4	5	6	7	8
1234567890123456789012345678901234567890123456789012345678901234567890								
SIMPLE =	T / Standard FITS Format							
BITPIX =	8 / 8-bit integer pixels							
NAXIS =	2 / Two-dimensional image							
NAXIS1 =	768 / Dimension along x-axis							
NAXIS2 =	768 / Dimension along y-axis							
CTYPE1 = 'SAMPLE '	/ x-axis							
CTYPE2 = 'LINE '	/ y-axis							
BUNIT = 'DN '	/ Data Numbers							
TELESCOP= 'IUE '	/ International Ultraviolet Explorer							
FILENAME= 'LWR05625.RILO'	/ Filename(camera)(number).RI(disposition)							
DATE = '15/03/97'	/ Date file was written							
ORIGIN = 'GSFC '	/ Institution generating the file							
DATAMIN =	0.0 / Minimum pixel value							
DATAMAX =	255.0 / Maximum pixel value							
COMMENT *								
COMMENT * CORE DATA ITEMS - COMMON SET								
COMMENT *								
CAMERA = 'LWR '	/ Camera							
IMAGE =	5625 / Sequential image number							
DISPERSN= 'LOW '	/ Spectrograph dispersion mode							
APERTURE= 'BOTH '	/ Aperture							
DISPTYPE= 'LOW '	/ Dispersion processing type							
READMODE= 'FULL '	/ Read mode							
READGAIN= 'LOW '	/ Read gain							
EXPOGAIN= 'MAXIMUM '	/ Exposure gain							
UVC-VOLT=	-5.0 / UVC voltage							
ABNNSTD= 'NO '	/ Non-standard image acquisition							
ABNBADSC= 'NO '	/ LWP bad scans							
ABNHTRWU= 'NO '	/ LWR heater warmup							
ABNREAD = 'NO '	/ Read at other than 20 KB							
ABNUVC = 'NO '	/ Non-standard UVC voltage							
ABNHISTR= 'NO '	/ History replay							
ABNOTHER= 'NO '	/ Other abnormality							
THDAREAD=	12.84 / THDA at read of image							
EQUINOX =	1950.00 / Epoch of coordinates							
STATION = 'GSFC '	/ Observing station							
ORBEOPOCH= '13/09/79'	/ Orbital elements epoch							
ORBSAXIS=	42158.2 / Semi-major axis in kilometers							
ORBECCEN=	0.2363013 / Eccentricity							
ORBINCLI=	28.324 / Inclination in degrees							
ORBASCEN=	195.328 / Ascending node in degrees							

```

ORBPERIG=          269.795 / Argument of perigee in degrees
ORBANOMA=          174.024 / Mean anomaly in degrees
POSANGLE=          136.46 / Pos angle of the large aperture (deg)
LAMP   = 'NONE   '      / Lamp
PGM-ID  = 'CMBBS  '      / Program identification
ABNMINFR= 'NO      '      / Bad/missing minor frames
ABNMICRO= 'NO      '      / Microphonics
CC-PERCN=          97.3 / Cross-correlation % successful
CC-WINDW=          29 / Cross-correlation window size
CC-TEMPL=          23 / Cross-correlation template size
CC-MEDN =          0.807 / Median cross-correlation coefficient
CC-STDEV=          0.134 / St dev of cross-corr coefficients
SHFTMEAN=          0.084 / Mean shift between image and ITF
SHFTMAX =          0.515 / Maximum shift between image and ITF
ITF     = 'LWR83R96A'    / ITF identification
TILTCORR= 'NO      '      / Tilt correction flag
MEANRAT =          1.004 / SI vs LI mean
STDEVRA=          0.968 / SI vs LI standard deviation
COMMENT BY RA: EXP 1 APER L C=260,B=22
COMMENT BY RA: EXP 2 APER S B=22
COMMENT BY RA: LWR 0-MINUTE HEATER WARMUP
COMMENT BY RA: 0 MISSING MINOR FRAMES NOTED ON SCRIPT
COMMENT BY RA: EXP 1 TRACKED ON GYROS
COMMENT BY RA: EXP 2 TRACKED ON FES
COMMENT BY RA: XS PREP USED
COMMENT *
COMMENT * CORE DATA ITEMS - LARGE APERTURE SET
COMMENT *
LDATEOBS= '19/09/79'      / Observing date
LTIMEOBS= '06:46:55'      / Observing time
LJD-OBS =          2444135.78258 / Julian Date start of obs.
LEXPTRMD= 'NO-TRAIL'      / Trail mode
LEXPMULT= 'NO      '      / Multiple exposure mode
LEXPSEGM= 'NO      '      / Segmented exposure code
LEXPTIME=          4.789 / Integration time in seconds
LTHDASTR=          12.84 / THDA at start of exposure
LTHDAEND=          12.84 / THDA at end of exposure
LRA      =          119.3604 / Homogeneous R.A. in degrees
LDEC     =          -45.0787 / Homogeneous Dec. in degrees
LLAPSTAT= 'OPEN   '      / Large aperture status
LFES2MD  = 'FO     '      / FES(2) mode
LFES2CN  =          13578 / FES(2) counts on target
LTARGET  = 'HD 65904'      / Object as given by Guest Observer
LTARGRA  =          119.3604 / R.A. in degrees (given by GO)
LTARGDEC=          -45.0786 / Dec. in degrees (given by GO)
LOBJECT  = 'HD 65904'      / Homogeneous Object ID
LIUECLAS=          21 / Object class
LFOCUS   =          -1.08 / Focus
LFPM     =          0.44 / Flux particle monitor
LGSTAR2M= 'NO      '      / Guide star mode FES2
LJD-MID  =          2444135.78261 / Julian Date middle of obs.
LHEL CORR=          -.00212 / Heliocentric corr to midpoint (days)
LDATABKG=          27 / Estimated mean background level (DNs)
LDATACNT=          255 / Estimated maximum continuum level (DNs)
LCNTRAPR=          51.0 / Predicted center line of spectrum
LXTRMODE= 'POINT   '      / Extraction mode
LXTRPROF= 'EMPIRICAL'      / Profile used
LXTRASYM= 'NO      '      / Asymmetrical profile in extraction
LXTRCNTR=          51.0 / Center line of extracted spectrum
LFLUXAVE=          196.1 / Average flux (FNs)
COMMENT *
COMMENT * CORE DATA ITEMS - SMALL APERTURE SET
COMMENT *
SDATEOBS= '19/09/79'      / Observing date

```

```

STIMEOBS= '06:57:36'           / Observing time
SJD-OBS =      2444135.79000 / Julian Date start of obs.
SEXPTRMD= 'NO-TRAIL'          / Trail mode
SEXPMLT= 'NO'                 / Multiple exposure mode
SEXPSEGM= 'NO'                 / Segmented exposure code
SEXPTIME=      6.837 / Integration time in seconds
STHDASTR=      12.51 / THDA at start of exposure
STHDAEND=      12.84 / THDA at end of exposure
SRA =          119.3604 / Homogeneous R.A. in degrees
SDEC =         -45.0787 / Homogeneous Dec. in degrees
SLAPSTAT= 'CLOSED'           / Large aperture status
SFES2MD = 'FO'               / FES(2) mode
SFES2CN =      13704 / FES(2) counts on target
STARGET = 'HD 65904'          / Object as given by Guest Observer
STARGRA =      119.3604 / R.A. in degrees (given by GO)
STARGDEC=     -45.0786 / Dec. in degrees (given by GO)
SOBJECT = 'HD 65904'          / Homogeneous Object ID
SIUECLAS=      21 / Object class
SFOCUS =       -1.08 / Focus
SJD-MID =      2444135.79004 / Julian Date middle of obs.
SHEL CORR=     -0.00212 / Heliocentric corr to midpoint (days)
SDATABKG=      27 / Estimated mean background level (DNs)
SDATACNT=      176 / Estimated maximum continuum level (DNs)
SCNTRAPR=      24.6 / Predicted center line of spectrum
SXTRMODE= 'POINT'            / Extraction mode
SXTRPROF= 'EMPIRICAL'        / Profile used
SXTRASYM= 'NO'               / Asymmetrical profile in extraction
SXTRCNTR=      24.7 / Center line of extracted spectrum
SFLUXAVE=      132.3 / Average flux (FNs)
COMMENT *
COMMENT * THE IUE VICAR HEADER
COMMENT *
COMMENT IUE-VICAR HEADER START
                                0001000107680768   1 1 012105625           1 C
1448* 4*IUESOC * * * 12* * * * * * * * * * * * * * * * * * * * * * * * 2 C
LWR 5625, HD 65904, LOW DISP, SM 7 SEC, LG 5 SEC, US1                      3 C
                                                                4 C
OBSERVER: B.SAVAGE PROGRAM: IMBBS DATE: 1979.262 19 SEP                  5 C
                                                                6 C
                                                                7 C
                                                                8 C
                                                                9 C
79262075460* 9 * 218 *OPSDEV14*074851 TARGET FROM SWLA * 10 C
065220 EXPOBC 3 0 5 MAXG NOL *074925 APERTURE CLOSED * 11 C
065257 FIN 3 T 9 S 97 U 109 *075147 TARGET IN SWSA * 12 C
065338 TARGET FROM SWSA *075251 FESTRK TRACKING * 13 C
065521 TARGET IN LWSA *075343 EXPOBC 3 9 59 MAXG NOL * 14 C
065618 FESTRK TRACKING *075433 TLM,LWRROM * 15 C
065740 EXPOBC 2 0 6 MAXG NOL *075460 READPREP 2 IMAGE 5625 * 16 C
065818 FIN 2 T 11 S 98 U 109 *075532 SCAN READLO SS 1 G3 58 * 17 C
065859 TARGET FROM LWSA *075547 X 56 Y 72 G1 99 HT 106 * 18 C
070225 TLM,SWPROM *075523 * 19 C
070527 S/C READY FOR MANEUVER *075546 * 20 C
070605 READPREP 3 IMAGE 6565 *064206 TARGET IN SWLA * 21 C
070638 SCAN READLO SS 1 G3 44 *064222 FES 13265 IN 24 0 0 * 22 C
070656 X 60 Y 76 G1 82 HT 105 *064321 EXPOBC 3 0 3 MAXG NOL * 23 C
072635 TLM,FES2ROM *064357 FIN 3 T 3 S 97 U 109 * 24 C
072758 APERTURE OPEN *064441 TARGET FROM SWLA * 25 C
073729 FESIMAGE 0 0 81 *064610 TARGET IN LWLA * 26 C
073929 ACQ STARTED *064659 EXPOBC 2 0 4 MAXG NOL * 27 C
074243 TARGET IN SWLA *064735 FIN 2 T 4 S 98 U 109 * 28 C
074257 FES 6065 IN 12 0 0 *064816 TARGET FROM LWLA * 29 C
074427 FESTRK TRACKING *064839 APERTURE CLOSED * 30 C
074522 EXPOBC 3 2 29 MAXG NOL *065027 TARGET IN SWSA * 31 C

```

```

074757 FIN 3 T 149 S 97 U 109      *065123 FESTRK TRACKING      * 32 C
                                           33 C
                                           34 C
                                           35 C
IMBBS*1*02*SAVAGE      *   *   *H*   65904* *0*1* 13      36 C
0757264+450442* 0*B4*5* 6.0*      *   *   *   * 12*      37 C
                                           38 C
                                           39 C
                                           40 C
                                           41 C
                                           42 C
                                           43 C
                                           44 C
                                           45 C
                                           46 C
                                           47 C
                                           48 C
                                           49 C
                                           50 C
.
. (binary portion of the VICAR label suppressed in this example)
.
                                           83 C
                                           84 C
                                           85 C
.
. (binary portion of the VICAR label suppressed in this example)
.
00010082826B77697A2E7D00006140414000004040400204050B0C4040404040100 C
***RAW IMAGE*** C
*ARCHIVE 01:21Z SEP 23,'79 HL
COMMENT IUE-VICAR HEADER END
HISTORY IUE-LOG STARTED 15-MAR-1997 01:23:45
HISTORY PROCESSING SYSTEM: NEWSIPS VERSION 2.5.2
HISTORY ULTRIX VERSION
HISTORY LWR05625
HISTORY PROCESSED AT GODDARD SPACE FLIGHT CENTER
HISTORY *****
HISTORY *****
HISTORY START RAW_SCREEN 15-MAR-1997 01:25:47
HISTORY 18 BRIGHT SPOTS DETECTED
HISTORY 0 MISSING MINOR FRAMES DETECTED
HISTORY 0 LINES AFFECTED BY MICROPHONICS:
HISTORY LARGE APERTURE SPECTRUM WILL BE EXTRACTED AS
HISTORY POINT SOURCE
HISTORY LARGE APERTURE CONTINUUM DN LEVEL = 255
HISTORY SMALL APERTURE CONTINUUM DN LEVEL = 176
HISTORY BACKGROUND DN LEVEL = 27
HISTORY END RAW_SCREEN 15-MAR-1997 01:26:54
HISTORY *****
HISTORY START CROSS-CORR 15-MAR-1997 01:29:10
HISTORY WINDOW SIZE USED: 29 X 29 PIXELS
HISTORY TEMPLATE SIZE USED: 23 X 23 PIXELS
HISTORY ITF USED: LWR83R96A
HISTORY 97.4 PERCENT SUCCESSFUL CORRELATIONS (147 OUT OF 151)
HISTORY MEDIAN CORRELATION COEFFICIENT: 0.807
HISTORY STANDARD DEVIATION OF CORRELATION COEFFICIENT: 0.134
HISTORY ITF NOT USED: 0.653 MEDIAN CORRELATION COEFFICIENT
HISTORY MEAN SHIFT IN PIXELS: 0.084
HISTORY MAXIMUM SHIFT IN PIXELS: 0.515
HISTORY NUMBER OF SUCCESSFUL SHIFTS FILTERED AS UNRELIABLE IN
HISTORY POST-FILTER ROUTINE: 1
HISTORY END CROSS-CORR 15-MAR-1997 01:31:10
HISTORY *****

```

```

HISTORY START TTDC                                     15-MAR-1997 01:31:28
HISTORY TEMPERATURE USED FOR CORRECTING DISPERSION CONSTANTS = 12.84
HISTORY DATE OF OBSERVATION USED FOR CORRECTING
HISTORY          DISPERSION CONSTANTS = 19/ 9/79 06:46:55
HISTORY THIRD-ORDER FIT OVER TIME USED
HISTORY FIRST-ORDER FIT OVER TEMPERATURE USED
HISTORY ZERO-POINT CORRECTION = -0.82 ANGSTROMS
HISTORY SPATIAL CORRECTION = -2.18 PIXELS
HISTORY END TTDC                                       15-MAR-1997 01:31:30
HISTORY *****
HISTORY START PHOTOM                                   15-MAR-1997 01:31:49
HISTORY ITF USED: LWR83R96A
HISTORY MEAN TEMPERATURE OF ITF: 14.5 C
HISTORY ITF UVC=-5.0 KV; UVFLOOD WAVELENGTH = 2536 A; ITF SEC ==-6.1 KV
HISTORY ITF CONSTRUCTION: RAW SPACE, FOURIER FILTERED; SEP96
HISTORY END PHOTOM                                    15-MAR-1997 01:33:48
HISTORY *****
HISTORY START GEOM                                     15-MAR-1997 01:34:14
HISTORY WAVELENGTH LINEARIZATION APPLIED USING CHEBYSHEV COEFFICIENTS:
HISTORY          C(0) = 320.974
HISTORY          C(1) = 318.839
HISTORY          C(2) = -.47393
HISTORY          C(3) = 0.66076
HISTORY WAVELENGTH ZEROPOINT AND SPATIAL SHIFT APPLIED:
HISTORY          ZERO-POINT SHIFT = -23.30 ANGSTROMS
HISTORY          SPATIAL SHIFT = 1.29 PIXELS
HISTORY FINAL TIME/TEMP CORRECTED DISPERSION CONSTANTS USED:
HISTORY          1750.00 ANGSTROMS, 2.6692 ANGSTROMS/PIXEL
HISTORY PREDICTED CENTER LINE OF LARGE APERTURE = LINE 51.0
HISTORY PREDICTED CENTER LINE OF SMALL APERTURE = LINE 24.6
HISTORY END GEOM                                       15-MAR-1997 01:40:57
HISTORY *****
HISTORY START SWET                                     15-MAR-1997 01:41:25
HISTORY NOISE MODEL USED: LWR VERSION 1.0
HISTORY
HISTORY *****LARGE APERTURE DATA*****
HISTORY
HISTORY PREDICTED SPECTRUM CENTER AT LINE 51, CENTROID FOUND AT
HISTORY          LINE 51, PEAK AT LINE 51, AVERAGE PEAK FN = 196.1
HISTORY CROSS-DISPERSION PROFILES BINNED WITH A BLOCKSIZE OF 2 PIXELS,
HISTORY          FOR A TOTAL OF 300 BLOCKS, OF WHICH 61 ARE REJECTED
HISTORY FIT PROFILE WITH 15 NODES AND 3.50 SIGMA REJECTION
HISTORY PROFILE CENTROID AT LINE 51.0
HISTORY EXTRACT FLUX FROM LINES 45 THROUGH 57
HISTORY REJECT PIXELS DEVIATING BY 5.0 SIGMA
HISTORY OUT OF 8320 PIXELS 21 REJECTED AS COSMIC RAY HITS,
HISTORY          226 FLAGGED AS BAD
HISTORY ABSOLUTE FLUX CALIBRATION LWR VERSION 1.0 APPLIED USING:
HISTORY          MODE = LARGE APERTURE POINT SOURCE
HISTORY          CALIBRATION EPOCH = 1985.00
HISTORY          CAMERA RISE TIME = 0.126 SECONDS
HISTORY          EFFECTIVE EXPOSURE TIME = 4.789 SECONDS
HISTORY TEMPERATURE-DEPENDENT SENSITIVITY CORRECTION APPLIED USING:
HISTORY          THDA OF IMAGE = 12.84
HISTORY          REFERENCE THDA = 14.80
HISTORY          TEMPERATURE COEFFICIENT = -0.0089
HISTORY          TEMPERATURE CORRECTION FACTOR = 0.983
HISTORY SENSITIVITY DEGRADATION CORRECTION LWR VERSION 1.0 APPLIED USING:
HISTORY          MODE = LARGE APERTURE POINT SOURCE
HISTORY          CALIBRATION EPOCH = 1985.00
HISTORY          OBSERVATION DATE = 1979.718
HISTORY
HISTORY *****SMALL APERTURE DATA*****
HISTORY

```

```

HISTORY PREDICTED SPECTRUM CENTER AT LINE 25, CENTROID FOUND AT
HISTORY LINE 25, PEAK AT LINE 24, AVERAGE PEAK FN = 132.3
HISTORY CROSS-DISPERSION PROFILES BINNED WITH A BLOCKSIZE OF 1 PIXELS,
HISTORY FOR A TOTAL OF 600 BLOCKS, OF WHICH 122 ARE REJECTED
HISTORY FIT PROFILE WITH 15 NODES AND 3.50 SIGMA REJECTION
HISTORY PROFILE CENTROID AT LINE 24.7
HISTORY EXTRACT FLUX FROM LINES 19 THROUGH 31
HISTORY REJECT PIXELS DEVIATING BY 5.0 SIGMA
HISTORY OUT OF 8320 PIXELS 23 REJECTED AS COSMIC RAY HITS,
HISTORY 121 FLAGGED AS BAD
HISTORY ABSOLUTE FLUX CALIBRATION LWR VERSION 1.0 APPLIED USING:
HISTORY MODE = SMALL APERTURE POINT SOURCE
HISTORY CALIBRATION EPOCH = 1985.00
HISTORY CAMERA RISE TIME = 0.126 SECONDS
HISTORY EFFECTIVE EXPOSURE TIME = 6.837 SECONDS
HISTORY TEMPERATURE-DEPENDENT SENSITIVITY CORRECTION APPLIED USING:
HISTORY THDA OF IMAGE = 12.84
HISTORY REFERENCE THDA = 14.80
HISTORY TEMPERATURE COEFFICIENT = -0.0089
HISTORY TEMPERATURE CORRECTION FACTOR = 0.983
HISTORY SENSITIVITY DEGRADATION CORRECTION LWR VERSION 1.0 APPLIED USING:
HISTORY MODE = LARGE APERTURE POINT SOURCE
HISTORY APPLIED TO SMALL APERTURE DATA
HISTORY CALIBRATION EPOCH = 1985.00
HISTORY OBSERVATION DATE = 1979.718
HISTORY END SWET 15-MAR-1997 01:42:18
HISTORY *****
HISTORY START FITSCOPY 15-MAR-1997 01:42:30
END

```

### 12.2.4.2 High-dispersion Header Example

The following example shows the FITS header corresponding to an SWP high-dispersion RIHI.

```

      1      2      3      4      5      6      7      8
1234567890123456789012345678901234567890123456789012345678901234567890
SIMPLE = T / Standard FITS Format
BITPIX = 8 / 8-bit integer pixels
NAXIS = 2 / Two-dimensional image
NAXIS1 = 768 / Dimension along x-axis
NAXIS2 = 768 / Dimension along y-axis
CTYPE1 = 'SAMPLE' / x-axis
CTYPE2 = 'LINE' / y-axis
BUNIT = 'DN' / Data Numbers
TELESCOP = 'IUE' / International Ultraviolet Explorer
FILENAME = 'SWP37983.RIHI' / Filename(camera)(number).RI(dis)
DATE = '10/01/97' / Date file was written
ORIGIN = 'GSFC' / Institution generating the file
DATAMIN = 0.0 / Minimum pixel value
DATAMAX = 255.0 / Maximum pixel value
COMMENT *
COMMENT * CORE DATA ITEMS - COMMON SET
COMMENT *
CAMERA = 'SWP' / Camera
IMAGE = 37983 / Sequential image number
DISPERSN = 'HIGH' / Spectrograph dispersion mode
APERTURE = 'LARGE' / Aperture
DISPTYPE = 'HIGH' / Dispersion processing type
READMODE = 'FULL' / Read mode
READGAIN = 'LOW' / Read gain
EXPORGAIN = 'MAXIMUM' / Exposure gain

```

```

UVC-VOLT=          -5.0 / UVC voltage
ABNNOSTD= 'NO      ' / Non-standard image acquisition
ABNBADSC= 'NO      ' / LWP bad scans
ABNHTRWU= 'NO      ' / LWR heater warmup
ABNREAD = 'NO      ' / Read at other than 20 KB
ABNUVC = 'NO      ' / Non-standard UVC voltage
ABNHISTR= 'NO      ' / History replay
ABNOTHER= 'NO      ' / Other abnormality
THDAREAD=          10.84 / THDA at read of image
EQUINOX =          1950.00 / Epoch of coordinates
STATION = 'GSFC    ' / Observing station
ORBEOCH= '09/01/90' / Orbital elements epoch
ORBSAXIS=          42162.1 / Semi-major axis in kilometers
ORBECCEN=          0.1507207 / Eccentricity
ORBINCLI=          32.096 / Inclination in degrees
ORBASCEN=          121.734 / Ascending node in degrees
ORBPERIG=          349.052 / Argument of perigee in degrees
ORBANOMA=          308.612 / Mean anomaly in degrees
POSANGLE=          181.87 / Pos angle of the large aperture (deg)
LAMP = 'NONE      ' / Lamp
PGM-ID = 'PHCAL    ' / Program identification
ABNMINFR= 'NO      ' / Bad/missing minor frames
CC-PERCN=          81.3 / Cross-correlation % successful
CC-WINDW=          29 / Cross-correlation window size
CC-TEMPL=          23 / Cross-correlation template size
CC-MEDN =          0.385 / Median cross-correlation coefficient
CC-STDEV=          0.140 / St dev of cross-corr coefficients
SHFTMEAN=          0.467 / Mean shift between image and ITF
SHFTMAX =          2.850 / Maximum shift between image and ITF
ITF = 'SWP85R92A' / ITF identification
TILTCORR= 'NO      ' / Tilt correction flag
MEANRAT =          1.014 / SI vs LI mean
STDEVSTAT=          0.984 / SI vs LI standard deviation
COMMENT BY RA: EXP 1 APER L C=165,B=30
COMMENT BY RA: 0 MISSING MINOR FRAMES NOTED ON SCRIPT
COMMENT BY RA: EXP 1 TRACKED ON GYROS
COMMENT BY RA: S PREP USED
COMMENT *
COMMENT * CORE DATA ITEMS - LARGE APERTURE SET
COMMENT *
LDATEOBS= '10/01/90' / Observing date
LTIMEOBS= '03:56:12' / Observing time
LJD-OBS =          2447901.66403 / Julian Date start of obs.
LEXPTRMD= 'NO-TRAIL' / Trail mode
LEXPMLT= 'NO      ' / Multiple exposure mode
LEXPSEGM= 'NO      ' / Segmented exposure code
LEXPTIME=          5.604 / Integration time in seconds
LTHDASTR=          11.18 / THDA at start of exposure
LTHDAEND=          11.18 / THDA at end of exposure
LRA =          206.3929 / Homogeneous R.A. in degrees
LDEC =          49.5623 / Homogeneous Dec. in degrees
LLAPSTAT= 'OPEN    ' / Large aperture status
LFES2MD = 'FU      ' / FES(2) mode
LFES2CN =          3935 / FES(2) counts on target
LTARGET = 'ETA UMA ' / Object as given by Guest Observer
LTARGRA =          206.3925 / R.A. in degrees (given by GO)
LTARGDEC=          49.5619 / Dec. in degrees (given by GO)
LOBJECT = 'HD 120315' / Homogeneous Object ID
LIUECLAS=          21 / Object class
LFOCUS =          -0.23 / Focus
LFPM =          0.59 / Flux particle monitor
LGSTAR2M= 'NO      ' / Guide star mode FES2
LJD-MID =          2447901.66406 / Julian Date middle of obs.
LHELCCORR=          0.00131 / Heliocentric corr to midpoint (days)

```

```

LDATABKG=                29 / Estimated mean background level (DNs)
LDATACNT=                156 / Estimated maximum continuum level (DNs)
LCNTRAPR=                290.74 / Predicted center line of spectrum
LXTRMODE= 'POINT'        / Extraction mode
LXTRCNTR=                290.5 / Center line of extracted spectrum
LRADVELO=                19.59 / Heliocentric velocity correction in km/s
COMMENT *
COMMENT * THE IUE VICAR HEADER
COMMENT *
COMMENT IUE-VICAR HEADER START
      895 895 768 768    1 1 013037983    +101    1 C
      8964* 12*IUESOC * * * 6* * * * * * * * * * 2 C
SWP 37983, ETA UMA, 6 SEC EXPO, HIGH DISPERSION, LGAP    3 C
ERRORS AT REF POINT AFTER EXPO: EX = 1 , EY = -1    4 C
                                                    5 C
                                                    6 C
OBSERVER: GARHART      ID: PHCAL    10 JAN 1990, DAY 010    7 C
                                                    8 C
                                                    9 C
90 10045117* 10 * 218 *OPS2PR11*043729 TLM,FES2ROM    * 10 C
031754 MODE LWH      *045023 TLM,SWPROM    * 11 C
031921 TLM,LWPROM      *045117 READPREP 3 IMAGE 37983    * 12 C
031952 READPREP 1 IMAGE 17119    *045200 SCAN READLO SS 1 G3 44    * 13 C
032031 SCAN READLO SS 1 G3 47    *045217 X 60 Y 76 G1 82 HT 105    * 14 C
032046 X 53 Y 71 G1 97 HT 106    *045151    * 15 C
034446 TLM,FES2ROM      *045216    * 16 C
034926 FES CTS 3921 0 1 2560    *022057 TRAIL 3 .460830E 00    * 17 C
035000 TARGET IN LWLA      *022128 FES CTS 473 0 0 2560    * 18 C
035111 EXPOBC 1 0 5      MAXG NOL    *022204 TARGET IN SWLA    * 19 C
035152 FIN 1 T 4 S 97 U 108    *022559 EXPOBC 3 25 0      MAXG NOL    * 20 C
035243 TARGET FROM LWLA      *022918 MODTIME 3 0 0    * 21 C
035429 FES CTS 3935 0 1 1024    *022953 FIN 3 T 193 S 97 U 109    * 22 C
035507 TARGET IN SWLA      *023107 TARGET FROM SWLA    * 23 C
035617 EXPOBC 3 0 6      MAXG NOL    *023158 ITER 1 TIME .433999E 02    * 24 C
035701 FIN 3 T 5 S 97 U 109    *024404 S/C READY FOR MANEUVER    * 25 C
035758 TARGET FROM SWLA      *024427 MODE SWH    * 26 C
041054 S/C READY FOR MANEUVER    *024459 TLM,SWPROM    * 27 C
041121 TLM,LWPROM      *024547 READPREP 3 IMAGE 37982    * 28 C
041202 READPREP 1 IMAGE 17120    *024622 SCAN READLO SS 1 G3 44    * 29 C
041234 SCAN READLO SS 1 G3 47    *024637 X 60 Y 76 G1 82 HT 105    * 30 C
041255 X 53 Y 71 G1 97 HT 106    *025155 S/C MANEUVERING    * 31 C
041751 S/C MANEUVERING      *030825 TLM,FES2ROM    * 32 C
                                                    33 C
                                                    34 C
                                                    35 C
PHCAL*1*20*GARHART      * 21* *0* ETA UMA*0*0*1* 21    36 C
1345342+493343* 0*B3*5*1.84* 0.02*      * * 999.99* *    37 C
                                                    38 C
                                                    39 C
                                                    40 C
                                                    41 C
                                                    42 C
                                                    43 C
                                                    44 C
                                                    45 C
                                                    46 C
                                                    47 C
                                                    48 C
                                                    49 C
                                                    50 C
.
. (binary portion of the VICAR label suppressed in this example)
.
2447886.5      .0 42163.1 .151032 32.0417121.9482-11.4203294.824 83 C

```



```

10025151 1345342+493343251 8 2 10041747 034102+5337181124420 84 C
9231403 1045335+3750 32744921 10004626 8 4431+75 6473473851 85 C
.
. (binary portion of the VICAR label suppressed in this example)
.
AED9D443496CB76DB731B73142614000000000404040010319F1C2404040404040100 C
90123104337983L 000006 G 1APC
PHCALGO* ETA UMA 1345342493343+00112 2APC
GARHART 3APC
90365 6 90 1003570190 1004511714221108001H 4APC
***** RAW IMAGE: T3HLAC ***** C
*GOT_FMTOUTTAPE/GOT_MASKCON 14:27Z JAN 10,'90 HL
COMMENT IUE-VICAR HEADER END
HISTORY IUE-LOG STARTED 10-JAN-1997 03:09:04
HISTORY PROCESSING SYSTEM: NEWSIPS VERSION 3.1_A
HISTORY OPEN VMS VERSION
HISTORY SWP37983
HISTORY PROCESSED AT GODDARD SPACE FLIGHT CENTER
HISTORY *****
HISTORY *****
HISTORY START RAW_SCREEN 10-JAN-1997 03:09:14
HISTORY 9 BRIGHT SPOTS DETECTED
HISTORY 0 MISSING MINOR FRAMES DETECTED
HISTORY LARGE APERTURE SPECTRUM WILL BE EXTRACTED AS
HISTORY POINT SOURCE
HISTORY LARGE APERTURE CONTINUUM DN LEVEL = 156
HISTORY BACKGROUND DN LEVEL = 29
HISTORY ORDER REGISTRATION
HISTORY GLOBAL OFFSET -0.08 PIXELS RELATIVE TO FIDUCIAL: SWP 13589
HISTORY RELATIVE ORDER LOCATIONS DETERMINED FROM EMPIRICAL POSITIONS
HISTORY END RAW_SCREEN 10-JAN-1997 03:09:39
HISTORY *****
HISTORY START TTDC 10-JAN-1997 03:09:42
HISTORY TEMPERATURE USED FOR CORRECTING DISPERSION CONSTANTS = 11.18
HISTORY DATE OF OBSERVATION USED FOR CORRECTING
HISTORY DISPERSION CONSTANTS = 10/ 1/90 03:56:12
HISTORY ORDER 66 ZERO-POINT CORRECTION = -0.071 ANGSTROMS
HISTORY ORDER 67 ZERO-POINT CORRECTION = -0.071 ANGSTROMS
HISTORY ORDER 68 ZERO-POINT CORRECTION = -0.070 ANGSTROMS
HISTORY ORDER 69 ZERO-POINT CORRECTION = -0.067 ANGSTROMS
HISTORY ORDER 70 ZERO-POINT CORRECTION = -0.066 ANGSTROMS
HISTORY ORDER 71 ZERO-POINT CORRECTION = -0.065 ANGSTROMS
HISTORY ORDER 72 ZERO-POINT CORRECTION = -0.066 ANGSTROMS
HISTORY ORDER 73 ZERO-POINT CORRECTION = -0.066 ANGSTROMS
HISTORY ORDER 74 ZERO-POINT CORRECTION = -0.066 ANGSTROMS
HISTORY ORDER 75 ZERO-POINT CORRECTION = -0.065 ANGSTROMS
HISTORY ORDER 76 ZERO-POINT CORRECTION = -0.063 ANGSTROMS
HISTORY ORDER 77 ZERO-POINT CORRECTION = -0.063 ANGSTROMS
HISTORY ORDER 78 ZERO-POINT CORRECTION = -0.062 ANGSTROMS
HISTORY ORDER 79 ZERO-POINT CORRECTION = -0.063 ANGSTROMS
HISTORY ORDER 80 ZERO-POINT CORRECTION = -0.061 ANGSTROMS
HISTORY ORDER 81 ZERO-POINT CORRECTION = -0.060 ANGSTROMS
HISTORY ORDER 82 ZERO-POINT CORRECTION = -0.060 ANGSTROMS
HISTORY ORDER 83 ZERO-POINT CORRECTION = -0.059 ANGSTROMS
HISTORY ORDER 84 ZERO-POINT CORRECTION = -0.059 ANGSTROMS
HISTORY ORDER 85 ZERO-POINT CORRECTION = -0.058 ANGSTROMS
HISTORY ORDER 86 ZERO-POINT CORRECTION = -0.059 ANGSTROMS
HISTORY ORDER 87 ZERO-POINT CORRECTION = -0.057 ANGSTROMS
HISTORY ORDER 88 ZERO-POINT CORRECTION = -0.056 ANGSTROMS
HISTORY ORDER 89 ZERO-POINT CORRECTION = -0.056 ANGSTROMS
HISTORY ORDER 90 ZERO-POINT CORRECTION = -0.055 ANGSTROMS
HISTORY ORDER 91 ZERO-POINT CORRECTION = -0.056 ANGSTROMS
HISTORY ORDER 92 ZERO-POINT CORRECTION = -0.055 ANGSTROMS
HISTORY ORDER 93 ZERO-POINT CORRECTION = -0.054 ANGSTROMS

```

```

HISTORY ORDER 94 ZERO-POINT CORRECTION = -0.055 ANGSTROMS
HISTORY ORDER 95 ZERO-POINT CORRECTION = -0.058 ANGSTROMS
HISTORY ORDER 96 ZERO-POINT CORRECTION = -0.052 ANGSTROMS
HISTORY ORDER 97 ZERO-POINT CORRECTION = -0.051 ANGSTROMS
HISTORY ORDER 98 ZERO-POINT CORRECTION = -0.053 ANGSTROMS
HISTORY ORDER 99 ZERO-POINT CORRECTION = -0.050 ANGSTROMS
HISTORY ORDER 100 ZERO-POINT CORRECTION = -0.052 ANGSTROMS
HISTORY ORDER 101 ZERO-POINT CORRECTION = -0.050 ANGSTROMS
HISTORY ORDER 102 ZERO-POINT CORRECTION = -0.047 ANGSTROMS
HISTORY ORDER 103 ZERO-POINT CORRECTION = -0.046 ANGSTROMS
HISTORY ORDER 104 ZERO-POINT CORRECTION = -0.045 ANGSTROMS
HISTORY ORDER 105 ZERO-POINT CORRECTION = -0.044 ANGSTROMS
HISTORY ORDER 106 ZERO-POINT CORRECTION = -0.043 ANGSTROMS
HISTORY ORDER 107 ZERO-POINT CORRECTION = -0.043 ANGSTROMS
HISTORY ORDER 108 ZERO-POINT CORRECTION = -0.042 ANGSTROMS
HISTORY ORDER 109 ZERO-POINT CORRECTION = -0.041 ANGSTROMS
HISTORY ORDER 110 ZERO-POINT CORRECTION = -0.040 ANGSTROMS
HISTORY ORDER 111 ZERO-POINT CORRECTION = -0.039 ANGSTROMS
HISTORY ORDER 112 ZERO-POINT CORRECTION = -0.038 ANGSTROMS
HISTORY ORDER 113 ZERO-POINT CORRECTION = -0.037 ANGSTROMS
HISTORY ORDER 114 ZERO-POINT CORRECTION = -0.036 ANGSTROMS
HISTORY ORDER 115 ZERO-POINT CORRECTION = -0.035 ANGSTROMS
HISTORY ORDER 116 ZERO-POINT CORRECTION = -0.033 ANGSTROMS
HISTORY ORDER 117 ZERO-POINT CORRECTION = -0.032 ANGSTROMS
HISTORY ORDER 118 ZERO-POINT CORRECTION = -0.031 ANGSTROMS
HISTORY ORDER 119 ZERO-POINT CORRECTION = -0.030 ANGSTROMS
HISTORY ORDER 120 ZERO-POINT CORRECTION = -0.029 ANGSTROMS
HISTORY ORDER 121 ZERO-POINT CORRECTION = -0.027 ANGSTROMS
HISTORY ORDER 122 ZERO-POINT CORRECTION = -0.026 ANGSTROMS
HISTORY ORDER 123 ZERO-POINT CORRECTION = -0.025 ANGSTROMS
HISTORY ORDER 124 ZERO-POINT CORRECTION = -0.024 ANGSTROMS
HISTORY ORDER 125 ZERO-POINT CORRECTION = -0.022 ANGSTROMS
HISTORY
HISTORY SPACECRAFT VELOCITY:
HISTORY X= -2.59      Y= -1.57      Z=  1.90
HISTORY EARTH VELOCITY:
HISTORY X=-28.54     Y= -9.29      Z= -4.03
HISTORY NET CORRECTION VECTOR TO HELIOCENTRIC VELOCITY:
HISTORY X=-31.13     Y=-10.86     Z= -2.13
HISTORY HELIOCENTRIC VELOCITY CORRECTION: +19.59 KM/S
HISTORY END      TTDC                                10-JAN-1997 03:09:50
HISTORY *****
HISTORY START CROSS-CORR                                10-JAN-1997 03:09:56
HISTORY WINDOW SIZE USED:    29 X  29 PIXELS
HISTORY TEMPLATE SIZE USED:  23 X  23 PIXELS
HISTORY ITF USED:  SWP85R92A
HISTORY 81.4 PERCENT SUCCESSFUL CORRELATIONS (415 OUT OF 510)
HISTORY MEDIAN CORRELATION COEFFICIENT: 0.385
HISTORY STANDARD DEVIATION OF CORRELATION COEFFICIENT: 0.140
HISTORY MEAN SHIFT IN PIXELS: 0.467
HISTORY MAXIMUM SHIFT IN PIXELS: 2.850
HISTORY NUMBER OF SUCCESSFUL SHIFTS FILTERED AS UNRELIABLE IN
HISTORY POST-FILTER ROUTINE: 7
HISTORY END      CROSS-CORR                                10-JAN-1997 03:10:47
HISTORY *****
HISTORY START PHOTOM                                10-JAN-1997 03:10:54
HISTORY ITF USED:  SWP85R92A
HISTORY MEAN TEMPERATURE OF ITF: 9.3 C
HISTORY ITF UVC=-5.0 KV; UVFLOOD WAVELENGTH = 2536 A; ITF SEC ==-6.1 KV
HISTORY ITF CONSTRUCTION: RAW SPACE, FOURIER FILTERED; JAN92
HISTORY END      PHOTOM                                10-JAN-1997 03:12:24
HISTORY *****
HISTORY START GEOM                                10-JAN-1997 03:12:26
HISTORY INTERIM EPOCH ORDER SPATIAL DEVIATION CORRECTION APPLIED

```

```
HISTORY DE-SPLOYING ANGLE OF -0.29E-04 RADIANS
HISTORY PREDICTED CENTER LINE OF ORDER 100 - LINE 290.74
HISTORY END      GEOM                      10-JAN-1997 03:21:27
HISTORY *****
HISTORY START COSMIC_RAY                  10-JAN-1997 03:21:43
HISTORY MEAN FN VALUE OF INTERORDER BACKGROUND =    9.566
HISTORY 13789 PIXELS GREATER THAN 2.000 SIGMA FLAGGED IN
HISTORY COSMIC_RAY IMAGE
HISTORY END      COSMIC_RAY              10-JAN-1997 03:22:08
HISTORY *****
HISTORY START BCKGRD                     10-JAN-1997 03:22:09
HISTORY INTERORDER POINTS IDENTIFIED FOR POINT SOURCE
HISTORY GLOBAL BACKGROUND DETERMINATION SUCCESSFUL
HISTORY NORMAL GRID INTERPOLATION
HISTORY END      BCKGRD                 10-JAN-1997 03:22:58
HISTORY *****
HISTORY START EXTRACT                    10-JAN-1997 03:23:01
HISTORY BOXCAR EXTRACTION
HISTORY NOISE MODEL USED: SWP VERSION 1.0
HISTORY *****
HISTORY *****LARGE APERTURE DATA*****
HISTORY MEAN SLIT HEIGHT FOR LARGE APERTURE POINT SOURCE USED FOR EACH ORDER
HISTORY ORDER 100 FOUND AT LINE 290.51
HISTORY *** WARNING: ORDER 111 EXPLICIT CENTROID DETERMINATION INVALID.
HISTORY FIDUCIAL CENTROID USED.
HISTORY *** WARNING: ORDER 114 EXPLICIT CENTROID DETERMINATION INVALID.
HISTORY FIDUCIAL CENTROID USED.
HISTORY *** WARNING: ORDER 118 EXPLICIT CENTROID DETERMINATION INVALID.
HISTORY FIDUCIAL CENTROID USED.
HISTORY *** WARNING: ORDER 120 EXPLICIT CENTROID DETERMINATION INVALID.
HISTORY FIDUCIAL CENTROID USED.
HISTORY *** WARNING: ORDER 121 EXPLICIT CENTROID DETERMINATION INVALID.
HISTORY FIDUCIAL CENTROID USED.
HISTORY *** WARNING: ORDER 122 EXPLICIT CENTROID DETERMINATION INVALID.
HISTORY FIDUCIAL CENTROID USED.
HISTORY *** WARNING: ORDER 123 EXPLICIT CENTROID DETERMINATION INVALID.
HISTORY FIDUCIAL CENTROID USED.
HISTORY *** WARNING: ORDER 124 EXPLICIT CENTROID DETERMINATION INVALID.
HISTORY FIDUCIAL CENTROID USED.
HISTORY *** WARNING: ORDER 125 EXPLICIT CENTROID DETERMINATION INVALID.
HISTORY FIDUCIAL CENTROID USED.
HISTORY SWP RIPPLE CORRECTION VERSION 2.0 APPLIED.
HISTORY ABSOLUTE FLUX CALIBRATION DERIVED FROM LOW DISPERSION FLUX
HISTORY CALIBRATION.
HISTORY ABSOLUTE FLUX CALIBRATION SWP VERSION 1.2 APPLIED USING:
HISTORY MODE = LARGE APERTURE POINT SOURCE
HISTORY CALIBRATION EPOCH = 1985.00
HISTORY CAMERA RISE TIME = 0.130 SECONDS
HISTORY EFFECTIVE EXPOSURE TIME =    5.604 SECONDS
HISTORY TEMPERATURE-DEPENDENT SENSITIVITY CORRECTION APPLIED USING:
HISTORY THDA OF IMAGE = 11.18
HISTORY REFERENCE THDA = 9.40
HISTORY TEMPERATURE COEFFICIENT = -0.0046
HISTORY TEMPERATURE CORRECTION FACTOR =    1.008
HISTORY SENSITIVITY DEGRADATION CORRECTION SWP VERSION 2.0 APPLIED USING:
HISTORY MODE = LARGE APERTURE POINT SOURCE
HISTORY CALIBRATION EPOCH = 1985.00
HISTORY OBSERVATION DATE = 1990.027
HISTORY END      EXTRACT                10-JAN-1997 03:23:20
HISTORY *****
HISTORY START FITSCOPY                   10-JAN-1997 03:23:24
END
```

## 12.3 Raw Image FITS File (RILO/RIHI)

The RI is the fundamental input for NEWSIPS. For the final archive, the original GO format RIs have been converted to FITS. Although the RI data remains unaltered, the VICAR label has been converted to FITS commentary keywords (including the conversion of the binary information to hexadecimal ASCII characters).

The RILO/RIHI contain a two-dimensional (2-D) primary array consisting of  $768 \times 768$  pixels. Each pixel is a data number (DN), coded as an 8-bit unsigned integer ranging from 0 to 255. The basic keywords are shown in Table 12.4.

During the preparation of input data for Final Archive processing, it was discovered that some low-dispersion partial read images were not properly registered for processing. These raw images are therefore shifted to put them into proper registration for future processing by NEWSIPS. In order to preserve the original (unaltered) data, the RILO contain both the corrected data in the primary array and the original unshifted RI data in an image extension. The format of the image extension data is identical to that described above for the primary array. Note that the RIHI are not affected, and in low dispersion only the corrected data, in the primary array, is used for further processing by NEWSIPS. The basic keywords for partial-read files are shown in Table 12.5.

Table 12.4: RILO/RIHI - Basic FITS Keywords

Keyword and value			Description
SIMPLE	=	T	Standard FITS Format
BITPIX	=	8	8-bit integer pixels
NAXIS	=	2	Two-dimensional image
NAXIS1	=	768	Dimension along x-axis
NAXIS2	=	768	Dimension along y-axis
CTYPE1	=	'SAMPLE '	x-axis
CTYPE2	=	'LINE '	y-axis
BUNIT	=	'DN '	Data Numbers
TELESCOP	=	'IUE '	International Ultraviolet Explorer
FILENAME	=	'AAAnnnnn.RIdd'	Filename (camera)(number).RI(dis)
DATE	=	'dd/mm/yy'	Date file was written
ORIGIN	=	'VILSPA '	Institution generating the file
DATAMIN	=	nnn.0	Minimum pixel value
DATAMAX	=	nnn.0	Maximum pixel value

Table 12.5: RILO Partial Read - Basic FITS Keywords

Keyword and value	Description
SIMPLE = T	Standard FITS Format
BITPIX = 8	8-bit integer pixels
NAXIS = 2	Two-dimensional image
NAXIS1 = 768	Dimension along x-axis
NAXIS2 = 768	Dimension along y-axis
EXTEND = T	Extension exists
CTYPE1 = 'SAMPLE '	x-axis
CTYPE2 = 'LINE '	y-axis
BUNIT = 'DN '	Data Numbers
TELESCOP= 'IUE '	International Ultraviolet Explorer
FILENAME= 'AAAnnnnn.RILO'	Filename (camera)(number).RI(disposition)
DATE = 'dd/mm/yy'	Date file was written
ORIGIN = 'VILSPA '	Institution generating the file
DATAMIN = nnn.0	Minimum pixel value
DATAMAX = nnn.0	Maximum pixel value
XTENSION= 'IMAGE '	Image extension
BITPIX = 8	Binary data
NAXIS = 2	Two-dimensional image
NAXIS1 = 768	Dimension of x-axis
NAXIS2 = 768	Dimension of y-axis
PCOUNT = 0	number of bytes following data matrix
GCOUNT = 1	number of groups
CTYPE1 = 'SAMPLE '	x-axis
CTYPE2 = 'LINE '	y-axis
BUNIT = 'DN '	Data Numbers
FILENAME= 'AAAnnnnn.ROLO'	Filename (camera)(number).RO(disposition)
EXTNAME = 'RISV '	Original raw image

## 12.4 Linearized Image FITS File (LILO/LIHI)

The LILO/LIHI contains linearized (i.e., photometrically-corrected) pixels expressed in flux number (FN) units and situated in RI space. Only the pixels in a swath along the spectrum (low dispersion) and inside the target ring (high dispersion) have been photometrically corrected. The actual FN values have been scaled up by a factor of 32 for storage. The LILO/LIHI contains the LI as a 2-D primary array consisting of  $768 \times 768$  pixels, with each pixel value coded as 16-bit, two's complement integers with bits stored in decreasing order of significance.

The associated  $\nu$  flags are stored as a 2-D array the same size as the LI data, in a FITS image extension using 16-bit, two's complement integers. No scaling is used for the array of  $\nu$  flags. For every pixel that is photometrically corrected, this image contains a corresponding  $\nu$  flag describing specific error conditions (if applicable) in the LI. Flagged pixels include those which suffer from saturation, are close to the edge of the photometric correction region, or require ITF curve extrapolation to compute an FN value. In addition, all pixels that have not been photometrically corrected, or are known to suffer from bright spots, reseaux, microphonics and/or missing minor frames, are appropriately flagged. Checking for microphonic noise is performed over the entire  $768 \times 768$  image for the LWR camera only. Each error condition is flagged by setting specific bits in the data quality integer array. (See Chapter 3 for more information on how the various error conditions are encoded.) Basic keywords in the main header and the image extension header are shown in Table 12.6.

Table 12.6: LILO/LIHI - Basic FITS Keywords

Keyword and value	Description
SIMPLE = T	Standard FITS Format
BITPIX = 16	16-bit 2's complement pixels
NAXIS = 2	Two-dimensional image
NAXIS1 = 768	Dimension along x-axis
NAXIS2 = 768	Dimension along y-axis
EXTEND = T	Extensions are present
CTYPE1 = 'SAMPLE '	x-axis
CTYPE2 = 'LINE '	y-axis
BUNIT = 'FN '	Flux Numbers
BSCALE = 3.1250E-02	real=tape*b scale+bzero
BZERO = 0.	offset
TELESCOP= 'IUE '	International Ultraviolet Explorer
FILENAME= 'AAAnnnnn.LIdd'	Filename(camera)(number).LI(dis)
DATE = 'dd/mm/yy'	Date file was written
ORIGIN = 'VILSPA '	Institution generating the file
DATAMIN = nnnnn.n	Minimum pixel value
DATAMAX = nnnnn.n	Maximum pixel value
XTENSION= 'IMAGE '	Image extension
BITPIX = 16	16-bit, 2's complement pixels
NAXIS = 2	Two-dimensional image
NAXIS1 = 768	Dimension along the x-axis
NAXIS2 = 768	Dimension along the y-axis
PCOUNT = 0	Number of bytes following data matrix
GCOUNT = 1	Number of groups
CTYPE1 = 'SAMPLE '	x-axis
CTYPE2 = 'LINE '	y-axis
BUNIT = ' '	Unitless
FILENAME= 'AAAnnnnn.LFdd'	Filename (camera)(number).LF(dis)
EXTNAME = 'LIF '	LIF pixel quality flags

## 12.5 Vector Displacement FITS File (VDLO/VDHI)

The VD defines the final SI coordinate values in the  $x$  (wavelength) and  $y$  (spatial) directions for every LI pixel. The final coordinates in SI space for any photometrically-corrected pixel in the LILO/LIHI are determined by:

$$x_{final} = VD(i, j, 1) - x\_offset(cam, disp)$$

$$y_{final} = VD(i, j, 2) - y\_offset(cam, disp)$$

where  $i$  and  $j$  range from 1 to 768, and  $x\_offset$  and  $y\_offset$  are given in the following table.

	$x\_offset$		$y\_offset$	
	disp=L	H	L	H
LWP	100	0	297	0
LWR	100	0	250	0
SWP	130	0	490	0

The output displacements between the SI and LI coordinates are recoverable by:

$$DELTA_x = VD(i, j, 1) - i \quad \text{and} \quad DELTA_y = VD(i, j, 2) - j,$$

where  $i$  and  $j$  range from 1 to 768.  $x_{final}$  and  $y_{final}$  contain the final x and y coordinates in the SILO/SIHI. The x and y coordinates of the displacement vectors are stored as a 3-D primary array consisting of 768x768x2 elements. The displacements are coded as 32-bit, floating point numbers.

The XC allow the user to recover the calculated displacement vectors, mapping the science image (in raw space) to the ITF. For each of the approximately 500 (140 for low dispersion) points used to obtain the displacement between the science image and the corresponding level of the ITF, the binary table extension will contain the following columns of information: science image  $x$ -position (I\*2), science image  $y$ -position (I\*2), ITF  $x$ -position at position of best match (R\*4), ITF  $y$ -position at position of best match (R\*4), the cross-correlation coefficient (R\*4), number of points used to calculate the coefficient (I\*2), and the ITF level used in the correlation (I\*2). The  $x$  and  $y$  positions correspond to the sample and line numbers in the RI. The resulting ITF positions of the best match are pre-filtered positions (before invalid matches have been identified and deleted) and will not necessarily correspond exactly to the photometric registration displacement components utilized to create the final displacement vector.

Basic keywords in the VDLO/VDHI headers and binary table extensions are shown in Table 12.7. Note that the CTYPE1 and CTYPE3 keyword values listed and as stored in the archived VDLO/VDHI are incorrect and should be interchanged. Unfortunately, this error was not discovered until the majority of images were processed and so was left uncorrected for consistency. Note also that the VDLO/VDHI will not be available for images processed at VILSPA, nor for images processed at GSFC after July 31, 1997.



Table 12.7: VDLO/VDHI - Basic FITS Keywords

Keyword and value	Description
SIMPLE = T	Standard FITS Format
BITPIX = -32	IEEE single precision floating point
NAXIS = 3	Three-dimensional image
NAXIS1 = 768	Dimension along x-axis
NAXIS2 = 768	Dimension along y-axis
NAXIS3 = 2	Dimension along z-axis
EXTEND = T	Extensions are present
CTYPE1 = ' ' ,	Units x-axis
CTYPE2 = 'PIXEL ' ,	Units y-axis
CTYPE3 = 'PIXEL ' ,	Units z-axis
BUNIT = 'PIXEL ' ,	Pixel units
TELESCOP= 'IUE ' ,	International Ultraviolet Explorer
FILENAME= 'AAAnnnnn.VDdd'	Filename(camera)(number).VD(disp)
DATE = 'dd/mm/yy'	Date file was written
ORIGIN = 'VILSPA ' ,	Institution generating the file
DATAMIN = nnnnn.n	Minimum pixel value
DATAMAX = nnnnn.n	Maximum pixel value
XTENSION= 'BINTABLE'	Table extension
BITPIX = 8	Binary data
NAXIS = 2	Two-dimensional table array
NAXIS1 = 20	Width of table in bytes
NAXIS2 = nnn	Number of entries in table
PCOUNT = 0	Number of bytes following data matrix
GCOUNT = 1	Number of groups
TFIELDS = 7	Number of fields in each row
TFORM1 = '1I ' ,	Count and data type for field 1
TTYPE1 = 'XRAW ' ,	Science image x-position
TUNIT1 = 'PIXEL ' ,	Unit is pixels
TFORM2 = '1I ' ,	Count and data type for field 2
TTYPE2 = 'YRAW ' ,	Science image y-position
TUNIT2 = 'PIXEL ' ,	Unit is pixel
TFORM3 = '1E ' ,	Count and data type for field 3
TTYPE3 = 'XITF ' ,	ITF x-position of best match
TUNIT3 = 'PIXEL ' ,	Unit is pixel
TFORM4 = '1E ' ,	Count and data type for field 4
TTYPE4 = 'YITF ' ,	ITF y-position of best match
TUNIT4 = 'PIXEL ' ,	Unit is pixel
TFORM5 = '1E ' ,	Count and data type for field 5
TTYPE5 = 'XCoeff ' ,	Cross correlation coefficient
TUNIT5 = ' ' ,	Unitless
TFORM6 = '1I ' ,	Count and data type for field 6
TTYPE6 = 'NPOINTS ' ,	Number of points used
TUNIT6 = ' ' ,	Unitless
TFORM7 = '1I ' ,	Count and data type for field 7
TTYPE7 = 'ITFLEVEL' ,	ITF level
TUNIT7 = ' ' ,	Unitless
FILENAME= 'AAAnnnnn.XCdd'	Filename (camera)(number).XC(disp)
EXTNAME = 'XCoeff ' ,	Cross correlation coefficients

## 12.6 Low-Dispersion Resampled Image FITS File (SILO)

The low-dispersion SI is produced by resampling the photometrically-corrected portion of the low-dispersion LI using the modified Shepard algorithm taken from the Numerical Algorithms Group (NAG) software package. Each pixel is resampled to the position determined by the summation of the vectors computed for:

- shift to photometric correction (ITF) raw space,
- shift from ITF space to geometrically-rectified space,
- rotation such that orders are horizontal,
- wavelength linearization,
- detilting of large-aperture spectra for extended sources only,
- alignment of the apertures for constant wavelength in the line direction,
- adjustment so that both long wavelength cameras provide coverage of the same spectral range,
- adjustment to maintain the spectrum at approximately the same location in the file in the spatial direction,
- adjustment to LWP data to put the large-aperture data at the top of the file, and
- corrections for the spatial deviations (cross-dispersion wiggles) for LWP and LWR data.

The low-dispersion SI is stored in the SILO as a 2-D (640 samples  $\times$  80 lines) primary array, with the  $y$  coordinate in pixels and the  $x$  coordinate in Ångströms. Each pixel represents a flux number (FN) scaled up by a factor of 32 for storage purposes. The pixels are coded as 16-bit, two's complement integers, with the bits stored in decreasing order of significance. When the image is displayed with the origin in the lower left corner, the large-aperture data appears at the top of the file and the wavelengths increase from left to right. The associated  $\nu$  flags are stored as a SILO image extension, which has the same dimensions as the primary array. Table 12.8 shows the basic FITS keywords for the main header and the image extension header. The starting wavelength and wavelength increment are stored as keywords in the primary header.

Table 12.8: SILO - Basic FITS Keywords

Keyword and value	Description
SIMPLE = T	Standard FITS Format
BITPIX = 16	16-bits 2's complement pixels
NAXIS = 2	Two-dimensional image
NAXIS1 = 640	Dimension along x-axis
NAXIS2 = 80	Dimension along y-axis
EXTEND = T	Extensions are present
CRPIX1 = 1.	x reference pixel
CRPIX2 = 1.	y reference pixel
CRVAL1 = nnnn.nn	Wavelength at reference pixel
CRVAL2 = 1.	Coordinate of CRPIX2
CDEL1 = nn.nnnn	Increment in wavelengths
CDEL2 = 1.	Increment unit along y-axis
CTYPE1 = 'WAVELENGTH'	Units along x-axis
CTYPE2 = 'SCAN'	Units along y-axis
BUNIT = 'FN'	Flux Numbers
BSCALE = 3.1250E-02	real=tape*bscale+bzero
BZERO = 0.	Pixel offset
TELESCOP= 'IUE'	International Ultraviolet Explorer
FILENAME= 'AAAnnnnn.SILO'	Filename(camera)(number).SILO
DATE = 'dd/mm/yy'	Date file was written
ORIGIN = 'VILSPA'	Institution generating the file
DATAMIN = nnnnn.n	Minimum pixel value
DATAMAX = nnnnn.n	Maximum pixel value
XTENSION= 'IMAGE'	Image extension
BITPIX = 16	16-bit 2's complement pixels
NAXIS = 2	Two-dimensional image
NAXIS1 = 640	Dimension along the x-axis
NAXIS2 = 80	Dimension along the y-axis
PCOUNT = 0	Number of bytes following data matrix
GCOUNT = 1	Number of groups
CRPIX1 = 1.	x reference pixel
CRPIX2 = 1.	y reference pixel
CRVAL1 = nnnn.nn	Coordinate of CRPIX1
CRVAL2 = 1.	Coordinate of CRPIX2
CDEL1 = nn.nnnn	Increment unit along the x-axis
CDEL2 = 1.	Increment unit along the y-axis
CTYPE1 = 'WAVELENGTH'	x-axis units
CTYPE2 = 'SCAN'	y-axis units
BUNIT = ''	Unitless
FILENAME= 'AAAnnnnn.SFLO'	Filename (camera)(number).SF(disposition)
EXTNAME = 'SILOF'	SILO pixel quality flags

## 12.7 High-Dispersion Resampled Image FITS File (SIHI)

The SIHI contains more information than stored in the corresponding low-dispersion file and, as a result, the FITS format is slightly more complex. Overall, the SIHI is comprised of a primary array containing the resampled image, a binary table of wavelengths and both predicted and found line positions, an image extension of  $\nu$  flags, and a second image extension of background cosmic ray flags.

The high-dispersion SI data is similar to the low-dispersion SI data except that the high-dispersion wavelength linearization varies with spectral order, and the entire image is stored in the primary array. Each pixel is resampled to the position determined by the summation of the vectors computed for:

- shift to photometric correction (ITF) raw space,
- shift from ITF space to geometrically-rectified space,
- rotation such that orders are horizontal,
- wavelength linearization,
- adjustment to maintain the echelle orders at approximately the same locations in the file in the spatial direction,
- corrections for the spatial deviations (cross-dispersion wiggles) for LWP, LWR, and SWP data,
- heliocentric velocity correction, and
- de-splaying correction.

The high-dispersion SI is stored in the SIHI as a 2-D (768 samples  $\times$  768 lines) primary array. Each pixel represents an FN scaled up by a factor of 32 for storage purposes. The pixels are coded as 16-bit, two's complement integers, with the bits stored in decreasing order of significance. When the image is displayed with the origin in the lower left corner, the short-wavelength, closely-spaced high order numbers appear at the bottom, and the long-wavelength, low order numbers appear at the top. Within each order, the wavelengths increase from left to right.

Because the wavelength linearization varies with spectral order, the starting wavelength and wavelength increment values vary with each order. This information is stored in a binary table extension to the SIHI, which follows the primary array. The entire contents of the binary table extension include:

- Order Number, one 8-bit integer.
- Starting wavelength, one double-precision floating point number. Heliocentric velocity correction has been applied.

- Wavelength increment, one double-precision floating point number.
- predicted line position of order centroid, one single-precision floating point number.
- line position where spectral centroid is found, one single-precision floating point number. (This is determined by the high-dispersion spectral flux extraction module and written back into the SIHI file retroactively.)

The associated  $\nu$  flags and cosmic ray flags are stored in the SIHI image extensions with the same dimensions and orientation as the high-dispersion SI data contained in the primary array. The pixel quality flags are stored as unscaled 16-bit integers, and the cosmic ray flags are unscaled 8-bit integers. Table 12.9 shows the basic FITS keywords for the main and extension headers for the SIHI.

Table 12.9: SIHI - Basic FITS Keywords (continued on next page)

Keyword and value	Description
SIMPLE = T	Standard FITS Format
BITPIX = 16	16-bit 2's complement pixels
NAXIS = 2	Two-dimensional image
NAXIS1 = 768	Dimension along x-axis
NAXIS2 = 768	Dimension along y-axis
EXTEND = T	Extensions are present
CTYPE1 = 'SAMPLE '	x-axis
CTYPE2 = 'LINE '	y-axis
BUNIT = 'FN '	Flux Numbers
BSCALE = 3.1250E-02	real=tape*b scale+bzero
BZERO = 0.	offset
TELESCOP= 'IUE '	International Ultraviolet Explorer
FILENAME= 'AAAnnnnn.SIHI'	Filename (camera)(number).SIHI
DATE = 'dd/mm/yy'	Date file was written
ORIGIN = 'VILSPA '	Institution generating the file
DATAMIN = nnnnn.n	Minimum pixel value
DATAMAX = nnnnn.n	Maximum pixel value
XTENSION= 'BINTABLE'	Binary table extension
BITPIX = 8	Binary data
NAXIS = 2	Two-dimensional table array
NAXIS1 = 25	Width of table in bytes
NAXIS2 = nn	Number of entries in table
PCOUNT = 0	Number of bytes following data matrix
GCOUNT = 1	Only one group
TFIELDS = 5	Number of fields in each row
TFORM1 = '1B '	8-bit byte
TTYPE1 = 'ORDER '	Order number
TUNIT1 = ' '	Unitless
TFORM2 = '1D '	Double precision floating point
TTYPE2 = 'WAVELENGTH'	Starting wavelength
TUNIT2 = 'ANGSTROM'	Unit is angstroms
TFORM3 = '1D '	Double precision floating point
TTYPE3 = 'DELTAW '	3rd field is wavelength increment
TUNIT3 = 'ANGSTROM'	Unit is angstrom
TFORM4 = '1E '	Single precision floating point
TTYPE4 = 'LINE_PREDICTED'	Predicted line position of order centroid
TUNIT4 = 'PIXEL '	Unit is pixel
TFORM5 = '1E '	Single precision floating point
TTYPE5 = 'LINE_FOUND'	Line number where spectral centroid is found
TUNIT5 = 'PIXEL '	Unit is pixel
FILENAME= 'AAAnnnnn.WLHI'	Filename (camera)(number).WLHI
EXTNAME = 'SIHIW '	Name of table

Table 12.9 SIHI File - continued

Keyword and value		Description
XTENSION= 'IMAGE '		Image extension
BITPIX =	16	16-bit 2's complement pixels
NAXIS =	2	Two-dimensional image
NAXIS1 =	768	Dimension of x-axis
NAXIS2 =	768	Dimension of y-axis
PCOUNT =	0	Number of bytes following data matrix
GCOUNT =	1	Number of groups
CTYPE1 = 'SAMPLE '		X-axis
CTYPE2 = 'LINE '		Y-axis
BUNIT = ' '		Unitless
FILENAME= 'AAAnnnnn.SFHI '		Filename (camera)(number).SF(disposition)
EXTNAME = 'SIHIF '		SIHI pixel quality flags
XTENSION= 'IMAGE '		Image extension
BITPIX =	8	8-bit integer pixels
NAXIS =	2	Two-dimensional image
NAXIS1 =	768	Dimension of x-axis
NAXIS2 =	768	Dimension of y-axis
PCOUNT =	0	Number of bytes following data matrix
GCOUNT =	1	Number of groups
CTYPE1 = 'SAMPLE '		X-axis
CTYPE2 = 'LINE '		Y-axis
BUNIT = ' '		Unitless
FILENAME= 'AAAnnnnn.CRHI '		Filename (camera)(number).CR(disposition)
EXTNAME = 'SIHIC '		SIHI cosmic ray background flags

## 12.8 Low-Dispersion Merged Extracted Image FITS File (MXLO)

The data extracted from the low-dispersion SI are stored in the MXLO using a binary table extension with fixed-length floating point vectors to contain the extracted fluxes and associated  $\nu$  flags. Since no primary data are included, the extension header immediately follows the primary header. Each row of the binary table includes the following columns:

- Aperture designation as ‘LARGE’ or ‘SMALL’, stored in 5 ASCII characters.
- Number of extracted points, one 16-bit integer. The number of extracted points is always 640.
- Starting wavelength, one single-precision floating point value.
- Wavelength increment, one single-precision floating point value.
- Net flux spectrum, array with 640 single-precision floating point values.
- Background flux spectrum, array with 640 single-precision floating point values.
- Sigma vector, array with 640 single-precision floating point values.
- $\nu$  flags, array of 640 16-bit integers stored in two’s complement form.
- Absolutely-calibrated net flux spectrum, array with 640 single-precision floating point values.

Wavelengths are linearly sampled to a uniform step size and measured in vacuum. Double aperture low-dispersion spectra will contain two rows in the above format, with one row for each aperture (LARGE first, then SMALL). Note the NAXIS1 keyword in the Binary table extension defines the number of bytes per row in the table and is equal to  $15 + 18 * 640$ , or 11,535 bytes.

The absolute calibration covers the range of 1150–1980Å for short-wavelength spectra and 1850–3350Å for long-wavelength spectra. Since the NEWSIPS software extracts data over a slightly larger wavelength range, data points outside this wavelength range are set to 0 in the absolutely-calibrated flux vector and  $-1$  in the sigma vector. The net and background vectors are not affected. The uncalibrated data points are also flagged in the  $\nu$  flag vector with the value of  $-2$ . Table 12.10 shows the basic FITS Keywords for the MXLO.



Table 12.10: MXLO - Basic FITS Keywords

Keyword and value			Description
SIMPLE	=	T	Standard FITS Format
BITPIX	=	8	8 bits ASCII
NAXIS	=	0	No image data
EXTEND	=	T	Extensions are present
TELESCOP	= 'IUE'		International Ultraviolet Explorer
DATE	= 'dd/mm/yy'		Date file is written
ORIGIN	= 'VILSPA'		Institution generating the file
XTENSION	= 'BINTABLE'		Table extension
BITPIX	=	8	Binary data
NAXIS	=	2	Two-dimensional table array
NAXIS1	=	11535	Bytes per row (15+18*NPOINTS)
NAXIS2	=	n	Number of apertures (1-single, 2-both)
PCOUNT	=	0	Number of bytes following data matrix
GCOUNT	=	1	Only one group
TFIELDS	=	9	Number of columns in the table
TFORM1	= '5A'		Count and data type of field 1
TTYPE1	= 'APERTURE'		Aperture type (large or small)
TUNIT1	= ''		Unitless
TFORM2	= '1I'		Field 2 has one 2-byte integer
TTYPE2	= 'NPOINTS'		Number of points
TUNIT2	= ''		Unitless
TFORM3	= '1E'		Count and data type of field 3
TTYPE3	= 'WAVELENGTH'		3rd field is starting wavelength
TUNIT3	= 'ANGSTROM'		Unit is angstrom
TFORM4	= '1E'		Count and data type of field 4
TTYPE4	= 'DELTAW'		4th field is wavelength increment
TUNIT4	= 'ANGSTROM'		Unit is Angstrom
TFORM5	= '640E'		Count and data type of field 5
TTYPE5	= 'NET'		5th field is net flux array
TUNIT5	= 'FN'		Unit is IUE FN
TFORM6	= '640E'		Count and data type of field 6
TTYPE6	= 'BACKGROUND'		6th field is background flux array
TUNIT6	= 'FN'		Unit is IUE FN
TFORM7	= '640E'		Count and data type of field 7
TTYPE7	= 'SIGMA'		7th field is the sigma
TUNIT7	= 'ERG/CM2/S/A'		Unit is erg/cm2/sec/Angstrom
TFORM8	= '640I'		Count and data type of field 8
TTYPE8	= 'QUALITY'		8th field is the data quality flag
TUNIT8	= ''		Unitless
TFORM9	= '640E'		Count and data type of field 9
TTYPE9	= 'FLUX'		9th field is the calibrated flux
TUNIT9	= 'ERG/CM2/S/A'		Unit is erg/cm2/sec/Angstrom
FILENAME	= 'AAAAnnnn.MXLO'		Filename (camera)(number).MXLO
EXTNAME	= 'MXLO'		Name of table

## 12.9 High-Dispersion Merged Extracted Image FITS File (MXHI)

The wavelengths,  $\nu$  flags, and fluxes extracted from the SIHI are stored in the MXHI as a binary table extension using fixed-length floating point vectors. No primary data or additional extensions are included.

The binary table contains 17 fields of various data types. All vectors are padded with zeroes (both before and after the extracted data) to maintain a fixed length of 768 points. Wavelengths are uniformly sampled for each order, are measured in vacuum, and have had the heliocentric velocity correction applied. The width of each row (i.e., **NAXIS1**) is  $65 + 22 \times 768 = 16,961$  bytes, and the number of rows (i.e., **NAXIS2**) is equal to the number of extracted orders. In this manner, all the information pertaining to one spectral order is contained in one row of the binary table. The fields are defined in the order shown below:

- Order number, one 8-bit byte.
- Number of extracted points **n**, one 16-bit integer.
- Starting wavelength, one double-precision floating point value.
- Starting pixel at starting wavelength, one 16-bit integer.
- Wavelength increment, one double-precision floating point value.
- Slit height in pixels, one single-precision floating point number.
- Line number for found centroid of spectrum, one single-precision floating point number.
- Net flux spectrum, 768 single-precision floating point numbers with **n** extracted data points.
- Background flux spectrum, 768 single-precision floating point numbers with **n** extracted data points.
- Noise vector, 768 single-precision floating point numbers with **n** extracted data points.
- $\nu$  flags as **n** 16-bit integers stored in two's complement form.
- Ripple-corrected net flux spectrum, 768 single-precision floating with **n** extracted data points.
- Absolutely-calibrated, ripple-corrected net flux spectrum, 768 single-precision floating point numbers. with **n** extracted data points.
- Start pixel for background fit, one 16-bit integer number.\*
- End pixel for background fit, one 16-bit integer number.\*

- Chebyshev scale factor, one single-precision floating point number.\*
- Chebyshev polynomial coefficients for global background correction, 7 single-precision floating point numbers.\*

Note that unlike the MXLO, SILO, and SIHI, the starting wavelengths listed in the MXHI table do not refer to the first data point in the flux vectors, but rather the starting pixel listed in field four. In this manner, the 768-point flux vector can be mapped directly to the 768-pixel wide high-dispersion SI array.

As in low dispersion, since the absolute calibration covers the range of 1150–1980Å for short-wavelength spectra and 1850–3350Å for long-wavelength spectra, data points outside this wavelength range are set to 0 in the absolutely-calibrated flux vector. The net, background, and noise vectors are not affected. (Note that unlike the sigma vector in the MXLO file, the MXHI noise vector is uncalibrated.) Uncalibrated data points are also flagged in the  $\nu$  flag vector with a value of  $-2$ . Table 12.11 shows the basic FITS Keywords for the MXHI.

\* **IMPORTANT NOTE:** Several adjustments must be made to the last four parameters (fields 14–17) if the user wishes to evaluate the Chebyshev coefficients in order to reproduce the background fluxes as stored in the ninth field of the MXHI extension header. First, the parameters have inadvertently been stored in the reverse order (i.e., the parameters written in the first row of the table should have been stored in the last row, the parameters for the second row in the second to last row, etc.). So, for example, in the case of the LWR camera, the starting and ending pixels, Chebyshev scale factor, and Chebyshev coefficients found in row 1 (echelle order 127) actually pertain to row 61 (echelle order 67). Second, the true starting pixel is 768 minus the stored ending pixel and the true ending pixel is 768 minus the stored starting pixel. These true pixel values must be used to correctly evaluate the Chebyshev coefficients. Third, once the Chebyshev coefficients have been evaluated, the resultant background “fluxes” must be scaled in the following manner: multiply each background value by both the Chebyshev scale factor and the corresponding extraction slit height then divide this result by 32. Finally, the resultant array of background fluxes which are produced upon evaluation of the Chebyshev coefficients must be reversed (i.e., the computed background flux for pixel 1 becomes the background flux for pixel 768 and vice versa). We emphasize that these reversals and scalings are needed *only* when using the Chebyshev parameters in fields 14–17 to reproduce the background fluxes—the background fluxes themselves as contained in the ninth field are correct.

Table 12.11: MXHI - Basic FITS Keywords (continued on next page)

Keyword and value			Description
SIMPLE	=	T	Standard FITS Format
BITPIX	=	8	Binary data
NAXIS	=	0	No image data
EXTEND	=	T	Extensions are present
TELESCOP	= 'IUE'		International Ultraviolet Explorer
DATE	= 'dd/mm/yy'		Date file was written
ORIGIN	= 'VILSPA'		Institution generating the file
XTENSION	= 'BINTABLE'		Binary table extension
BITPIX	=	8	Binary data
NAXIS	=	2	Two-dimensional table array
NAXIS1	=	16961	Width of row in bytes
NAXIS2	=	nn	Number of orders
PCOUNT	=	0	Number of bytes following data matrix
GCOUNT	=	1	Only one group
TFIELDS	=	17	Number of columns in the table
TFORM1	= '1B'		8-bit byte
TTYPE1	= 'ORDER'		Order number
TUNIT1	= ''		Unitless
TFORM2	= '1I'		16-bit integer
TTYPE2	= 'NPOINTS'		Number of non-zero points
TUNIT2	= ''		Unitless
TFORM3	= '1D'		Double precision
TTYPE3	= 'WAVELENGTH'		Starting wavelength
TUNIT3	= 'ANGSTROM'		Unit is Angstrom
TFORM4	= '1I'		16-bit integer
TTYPE4	= 'STARTPIX'		Starting pixel at starting wavelength
TUNIT4	= 'PIXEL'		Unit is pixel
TFORM5	= '1D'		Double precision value
TTYPE5	= 'DELTAW'		Wavelength increment
TUNIT5	= 'ANGSTROM'		Unit is Angstrom
TFORM6	= '1E'		Single precision
TTYPE6	= 'SLIT HEIGHT'		Height of extraction slit
TUNIT6	= 'PIXEL'		Unit is pixel
TFORM7	= '1E'		Single precision
TTYPE7	= 'LINE_FOUND'		Line number where spectral centroid is found
TUNIT7	= 'PIXEL'		Unit is pixel

Table 12.11 MXHI - continued

Keyword and value	Description
TFORM8 = '768E '	Single precision array
TTYPE8 = 'NET '	Net flux array
TUNIT8 = 'FN '	Unit is IUE Flux Number (FN)
TFORM9 = '768E '	Single precision array
TTYPE9 = 'BACKGROUND'	Background flux array
TUNIT9 = 'FN '	Unit is IUE Flux Number(FN)
TFORM10 = '768E '	Single precision array
TTYPE10 = 'NOISE '	Noise spectrum
TUNIT10 = 'FN '	Unit is IUE Flux Number (FN)
TFORM11 = '768I '	16-bit integer array
TTYPE11 = 'QUALITY '	Data quality flag
TUNIT11 = ' '	Unitless
TFORM12 = '768E '	Single precision array
TTYPE12 = 'RIPPLE '	Ripple-corrected net flux array
TUNIT12 = 'FN '	Unit is IUE Flux Number (FN)
TFORM13 = '768E '	Single precision array
TTYPE13 = 'ABS_CAL '	Absolutely-calibrated net flux
TUNIT13 = 'ERGS/CM2/S/A'	Unit is ergs/cm2/sec/Angstrom
TFORM14 = '1I '	16-bit integer
TTYPE14 = 'START-BKG'	Beginning pixel of background fit
TUNIT14 = 'PIXEL '	X-axis in SIHI image
TFORM15 = '1I '	16-bit integer
TTYPE15 = 'END-BKG '	End pixel of background fit
TUNIT15 = 'PIXEL '	X-axis in SIHI image
TFORM16 = '1E '	Single precision
TTYPE16 = 'SCALE_BKG'	Chebyshev scale factor
TUNIT16 = ' '	Unitless
TFORM17 = '7E '	Single precision array
TTYPE17 = 'COEFF '	Chebyshev coefficients of background fit
TUNIT17 = ' '	Unitless
FILENAME= 'AAAnnnnn.MXHI'	Filename (camera) (number) .MXHI
EXTNAME = 'MEHI '	Name of table

# Chapter 13

## Assessing NEWSIPS Data Quality

The processing techniques described in this manual provide some information on the quality of the image and the extracted spectral data which was not available with the previous IUESIPS processing. This information can be found in the processing HISTORY portion of the FITS label for each image. Each of these parameters is described below. In some cases, these output parameters can alert the user to the fact that the raw image data are corrupted or that the distortion of a particular image with respect to the ITF is unusually severe. Such problems are inherent in the raw data and cannot be overcome with processing techniques. Other parameters alert the user to difficulties with the extraction of the spectral data. In these cases, alternate extraction methods customized by the user may yield better results.

The “ITF cross-correlation parameters” (Item 3) refer to statistical information based on data obtained from the entire photometrically corrected region of the image. While these numbers can be useful for quick-look evaluations, the spatial data represented must be examined in two dimensions to understand fully the distortion characteristics of a particular image. These warnings therefore should be used with caution for anything but a gross categorization of image quality.

### 1. Raw Image Data Number (DN) levels:

These estimates are determined automatically during the raw-image screening process using the algorithms described in Chapter 4.8. These values may differ significantly from the estimates given in the RA comments field in the database, which is based on a manual estimate at the time the exposure was read down. The estimate of the exposure levels in the RA comments field is made in slightly different ways at GSFC and at VILSPA and is not necessarily consistent from image to image. The NEWSIPS background and continuum DN levels, on the other hand, are consistent for the entire archive.

*Maximum continuum.* This parameter gives an estimate of the exposure level of the raw spectral data. The maximum continuum DN level can be used to determine relative exposure differences between various observations of the same object. Of course, the spectral morphology of the object must be taken into account in evaluating the ex-

posure level of an image. In particular, one must be careful when using these numbers if they were determined from emission line objects. Contamination of the continuum level reading from an emission feature may occur in some instances when there is a large spectral format shift (e.g., due to target centering errors or objects with large redshifts).

*Mean Background.* The mean background DN level for a short exposure taken during a time of low radiation is about 20–40 DN. This is then the minimum background one would expect. Long exposures and exposures taken on high radiation shifts will have higher mean background DN levels. If the maximum continuum DN level is not at least 50 DN above the mean background DN level, the spectrum will most likely contain little useful data unless it is an emission line source.

## 2. High-dispersion order registration warnings:

Several warning conditions can occur during the high-dispersion order registration process which alert the user to a potential error in the spatial alignment of the science image relative to the fiducial. In each case, this may lead to a loss of flux in the extracted spectrum.

*Insufficient flux for empirical order registration. RMS of found vs. actual order positions > noise criterion. Predictions based on time and temperature will be used.* Indicates that the average RMS of the differences between the found and fiducial order positions exceeds 1.5 pixels or is equal to zero. The former condition usually occurs as a result of a lack of flux in the spectral orders, while an RMS of zero can be produced by images with heavy saturation or unusually large numbers of missing minor frames (MMFs). A potential error in the alignment of the high-dispersion resampled image (SI) with respect to the fiducial image may take place, as use of the predicted time and temperature motions do not take into account target centering errors or the use of an offset reference point when placing the target in the aperture. As a result of the misalignment of the high-dispersion SI, a loss of flux may be seen in the extracted spectrum.

*Insufficient flux for empirical order registration. Too few valid orders found. Predictions based on time and temperature will be used.* Denotes that the total number of orders found is less than 3 (5 for the SWP). The potential errors involved in the use of predicted time and temperature motions are the same as those described in the previous condition.

*Global offset nn pixels relative to fiducial. Relative order locations defaulted to those of the fiducial.* Signals the user that the distribution of the orders is incorrect and that only the global offset will be used. Usage of the global offset for alignment of the high-dispersion SI does not take into account differential expansions and contractions of the order separations. As a result, minor miscenterings of the extraction slit for orders at the short- and long-wavelength ends of the camera may occur resulting in a slight loss of flux for particular orders.

*Found offset exceeds threshold of 4 pixels. Predictions based on global offset will be used.* This condition happens when the maximum shift for an individual order exceeded the threshold value. Use of the global offset may yield extraction errors as defined in the previous condition. This error condition is only applicable to the long-wavelength cameras.

### 3. ITF cross-correlation parameters:

These numbers are generated during the cross-correlation portion of NEWSIPS processing and are usually a good indicator of the signal-to-noise ratio (S/N).

*Percent successful cross correlations.* The percent of successful cross correlations for each image is recorded in the HISTORY portion of the FITS header. For most low-dispersion images, greater than 95% of the attempted cross correlations are successful, according to the criteria described in Chapter 5. If less than 90% of the cross correlations were successful, the image either suffers from unusually large local or global distortions, the raw image background is heavily saturated, the image is a partial read, or the raw image data are corrupted. For high-dispersion data, the above stated thresholds are much lower due to the smaller area background available for cross correlations. The majority ( $\sim 75\%$ ) of high-dispersion images have 80% or better successful cross correlations.

*Median cross-correlation coefficient.* The median cross-correlation coefficient for an image is the median of the cross-correlation coefficients for all patches of the image. In general, the best signal-to-noise in a low-dispersion extracted spectrum can be expected when this parameter is greater than 0.7. When this parameter is less than 0.6, the S/N of the photometrically corrected data, and ultimately the low-dispersion extracted spectrum, may be degraded. In high dispersion, this number tends to be lower for optimally exposed images; most high-dispersion images have a median cross-correlation coefficient of 0.4 or better.

*Mean shift.* This parameter is the mean of the magnitudes of the shift vectors for all patches used in the cross correlation. In general, the mean shift is inversely correlated with the median cross-correlation coefficient. Mean shifts of less than 0.5 pixel tend to yield the best S/N. This value holds true for both high- and low-dispersion images.

*Maximum shift.* The maximum shift is the largest magnitude of a shift vector in the array of patches used for the cross correlation. This value can be misleading as it may represent a correlation with a correspondingly large displacement which, during the filtering portion of the processing, is declared “invalid” (i.e., it does not conform to the overall trend of spatial deviations in the data). A low-dispersion image having a maximum shift of more than 1 pixel may suffer from unusual local distortions. Such local distortions can signify regions of the spectrum which may have degraded S/N. On average, high-dispersion images have maximum shifts of approximately 2 pixels.



## 4. Camera Temperature:

It is known that images acquired at camera head amplifier temperature (THDA) readings of more than a few degrees from the mean THDA of the ITF images almost always suffer from unusually large distortions compared to the majority of the images in the archive. The cross-correlation algorithm has a significantly higher confidence in the pattern recognition and the mean shifts are smaller when the THDA of the image is close to that of the ITF (see Table 13.1). Images with THDAs more than a few degrees from the mean ITF THDA for that camera will probably have a poor S/N. Note that the THDA is a secondary indicator of image registration quality; the median correlation coefficient is a more direct measure of registration quality.

Table 13.1: Mean ITF THDAs

Camera	LWP	LWR	SWP
ITF	1992	1983	1985
THDA	9.6	14.5	9.3

## 5. High-dispersion background determination warnings:

During the extraction of the background fluxes, various warning/failure messages may be produced, which point towards errors in the calculation of the background fluxes.

*Background determination failed due to insufficient flux; background flux set to zero.* This failure most likely indicates that a large portion of the image is affected by MMFs. Therefore, the background extraction algorithm has determined that background fluxes are not reliably sampled.

*Flare detected.* This condition only occurs for the LWR camera and signifies that the background determination module found a flare. The presence of a flare will most certainly lead to localized errors in the background solutions. The potential also exists for the effect of the flare to propagate across much of the image.

## 6. High-dispersion boxcar extraction warnings:

Several warning messages may be generated during the extraction of high-dispersion fluxes and are indicative of abnormalities in the centroiding of the extraction slit.

*Order nnn found at > 0.5 pixel position from line xxx.xx - yellow light.* nnn is 100 for the SWP and 90 for the LWP and LWR. xxx.xx is 290.74 for the SWP, 412.71 for the LWP, and 404.20 for the LWR. This condition is triggered when the appropriate “checkpoint” order (either 90 or 100 depending on the camera) deviates half a pixel or more from its fiducial (expected) location. These “checkpoint” orders are selected to be representative of the image as a whole, and fall in regions of the image where the camera

sensitivity is reasonably high. An occurrence of this warning alone is not necessarily indicative of a serious problem; however, the user should be aware that the apparent location of this “checkpoint” order is beyond the normally expected bounds and may indicate a larger than normal misalignment of the high-dispersion SI relative to the fiducial. The LWP processing HISTORY initially reported the line position for order 100 (sample position 316.02). This was subsequently changed to order 90 after the start of the processing effort, as this order is in a region of higher sensitivity than order 100 for the LWP and LWR. This change only affects LWP and LWR high-dispersion images processed after July 28, 1997.

*Order nnn explicit centroid determination invalid. Fiducial centroid used.* Occurs when there is a lack of flux in a particular order. As a result, the positioning of the extraction slit defaults to a predetermined order position which may result in a loss of flux.

*Order nnn spectrum centroid found beyond tolerance region. Fiducial centroid used.* Indicates that the center of the order was found outside a preset limit which varies from 3.0 pixels to 0.5 pixels depending upon the order number. This warning is indicative of either a lack of flux in this order or a potential misalignment of the high-dispersion SI relative to the fiducial. As a result, the positioning of the extraction slit defaults to a predetermined order position which may result in a loss of flux.

#### 7. Low-dispersion *SWET* extraction parameters and warnings:

The following messages appear in the HISTORY position of the FITS header and alert the user to potential problems with the flux extraction.

*Spectrum centroid displacement from predicted center.* The centroid of the spectrum was found more than 2 pixels from the predicted center of the spectrum, based on time and temperature dependencies. In this case, it is likely that the image suffers from unusually large spectral format shifts or that there were large target centering errors. As a result, the wavelength calibration could be in error due to a global displacement along the dispersion or local distortions not corrected for in the wavelength linearization and wavelength calibration.

*Spectrum peak displacement from the spectrum centroid.* The peak of the flux in the spectrum was found more than 1 pixel from the centroid of the spectrum, in the direction perpendicular to the dispersion. The spectrum may not be a point source and may benefit from re-extraction with a wider slit.

*Average peak FN.* Images with an average peak of less than 5 FN revert to the use of a default extraction center and profile. These images suffer from very poor signal strength and should be used with caution.

*Size of cross-dispersion profile bins.* A bin size of greater than 1 pixel may indicate that a large fraction of the spectral data are bad, missing, or have little or no flux above the background level. In most cases, these images revert to the use of a default extraction profile. Extracted data should be examined carefully.

*Number of spline nodes.* Spline nodes are used to determine the shape of the spectrum along the dispersion direction. Spectral data which require 2 or 3 spline nodes have a very low overall signal strength or are quite noisy, and may have significantly lower than average S/N. Spectral data utilizing only 2 spline nodes are, in fact, forced to revert to use of a default profile. Spectral profile fitting is discussed in Chapter 9.4.

*Percent of flagged pixels in the extracted spectrum.* If more than 10% of the extracted points in the MXLO file are flagged as either bad or cosmic ray hits, the error flags and the sigma vector should be examined carefully for the image.

8. Non-standard read and/or exposure gain:

The photometric quality of images acquired using non-standard read/exposure gains is not well known. Careful examination of this type of data is recommended prior to its use. See Chapter 11.1.3 for a discussion of the gain correction factors.

9. Extrapolated wavelength calibration and/or time-dependent sensitivity degradation correction:

The image was acquired at a time outside the range of the dates used to generate the wavelength calibration or sensitivity degradation correction. These calibrations were extrapolated in time and could in principle be slightly in error. Note, however, that analysis of late-epoch data by Garhart (1997) has shown that the extrapolations of the LWP point/extended/trailed and SWP trailed time-dependent sensitivity degradation corrections are nonetheless valid.

10. Extrapolated temperature-dependent sensitivity degradation correction:

The THDA at which the image was acquired is outside the range of temperatures used to derive the correction. Flux corrections performed using extreme THDAs could be slightly in error.

11. Data quality ( $\nu$ ) flags:

These flags indicate abnormal conditions in the data which can range from fairly minor to quite serious situations. The  $\nu$  flags for the merged extracted image should be examined carefully in order to ascertain whether or not a particular data point is good or bad. In general,  $\nu$  flag values of  $-8$  or more negative (bits 4–15) are indicative of unreliable data. See Chapter 3 for a detailed discussion of  $\nu$  flags.

More error conditions are flagged in NEWSIPS data than were flagged in IUESIPS data. In addition, *all* error conditions that affect a pixel in the two-dimensional data are bit-encoded into the  $\nu$  flag data, while only the most severe error condition affecting a pixel could be recovered from IUESIPS data. The attentive investigator will have a better understanding of the errors inherent in the NEWSIPS data than was possible with IUESIPS.

It is particularly important to consider the  $\nu$  flag values when analyzing extracted low-dispersion spectral data. The  $\nu$  flag assigned to each extracted point in low dispersion

is determined from statistical considerations and does not represent *all* error conditions for the pixels used in the calculation of the extracted spectral point. Examination of the low-dispersion resampled  $\nu$  flag image allows recovery of this error information and should always be performed in order to determine the locations and nature of the error conditions as identified on a pixel-by-pixel basis. See Chapter 9.6 for details concerning the generation of the one-dimensional (1-D)  $\nu$ -flag spectrum in low dispersion. In high dispersion, *all*  $\nu$  flags assigned to pixels used in the calculation of the extracted spectral point are carried over to the 1-D  $\nu$ -flag spectrum.

# Chapter 14

## Core Data Items

To fully and accurately characterize the *IUE* dataset and facilitate future analysis, a group of “core data items” descriptive of each image was identified. These core data items (CDIs) are defined as all parameters related to the acquired images which are either necessary for image processing with the NEWSIPS system or for scientific analysis of the data. This chapter identifies and defines each CDI, indicates valid values for the CDI, the sources used to verify the CDI, and any comments relevant to the use of the CDI.

The CDIs are of two types: input and output CDIs. All input CDIs for each image are verified for accuracy before NEWSIPS processing of the image by the *IUE* Project. Images are verified at the acquiring observation station. Sources for verification of the CDIs include the original observing script at GSFC and the observing log at VILSPA, the original VICAR image label, engineering data, and handwritten records. The output CDIs are generated by the NEWSIPS processing.

### 14.1 The Sources for Core Data Items

There are three primary sources for the input CDIs: the VICAR image label (which contains the Event Round Robin), the GSFC observing scripts or the VILSPA observing log, and the NEWSIPS processing system. The image label is machine readable and was used as the initial source when possible. The observing scripts are more accurate and were used to verify the accuracy of the data taken from the image label. The output CDIs are determined as part of the image processing system. A detailed description of the image label contents, including the “round robin” series of sequential spacecraft commands, can be found in an article by Van Steenberg (1989).

### 14.2 The Core Data Items

The following is an alphabetized list of the FITS keywords for the CDIs. Each entry includes a definition and the sources used to verify the data. Where appropriate, a definition of the

valid values and any further comments are included.

*The FITS keywords for aperture-dependent CDIs are alphabetized by the second letter, ignoring the “x” that represents the aperture designation (L or S) in the actual keyword. Where the FITS keywords indicate Fine Error Sensor (FES) data, an “n” represents the FES number (1 or 2).*

- **ABNBADSC**

Bad Scan Flag

**VALID VALUES:** YES, NO

**SOURCE:** The number of bad scans occurring during a read was noted on the observing script.

**COMMENTS:** This flag is set to YES to indicate that a bad camera static pointing was found at the beginning of a camera read. In this case, the read beam was repositioned to the original static pointing. The read was not restarted until a good scan was detected. This problem occurred almost exclusively during the first 2 years of operation for the LWP camera and is only flagged for that camera. For images acquired at GSFC, the number of bad scans is included in the COMMENT BY RA. This CDI supplements this comment.

- **ABNHISTR**

History Replay Flag

**VALID VALUES:** YES, NO

**SOURCE:** Images that required a history replay were noted on the observing script.

**COMMENTS:** This flag is set to YES when the original image reconstruction was flawed and the image had to be recovered from the engineering history tape to obtain a good copy. Since the full image label is not available on these history tapes, the observatory spliced the full image label from the original reconstruction with the history replay version of the image. If this attempt was unsuccessful, the history tape version of the label was used which contains only the first few lines of the VICAR label. The users are warned that the VICAR label may be truncated.

- **ABNHTRWU**

Heater Warm-up Flag

**VALID VALUES:** YES, NO

**SOURCE:** The use of the heater warm-up for the LWR camera was noted on the observing scripts.

**COMMENTS:** This flag is set to YES when a heater warm-up (usually 4 minutes) was performed during the prep sequence for the LWR camera. The heater warm-up procedure was used to reduce the occurrence of microphonics (see Chapter 4.2) which

affected most LWR images. This flag is set only for LWR images. Note that while the occurrence of microphonics is significantly reduced with the use of the heater warm-up procedure, it is not eliminated.

- **ABNMICRO**

Microphonics Flag

**VALID VALUES:** YES, NO

**SOURCE:** NEWSIPS processing

**COMMENTS:** This flag is set to YES if microphonics are detected in the raw image. For images acquired at GSFC, the number and location of microphonics are noted on the observing script and in the COMMENT BY RA. This CDI supplements this comment. Only LWR images are screened for microphonics, although SWP images occasionally have microphonics.

- **ABNMINFR**

Missing Minor Frame Flag

**VALID VALUES:** YES, NO

**SOURCE:** NEWSIPS processing

**COMMENTS:** This flag is set to YES if missing minor frames are detected in the raw image by an automated procedure in the NEWSIPS processing. For images acquired at GSFC, the number of missing minor frames is noted on the observing script and subsequently in COMMENT BY RA. This CDI supplements this comment. The number of missing minor frames determined by NEWSIPS may differ from the number recorded by the RA.

- **ABNNSTD**

Non-standard Read Flag

**VALID VALUES:** YES, NO

**SOURCE:** This flag was set at the time the input CDIs for the image were manually verified, using the observing script and the TO and RA comments.

**COMMENTS:** This flag is set to YES for images taken in a non-standard manner. An example of a non-standard condition is an image read down with the G1 grid turned off. The reason this flag is set to YES is documented in the comments.

- **ABNOTHER**

Image Abnormality Flag

**VALID VALUES:** YES, NO, DMU, DMU+YES

**SOURCE:** Various observatory sources are used to set this flag including the observing script and problems that arise during image processing. For images affected by DMU corruption, this flag is set by a raw image screening routine.

**COMMENTS:** This flag is set to YES for corrupted image reconstructions. It is unlikely that images with a corrupted reconstruction can be processed successfully by NEWSIPS. This flag is set to either DMU or DMU+YES if the image is affected by DMU corruption. The number of pixels at 159 DN as well as the estimated number of corrupted pixels and associated one-sigma error estimate are included in the Comments by RA.

- **ABNREAD**

Read Rate Flag

**VALID VALUES:** YES, NO

**SOURCE:** Non-standard read rates are noted on the observing script.

**COMMENTS:** This flag is set to YES when the image was read at a rate other than the standard 20 kb/s telemetry rate. The possible telemetry rates are: 40, 20, 10, 5, 2.5 and 1.25 kb/s. Since most calibration images were taken at 20 kb/s, only images read at that rate are well calibrated.

- **ABNUVC**

UVC Voltage Flag

**VALID VALUES:** YES, NO

**SOURCE:** Non-standard values were recorded on the observing script.

**COMMENTS:** This flag is set to YES when a non-standard Ultraviolet to Visible Converter (UVC) voltage was used during the exposure. The standard UVC setting for the LWP and SWP cameras is  $-5.0$  kV, while the LWR camera has settings of either  $-4.5$  or  $-5.0$  kV. See also UVC-VOLT.

- **APERTURE**

Aperture Mode

**VALID VALUES:** LARGE, SMALL, BOTH, NA

**SOURCE:** The aperture is found in the round robin portion of the image label. It is determined by locating a line preceded by 'TARGET' for the image and reading the third character in the last character string in the line. The observing script also contains this information. When the image processing software identifies undocumented spectral data in either aperture, the keyword is changed to BOTH.

**COMMENTS:** The aperture is one of the two entrance apertures in the focal plane of the telescope. When spectral data were collected through both apertures, either intentionally or serendipitously, APERTURE will be BOTH. This will give rise to two



sets of aperture-dependent CDIs which may have different values. NA is used only for Flat-field images or Nulls.

Each spectrograph has a pair of entrance apertures consisting of a large (L) nominally  $10 \times 20$  arcsecond slot with rounded ends, and a small (S) nominally 3 arcsecond diameter circle (see Chapter 2.2 for precise dimensions). The large aperture can be used for observing point-source objects, obtaining spatial information of extended sources, multiple exposures, and trailed exposures. The small aperture is unresolved and not photometrically accurate. Since the small aperture is never closed, large aperture exposures may generate a serendipitous image in the small aperture.

- **xBKGMODE**

Background Determination Mode (high dispersion only)

**VALID VALUES:** GLOBAL, LOCAL, NULL

**SOURCE:** This CDI is set by the high-dispersion background determination algorithm (*BCKGRD*).

**COMMENTS:** Indicates the background determination method used to generate the background fluxes. An output value of GLOBAL implies that the background was determined for a continuum source using the 2-pass method. A value of LOCAL denotes the use of the 1-pass background determination for non-continuum sources. A value of NULL usually indicates that a substantial portion of the image is missing due to telemetry dropouts. In this case (only), the background fluxes are set to zero.

- **CAMERA**

Detector Designation

**VALID VALUES:** LWP, LWR, SWP, SWR, FES1, FES2

**SOURCE:** The camera identification is found on line 1 byte 50 of the *IUE* VICAR image label. The camera is designated by number in the label as follows:

- 1 - Long Wavelength Prime camera (LWP)
- 2 - Long Wavelength Redundant camera (LWR)
- 3 - Short Wavelength Prime camera (SWP)
- 4 - Short Wavelength Redundant camera (SWR)
- 8 - Fine Error Sensor 1 (FES1)
- 9 - Fine Error Sensor 2 (FES2)

The camera was also noted on the observing scripts.

**COMMENTS:** The default cameras initially used were the LWR and SWP cameras. In October 1983, the LWP camera replaced the LWR as the primary long wavelength

camera. Only a few images were obtained with the SWR camera which has never operated to specification.

The camera number or name is noted many times in the VICAR label. At times (especially during the very early years of the *IUE* mission), the camera name and number for the image are not consistently noted in locations in the label. The camera designated in the first line of the VICAR label is taken to be the correct camera identification.

- **CC-MEDN**

Median Cross-correlation Coefficient

**VALID VALUES:** 0.0 to 1.0 (unitless)

**SOURCE:** NEWSIPS processing

**COMMENTS:** Median of the cross-correlation coefficients of all patches of the image for which cross correlation was successful (see Chapter 5.3).

- **CC-PERCN**

Percentage of Successful Cross Correlations

**VALID VALUES:** 0 to 100 %

**SOURCE:** NEWSIPS processing

**COMMENTS:** Percentage of the total number of sub-image arrays for which cross correlations were successful (see Chapter 5.3).

- **CC-STDEV**

Standard Deviation of Cross-correlation Coefficients

**VALID VALUES:** 0.0 to 1.0 (unitless)

**SOURCE:** NEWSIPS processing

**COMMENTS:** Standard deviation about the mean of the cross-correlation coefficients for all sub-image arrays for which cross correlation was successful (see Chapter 5.3).

- **CC-TEMPL**

Cross-correlation Template Size

**VALID VALUES:**  $5 \times 5$  to  $60 \times 60$  pixels

**SOURCE:** NEWSIPS processing

**COMMENTS:** While the template size may vary, the value of  $23 \times 23$  pixels is most commonly used (see Chapter 5.2).

- **CC-WINDOW**

Cross-correlation Window Size

**VALID VALUES:**  $5 \times 5$  to  $60 \times 60$  pixels

**SOURCE:** NEWSIPS processing

**COMMENTS:** While the window size is variable, the value of  $29 \times 29$  pixels is the most commonly used (see Chapter 5.2).

- **xCNTRAPR**

Predicted Center of Spectrum in SI File (low dispersion only)

**VALID VALUES:** 1 to 80 pixels

**SOURCE:** NEWSIPS processing

**COMMENTS:** NEWSIPS processing automatically takes into account predicted spectral format shifts based on time and THDA. Therefore, this CDI will normally be constant for each camera and aperture in low dispersion. The line number is normally 51 for the large aperture and 25 for the small aperture.

- **COMMENT BY GO**

GO Comments about the Image

**SOURCE:** The *IUE* GO for images taken at GSFC.

**COMMENTS:** The GSFC *IUE* Project asked all GOs to provide pertinent comments for images acquired under their observing programs. Any responses from this survey are provided under this keyword and include such comments as: high background, poor S/N, target is brightest star in field, continuum has Mg II h/k lines of primary. If the GO responded but had no comments about an image, the phrase ‘GO had no special comments’ is placed in this keyword. Many GSFC images do not include a COMMENT BY GO.

- **COMMENT BY RA**

RA Comments about the Image

**SOURCE:** The GSFC observing scripts or the VILSPA observing log and the VICAR image label.

**COMMENTS:** These comments include additional information about the image or the verification of the CDIs for the image that did not fit into the FITS CDI keywords. Explicit information about each exposure (e.g., offset reference points for multiple exposures or exposure lengths for segmented observations) are included in these comments. Attached are examples of GSFC comments that are always in the same format. Not all the comments pertain to every image. Following the list of generalized examples are some specific examples. Note: “x” indicates data that vary and may not accurately indicate format as it might change slightly depending on the value.

EXP x APER x E=x,C=x,B=x

\* Note: This comment incorporates the old database comments field and was included at the request of users.

READ GAIN = HIGH

PARTIAL READ

EXPOSURE GAIN = MEDIUM FOR EXPOSURE x

EXPOSURE GAIN = MINIMUM FOR EXPOSURE x

BOTH DISPERSIONS

10 Kb/s READ

LWR xx-MINUTE HEATER WARMUP

xx MISSING MINOR FRAMES NOTED ON SCRIPT

xx BAD SCAN STARTS NOTED ON SCRIPT

EX = xxx, EY = xxx

TARGET + TFLOOD

TARGET + UVFLOOD

EXP x TRACKED ON GYROS

EXP x TRACKED ON FES

EXP x TRACKED ON GYROS AND FES

xx PREP USED

OFFSET x FROM: xxxxxxxxxxxxxxxx

OFFSET x COORDINATES: hh mm ss.s sdd hh mm

OFFSET x MAGNITUDE: xx.xxx

\*\*\*\*\*

Example of comments for a multiple exposure

\*\*\*\*\*

INFORMATION ABOUT MULTIPLE EXPOSURES FOLLOWS

EXPOSURE x INFORMATION

DATEOBS x dd/mm/yy hh:mm:ss

EXPTIME x xxxxx.xxx SEC/(EFF); xxxxx.x SEC.(COM)

OFFSET REFERENCE POINT x IS UNKNOWN

OFFSET REFERENCE POINT x X= xxxxx,Y = xxxxx

FOCUS x = xx.xx

THDASTR x = x.xx

FPM x = x.xx

FESCOUNT x = FESMODE x = xx

R.P. USED FOR EXP x: xxxx, xxxx

\*\*\*\*\*

Specific example of comments for a blind offset exposure

\*\*\*\*\*

COMMENT BY RA: EXP 1 APER L E=255,C=210,B=47

COMMENT BY RA: 0 MISSING MINOR FRAMES NOTED ON SCRIPT

COMMENT BY RA: EXP 1 TRACKED ON FES

COMMENT BY RA: S PREP USED

COMMENT BY RA: OFFSET 1 FROM: Star-3210480

COMMENT BY RA: OFFSET 1 COORDINATES: 14 53 27.6 -32 26 06

COMMENT BY RA: OFFSET 1 MAGNITUDE: 6.200

COMMENT BY RA: OFFSET 2 FROM: Star-3111600

COMMENT BY RA: OFFSET 2 COORDINATES: 14 50 7.3 -31 34 26

COMMENT BY RA: OFFSET 2 MAGNITUDE: 8.800

\*\*\*\*\*

Specific example of comments for a multiple exposure

\*\*\*\*\*

COMMENT BY RA: EXP 1 APER L C=181,B=40

COMMENT BY RA: EXP 2 APER L C=181,B=40

COMMENT BY RA: EXP 3 APER L C=181,B=40

COMMENT BY RA: EXP 4 APER L C=181,B=40

COMMENT BY RA: 0 MISSING MINOR FRAMES NOTED ON SCRIPT

COMMENT BY RA: EXP 1 TRACKED ON FES

COMMENT BY RA: EXP 2 TRACKED ON FES

COMMENT BY RA: EXP 3 TRACKED ON FES

COMMENT BY RA: EXP 4 TRACKED ON FES

```

COMMENT BY RA: S    PREP USED
COMMENT BY RA: OFFSET 1  FROM: UNKNOWN
COMMENT BY RA: OFFSET 1  COORDINATES: 01 09 11.3 +11 12 07
COMMENT BY RA: OFFSET 1  MAGNITUDE: 8.800
COMMENT BY RA: INFORMATION ABOUT MULTIPLE EXPOSURES FOLLOWS
COMMENT BY RA: EXPOSURE 1 INFORMATION
COMMENT BY RA: DATEOBS 1 18/11/79 03:09:32
COMMENT BY RA: EXPTIME 1 1499.825 SEC.(EFF); 1500.0 SEC.(COM)
COMMENT BY RA: OFFSET REFERENCE POINT 1 X =  -31, Y =  -208
COMMENT BY RA: FOCUS 1 =  -0.64
COMMENT BY RA: THDASTR1 1 =  6.80
COMMENT BY RA: FPM 1 =  0.08
COMMENT BY RA: FESCOUNT 1 =                FES-MODE 1 = BO
COMMENT BY RA: EXPOSURE 2 INFORMATION
COMMENT BY RA: DATEOBS 2 18/11/79 03:40:06
COMMENT BY RA: EXPTIME 2 1499.825 SEC.(EFF); 1500.0 SEC.(COM)
COMMENT BY RA: OFFSET REFERENCE POINT 2 X =  -18, Y =  -208
COMMENT BY RA: FOCUS 2 =  -1.08
COMMENT BY RA: THDASTR1 2 =  6.80
COMMENT BY RA: FPM 2 =  0.50
COMMENT BY RA: FESCOUNT 2 =                FES-MODE 2 = BO
COMMENT BY RA: EXPOSURE 3 INFORMATION
COMMENT BY RA: DATEOBS 3 18/11/79 04:10:36
COMMENT BY RA: EXPTIME 3 1499.825 SEC.(EFF); 1500.0 SEC.(COM)
COMMENT BY RA: OFFSET REFERENCE POINT 3 X =  -4, Y =  -208
COMMENT BY RA: FOCUS 3 =  -1.10
COMMENT BY RA: THDASTR1 3 =  7.20
COMMENT BY RA: FPM 3 =  0.80
COMMENT BY RA: FESCOUNT 3 =                FES-MODE 3 = BO
COMMENT BY RA: EXPOSURE 4 INFORMATION
COMMENT BY RA: DATEOBS 4 18/11/79 04:40:07
COMMENT BY RA: EXPTIME 4 1499.825 SEC.(EFF); 1500.0 SEC.(COM)
COMMENT BY RA: OFFSET REFERENCE POINT 4 X =  11, Y =  -208
COMMENT BY RA: FOCUS 4 =  -1.20
COMMENT BY RA: THDASTR1 4 =  7.20
COMMENT BY RA: FESCOUNT 4 =                FES-MODE 4 = BO

```

```

*****

```

```

Specific example of comments for a segmented image

```

```

*****

```

```

COMMENT BY RA: EXP 1 APER L E=5X,B=45

```

```

COMMENT BY RA:      0 MISSING MINOR FRAMES NOTED ON SCRIPT

```

```

COMMENT BY RA:      0 BAD SCAN STARTS NOTED ON SCRIPT
COMMENT BY RA:  EXP 1 TRACKED ON GYROS
COMMENT BY RA:  S   PREP USED
COMMENT BY RA:  EXPOSURE 1 SEGMENTED ( 5 EXPOSURES)
COMMENT BY RA:  SEGMENT 1 EXPOSED   899.768 SEC.(EFF);  900.0 SEC.(COM)
COMMENT BY RA:  SEGMENT 2 EXPOSED  1199.595 SEC.(EFF); 1200.0 SEC.(COM)
COMMENT BY RA:  SEGMENT 3 EXPOSED   899.768 SEC.(EFF);  900.0 SEC.(COM)
COMMENT BY RA:  SEGMENT 4 EXPOSED  1199.595 SEC.(EFF); 1200.0 SEC.(COM)
COMMENT BY RA:  SEGMENT 5 EXPOSED  1199.595 SEC.(EFF); 1200.0 SEC.(COM)

```

```

*****
Specific example of comments for a DMU corrupted image
*****
WARNING: Image affected by the 159 DN anomaly
        172 pixels with 159 DN, corrupted:    86 +29 /- 29

```

- **xDATABKG**

Estimated Background Level

**VALID VALUES:** 0 to 255 DN

**SOURCE:** NEWSIPS processing

**COMMENTS:** This CDI is based on an algorithm applied uniformly to all images and will often differ from the value indicated in the COMMENT BY RA. The value in the comments is based on measurements made at the the time of acquisition and is not uniform over the entire *IUE* mission.

- **xDATACNT**

Estimated Continuum Level

**VALID VALUES:** 0 to 255 DN

**SOURCE:** NEWSIPS processing

**COMMENTS:** This CDI is based on an algorithm applied uniformly to all images and will often differ from the value indicated in the COMMENT BY RA. The value in the comments is based on measurements made at the the time of acquisition and is not uniform over the entire *IUE* mission.

- **xDATEOBS**

Date at the Start of Observation (UT)

**VALID VALUES:** Dates for the life of the satellite starting at January 28, 1978.

**SOURCE:** The date of read is extracted from bytes 1–5 in line 10 of the image label. Time stamps found in the round robin are used to correct the read date to the start

date when needed. The start date of the observation is also found on the observing script. The start date for null images is set equal to the read date.

**COMMENTS:** This is an aperture-dependent keyword. For multiple and segmented exposures, only the date of observation for the first exposure is placed in the FITS keyword. The dates of observation for the remaining exposures are entered as comments.

- **xDEC**

Declination of the Observed Target (1950)

**VALID VALUES:**  $-90$  to  $+90$  degrees

**SOURCE:** For non-solar system objects, the declination stored in this field is extracted from the SIMBAD database by the Astronomical Data Center of Strasbourg (CDS) for the *IUE* Project. For targets not found in the SIMBAD database, the coordinates as designated by the GO are used, but the majority of the time, all observations of the same target have identical homogeneous coordinates regardless of the coordinates supplied by the GO. Comet coordinates for data acquired through 1989 were provided by M. Festou of Observatoire de Besancon, France and documented in ULDA, Guide 2: Comets (ESA SP 1134, May 1990). Coordinates for other solar system objects and for sky background acquisitions are duplicated for this CDI from the original coordinates supplied by the GO. *No offsets have been applied to the homogeneous coordinates of the target. The offsets are documented in the COMMENT BY RA field.* If the pointed coordinates are available for WAVECAL, Null, T-flood, and UV-flood images, they appear in this field; otherwise, this field is zero-filled.

**COMMENTS:** The declination stored in this keyword is also known as the HOMOGENOUS DEC. The homogeneous declination is used by NEWSIPS processing whenever coordinates are required by a reduction algorithm.

- **DISPERSN**

Spectrograph Dispersion Mode

**VALID VALUES:** HIGH, LOW, BOTH, NA

**SOURCE:** The observing scripts are the most accurate source for the dispersion and were used as the primary source during image verification. The dispersion is found in the binary portion (camera snapshots) of the VICAR label in lines 86–100. Characters 22–25 are read into character format and converted to byte format, then separated into bits. If the bits 4 or 6 are equal to 1, then DISPRS='L', else DISPRS='H'. One cannot tell easily from the label if both dispersions were used during acquisition of an image.

**COMMENTS:** This CDI describes the dispersion mode of the spectrograph used in obtaining the image. The options are HIGH (echelle grating), LOW (single order), BOTH (for those images acquired with both dispersions superimposed) or NA (for



Flat-field images). Note that the CDI “DISPTYPE”, discussed below, records the dispersion parameter used in NEWSIPS processing.

- **DISPTYPE**

Dispersion Designated for Processing

**VALID VALUES:** HIGH, LOW

**SOURCE:** This value is determined prior to processing by the image processing staff.

**COMMENTS:** The value may be HIGH or LOW and may differ from the designated dispersion for images acquired with both dispersions, for images with no dispersion designated, and for certain types of engineering data (Nulls and Flat-field images). Images with DISPERSN=‘BOTH’ will be processed twice, once with DISPTYPE=‘LOW’ and once with DISPTYPE=‘HIGH’. Output files from both processings will be available in the archive.

- **EPOCH**

Epoch of the Coordinates

**VALID VALUES:** 1950

**SOURCE:** The 1950 epoch is constant for the *IUE* mission.

- **xEXPMULT**

Multiple Exposure Flag

**VALID VALUES:** Y-OFFSETS, X-OFFSETS, ALONG-APER, OTHER, NO

**SOURCE:** Exposure information is extracted from the round robin for each exposed spectrum of a multiple or a double aperture exposure. However, one cannot tell from this information alone whether the image contains multiple spectra spatially offset or time-segmented spectra superimposed (see xEXPSEGM CDI). Thus the notations made on the observing script are needed to differentiate these types of images.

**COMMENTS:** This flag indicates the acquisition of multiple spectra in the large aperture. Multiple exposures result in 2 or more individual spectra spatially displaced from one another. The flag is set to indicate that these spectra were displaced along the FES X-axis, the FES Y-axis, the major axis of the large aperture or another configuration. If the image does not contain multiple spectra, the flag is set to NO. Multiple spectra in the large aperture can be of the same object or of different objects. Multiple spectra may have been acquired by deliberately re-pointing the spacecraft for each separate spectrum or serendipitously, with a nearby object yielding an additional spectrum. The CDIs stored as FITS keywords are for the first exposure in the large aperture with the exception of exposure length which is the sum of all effective exposure lengths. A subset of data for subsequent large-aperture exposures is stored in the COMMENT BY RA keyword. This subset includes the start date and time of each

exposure, the length of exposure (both commanded and effective), the offset reference point, focus, THDA at the start of the exposure, radiation counts, and the FES mode and counts.

- **EXPOGAIN**

SEC Exposure Gain Mode

**VALID VALUES:** MAXIMUM, MEDIUM, MINIMUM

**SOURCE:** The exposure gain can be extracted from the VICAR label by finding the line in the round robin preceded by 'EXPOBC' and reading character 26. The exposure gain is also noted on the observing script if it is not the normal value of MAXIMUM.

**COMMENTS:** The exposure gain depends on the accelerating voltage applied in the Secondary Electron Conduction (SEC) photocathode. The maximum gain is equal to  $-6.1$  kV, medium gain  $-4$  kV, and minimum gain  $-3.2$  kV. The exposure gain can have different values for each exposure of a multiple exposure image or for dual aperture images. However, since this is an extremely rare (if existing) occurrence, the exposure gain is assumed to be the same for both. This rare situation will be noted in the COMMENT BY RA.

- **xEXPSEGM**

Segmented Exposure Flag

**VALID VALUES:** YES, NO

**SOURCE:** Exposure information can be extracted from the round robin for each exposure of a segmented image. However, one cannot tell explicitly from this information alone whether the image contains multiple spectra spatially offset or time segmented spectra superimposed. Thus the notations made on the observing script are needed to differentiate these types of images.

**COMMENTS:** This CDI flags superimposed segmented spectra obtained by more than one commanded exposure. This situation may occur if no guide star is available for FES tracking during a long exposure and the target must be re-centered in the aperture or if the length of the exposure is greater than the maximum commandable exposure time (447 minutes). Segmented exposures result in a single spectrum, as opposed to multiple exposures described under the xEXPMULT CDI. Where available, the number of segmented exposures and the commanded and effective exposure times for each exposure are stored in the FITS keyword COMMENT BY RA.

- **xEXPTIME**

Effective Exposure Time

**VALID VALUES:** 0.000 to 90000.000 seconds

**SOURCE:** The effective exposure time is derived from the commanded exposure time. The commanded exposure time is extracted from the round robin portion of the VICAR

label by reading characters 8–13 from a line preceded by ‘EXPOBC’ into an integer variable compacted into the format mmmss (5 digits). When the TO has modified the initial commanded length of exposure, the modified commanded time is extracted from characters 16–21 of a line preceded by ‘FIN’. The commanded exposure time is also noted on the observing script.

**COMMENTS:** The effective exposure time is used in the absolute calibration of spectral data. Both commanded and effective exposure times are retained in the Final Archive database for images acquired at GSFC. Only the effective exposure is retained for images acquired by VILSPA.

The effective exposure time is determined from the commanded exposure time by correcting for various known instrumental properties (i.e., OBC quantization and camera rise time). Details of the exposure time corrections for both point and trailed sources can be found in Chapter 11.1.1.

For multiple exposures, the effective exposure is calculated for each exposure and the results are added together for the FITS keyword (xEXPTIME). The effective exposure time for each exposure (where known) is placed in the FITS keyword COMMENT BY RA.

For segmented exposures, the effective exposure time is calculated for each segment of the exposure and the results are then added together. The commanded and effective exposure times for each segment are recorded in the FITS keyword COMMENT BY RA.

Trailed exposure times are not based on a commanded exposure time, but on the effective trail rate, the aperture size, and the number of passes through the aperture. The effective trail rate is derived from the commanded trail rate by applying an OBC quantization correction. The determination of trailed exposure times is discussed in detail in Chapter 11.1.1.

- **xEXPTRMD**

Trail Mode Flag

**VALID VALUES:** X-TRAIL, Y-TRAIL, NO-TRAIL

**SOURCE:** The trail mode is taken from the observing script.

**COMMENTS:** The trail mode indicates if the target was trailed along either the FES X-axis, the FES Y-axis, or not trailed. If this flag is set, the keywords xTRAILRT and xTRAILNR indicating the trail rate and the number of passes will also be set.

- **xFESnBK**

FES Background Counts

**VALID VALUES:** 0 to 28672 FES counts

**SOURCE:** The FES background counts are taken from the observing script.

**COMMENTS:** This value records the intensity of scattered light from the FES anomaly and is only listed for data acquired since January 1991.

- **xFESnCN**

FES Target Counts

**VALID VALUES:** 0 to 28672 FES counts

**SOURCE:** The FES counts may be extracted from the round robin of the VICAR label by reading the first integer field of a line preceded by 'FES CTS' or 'FESCT'.

- **xFESnMD**

FES Tracking Mode for the Target

**VALID VALUES:** F, S, O, U, FO, FU, SO, BO

**SOURCE:** The FES mode is extracted from the round robin of the VICAR label and is stored in the second and third integer fields in the line preceded by 'FES CTS' or 'FESCT'. The mode is also noted on all observing scripts.

**COMMENTS:** The track mode of the Fine Error Sensor (FES) with the target at the reference point. Fast (F) or Slow (S) track - Overlap (O) or Underlap (U), or Blind Offset (BO). If the track mode is missing, the corresponding CDI will be left blank.

- **FLARE**

LWR Flare Flag (high dispersion only)

**VALID VALUES:** YES, NO

**SOURCE:** The LWR flare flag is set by the *BCKGRD* module.

**COMMENTS:** This flag is set to YES when a flare is detected in an LWR image by the *BCKGRD* module.

- **xFLUXAVE**

Average Extracted FN (low dispersion only)

**VALID VALUES:** -1024 to +1024

**SOURCE:** NEWSIPS processing

**COMMENTS:** The average FN of the spectral data determined in the spectral extraction procedure (*SWET*). The average FN value is used to determine which fit will be used: an empirical or a default profile fit. See Chapter 9 for a detailed discussion of *SWET*.

- **xFOCUS**

Camera Focus

**VALID VALUES:** -25.0 to +25.0

**SOURCE:** The focus step is calculated by extracting three temperatures from the spacecraft snapshots, converting them from raw telemetry units to engineering units, and inserting these numbers into a formula. The focus value is also recorded on the observing scripts by the TO.

**COMMENTS:** The focus step is the value measured at the beginning of the exposure. This value is a linear function of three telescope temperatures. Typical values range from  $-10$  to  $+5$ .

- **xFPM**

Flux Particle Monitor Voltage

**VALID VALUES:** 0.0 to 4.0 Volts

**SOURCE:** This value was recorded on the observing script at the start of each exposure.

**COMMENTS:** A measurement of solar radiation (both direct and from the Van Allen belts) at the beginning of the exposure. The background radiation fluxes were detected as an output voltage from a Geiger counter which had a threshold of 960 keV for electrons and 15 Mev for protons. The Flux Particle Monitor (FPM) malfunctioned in May 1991 and was turned off in October 1991. Therefore, only images taken prior to May 1991 have valid radiation values. The rate at which the background level accumulates on the most sensitive part of a detector is an exponential function of FPM, and is given by:

$$DN/hour = A \times 10^{FPM}$$

where  $A$  is 1.35 for the LWP, 0.73 for the SWP, and 1.00 for the LWR.

- **xGSTARnC**

FES Guide Star Counts

**VALID VALUES:** 0 to 28672 FES counts

**SOURCE:** This value was recorded on the observing script.

**COMMENTS:** The guide star counts are measured with either FES1 or FES2.

- **xGSTARnM**

FES Tracking Mode for the Guide Star

**VALID VALUES:** FO,FU,SO,F,S,NO

**SOURCE:** This value is recorded on the observing script.

**COMMENTS:** Similar to the FES tracking mode of the target.

- **xGSTARnX**

FES Guide Star X-coordinate

**VALID VALUES:**  $-2016$  to  $+2047$  FES Units

**SOURCE:** This value is extracted from the round robin portion of the VICAR label and is the first integer value of a line preceded by ‘GDE’. The value is also found on the observing script.

**COMMENTS:** This entry can refer to either FES1 or FES2.

- **xGSTARnY**

FES Guide Star Y-coordinate

**VALID VALUES:**  $-2016$  to  $+2047$  FES Units

**SOURCE:** This value is extracted from the round robin portion of the VICAR label and is the second integer value of a line preceded by ‘GDE’. The value is also found on the observing script.

**COMMENTS:** This entry can refer to either FES1 or FES2.

- **xHELCORR**

Heliocentric Time Correction to the Midpoint of Observation

**VALID VALUES:**  $< 1.0$  days

**SOURCE:** NEWSIPS processing

**COMMENTS:** The heliocentric time correction is computed during processing for the midpoint of observation (xJD-MID) such that  $JD_{corr} = xJD-MID + HELCORR$ . This may be important for some variable targets.

- **IMAGE NUMBER**

Camera Image Sequence Number

**VALID VALUES:**  $\geq 500$

**SOURCE:** The image number is found on line 1 bytes 52–56 on the image label. This number is also found on the second line but is not always accurate, as it is hand entered by the TO. In addition, the image number is found on the observing script.

**COMMENTS:** Camera-dependent sequential image number was assigned to an image at acquisition starting at 1000. Images that were inadvertently assigned duplicate image numbers at the time of observation have been reassigned numbers starting at 500 for each camera.

- **ITF**

The Intensity Transfer Function Used in Image Processing

**VALID VALUES:** LWP92R94A, LWR83R94A (ITF A), LWR83R96A (ITF B), SWP85R92A

**SOURCE:** NEWSIPS processing

**COMMENTS:** Indication is given for the camera, last 2 digits of the year of acquisition, last 2 digits of the year of construction, and an alphabetic character representing the sequence of construction within the year. The “R” character denotes “release”.

- **xIUECLAS**

*IUE* Object Class

00 SUN	51 LONG PERIOD VARIABLE STARS
01 EARTH	52 IRREGULAR VARIABLES
02 MOON	53 REGULAR VARIABLES
03 PLANET	54 DWARF NOVAE
04 PLANETARY SATELLITE	55 CLASSICAL NOVAE
05 MINOR PLANET	56 SUPERNOVAE
06 COMET	57 SYMBIOTIC STARS
07 INTERPLANETARY MEDIUM	58 T TAURI
08 GIANT RED SPOT	59 X-RAY
09	60 SHELL STAR
10 W C	61 ETA CARINAE
11 WN	62 PULSAR
12 MAIN SEQUENCE O	63 NOVA-LIKE
13 SUPERGIANT O	64 OTHER
14 OE	65 MISIDENTIFIED TARGETS
15 OF	66 INTERACTING BINARIES
16 SD O	67
17 WD O	68
18	69 HERBIG-HARO OBJECTS
19 OTHER STRONG SOURCES	70 PLANETARY NEBULA + CENTRAL STAR
20 B0-B2 V-IV	71 PLANETARY NEBULA - CENTRAL STAR
21 B3-B5 V-IV	72 H II REGION
22 B6-B9.5 V-IV	73 REFLECTION NEBULA
23 B0-B2 III-I	74 DARK CLOUD (ABSORPTION SPECTRUM)
24 B3-B5 III-I	75 SUPERNOVA REMNANT
25 B6-B9.5 III-I	76 RING NEBULA (SHOCK IONIZED)
26 BE	77
27 BP	78
28 SDB	79
29 WDB	80 SPIRAL GALAXY
30 A0-A3 V-IV	81 ELLIPTICAL GALAXY
31 A4-A9 V-IV	82 IRREGULAR GALAXY
32 A0-A3 III-I	83 GLOBULAR CLUSTER
33 A4-A9 III-I	84 SEYFERT GALAXY
34 AE	85 QUASAR

35 AM	86 RADIO GALAXY
36 AP	87 BL LACERTAE OBJECT
37 WDA	88 EMISSION LINE GALAXY (NON-SEYFERT)
38 HORIZONTAL BRANCH STARS	89
39 COMPOSITE SPECTRAL TYPE	90 INTERGALACTIC MEDIUM
40 F0-F2	91
41 F3-F9	92
42 FP	93
43 LATE-TYPE DEGENERATES	94
44 G V-IV	95
45 G III-I	96
46 K V-IV	97
47 K III-I	98 WAVELENGTH CALIBRATION LAMP
48 M V-IV	99 NULLS AND FLAT FIELDS
49 M III-I	
50 R, N, OR S TYPES	

**VALID VALUES:** 0 to 99 (unitless)

**SOURCE:** The object class was designated by the GO as part of the proposal target list. This designation is found in bytes 54–56 of line 36 of the VICAR label. The GO also designated the object class on the observing scripts. If the designations differed, the object class on the scripts was used.

**COMMENTS:** *IUE* Project staff *did not* standardize the object classes. Object classes were changed from the GO designation only when the designation was obviously wrong (e.g., sky around Jupiter designated as planetary nebula) or when a new classification was created (e.g., Herbig-Haro objects). *Therefore, a single target observed multiple times may have several different object class identifications in the database.*

- **LAMP**

Flood Lamp Flag

**VALID VALUES:** TFLOOD, CALUV, NONE

**SOURCE:** This information is extracted from the round robin portion of the VICAR label by locating a line preceded by the ‘EXPOBC’ command and reading the characters in bytes 29 through 31. This information is also noted on the observing script.

**COMMENTS:** This keyword indicates if one of the on-board lamps was activated at any time after the camera prep and before the read. If no lamp was activated then this keyword is set to NONE. This keyword does not indicate the use of the Platinum-Neon (Pt-Ne) Wavelength Calibration (WAVECAL) lamps, because they produce spectral data and are handled as science data. The lamp types are as follows:



**TFLOOD:** Tungsten Flood lamps normally used in the camera preparation sequence. However, they are also used in conjunction with the WAVECAL lamps to illuminate the reseau marks needed for the geometric correction and to raise the DN level of the fainter emission lines. In addition, they are occasionally exposed in conjunction with stellar images for test purposes to enhance the background.

**CALUV:** Ultraviolet (mercury discharge) Flood lamps that produce a monochromatic output at 2537Å. They are primarily utilized in generating the ITF images used for the photometric correction process.

- **xLAPSTAT**

Large Aperture Status Flag

**VALID VALUES:** CLOSED, OPEN

**SOURCE:** The status of the large aperture is recorded in the binary camera snapshots portion (lines 86–100) of the VICAR label. Characters 22–25 are read into character format and converted to byte format, then separated into bits. If the bits 7 and 8 are both equal to 0, then the large aperture was open, otherwise it was closed. This information was also recorded on the observing script.

**COMMENTS:** This CDI describes whether the spectrograph large aperture was closed (C) or open (O) during the observation. Because opening and closing the large aperture may shift the reference point for centering objects in the aperture, the large aperture generally remains open. The small aperture is always open. The large aperture is typically only closed during wavelength calibration exposures and during high-dispersion observations of targets where light from a nearby source in the large aperture might contaminate the small-aperture spectrum.

- **MEANRAT**

Ratio of Mean Flux in SI File to Mean Flux in LI File

**VALID VALUES:**  $-\infty$  to  $+\infty$  (unitless)

**SOURCE:** NEWSIPS processing

**COMMENTS:** This CDI can give an indication of how well the flux was conserved in the resampling step. If the mean flux value in the LI image is near zero, however, the ratio is unreliable.

- **xJD-MID**

Mid-Point Date and Time of the Observation

**VALID VALUES:** 2443534.0 to end of *IUE* mission

**SOURCE:** NEWSIPS processing

**COMMENTS:** This value is stored as a Julian Date. In the case of multiple or segmented exposures, xJD-MID is calculated by adding half the total exposure time

to the starting Julian Date of the observations. This may not coincide with the true mid-point of the observations as it does not take into account the operational overhead involved (e.g., setup time for obtaining multiple exposures).

- **xJD-OBS**

Starting Date and Time of Observation

**VALID VALUES:** 2443534.0 to end of *IUE* mission

**SOURCE:** NEWSIPS processing

**COMMENTS:** This value is stored as a Julian Date. In the case of multiple exposures in the large aperture, the Julian Date is calculated only for the first exposure.

- **xOBJECT**

Homogeneous Target Identifier

**SOURCE:** The Homogeneous Target Identifier was, in most cases, provided by CDS for the *IUE* Project. CDS used the original target designation from the GO for each image in the *IUE* archive to cross-match with the SIMBAD database, thus identifying all images of a particular target, regardless of the nomenclature used by the GO. CDS then assigned a homogeneous target ID according to the following priority list:

HD, BD, CD, CPD, V\*, WD, GD, NGC, IC, PK, SK, AzV, LIN, LHA, DEM, MRK, PG, QSO, ABCG, NOVA, SN, LS, PHL, FEIG, ROSS, 3C, X, PKS.

When none of these identifiers existed for a target, usually the first identifier listed by SIMBAD was adopted. SK, AxV, LIN, LHA, and DEM were later transformed to MC. LS, PHL, FEIG, ROSS, 3C, X, PKS, and a few other catalogs were later transformed to AOO LS, etc. to facilitate searches for “any other object”. The homogeneous target IDs for a few images were supplied or modified by VILSPA and GSFC for accuracy during the final check.

**COMMENTS:** This item consists of three sections. The first four characters of the field are a catalog identifier, most of which are standard astronomical catalog abbreviations. The catalog designation ZZ stands for solar system objects and the designation ‘IUE’ is used for images acquired for *IUE* engineering and calibration purposes. The next 12 characters identify the object. The final 12 characters are the optional complementary ID, used to give additional or more specific identification of the target. Some examples of complementary IDs include a nearby object for a sky background exposure or an area of a nebula or planet.

- **xOFFSET**

Global Spectral Format Offset (high dispersion only)

**VALID VALUES:** no limits exist

**SOURCE:** NEWSIPS processing.

**COMMENTS:** Indicates the “global average” shift in pixels calculated to achieve spatial registration of the orders in high dispersion. In most cases, this global offset is further refined to account for differential shifts of individual orders before being actually applied to the image. See Chapter 4.9 for details concerning the high-dispersion order registration process.

- **ORBANOMA**

Mean Anomaly of the Orbit

**VALID VALUES:** 0 to 359.999999 degrees

**SOURCE:** GSFC Flight Dynamics Predictions.

- **ORBASCEN**

Right Ascension of Ascending Node of the Orbit

**VALID VALUES:** 0 to 359.999999 degrees

**SOURCE:** GSFC Flight Dynamics Predictions.

**COMMENTS:** Typical values range from 98 – 208 degrees.

- **ORBECCEN**

Orbit Eccentricity

**VALID VALUES:** 0 to 1 (unitless)

**SOURCE:** GSFC Flight Dynamics Predictions.

**COMMENTS:** Typical values range from 0.13 – 0.24

- **ORBEPOCH**

Date of the Orbital Elements (UT)

**VALID VALUES:** February 22, 1978 to end of *IUE* mission

**SOURCE:** GSFC Flight Dynamics Predictions.

**COMMENTS:** The appropriate set of orbital elements for an image is determined using the date of exposure and the orbital elements epoch. Images are assigned the set of orbital elements that have the nearest preceding date. The only exception is for images taken after a Delta V, which are assigned the set of orbital elements with the nearest succeeding date.

- **ORBINCLI**

Inclination of the Orbit

**VALID VALUES:** –90 to +90 degrees

**SOURCE:** GSFC Flight Dynamics Predictions.

**COMMENTS:** Typical values range from 28 – 35 degrees.

- **ORBSAXIS**

Semi-major Axis of the Orbit

**VALID VALUES:** 0 to  $\infty$  kilometers

**SOURCE:** GSFC Flight Dynamics Predictions.

**COMMENTS:** Typical values range from 42150 – 42180 kilometers.

- **PGM-ID**

Observer Program ID

**SOURCE:** The program ID is stored on line 36 of the VICAR label in the first 5 characters. The program ID is also noted on the observing script.

**COMMENTS:** An alphanumeric code that identifies the observing program for which the observation was made. The program ID contains 5 characters. For NASA-approved programs of the first year, the first two letters identify the type of observing program and the last three are the initials of the principal investigator. After the first year of operation, the first two letters identify the type of observing program, the third letter represents the year, and the last two letters are the initials of the principal investigator. The program IDs for NASA discretionary programs begin with the letters OD. The last three characters are a sequential number and a letter. For ESA- and SERC-approved programs the program IDs are generally two letters followed by three numbers where the first letter designates the year. Program IDs are also assigned for images obtained for project-related programs such as calibration monitoring and camera testing.

- **POSANGLE**

Spacecraft Position Angle

**VALID VALUES:** 0.0 to 359.999999 degrees

**SOURCE:** For images acquired at GSFC, the position angle of the large aperture is calculated from the roll angle coordinates. The roll angle is entered during verification of the CDIs from the observing script. For images acquired at VILSPA, the position angle is computed from the coordinates and exposure start time.

**COMMENTS:** The position angle in the plane of the sky is defined such that 0 degrees points north and 90 degrees points east. The position angle is related to the spacecraft roll angle by:

$$\text{Position Angle} = \text{Aperture Orientation Angle} - \text{Spacecraft Roll Angle}$$

where the aperture orientation angles are defined with respect to the reference vector and increase counterclockwise from the reference vector. Note that the roll angle has been retained in the GSFC database for images read at GSFC.

- **xRA**

Right Ascension of the Observed Target

**VALID VALUES:** 0 to 359.999999 degrees

**SOURCE:** For non-solar system objects, the right ascension stored in this field is extracted from the SIMBAD database by the CDS for the *IUE* Project. For targets not found in the SIMBAD database, the coordinates as designated by the GO are used, but the majority of the time, all observations of the same target have identical homogeneous coordinates regardless of the coordinates supplied by the GO. Comet coordinates for data acquired through 1989 were provided by M. Festou of Observatoire de Besancon, France and documented in ULDA, Guide 2: Comets (ESA SP 1134, May 1990). Coordinates for other solar system objects and for sky background acquisitions are duplicated for this CDI from the original coordinates supplied by the GO. *No offsets have been applied to the homogeneous coordinates of the target. The offsets are documented in the COMMENT BY RA field.* If the pointed coordinates are available for WAVECAL, Null, T-flood, and UV-flood images, they appear in this field; otherwise, this field is zero-filled.

**COMMENTS:** The right ascension stored in this keyword is also designated the HOMOGENOUS RA. The homogeneous right ascension is used by NEWSIPS processing whenever coordinates are required by a reduction algorithm.

- **xRADVELO**

Heliocentric Radial Velocity Correction for (high dispersion only)

**VALID VALUES:** -34 to +34 kilometers per second

**SOURCE:** NEWSIPS processing

**COMMENTS:** Net radial velocity correction for high-dispersion data taking into account the motions of *IUE* and the Earth.

- **READGAIN**

Read Gain Mode

**VALID VALUES:** HIGH, LOW

**SOURCE:** This value can be found in the event round robin portion of the VICAR image label and on the observing script.

**COMMENTS:** This CDI is the gain of the camera head amplifier in the readout section of the SEC tube. Low gain is the standard mode and is the default where not noted explicitly on the observing script.

- **READMODE**

Image Read Flag

**VALID VALUES:** FULL, PARTIAL

**SOURCE:** This value can be found in the round robin portion of the image label and on the observing script.

**COMMENTS:** This keyword indicates if the image was read fully or partially. Partial reads are images for which only the part of the detector containing the spectrum was read. Full read is the standard read.

- **SHFTMAX**

Maximum Shift Between Image and ITF

**VALID VALUES:** 0 to 10.0 pixels

**SOURCE:** NEWSIPS processing

**COMMENTS:** Maximum of the magnitudes of the displacement vectors determined for the patches of the image used for cross correlation.

- **SHFTMEAN**

Mean Shift Between Image and ITF

**VALID VALUES:** 0 to 10.0 pixels

**SOURCE:** NEWSIPS processing

**COMMENTS:** Average of the magnitudes of the displacement vectors determined for the patches of the image used for cross correlation.

- **SERENDAP**

Serendipitous Image Flag (low dispersion only)

**VALID VALUES:** LARGE, SMALL

**SOURCE:** NEWSIPS processing

**COMMENTS:** This keyword is set equal to the aperture for which a serendipitous exposure is detected by the NEWSIPS software. This CDI only has a value when unexpected spectral data are detected in the NEWSIPS processing. If the presence of a serendipitous exposure, either in the other aperture or another camera, was indicated on the observing script, this CDI will be left blank.

- **STATION**

Observing Station Flag

**VALID VALUES:** GSFC, VILSPA

**SOURCE:** The observing station is found in character 49 of the first line of the VICAR label. This is an integer value where 1 equals GSFC and 2 equals VILSPA. The observing station is also documented on observing scripts and in Telescope Operation Control Center records.

**COMMENTS:** This flag indicates the observing station which read the image down from the satellite. For collaborative images (i.e., images initiated at one ground station and read down at the other), the station where the image was read is the designated observing station. The only time the observing station is not the one where the image was read is at times of equipment failure.

- **STDEV RAT**

Standard Deviation Ratio

**VALID VALUES:**  $-\infty$  to  $+\infty$  (unitless)

**SOURCE:** NEWSIPS processing

**COMMENTS:** The ratio of the standard deviation about the mean of the flux in the SI file to the standard deviation about the mean of the flux in the LI file. This CDI can give an indication of how well the noise characteristics in the LI image were preserved in the resampling step. If the standard deviation about the mean of the flux in the LI image is near zero, the ratio is unreliable.

- **xTARG DEC**

GO-designated Target Declination

**VALID VALUES:**  $-90.0$  to  $+90.0$  degrees

**SOURCE:** The GO defines the declination for the target as part of the target list submitted with the proposal. This declination is stored in line 37, bytes 8 through 14 of the VICAR label as degrees, minutes and seconds. The DEC is also recorded on the observing script. If the DEC from the VICAR label differs from that recorded on the observing script, the DEC from the script is used.

**COMMENTS:** The GO-designated declination is used for preliminary positioning of the spacecraft.

- **xTARGET**

GO-designated Target Name

**SOURCE:** The object name is located in bytes 39-46 of the line 36 of the VICAR label. The object name is also located on the observing script.

**COMMENTS:** The object name found in the VICAR label was supplied by the GO on the proposal target list. The GO may use a different target name on the observing script. GOs were encouraged to use the Henry Draper catalog designations for stars in this field, where appropriate.

- **xTARG RA**

GO-designated Target Right Ascension

**VALID VALUES:** 0 to 359.999999 degrees

**SOURCE:** The GO defines the right ascension for the target as part of the target list submitted with the proposal. This right ascension is stored in line 37, bytes 1 through 7 of the VICAR label in hour, minute, second format. The RA is also recorded on the observing script. If the RA from the VICAR label differs from that recorded on the observing script, the RA from the script is used.

**COMMENTS:** The GO-designated right ascension is used for preliminary positioning of the spacecraft.

- **xTHDAEND**

Camera Head Amplifier Temperature at Exposure End

**VALID VALUES:**  $-5.0$  to  $+57.640$  degrees Celsius

**SOURCE:** This value is found in the camera snapshot section of the binary section (lines 86–100) of the VICAR label and is not noted on the observing script. If the camera snapshot portion of the label is corrupted, the THDA is estimated using the THDA values from images taken before and after this image.

For images acquired before June 7, 1979 (day 158), THDA values cannot be obtained from the label. Thus THDAs for each camera at one hour intervals were digitized from the telemetry page snaps. Images were assigned the THDA value nearest in time to the end of the exposure for this time period.

**COMMENTS:** Temperatures generally range from 4.0 to 20.0 degrees Celsius. Average temperatures are typically about 9 degrees Celsius for the SWP and LWP cameras and 13 degrees Celsius for the LWR camera. This value cannot be verified against independent sources. The importance of THDA as a predictor of image quality was not established until the early 1980s.

- **THDAREAD**

Camera Head Amplifier Temperature at Read Start

**VALID VALUES:**  $-5.0$  to  $+57.640$  degrees Celsius

**SOURCE:** This value is found in the camera snapshots section of the binary section (lines 86–100) of the VICAR label and is not noted on the observing script. If the camera snapshots portion of the label is corrupted, the THDA is estimated using the THDA values from images taken before and after this image.

For images acquired before June 7, 1979 (day 158), THDA values for each camera at one hour intervals were digitized from the telemetry page snaps. Images were assigned the THDA value nearest in time to their read time.

**COMMENTS:** Temperatures generally range from 4.0 to 20.0 degrees Celsius. Average temperatures are typically about 9 degrees Celsius for the SWP and LWP cameras and 13 degrees Celsius for the LWR camera. This value cannot be verified against independent sources. The importance of THDA as a predictor of image quality was not established until the early 1980s.



- **xTHDASTR**

Camera Head Amplifier Temperature at Exposure Start

**VALID VALUES:**  $-5.0$  to  $+57.640$  degrees Celsius

**SOURCE:** This value is found in the camera snapshots section of the binary section (lines 86–100) of the VICAR label and is also noted on the observing script.

For images acquired before June 7, 1979 (day 158), THDA values for each camera at one hour intervals were digitized from the telemetry page snaps. Images were assigned the THDA value nearest in time to the start of the exposure.

**COMMENTS:** Temperatures generally range from 4.0 to 20.0 degrees Celsius. Average temperatures are typically about 9 degrees Celsius for the SWP and LWP cameras and 13 degrees Celsius for the LWR camera. This value cannot be verified against independent sources. The importance of THDA as a predictor of image quality was not established until the early 1980s.

- **TILTCORR**

Tilt Correction Flag

**VALID VALUES:** YES, NO

**SOURCE:** NEWSIPS module

**COMMENTS:** The tilt correction is only applied to large-aperture, low-dispersion extended-source data, when appropriate, and multiple exposures taken along the major-axis of the aperture.

- **xTIMEOBS**

Time (hour, minute and second) at Exposure Start (UT)

**VALID VALUES:** 00:00:00 to 23:59:59

**SOURCE:** The time of observation may be found in the image label by locating a line in the round robin preceded by 'EXPOBC', reading the characters 1–6 with format hhmmss and subtracting 6 seconds from it. However, when the exposure time has been modified, the time is extracted from the first 6 characters in the round robin line preceded by 'FIN'. This information is also found on the observing script.

**COMMENTS:** For multiple or segmented exposures in the large aperture the start time of the first exposure will be stored in the keyword. Subsequent exposure values will be stored in the COMMENT BY RA.

- **xTRAILNR**

Number of Passes in a Trailed Observation

**VALID VALUES:** 1 to 9 (unitless)

**SOURCE:** The number of passes (iterations) is extracted from the round robin portion of the VICAR label by locating a line preceded by 'ITER' and reading the one digit integer. This information is also recorded on the observing script.

**COMMENTS:** The number of passes is needed to determine the trailed exposure time.

- **xTRAILRT**

Effective Trail Rate

**VALID VALUES:** 0.03 to 120.0 arcseconds per second

**SOURCE:** The effective trail rate is a calculated value using the commanded trail rate and allowing for OBC quantization. The commanded trail rate can be extracted from the round robin portion of the VICAR label by locating a line preceded by 'TRAIL' and reading the real number value at the end of the line. The commanded trail rate is also noted on the script. See Chapter 11.1.1 for details on calculating an effective trail rate from the commanded trail rate.

**COMMENTS:** The effective trail rate is needed to determine the effective exposure time for trailed data.

- **UVC-VOLT**

UVC Voltage Setting

**VALID VALUES:**  $-5.0$  to  $0.0$  kV

**SOURCE:** The UVC voltage is found in the VICAR label by locating a line in the round robin preceded by 'FIN' and reading the integer value that follows the U field in that line. If a non-standard UVC voltage was commanded, this value would be noted on the script. The normal UVC voltage is  $-5.0$  kV (see also ABNUVC).

**COMMENTS:** After mid-1983 the LWR camera was routinely read at  $-4.5$  kV to reduce the negative effect of the flare on the detector.

- **xXTRCNTR**

Line Number in SI File at which the Peak Cross-dispersion Profile Flux was Found (low dispersion only)

**VALID VALUES:** 1.0 to 80.0 pixels

**SOURCE:** NEWSIPS processing

- **xXTRASYM**

Asymmetrical Extraction Profile (low dispersion only)

**VALID VALUES:** YES, NO

**SOURCE:** NEWSIPS processing

**COMMENTS:** A flag indicating if the peak of the cross-dispersion flux was found to be more than 2 pixels (two lines in the low-dispersion resampled image) away from the centroid of the profile.

- **xXTRMODE**

Processing Extraction Mode

**VALID VALUES:** POINT, EXTENDED

**SOURCE:** NEWSIPS processing

**COMMENTS:** The extraction mode in NEWSIPS processing is based entirely on the automated determination of spectral width and may differ from the original request by the acquiring GO on the observing script. As a result, the NEWSIPS spectral data may differ significantly from the original processing.

- **xXTRPROF**

Weighted Slit Extraction Profile (low dispersion only)

**VALID VALUES:** EMPIRICAL, DEFAULT POINT, UNIFORM

**SOURCE:** NEWSIPS processing

**COMMENTS:** If an empirical determination of the spectral cross-dispersion profile is not possible, a standard default profile is assumed. The standard default profile for point sources is a model based on standard-star images and for extended sources, a uniform boxcar weighting.

# Appendix A

## High-Dispersion Background Determination Algorithm (BCKGRD)

### A.1 Overview

The driving philosophy behind the NEWSIPS Project is to provide a homogeneous data product within a completely automated processing environment. An algorithm to compute background fluxes in high dispersion, *BCKGRD*, was designed with this philosophy. Although this algorithm generally provides a good background flux estimate, the results are not always optimal for particular regions of some images. A customized interactive determination of the background fluxes based on individual image characteristics can produce a more accurate estimate of the background in certain cases when data pathologies are present.

The determination of smoothed background fluxes follows the geometric resampling of pixels, so it is done with the high-dispersion resampled image (SI). A representative high-dispersion SI given in Figure A.1 shows echelle orders running horizontally and the spatial (cross-dispersion) direction running vertically. We will refer hereafter to the image sectors at the top and bottom as the “ends” of the image. The *BCKGRD* module produces smoothed background flux spectra which, together with the gross spectra, form the net spectra. The background model is created by computing continuous Chebyshev polynomial functions from pixels that sample valid background fluxes. For images with no continuum, the algorithm proceeds straightforwardly by sampling the neighboring interorder fluxes for each spectral order and fitting the result to a Chebyshev polynomial. The *BCKGRD* algorithm models the backgrounds of images having continuum flux in two one-dimensional passes, as described below.

For continuum source images, the background determination algorithm begins by sampling fluxes along the spatial direction with an extraction slit 5 pixels tall. We refer to these cuts as “swaths” and the steps taken for this group of vertical swaths as “Pass 1” operations. A total of 25 parallel swaths (26 for SWP) are taken in the spatial direction, each located at a column position  $\approx 27$  pixels larger than the preceding swath. Figure A.1 shows the positions of these Pass 1 swaths as dotted vertical lines. The mean flux is computed along the

extraction slit from pixels containing valid local background fluxes; pixels are given a weight of zero if they fall along the spectral orders or if they do not contain valid fluxes (i.e., they have negative  $\nu$  flags). The result of this process is a background-flux array for each swath that is discontinuous in spatial pixel number and contains noise. The array is adjusted to account for interorder contamination using a Point Spread Function (PSF) modeling technique described in Section A.2.2. The adjusted array is fit to a trial Chebyshev function of degree 7. This fitting degree is decreased if ringing is detected in the initial solution. The resulting solution is a smoothed continuous fit to the raw background fluxes. Each of the Pass 1 swaths is fit to a Chebyshev polynomial array in the same fashion.

In the second pass (Pass 2) solutions from Pass 1 are used to form a second and final set of 7th degree Chebyshev functions which model the background fluxes at the positions of the echelle orders. This solution is determined by sampling the solutions from the first pass at the locations where they intersect the echelle-order locations. The echelle-order locations are represented as solid lines in Figure A.1. The computation of a Chebyshev function from this sampling interpolates a continuous array of smoothed background fluxes at each wavelength along these orders. The solution is extrapolated beyond the target edges from the last calculated value.

The final background solutions are represented in two forms. First, a background vector of 768 values is saved and written to the high-dispersion merged extracted FITS file as a separate record for each order. Second, the 7 Chebyshev coefficients, together with a magnitude scale factor and starting and ending positions are written as FITS keywords. The “gross” spectrum may be reconstructed simply by adding the background and the net flux solutions.

## A.2 Background Determination: Step-by-Step

### A.2.1 Data Screening

Prior to the execution of the background determination algorithm, the fluxes and  $\nu$  flags of each Pass 1 swath are evaluated to ensure that enough valid pixels exist in a swath to produce a reliable fit to the data. Any pixels containing flags with excessively negative ITF extrapolations or cosmic ray hits are added to a “pixels-to-avoid” working template for each Pass 1 swath. A few checks are then made to ensure that the background-determining algorithm will run properly. For example, if too few valid pixels can be found in a given Pass 1 swath to permit a reliable background extraction, the solution is set to a zero-flux array. If this is not repeated for the next swath, then the solution for the zeroed-out swath is reset to the mean of the two adjacent swaths.

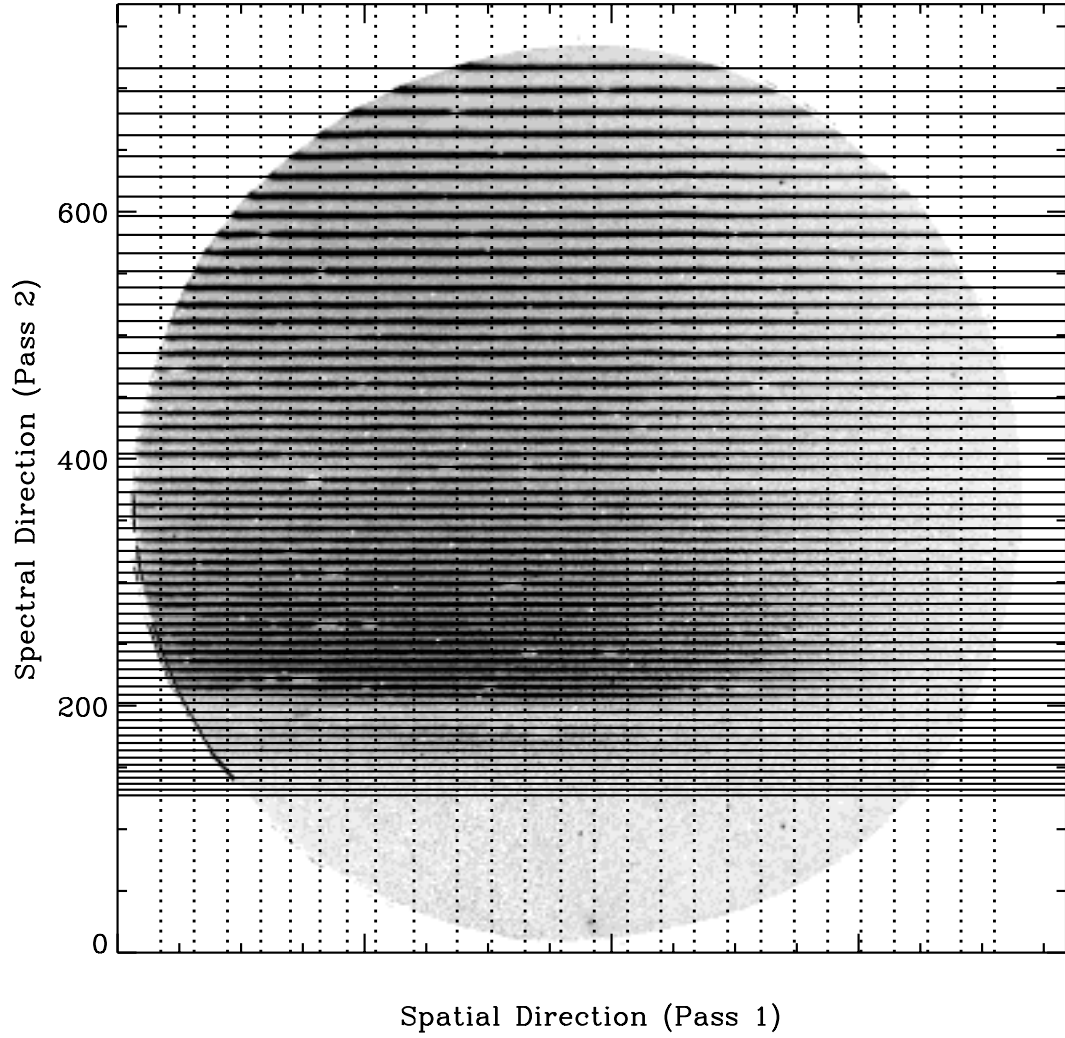


Figure A.1: Layout of the background extraction swaths on a sample SWP high-dispersion image. Lines running in vertical (spatial) direction are the Pass 1 extractions. Raw fluxes are sampled along these lines that are within the target ring and outside or between the echelle orders. The reconstructed background solutions created in Pass 2 are placed in the positions of the echelle orders (horizontal lines).

## A.2.2 Pass 1: Cross-Dispersion Swath Grid

### A.2.2.1 Basic Flow

For continuum source images, a series of 25 or 26 nearly equally spaced extraction swaths (slit height of 5 pixels) are made in the spatial direction of the high-dispersion SI, with a starting position at small spatial pixel numbers (short wavelength end). The swath sample positions were carefully selected to avoid contamination from any possible low-dispersion (double) exposure. Except for the first and last few Pass 1 swaths, which form short chords along the left and right edges of the camera image, each swath samples fluxes for nearly the entire range of sample positions; that is to say that they include pixels at the spatial ends of the camera which are not affected by contaminated interorder-overlap flux. The “interorder overlap” flux is described by a PSF model described below. The accumulated effects of overlapping PSFs increase as the orders become more closely spaced. The accumulation causes the interorder overlap to become increasingly severe until the camera sensitivity falls off at short wavelengths. It is this overlap which causes local background extractions in IUESIPS to be systematically high for short-wavelength orders and which necessitated a strategy for *BCKGRD* to sample background fluxes in distant uncontaminated regions as well as local contaminated ones.

The fluxes sampled from interorder pixels are modified if they are affected by contamination from neighboring orders. A model PSF provides an estimate of how much the fluxes should be offset before the Chebyshev fit is made (see “PSF Modeling” section below). The PSF model itself consists of two components, first, a monotonically decreasing function out to about four pixels and, second, a “halation ramp” which extends from four to about seven pixels from the center of each order profile. Each of these components is responsible for order overlap in a particular range of echelle orders. We will refer to the image area where the monotonic portion dominates as the “Interorder-Overlap Region” (IOR). The halation component is actually an extension of the IOR. However, *BCKGRD* treats it separately because, unlike the IOR, its characterization is independent of the order profiles.

The IOR and halation-dominated portions of the Pass 1 swath are indicated in Figure A.2. The initially sampled interorder fluxes in both the IOR and the halation regions are revised downward during the course of the calculations. The original and revised “working” fluxes are shown in this plot as squares and small crosses, respectively, and the flux revision for one point is shown as a downward pointing arrow. Fluxes for pixels in the halation-ramp region are affected by interorder contamination just like the triangle-inscribed IOR region, but in these cases only from the flat PSFs of the two neighboring orders. Because this overlap is constant, the algorithm may estimate it for several orders along the swath and determine a robust correction for halation. Note that the overwhelming majority of orders are subject to overlap by either the monotonic (IOR) or ramp components of the PSF.

In broad strokes, an initial estimate of the overlap for a given order is performed by computing peaks of adjacent orders above the interorder flux minimum and using the PSF to compute the fractional order flux to be subtracted from the sampled interorder fluxes. Before discussing this procedure in detail, it is necessary first to describe in more detail the

different domains of a Pass 1 swath where each of the PSF components dominates.

#### A.2.2.2 Differentiation of Swath Regions

The continuous undulating line in Figure A.2 is the Chebyshev solution for an actual Pass 1 swath of an SWP image. The IOR area is denoted by a dashed triangle with vertices at spatial pixel numbers  $nc$ ,  $nf$ , and  $nd$ . The normal execution of the background determination code requires that valid background pixels are sampled at these three points as well as the adjacent points  $nc - 1$ ,  $nf + 1$ , and  $nd + 1$ . In Figure A.2 the rise from  $nd$  to  $nf$  is determined largely by the width of the PSF. This slope may vary because of circumstances for a particular exposure. For example, the slope of the  $\overline{nf\ nd}$  leg of the IOR triangle is different for trailed images than for point-source images. Because this slope is a property of the swath itself, *BCKGRD* can use it to refine the overlap as estimated from the model PSF. The overlap between  $nc$  and  $nf$  depends primarily on source energy distribution and not exposure parameters. The effect of overlap near pixel  $nc$  appears to decrease in the figure, but this is an artifact of the rapidly decreasing camera sensitivity at short wavelengths.

#### A.2.2.3 Swath-Dependent Data Files

Default template files have been created that specify the spatial pixel numbers to be avoided in the Pass 1 background extraction for each camera and for all source types (point, extended, and noncontinuum) sources. The file also includes values for  $nc$ ,  $nf$ , and  $nd$  of the IOR. Initially, the list of spatial positions to be avoided includes only the starting and ending values and the echelle order positions, but this is modified for a particular image in the initial *Data Screening* step (Section A.2.1) from the  $\nu$  flags determined in the raw image screening (*RAW\_SCREEN*) step.

#### A.2.2.4 On-the-Fly Pathology Screening

The fluxes on and off the echelle orders are used in Pass 1 to determine representative order heights and to estimate a PSF scaling factor unique to every swath of the image processed. Checks are made at this point to clip aberrant background flux values not flagged by *RAW\_SCREEN* (e.g., from negative flux extrapolations or undetected cosmic rays). Anomalous interorder flux values in such cases are replaced with local means. The same procedure is repeated if necessary to substitute highly anomalous interorder fluxes with the means of the four neighboring interorder fluxes. This procedure was adopted to cope with small pixel clusters in the long-wavelength cameras that are prone to excessive negative extrapolations.

#### A.2.2.5 PSF Modeling

The estimate of the contamination of IOR and halation-ramp region fluxes by illumination from the spectral orders proceeds in two steps. Information from the PSF model and from the echelle order fluxes is not used in the first step, nor is a halation overlap region defined.



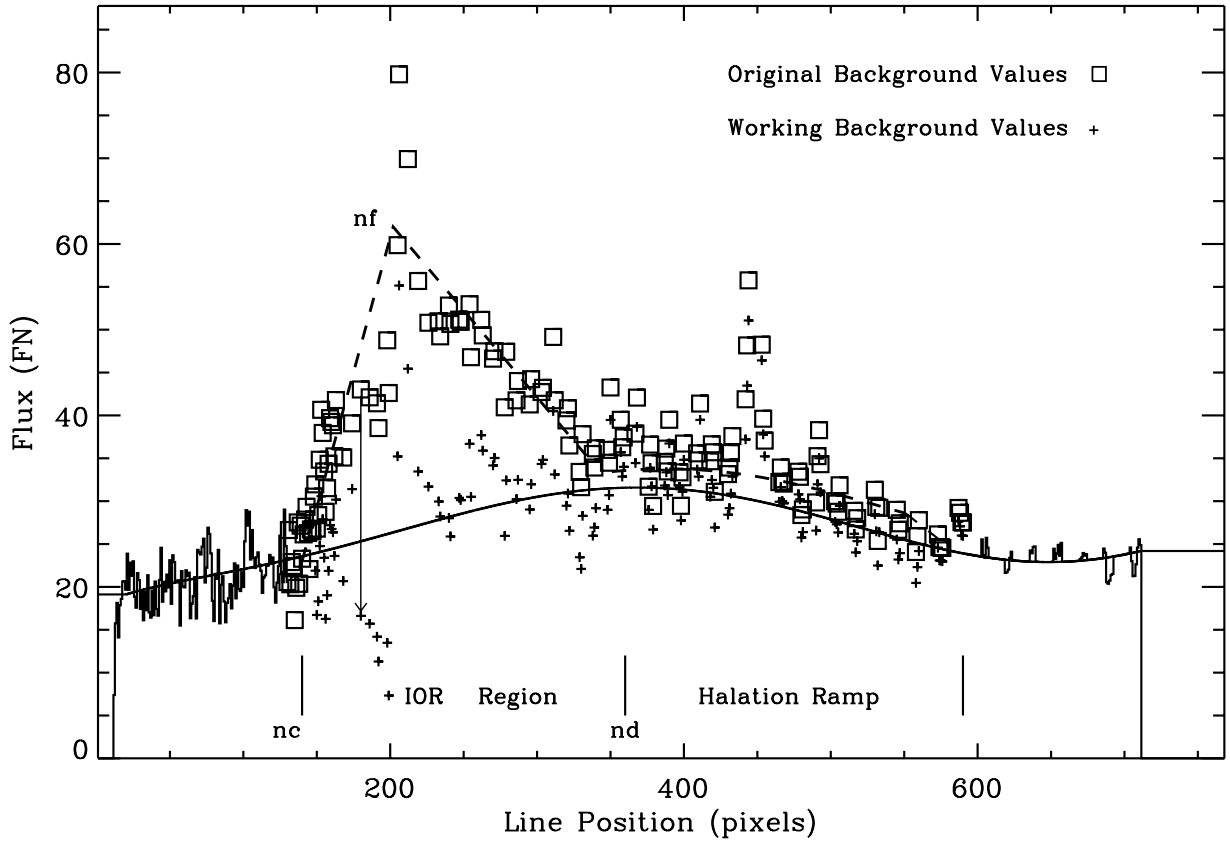


Figure A.2: Crosscut of background fluxes from a central “Pass 1” swath through an SWP image. Stellar fluxes are off-scale in this diagram. The triangular area describes the local raw background fluxes in the Interorder-Overlap Region where order crowding is severe; the halation region is shown to the right. Small crosses denote the raw fluxes corrected for overlap by the PSF model. The solid line is the Pass 1 solution, a Chebyshev, degree-7 polynomial.

The solution in this “Step 1” of Pass 1 is determined entirely from a Chebyshev interpolation from points in the end (non-IOR) regions of the swath. In the presence of certain image pathologies (Section A.2.4), as well as the first and last few Pass 1 swaths, this Step 1 is the only step; it becomes the final solution for the Pass 1 phase.

For the great majority of Pass 1 swaths, i.e. those passing through the middle of the camera image and not encountering poor statistical solutions, *BCKGRD* continues with a Step 2. This step uses the solution from Step 1 as a starting point to compute a PSF-compensated solution in which we attempt to subtract from the measured interorder fluxes the contamination from adjacent orders. As can be inferred from Figure A.3, the correction for this overlap can be determined by the simple relation:

$$Flux_{corr} = OrderHeight \times 2PSF_1/[1 - 2(PSF_1 - PSF_2)],$$

where  $Flux_{corr}$  and  $OrderHeight$  are given in FN flux units per pixel and  $PSF_1$  and  $PSF_2$  are given as a fraction of the *true* local order height. Step 2 concludes by subtracting  $Flux_{corr}$  from the local measured background at each interorder location and refitting a new Chebyshev solution through the adjusted Pass 1 swath values. Note particularly that in NEWSIPS an explicit effort is made to compensate for the contamination of the interorder fluxes (i.e., the background fluxes) in the manner described above, there is no adjustment made to correct the *on-order fluxes* (gross fluxes) for the effects of overlapping orders.

*BCKGRD* uses the same trial spatial PSF model for all types of continuum source types in a given camera. The algorithm also assumes that the PSF is global over the image. The model was determined by replicating the accumulation of flux overlap toward short wavelength orders from a large number of actual images.

Because the PSF may actually change from image to image, the algorithm attempts to accommodate such changes by using on-the-fly order information to refine the PSF model – specifically the slope of the  $\overline{nf\ nd}$  leg of the IOR triangle. This is accomplished by comparing the fractional flux overlap with the model result for a reference order within the IOR, that is by comparing the increase in overlap for this order to the overlap found at the start of the IOR (pixel  $nd$ ). If the measured and model slopes agree within a tolerance factor ( $1.5\times$ ), the program adopts the measured slope and scales the model PSF accordingly. Otherwise, the model PSF is used. Tests show that various Pass 1 swaths for a given image can either pass or fail this tolerance test independently.

### A.2.2.6 Post-Solution Pathology Tests

After a continuous Chebyshev solution is computed for a particular Pass 1 swath, a series of data pathology checks are performed on the solution (see Section A.2.5). These tests are performed only on images of point and extended sources containing continuum flux. If the solution fails any of the pathology checks, an appropriate condition is relaxed (e.g. the PSF is not used to calculate the true interorder background, or the degree of the Chebyshev fit is decreased by one). The solution is then recalculated iteratively. Since even adjacent Pass 1 swaths sometimes can pass different pathology tests, their solutions can occasionally

be different. This is a subtle but often important source of error in the final background solution. The results of these differing solutions are manifested as “spike structure” in Figure A.4, as described below.

### A.2.3 Pass 2: Dispersion Direction Swaths

In the second operation, Pass 2, inferred background fluxes at the order positions are sampled and assembled as arrays in the spectral direction. The fluxes from the Pass 1 solutions are used to compute a continuous Chebyshev solution for the background at each echelle order position. The generation of a fit along the positions of the echelle orders proceeds with the computation of a 7th-degree Chebyshev function interpolated for all sample (wavelength) positions. In this step it is not necessary to screen or exclude pixels or to test for data pathologies – only a single iteration is required. The Pass 2 operation tends to dilute the effects of poor solutions from a single Pass 1 swath. However, it also introduces a second smoothing into the final background surface.

Figure A.4 shows a final solution obtained for Order 95 of image SWP20931 on the B0 star HD93222. This order contains a strong Lyman- $\alpha$  feature. The spike pattern indicates samplings from the 26 swaths in Pass 1. A comparison of the residuals (comb pattern in the figure) shows that the solution for the Lyman- $\alpha$  order is less certain than those for long-wavelength orders where uncontaminated background pixels are common.

### A.2.4 Non-continuum images

The existence or absence of continuum flux in an *IUE* echellogram is determined by the order registration module. Because interorder-overlap flux can affect background determinations only for continuum images, in the noncontinuum case *BCKGRD* does not go through a Pass 1 step. The background estimates for these images are determined by sampling the interorder background on the long-wavelength side (spatial) of a given order with a one-pixel slit. A 7th degree Chebyshev solution is then computed for this nearly continuous array of interorder pixels. Note that tests show that some minor contamination from strongly saturated emission lines has been detected in neighboring orders.

### A.2.5 Data Pathology Assessments

Occasionally circumstances in the interorder fluxes lead to solutions that are slightly unstable, producing wiggles in an interpolated region that go beyond the flux range of sampled pixels at the two spatial ends of the camera. Such occurrences may be caused by abnormal conditions affecting the image (e.g. target-ring glow, cosmic ray hits, LWR flare, flux downturns at camera edge). A series of eight “pathology tests” has been added to *BCKGRD* to protect against blind solutions at the end of Pass 1 that do not agree with simple and often correct interpolations. These checks generally rely on a comparison of fluxes at two or more pixels along the swath or on a ratio of smoothed flux ranges. The rms statistic computed

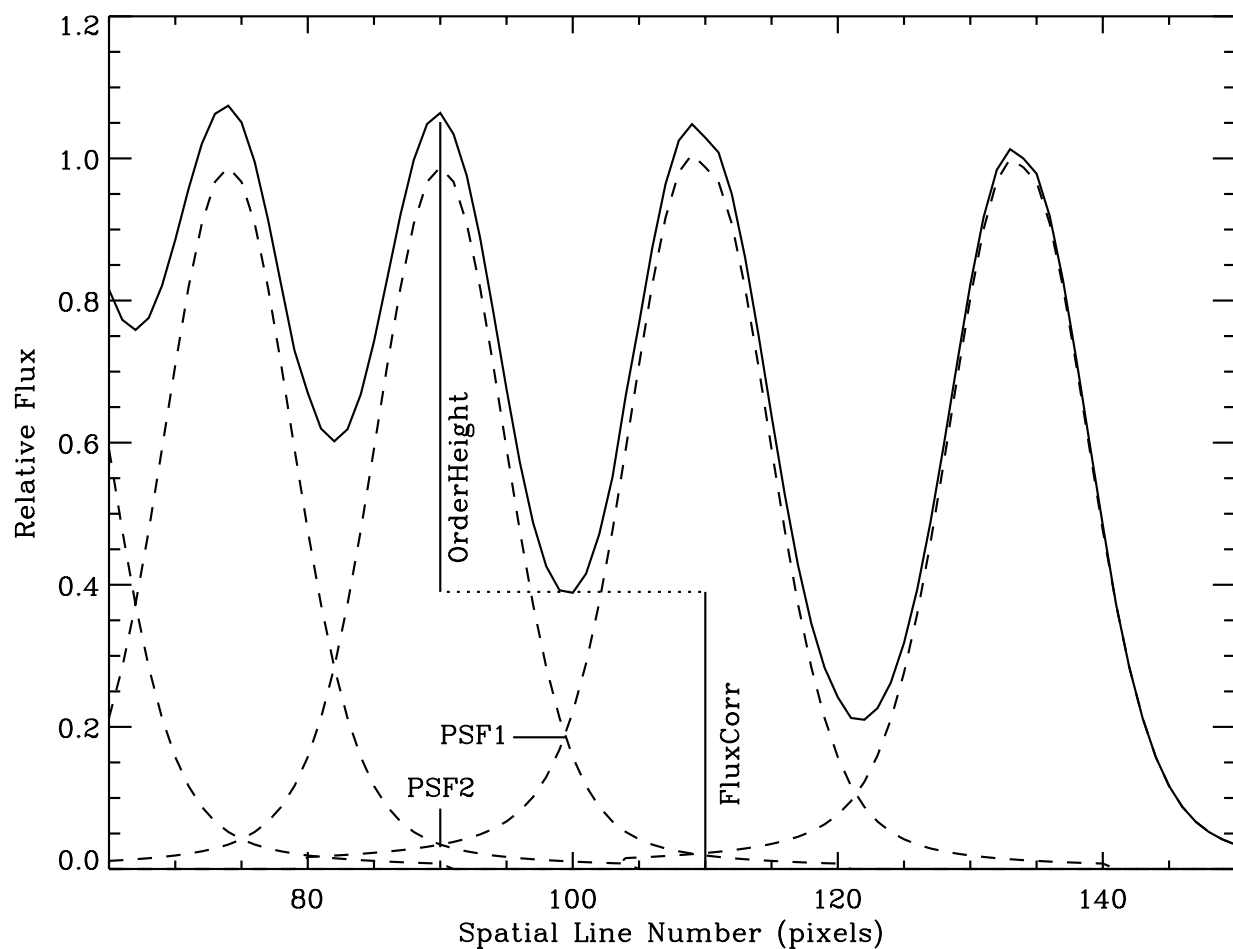


Figure A.3: A depiction of the influence of interorder overlap in progressively raising the intensity of (unit height) orders towards shorter wavelengths (left). The dashed lines represent intensities the orders would have if there were no overlap.

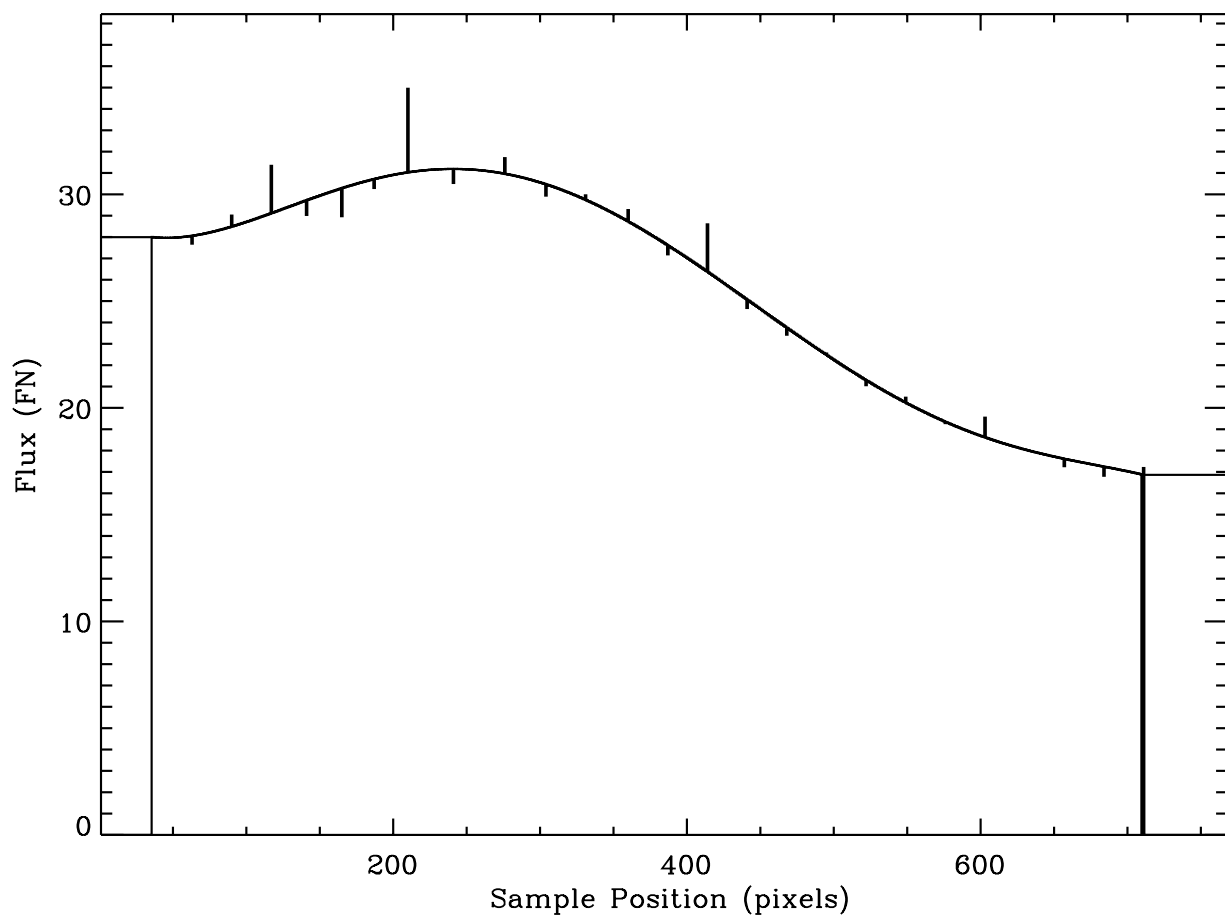


Figure A.4: Final background solution for SWP20931, order 95 (smooth solid line). The comb structure connected to the solution reflects the solutions for the various Pass 1 swaths sampled at the line position of this order.

from local raw background fluxes is a convenient unit of measure for flux ranges because it does not rely upon source brightness, exposure time, or an arbitrary flux level. In most cases a failure of a solution in a pathology test causes either the PSF information not to be used in Pass 1, the degree of the polynomial fit to the interorder data to be reduced, or both. Lowering the fitting degree has the effect of removing extra wiggles in the solution; however, the degree of the Chebyshev fit is never reduced below 3. In those cases where superfluous wiggles in the IOR region persist stubbornly after a few trials, a simple linear interpolation is adopted between “good” regions. This may occur for spatial positions toward the short wavelength (spatial) end of the IOR for certain swaths having reliable background samplings at the target edge. These tests are used only for continuum source images in Pass 1. Therefore, the final output background vectors from Pass 2 are still guaranteed to be pure continuous Chebyshev functions.

The data pathology tests keep track of the number of iterations through the swath-fitting routines, as well as a history of previous failure modes. Certain pathologies have been found to oscillate sometimes between two types of failures. If such patterns are detected, a fall-back exit option is adopted. Table A.1 summarizes the pathology checks and the strategies for circumventing them in subsequent iterations of the swath-fitting routine.

*BCKGRD* establishes a hierarchy of severity for the various pathologies it identifies. Tests 1–4 and 8 are the most critical, and the responses to failure of them are therefore more severe. Each test looks for a different and well known pathology. For example, Test 4 and Test 6 search for subtly different degrees of a similar pathology, so their response strategies are different. Test 2 searches for a solution minimum within the IOR (exceeding a tolerance) compared over the rest of the swath whereas Test 8 searches for a flux minimum in the solution anywhere within the swath. Test 2 permits a milder fix while Test 8 looks for a more severe IOR minimum. If Test 8 detects this condition, a linear interpolation between  $nc$  and 50 pixels beyond  $nd$  is used, with points in the halation ramp taken from the measured interorder flux values, without consideration of the PSF. If Test 2 repeatedly fails, the IOR-minimum pathology is guaranteed to be addressed by linear interpolation in Test 8.

Experience has shown that Test 7 is one of the most commonly occurring rejections of an initial solution. This test rejects having a local maximum at the high-sample number end of a swath. These rejections are often caused by an abnormal global shift of the spectral image format combined with target ring glow, but they can result also from any systematic rise in flux toward the short wavelength (spatial) end of the camera as well. If the pathology cannot be circumvented by decreasing the degree of the Chebyshev fit or by resorting to ignoring the PSF information in the swath-fitting routine, the solution is admitted. Test 7 is similar to Test 3 but checks for two maxima in the the middle of the short-wavelength (spatial) end of the image. In Test 3 one of the maxima searched for must be within the IOR, but this is not necessarily true for Test 7. Test 3 also checks for flare discharges which can occur in the long-wavelength corner of LWR images and computes two possible solutions: the first is a pure Chebyshev solution with the flare points dewighted and the second is a quadratic extrapolation of the solution without the flared region included. The solution with lower fluxes in the upturned flare region is then adopted, as this solution causes ringing less

frequently.

A rejection by Test 5a, which searches for a maximum in the IOR, causes the degree of the fit to be decreased on the first iteration and halves the trial PSF slope factor. It interpolates linearly over this region if additional iterations are necessary. Test 5b searches for an excessive minimum for spatial positions at the short wavelength (spatial) end of the image and the beginning of the IOR. A minimum in the IOR is usually caused either by a bright target ring at the beginning of the swath, or an overestimate of the PSF. Such conditions cause a false overcorrection for background contamination within the IOR and hence a background solution which is too low. Both tests are addressed by decreasing the Chebyshev degree.

### A.3 Failure Modes

The background swath fitting process is considered to fail a particular Pass 1 swath if any of the following conditions apply.

- Fewer than 20 valid background pixels exist in the swath.
- The first two valid background pixels in the swath are not continuous.
- There are no data gaps in the swath (continuum image only).
- The starting pixel for the IOR is less than spatial pixel number 3 in the swath (continuum sources only).
- The first and last pixel with usable background fluxes are on the same side of the IOR (continuum sources only).

When a solution for a Pass 1 swath fails any of these tests, the background solution is set to zero for the entire swath. If this occurs for an isolated swath, an interpolated solution based on the two neighboring Pass 1 swaths is substituted for the original solution. If two consecutive Pass 1 swaths, or a total of five, have null values based on these conditions, the background arrays for the entire image are set to zero, and *BCKGRD* has “given up” on the image. This occurs for an exceedingly small number of images (e.g., about 13 out of 12,898 images in the GSFC high-dispersion archives), usually as a consequence of a major portion of the image being missing. This condition is documented in the processing history log.

### A.4 Problem Areas

Tests have shown that high-dispersion spectra from each of the three *IUE* cameras have characteristics that impose unique challenges for automated background extraction algorithms. The great diversity of image types in the archives prohibits implementing any strategy that

Table A.1: Recourses to Various Pathological Trial Solutions

TEST NUMBER	CONDITION/RECOURSES
1 Short Swaths	Solution monotonic between $nd$ & $nf$ : If poly. degree $> 3$ , decrease degree; otherwise linearly interpolate.
2 IOR Min.	Min. in IOR between $nc$ & $nd$ ; decrease degree, on third attempt, give up.
3 Max. near swath end [LWR Flare]	Max. at high sample no.: decrease degree. [Lower weights for points in flare]
4 IOR Max.	Max. in IOR is max. for swath: decrease degree
5a Max. at or near swath start	Max. at low sample no.: decrease degree & reduce slope of PSF model
5b Min. at or near swath start	Min. at low sample no.: 1st time: go to Test 6; thereafter: decrease degree or interpolate linear solution
6 IOR max.	Max. within IOR: decrease degree or interpolate linearly across IOR
7 Max. at end	Max. at high sample no.: decrease degree
8 IOR min. Absolute!	Absolute min. is in IOR: interpolate linearly in IOR



makes assumptions about the behavior of source spectra in order to fix background problems, particularly in an automated processing environment.

The SWP camera has a unique confluence of conditions, a circular target ring and a blaze function shifted towards short wavelengths along the echelle-dispersion direction, which together make it impossible to sample local background at the short wavelength corner of the image. For spectra of early-type objects, these conditions almost guarantee that for the shortest-wavelength swaths in Pass 1 no pixels will be found at the short end (spatial) of the swath to use for interpolation in the IOR. In these cases the solutions will turn upwards in this region. This problem is addressed at the end of the first pass of *BCKGRD* by grafting a solution from a neighboring swath in place of the turned-up solution. Experience shows that this strategy is sometimes only partially successful for SWP images. As a result the final background solution in the short-wavelength corner is sometimes too high. This behavior can influence the background solutions for the blue wing of Lyman  $\alpha$  and lines of neighboring echelle orders that fall in the same blaze region to be as much as a few percent too high relative to the local continuum. This is probably the most significant systematic error produced by *BCKGRD*. However, we emphasize that this problem is inherent in the placement of these spectral features close to the target ring. Therefore, even customized extractions will not be able to model an accurate local background solution in this region.

Both long-wavelength cameras have the problem of a number of specific pixels being habitually converted from low DNs to highly negative FNs. In general, this is not a problem because *BCKGRD* clips highly aberrant fluxes before its Chebyshev fitting. However, the problem of clipping only aberrant fluxes is complicated for the LWP camera because of the turndown of the local background at the long-wavelength (spatial) end of the target. This complexity has been treated by disallowing clipping of anomalous fluxes in this region of the LWP image. Another complication is that although a 7th degree is usually sufficient to fit the flux turndown near the target ring, the solution may not adequately follow the turndown if the background fluxes are noisy or have caused the Chebyshev degree to be reduced to less than 6. Generally, there are no “notable” spectral lines in these orders, but a customized extraction can take care of this problem should the need arise.

An additional characteristic of the LWP camera fluxes is the abrupt increase in noise in the short (spatial) end of the image. It is not clear that this causes systematic background deviations, but it may cause a degraded accuracy in the background result.

The LWR camera exhibits a few patches of enhanced sensitivity that are not completely calibrated out in the photometric correction step. The most dramatic of these is the “flare” at the long spatial and short-wavelength (dispersion) corner of late-epoch images. Inspection of many images shows an upturn in the local background in this area even during the *IUE* Commissioning Period. Therefore, background fluxes extracted in this area either by NEWSIPS or by customized extractions should be used with caution.

# Appendix B

## Glossary

The following is a list of acronyms and abbreviations used in the text of this document, along with the corresponding definitions:

**1-D** – 1-Dimensional

**2-D** – 2-Dimensional

**3-D** – 3-Dimensional

**ASCII** – American Standard Code for Information Interchange

**BCKGRD** – High-Dispersion Background Determination Module

**CALUV** – Ultraviolet Flood Lamp

**CDI** – Core Data Item

**CDS** – Astronomical Data Center of Strasbourg

**CRHI** – Cosmic Ray Image Extension to the SIHI (NEWSIPS)

**CROSS-CORR** – Cross-Correlation Module

**DCG** – Data Coordination Group

**DMU** – Data Multiplexer Unit

**DN** – Data Number (pixel intensity from the raw image)

**EBCDIC** – Extended Binary Coded Decimal Interchange Code

**ELBL** – Extended Line-by-Line Image (IUESIPS)

**ESA** – European Space Agency

**EXTRACT** – High-Dispersion Boxcar Extraction Module

**FADC** – Final Archive Definition Committee

**FES** – Fine Error Sensor

**FITS** – Flexible Image Transport System

**FN** – Flux Number (pixel intensity from the photometrically corrected image)

**FPM** – Flux Particle Monitor

**FTP** – File Transfer Protocol

**GEOM** – Geometric Correction Module

**GMT** – Greenwich Mean Time

**GO** – Guest Observer

**GSFC** – Goddard Space Flight Center; Greenbelt, Maryland

**HDU** – Header and Data Unit

**ID** – Identification

**IOR** – Interorder Overlap Region

**IRAF** – Image Reduction and Analysis Facility

**ITF** – Intensity Transfer Function

**IUE** – International Ultraviolet Explorer

**IUEOCC** – IUE Operations Control Center

**IUESIPS** – IUE Spectral Image Processing System

**IUESOC** – IUE Science Operations Center

**LF** – Linearized  $\nu$ -Flag Image (NEWSIPS)

**LFHI** –  $\nu$ -Flag Image Extension to the LIHI (NEWSIPS)

**LFLO** –  $\nu$ -Flag Image Extension to the LILO (NEWSIPS)

**LI** – Linearized Image (NEWSIPS)

**LIHI** – High-Dispersion Linearized Image FITS File (NEWSIPS)

**LILO** – Low-Dispersion Linearized Image FITS File (NEWSIPS)

**LWLA** – Long Wavelength Large Aperture

**LWP** – Long Wavelength Prime Camera

**LWR** – Long Wavelength Redundant Camera

**LWSA** – Long Wavelength Small Aperture

**MMF** – Missing Minor Frame

**MX** – Merged Extracted Image (NEWSIPS)

**MXHI** – High-Dispersion Merged Extracted Image FITS File (NEWSIPS)

**MXLO** – Low-Dispersion Merged Extracted Image FITS File (NEWSIPS)

**NAG** – Numerical Algorithms Group, Ltd. (providers of certain FORTRAN routines used in NEWSIPS)

**NASA** – National Aeronautics and Space Administration

**NEWSIPS** – New Spectral Image Processing System

**NOST** – NASA/Science Office of Standards and Technology

**OBC** – On-board Computer

**ORDERG** – High-Dispersion Order Registration Module (part of *RAW\_SCREEN*)

**PHOTOM** – Photometric Correction Module

**PIXEL** – Picture Element

**POT** – Preplanned Observation Tape

**PSF** – Point Spread Function

**PT-NE** – Platinum-Neon

**RA** – Resident Astronomer

**RAW\_SCREEN** – Raw Image Screening Module

**RI** – Raw Image (NEWSIPS)

**RIHI** – High-Dispersion Raw Image FITS File (NEWSIPS)

**RILO** – Low-Dispersion Raw Image FITS File (NEWSIPS)

**ROLO** – Original Raw Image Extension to the RILO (NEWSIPS)

**S/C** – Spacecraft

**SCRIPTS** – Observing Specifications Log

**SEC** – Secondary Electron Conduction

**SERC** – Science and Engineering Research Council (U.K.)

**SF** – Resampled  $\nu$ -Flag Image (NEWSIPS)

**SFHI** –  $\nu$ -Flag Image Extension to the SIHI (NEWSIPS)

**SFLO** –  $\nu$ -Flag Image Extension to the SILO (NEWSIPS)

**SI** – Resampled Image (NEWSIPS)

**SIHI** – High-Dispersion Resampled Image FITS File (NEWSIPS)

**SILO** – Low-Dispersion Resampled Image FITS File (NEWSIPS)

**SIMBAD** – Set of Identifications, Measurements, and Bibliography for Astronomical Data

**S/N** – Signal-to-Noise Ratio

**SWET** – Signal Weighted Extraction Technique Module

**SWLA** – Short Wavelength Large Aperture

**SWP** – Short Wavelength Prime Camera

**SWR** – Short Wavelength Redundant Camera

**SWSA** – Short Wavelength Small Aperture

**TFLOOD** – Tungsten Flood Lamp

**THDA** – Camera Head Amplifier Temperature

**TO** – Telescope Operator

**TTDC** – Mean Dispersion Constant Correction Module

**ULDA** – Uniform Low-Dispersion Archive

**UT** – Universal Time

**UV** – Ultraviolet

**UVC** – Ultraviolet to Visible Converter

**UVFLOOD** – Ultraviolet Flood Lamp

**VD** – Vector Displacements

**VDHI** – High-Dispersion Vector Displacement Image FITS File (NEWSIPS)

**VDLO** – Low-Dispersion Vector Displacement Image FITS File (NEWSIPS)

**VICAR** – Video Image Communication and Retrieval

**VILSPA** – Villafranca del Castillo, Spain (European Ground Station)

**VMS** – Virtual Machine System

**WAVECAL** – Wavelength Calibration

**WLHI** – Wavelength Binary Table Extension to the SIHI (NEWSIPS)

**XC** – Cross-Correlation Coefficients

**XCHI** – Cross-Correlation Binary Table Extension to the VDHI (NEWSIPS)

**XCLO** – Cross-Correlation Binary Table Extension to the VDLO (NEWSIPS)

# Appendix C

## References

- Bevington, P.R. 1969, *Data Reduction and Error Analysis for the Physical Sciences* (New York, McGraw-Hill)
- Bianchi, L. 1980, in *IUE Data Reduction*, edited by W.W. Weiss et al. (Austrian Solar and Space Agency, Vienna), pp. 161–166
- Boggess, A., Bohlin, R.C., Evans, D.C., Freeman, H.R., Gull, T.R., Heap, S.R., Klingle-smith, D.A., Longanecker, G.R., Sparks, W., West, D.K., Holm, A.V., Perry, P.M., Schiffer, F.H., Turnrose, B.E., Wu, C.C., Lane, A.L., Linsky, J.L., Savage, B.D., Benvenuti, P., Cassatella, A., Clavel, J., Heck, A., Macchetto, F., Penston, M.V., Selvelli, P.L., Dunford, E., Gondhalekar, P., Oliver, M.B., Sanford, M.C.W., Stickland, D., Boksenberg, A., Coleman, C.I., Snijders, M.A.J., Wilson, R. 1978, *Nature*, 275, 377
- Boggess, A., Carr, F.A., Evans, D.C., Fischel, D., Freeman, H. R., Fuechsel, C.F., Klingle-smith, D.A., Krueger, V.L., Longanecker, G.W., Moore, J.V., Pyle, E.J., Rebar, F., Sizemore, K.O., Sparks, W., Underhill, A.B., Vitagliano, H.D., and West, D.K. 1978, *Nature*, 275, 372
- Bohlin, R.C. 1986, *ApJ*, 308, 1001
- Bushouse, H.A. 1991a, *IUE NASA Newsletter*, No. 45, 46
- Bushouse, H.A. 1991b, *Record of the IUE Three-Agency Coordination Meeting*, November 1991, p. D-17
- Cassatella, A. 1990, *Record of the IUE Three-Agency Coordination Meeting*, May 1990, p. II-60
- Cassatella, A. 1994, *Record to the IUE Three-Agency Coordination Meeting*, August 1994
- Cassatella, A. 1996, ‘Ripple Correction and Absolute Calibration For SWP IUE High Resolution Spectra Processed With NEWSIPS Using The Revised Extraction Slit Heights’, September 1997, internal report
- Cassatella, A. 1997a, ‘Ripple Correction and Absolute Calibration For LWP IUE High Resolution Spectra Processed With NEWSIPS’, April 1997, internal report
- Cassatella, A. 1997b, ‘Ripple Correction and Absolute Calibration For LWR IUE High Res-

- olution Spectra Processed With NEWSIPS', July 1997, internal report
- Cassatella, A., Barbero, J., and Benvenuti, P. 1985, *A&A*, 144, 335
- Cassatella, A., Martin, T., and Ponz D. 1981, *Report to the IUE Three-Agency Coordination Meeting*, October 1981
- Cassatella, A. and Martin, T. 1982, *Report to the IUE Three-Agency Coordination Meeting*, September 1982
- Cassatella, A., Selvelli, P.L., Ponz, J.D., González-Riestra, R., and Vogel, M. 1994, *A&A*, 281, 594
- Coleman, C., Golton, E., Gondhalekar, P., Hall, J., Oliver, M., Sanford, M., Snijders, T., and Stewart, B. 1977, *IUE Technical Note No. 31, Camera Users Guide*, October 1977, Appleton Laboratory, University College London
- Crenshaw, D.M., Bruegman, O.W., and Norman, D.J. 1990, *PASP*, 102, 463
- Crenshaw, D.M., Bruegman, O.W., Johnson, R., and Fitzurka, M. 1996, *PASP*, 108, 925
- Crenshaw, D.M. and Park, E.A. 1989, *Record of the IUE Three-Agency Coordination Meeting*, May 1989, p. II-14
- Data Coordination Group 1995, 'FITS Format for the IUE Final Archive', October 1995, internal report
- De La Peña, M.D. 1989, *IUE NASA Newsletter*, No. 38, 41
- De La Peña, M.D. 1992, *IUE NASA Newsletter*, No. 49, 63
- De La Peña, M.D. and Coulter, B.T. 1996, *IUE NASA Newsletter*, No. 56, 88
- De La Peña, M.D., Shaw, R.A., Linde, P., and Dravins, D. 1990, *Proc. Int. Symp. 'Evolution in Astrophysics'*, ESA SP-310, 617
- de Boer, K.S., Preussner, P.R., and Grewing, M. 1983, *IUE NASA Newsletter*, No. 20, 15
- Evans, D.C. 1975, *IUE File Memo #240*, unpublished.
- Evans, N.R. and Imhoff, C.L. 1985, *IUE NASA Newsletter*, No. 28, 77
- Fahey, R.P., Bogert, J.M., and Smith, M. 1994, *Record of the IUE Three-Agency Coordination Meeting*, August 1994
- Garhart, M.P. 1991, *IUE NASA Newsletter*, No. 46, 65
- Garhart, M.P. 1992a, *IUE NASA Newsletter*, No. 48, 80
- Garhart, M.P. 1992b, *IUE NASA Newsletter*, No. 48, 88
- Garhart, M.P. 1992c, *IUE NASA Newsletter*, No. 48, 98
- Garhart, M.P. 1993, *IUE NASA Newsletter*, No. 51, 1
- Garhart, M.P. 1996, *IUE NASA Newsletter*, No. 56, 9
- Garhart, M.P. 1997, *IUE NASA Newsletter*, No. 58, in print
- Goddard Space Flight Center 1976, *System Design Report for the International Ultraviolet Explorer: Scientific Instrument*, IUE-401-76-099, Volume 1, August 1976
- Goddard Space Flight Center 1986, *IUE Image Header Document, Version 2*, June 1986
- González-Riestra, R. 1991, *Record of the IUE Three-Agency Coordination Meeting*, June 1991, p. VI-82
- González-Riestra, R., Cassatella, A., and de la Fuente, A. 1992, *Record of the IUE Three-*



- Agency Coordination Meeting*, November 1992, p. D-78
- Grady, C.A., *Record of the IUE Three-Agency Coordination Meeting*, October 1985, p. U-2
- Harris, A.W. 1985, IUE NASA Newsletter, No. 28, 22
- Harris, A.W. and Cassatella, A. 1985, IUE ESA Newsletter, No. 22, 9
- Holm, A.V. and Panek, R.J. 1982, IUE NASA Newsletter, No. 18, 56
- Horne, K. 1986, PASP, 98, 609
- Imhoff, C.L. 1984a, private communication, cited from the *International Ultraviolet Explorer Image Processing Information Manual, Version 2.0*
- Imhoff, C.L. 1984b, *Record of the IUE Three-Agency Coordination Meeting*, April 1984, p. B7-1
- Imhoff, C.L. 1986, *Record of the IUE Three-Agency Coordination Meeting*, June 1986, p. 2a-1
- Imhoff, C.L. 1991, *Record of the IUE Three-Agency Coordination Meeting*, June 1991, p. VII-8
- Kinney, A.L., Bohlin, R.C., and Neill, J.D. 1991, PASP, 103, 694
- Nichols, J.S., Garhart, M.P., De La Peña, M.D., and Levay, K.L. 1993, *International Ultraviolet Explorer New Spectral Image Processing System Information Manual: Low-Dispersion Data, Version 1.0*, CSC/SD-93/6062
- Nichols-Bohlin, J. 1988, IUE NASA Newsletter, No. 34, 57
- Nichols-Bohlin, J. 1990, Proc. Int. Symp. 'Evolution in Astrophysics', ESA SP-310, 207
- Northover, K.J. 1980, in IUE Data Reduction, edited by W.W. Weiss et al. (Austrian Solar and Space Agency, Vienna), pp.61-73
- NASA/Science Office of Standards and Technology 1995, *Definition of the Flexible Image Transport System (FITS)*, NOST 100-1.1 (Greenbelt: NASA/Goddard Space Flight Center)
- Numerical Algorithms Group Limited 1990, Numerical Algorithms Group Fortran Library, Mark 14, Oxford, United Kingdom
- O'Brien, P.T., Mills, D., Smith, M., England, M., Gartart, M., and Coulter, B. 1993, *Proceedings of the IUE Three-Agency Coordination Meeting*, May 1993, p. VIII-43
- Panek, R.J. and Schiffer, F.H. 1981, *Minutes of the Meeting of the International Ultraviolet Explorer Users' Committee*, September 1981, Appendix H
- Panek, R.J. 1982, IUE NASA Newsletter, No. 18, 68
- Penston, M. 1979, *Report to the IUE Three-Agency Coordination Meeting*, March 1979
- Pérez, M.R., Huber, L.F., and Esper, J. 1990, IUE NASA Newsletter, No. 45, 31
- Pitts, R.E. 1988, *Record of the IUE Three-Agency Coordination Committee*, September 1988, p. I-81
- Ponz, J.D. 1980, in IUE Data Reduction, edited by W.W. Weiss et al. (Austrian Solar and Space Agency, Vienna), pp.75-83
- Ponz, J.D., Thompson, R.W., and Muñoz, J.R. 1994, AAS, 105, 53
- Reader, J., Acquista, N., Sansonetti, C.J., and Sansonetti, J.E. 1990, ApJS, 72, 831

- Sansonetti, J.E., Reader, J., Sansonetti, C.J., and Acquista, N. 1992, Journal of Research of the National Institute of Standards and Technology, Vol. 97, No. 1, 1
- Schiffer, F.H. 1980, *Report to the IUE Three-Agency Coordination Meeting*, November 1980
- Shaw, R.A. 1989, IUE NASA Newsletter, No. 38, 34
- Shaw, R.A. 1990, Proc. Int. Symp. 'Evolution in Astrophysics', ESA SP-310, 621
- Smith, M.A. 1990a, IUE NASA Newsletter, No. 41, 116
- Smith, M.A. 1990b, Proc. Int. Symp. 'Evolution in Astrophysics', ESA SP-310, 627
- Teays, T.J. and Garhart M.P. 1990, IUE NASA Newsletter, No. 41, 94
- Thompson, R.W. 1988, IUE NASA Newsletter, No. 35, 108
- Turnrose, B.E. and Harvel, C.A. 1980, *International Ultraviolet Explorer Image Processing Information Manual, Version 1.0*, Computer Sciences Corporation, CSC/TM-79/6301
- Turnrose, B.E., Harvel, C.A., and Stone, D.F. 1981, *International Ultraviolet Explorer Image Processing Information Manual, Version 1.1*, Computer Sciences Corporation, CSC/TM-81/6268
- Turnrose, B.E. and Thompson, R.W. 1984, *International Ultraviolet Explorer Image Processing Information Manual, Version 2.0*, Computer Sciences Corporation, CSC/TM-84/6058
- Van Steenberg, M.E. 1989, IUE NASA Newsletter, No. 40, 37
- Ward, A.K. 1977, *IUE Technical Note No. 30, Camera Operations Manual*, October 1977, Appleton Laboratory, University College London
- Weinstein, D. and Pérez, M.R. 1992, *Record of the IUE Three-Agency Coordination Meeting*, November 1992, p. D-112